The photoelectronic properties of chalcogenide glass ceramic

Yang Xu

Yang Xu. The photoelectronic properties of chalcogenide glass ceramic. Material chemistry. Université de Rennes, 2014. English. NNT : 2014REN1S037 . tel-01071400

HAL Id: tel-01071400
https://theses.hal.science/tel-01071400
Submitted on 4 Oct 2014

ANNÉE 2014

THÈSE / UNIVERSITÉ DE RENNES 1
sous le sceau de l'Université Européenne de Bretagne

pour le grade de

DOCTEUR DE L'UNIVERSITÉ DE RENNES 1
Mention : Sciences de Matériaux

Ecole doctorale Science de la Matière

présentée par

Yang Xu

Préparée au Laboratoire Verres & Céramiques
UMR CNRS 6226 Institut de Sciences Chimiques de Rennes
UFR Sciences et Propriétés de la Matiére

Les propriétés photoélectriques de vitrocéramiques de chalcogénures

Thèse soutenue à Rennes
le 05 Septembre 2014

devant le jury composé de :

Xingeng DING
Professeur, Zhejiang University / *rapporteur*

Marcel PASQUINELLI
Professeur, Université d'Aix-Marseille / *rapporteur*

Laurent CALVEZ
Maîte de conférences, Université de Rennes 1/ *examinateur*

Xianghua ZHANG
Directeur de Recherche au CNRS, Université de Rennes 1 / *directeur de thèse*

Alain LAFOND
Professeur, Université de Nantes / *co-directeur de thèse*

Acknowledgement

The research works presented here are accomplished in the Laboratoire de Verres et Céramiques of Université de Rennes 1.

Firstly, I would like to express my gratitude to my PhD supervisor Mr. Xianghua Zhang for his patience and knowledgeability that directed me through the three-year research experience. The sincere thanks are also given to my co-supervisor, Mr. Alain Lafond, for his help of crystallization and my previous supervisor, Mr. Xianping Fan, for recommending me to Université de Rennes 1.

I would like to thank the members of jury for agreeing to judge the thesis. I wish to express my sincere thanks to Ms. Xingeng Ding of Zhejiang University and Mr. Marcel Pasquinelli of Université d'Aix-Marseille for their acceptance to be the reporters of my thesis. Meanwhile, I want to thank Mr. Laurent Calvez of Université de Rennes 1 for participating in my PhD defense as an invite member.

I would like to give my sincere thanks to Mr. Qianhong Shen for his kindness and for the valuable discussion and demonstration about the photocatalytic properties of glass ceramics. My thanks are addressed particularly to Mr. Zhang, for his wise advise, his imagination, as well as his encouragement throughout this work. I wish to thank all the people who helped me in completion of the project. Thanks will give to Ms. Luo Qun for making a foundation of my research. I thank Mr. Xvsheng Qiao and Yimin Wu for their help in HRTEM. I would give my thanks to Mr. Jean-Jacques Simon for his advice in semiconductor properties of material. My gratitude also goes to Ms. Hongli Ma for her helps both for my work and life.

I wish to thank all my colleagues in the laboratory, especially Bo Fan and Mathieu Rose. At first year, Mathieu make me familiar with glass preparation and other lab equipments. And Bo gave me a support and a lot of whimsy to work during my three-year work. Gratitude is also given to Didier, Thierry J. and Thierry P. for their help of the experimental equipments. My Chinese fellows, Shuo Cui, Gang Zhou, Bo Fan, Bai Xue, gave me a lot of help and made my life in France colorful.

I would like to thank especially my boyfriend Minjia, for his company and encouragement. My final thanks are addressed to my family, who never doubted me and always supported me.

Table of contents

Chapter 1 Solar conversion

Chapter 2 Compositions, structure and photoelectric properties of glass ceramics in the $GeSe_2$-Sb_2Se_3-CuI system

Chapter 3 Optimization of the crystallization process of the $40GeSe_2$-$40Sb_2Se_3$-20CuI glass ceramic

Chapter 4 Microstructure and semiconducting properties of the $40GeSe_2$-$40Sb_2Se_3$-20CuI glass ceramic

Chapter 5 Photocatalytic properties of the $40GeSe_2$-$40Sb_2Se_3$-20CuI glass ceramic

Résumé détaillé

1 Introduction

La crise de l'énergie et les problèmes environnementaux sont parmi les grands défis de l’humanité. Une exploitation efficace de l’énergie solaire, grâce à son abondance sur la Terre, pourrait permettre de résoudre les problèmes liés à l’énergie.

L’effet photovoltaïque et la photo-catalyse permettent de transformer directement l’énergie solaire en électricité ou en combustibles chimiques. Ces deux technologies sont parmi les étudiées pour utiliser l’énergie solaire. Elles nécessitent des matériaux semi-conducteurs capables d’absorber efficacement la lumière solaire en générant des paires électron-trou qui doivent avoir une durée de vie suffisamment longue.

Ce travail de thèse, inédit dans le laboratoire des verres et céramiques, est la suite inattendue d’un travail antérieur consacré au développement des vitrocéramiques dans le système $GeSe_2$-Sb_2Se_3-CuI. L’objectif était de développer des matériaux transparents dans l’infrarouge ayant une résistance mécanique nettement supérieure au verre grâce à une cristallisation contrôlée du verre. Il a été découvert que ces vitrocéramiques possèdent des propriétés optiques inhabituelles et inintéressantes pour l’application envisagée, puisque la transmission diminue quand la longueur d’onde augmente, comme le montre la figure 1. Ces matériaux sont restés dans les « tiroirs » pendant quelques années malgré le fait que ce phénomène déjà connu dans certain semi-conducteurs a été attribué à la présence de porteurs de charge libres dans le matériau.

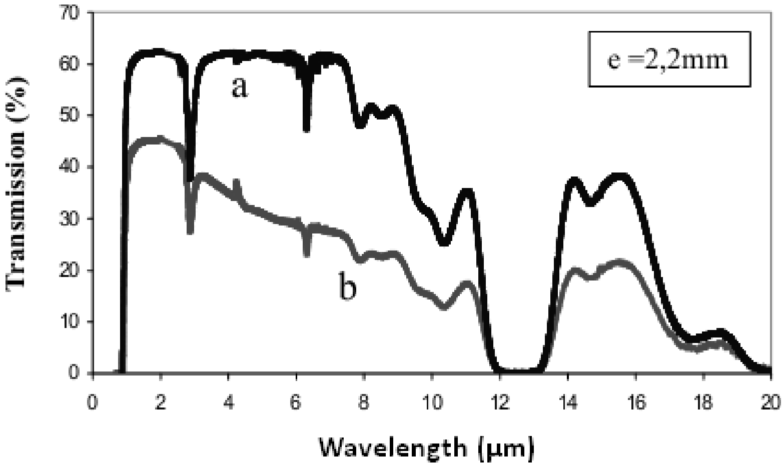

Figure 1. Courbe de transmission du verre (a) et de la vitrocéramique (b) de la même composition 60$GeSe_2$-30Sb_2Se_3-10CuI

Ce travail de thèse a débuté lorsque ces matériaux ont été testés, par curiosité, par des mesures de photo-courant sous illumination visible.

2 Optimisation de composition dans le système $GeSe_2$-Ga_2Se_3-CuI

Motivés par les premiers résultats intéressants avec un échantillon sélectionné par hasard, nous avons exploré systématiquement ce système ternaire (figure 2) avec la procédure suivante : Plusieurs séries de verres, illustrées dans ce domaine vitreux ont été préparés par la méthode de synthèse couramment utilisée pour les verres de chalcogénure. Elle consiste à mettre les matières de départ dans un tube de silice qui est ensuite scellé sous vide. Ce tube est chauffé dans un four basculant pendant environ 12 heures à une température entre 750-850°C selon la composition. Il est ensuite trempé dans l'eau à la température ambiante. Les températures caractéristiques, notamment la température de transition vitreuse et la ou les températures de cristallisation de tous les verres ont été déterminées par calorimétrie différentielle à balayage (DSC).

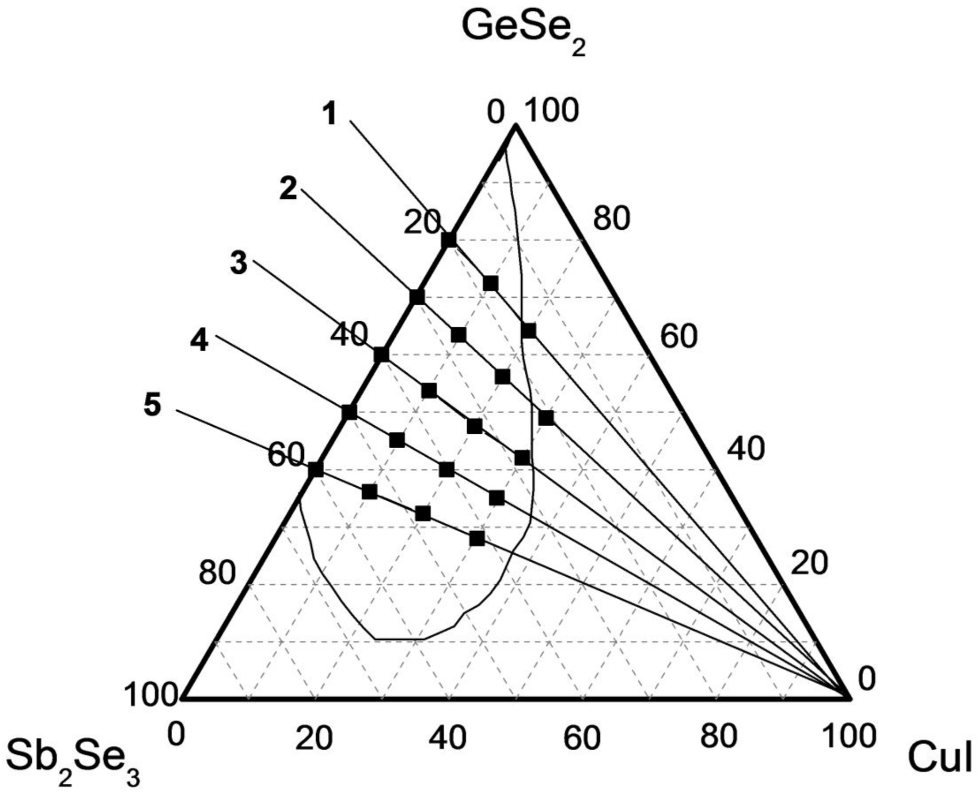

Figure 2. Domaine vitreux dans le système $GeSe_2$-Sb_2Se_3-CuI et les séries de verres étudiés

Pour permettre une comparaison rapide, une vitrocéramique est préparée à partir de tous les verres en les chauffant à la température de cristallisation pendant 1 heure. Le photocourant est mesuré sous illumination visible avec la méthode de trois électrodes illustrée à la figure 3.

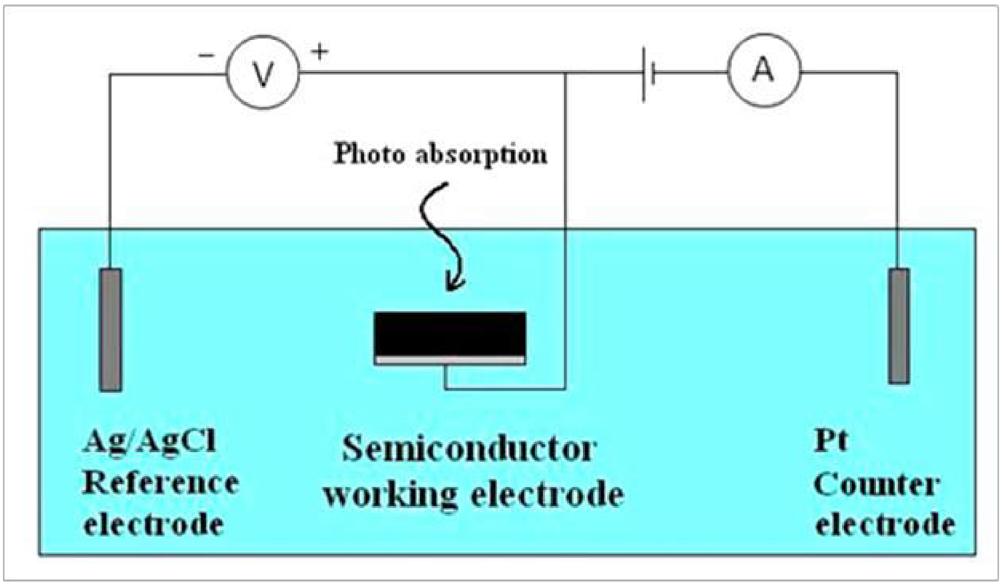

Figure 3. Méthode à trois électrodes pour mesures de photocourant

Dans ce résumé détaillé, les résultats sont donnés pour les vitrocéramiques de la série 4 ((50-x/2)$GeSe_2$-(50-x/2)Sb_2Se_3-xCuI) avec la même teneur en $GeSe_2$ et en Sb_2Se_3 qui a donné les meilleurs résultats. La figure 4 représente les spectres de diffraction aux rayons X de différentes vitrocéramiques.

Il peut être constaté que tous les pics de diffraction de la vitrocéramique obtenue à partir du verre de base sans CuI appartiennent à Sb_2Se_3, avec cependant une intensité relative de chaque pic différente par rapport au PDF standard (n ° 01-072-1184). Une étude plus détaillée est nécessaire pour comprendre les raisons. Il est vrai que la cristallisation d'une phase amorphe dans un environnement assez complexe à faible mobilité des atomes peut être très différente de la cristallisation d'un bain fondu avec la même composition.

Différentes propriétés de cette série de vitrocéramiques ont été mesurées et rassemblées dans le tableau ci-dessous (tableau I).

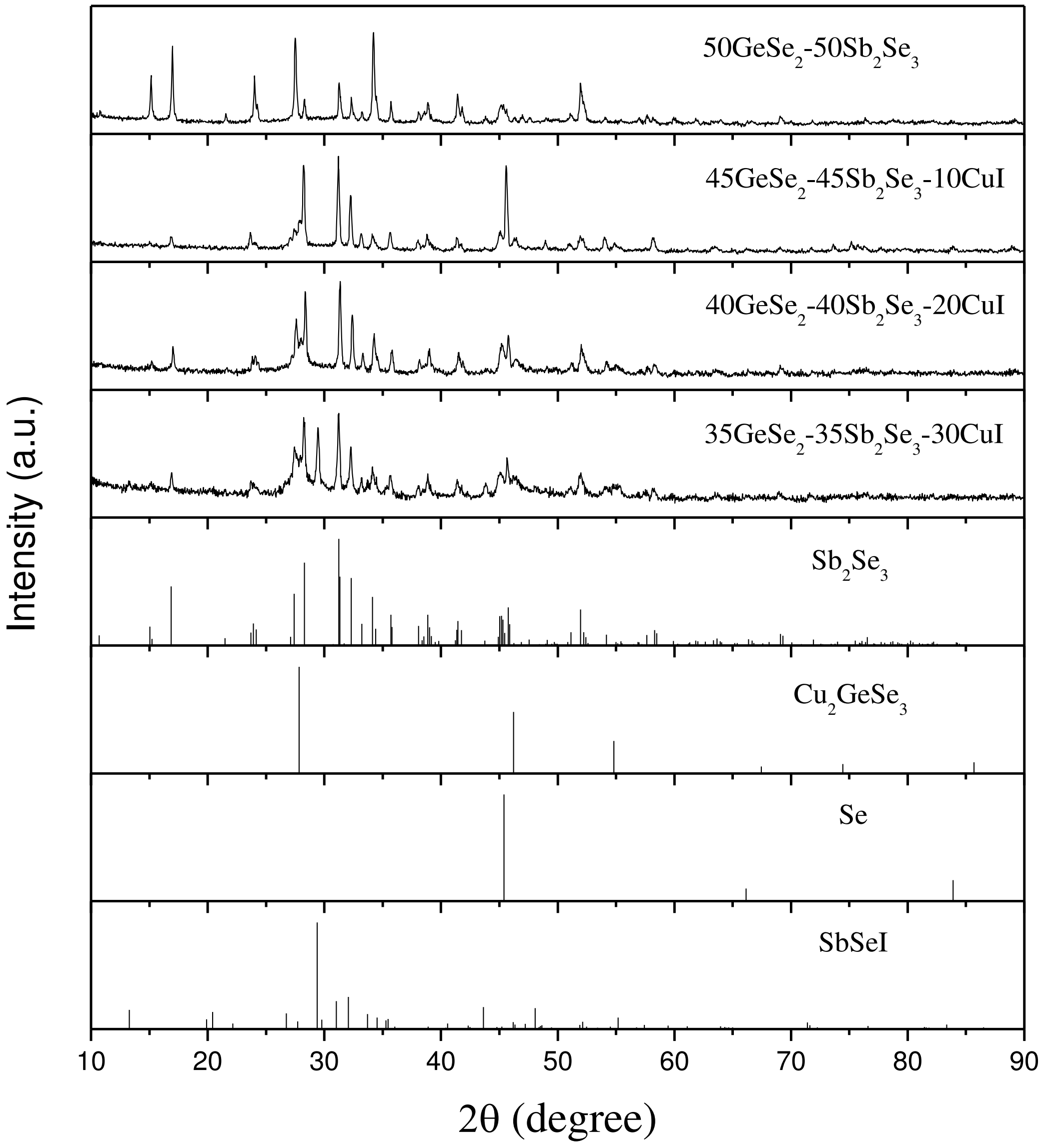

Figure 4. Diffraction aux rayons X des vitrocéramiques dans la série 4 ((50-x/2)GeSe$_2$-(50-x/2)Sb$_2$Se$_3$-xCuI)

Tableau I. différentes propriétés de la série 4 des vitrocéramiques

Echantillon	Traitement thermique	Phase cristallisée	Photocourant I_p à -0.5 V	Type	Conductivité ($\Omega^{-1}\cdot cm^{-1}$)
50GeSe$_2$-50Sb$_2$Se$_3$	353°C 1h	Sb$_2$Se$_3$	0	P	$<10^{-8}$
45GeSe$_2$-45Sb$_2$Se$_3$-10CuI	324°C 1h	Cu$_2$GeSe$_3$+Sb$_2$Se$_3$ + Se	0	P	1.8×10^{-4}
40GeSe$_2$-40Sb$_2$Se$_3$-20CuI	285°C 1h	Cu$_2$GeSe$_3$+Sb$_2$Se$_3$	-28.4 μA	N	4.4×10^{-2}
35GeSe$_2$-35Sb$_2$Se$_3$-30CuI	242°C 1h	Cu$_2$GeSe$_3$+Sb$_2$Se$_3$ + SbSeI	-23.2 μA	N	5.0×10^{-3}

Il est intéressant de noter que les deux vitrocéramiques avec 20% et 30% de CuI donnent un photocourant important. Si on examine ces deux mesures de photocourant plus en détail (figure 5), une grande différence existe. En effet, même si les deux vitrocéramiques ont été mesurées comme des semi-conducteurs du type N, la vitrocéramique avec 20% CuI montre. un photocourant au potentiel positif et négatif, supposant l'existence des phases du type P et du type N. Celle avec 30% de CuI est plus classique avec du photocourant uniquement au potentiel négatif.

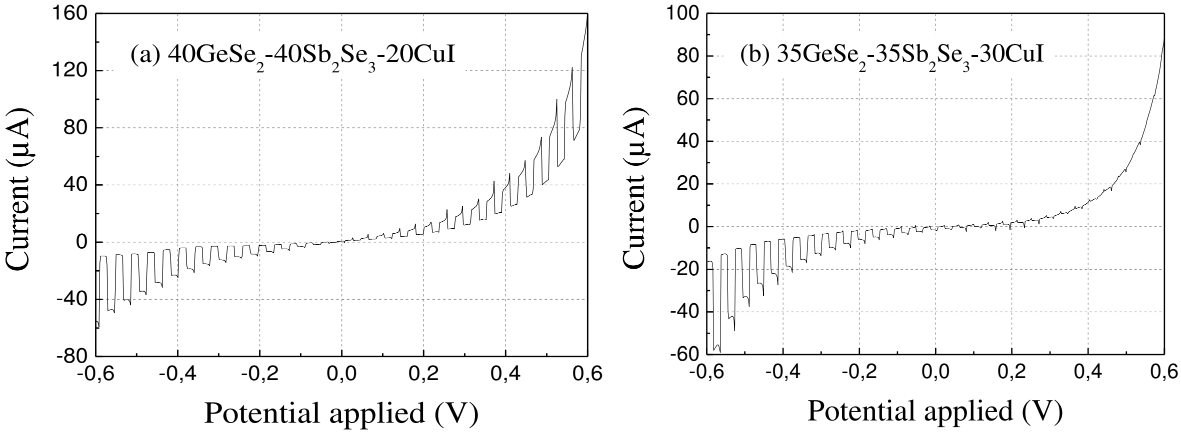

Figure 5. Photocourant des deux vitrocéramiques dans la série 4

3 Optimisation de la cristallisation du verre 40GeSe$_2$-40Sb$_2$Se$_3$-20CuI

Compte tenu de ces résultats, l étude est ensuite concentrée sur la composition 40GeSe$_2$-40Sb$_2$Se$_3$-20CuI. L'étude préliminaire montre également que la cristallisation a une influence déterminante sur les propriétés photoélectriques. Afin de mieux comprendre et de mieux maitriser ce processus, une étude dynamique a été effectuée à l'aide de la calorimétrie et a permis de déterminer des paramètres importants dans le contrôle de ce processus de cristallisation. L'exemple ici est donné par la détermination de la température et du temps optimaux pour la nucléation (figure 6).

Deux stratégies de cristallisation ont été testées. La 1$^{\text{ère}}$ consiste à chauffer le verre à une seule température pendant un temps assez long, de 1 à 9 heures typiquement. La 2$^{\text{ème}}$ méthode, appelée aussi méthode à deux étapes, consiste d'abord à faire nucléer le verre à la température optimale de nucléation (figure 6) et ensuite à faire croitre les nucléis à une température supérieure pendant un temps relativement court (1 heure environ).

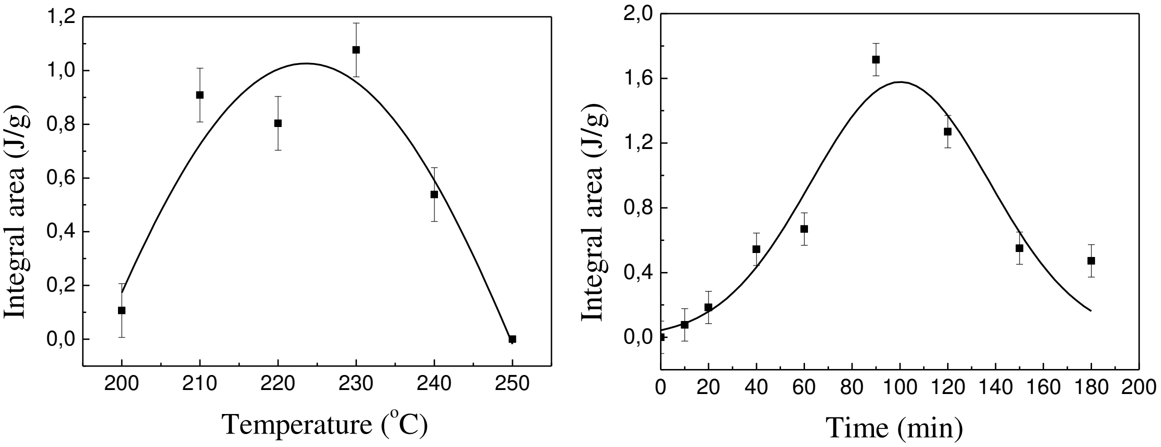

Figure 6. Optimisation de la température et du temps de nucléation pour 40GeSe$_2$-40Sb$_2$Se$_3$-20CuI

L'influence du procédé de cristallisation sur la microstructure et sur les propriétés photoélectriques des vitrocéramiques a été étudiée. Les résultats montrent que le processus de cristallisation a une influence déterminante sur la microstructure et sur les propriétés photoélectriques des vitrocéramiques. Le scénario idéal de cristallisation semble être la suivante: une génération des cristaux Sb_2Se_3 sous forme des aiguilles, suivie par la croissance in situ de nano-cristaux de Cu_2GeSe_3 sur les Sb_2Se_3. Par rapport au procédé de traitement thermique en deux étapes, le procédé en une seule étape à basse température est une stratégie plus efficace pour maximiser le photocourant.

4 Relations entre la microstructure et les propriétés (photo)électriques

La figure 7 montre la conductivité électrique des vitrocéramiques de composition 40GeSe$_2$-40Sb$_2$Se$_3$-20CuI, recuit à 260°C pendant différentes durées. On peut constater que cette conductivité augmente très rapidement pendant la 1ère heure de recuit et qu'elle se stabilise en suite à une valeur de l'ordre de $2.10^{-2}\ \Omega^{-1}\cdot\ cm^{-1}$.

Afin de comprendre ce phénomène, les échantillons ont été d'abord observés sous microscopes électroniques à balayage. Deux microstructures représentatives sont illustrées à la figure 8 pour deux vitrocéramiques avec respectivement 1 et 9 heures de recuit. On peut voir tout de suite que les cristaux sont connectés dans un cas et non dans la vitrocéramique insuffisamment recuite pendant une heure.

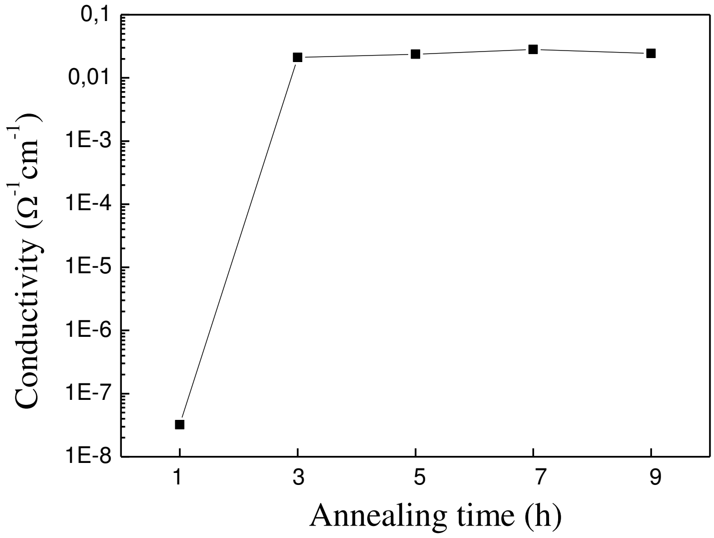

Figure 7. Conductivité électrique de la vitrocéramique 40GeSe$_2$-40Sb$_2$Se$_3$-20CuI glass en fonction du temps de recuit utilisé pour la fabrication

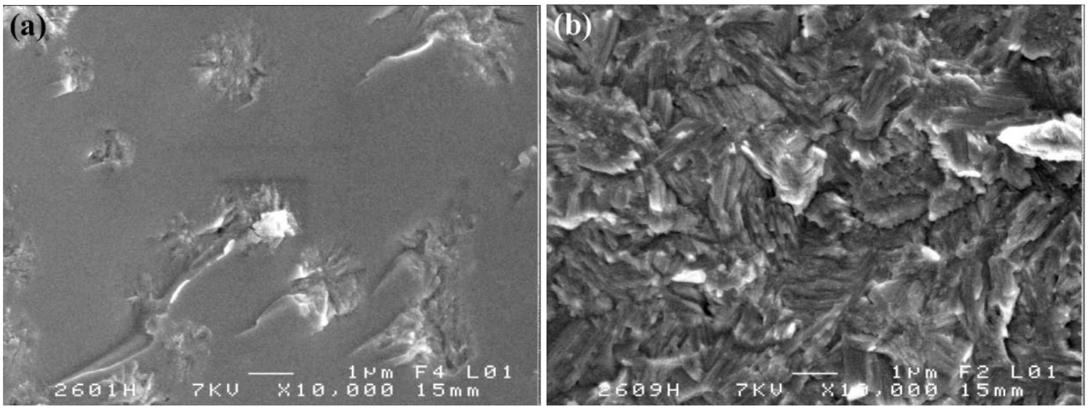

Figure 8. Images MEB de deux vitrocéramiques 40GeSe$_2$-40Sb$_2$Se$_3$-20CuI avec différente durée de recuit (a) 1h; (b) 9h

Les diffractions aux rayons X, précédemment discutées, montrent que les phases cristallisées correspondent aux phases Sb_2Se_3 et Cu_2GeSe_3. Afin d'examiner la répartition de ces deux phases cristallisées dans la vitrocéramique, la microscopie électronique en transmission haute résolution a été utilisée. Des images représentatives sont illustrées sur la figure 9.

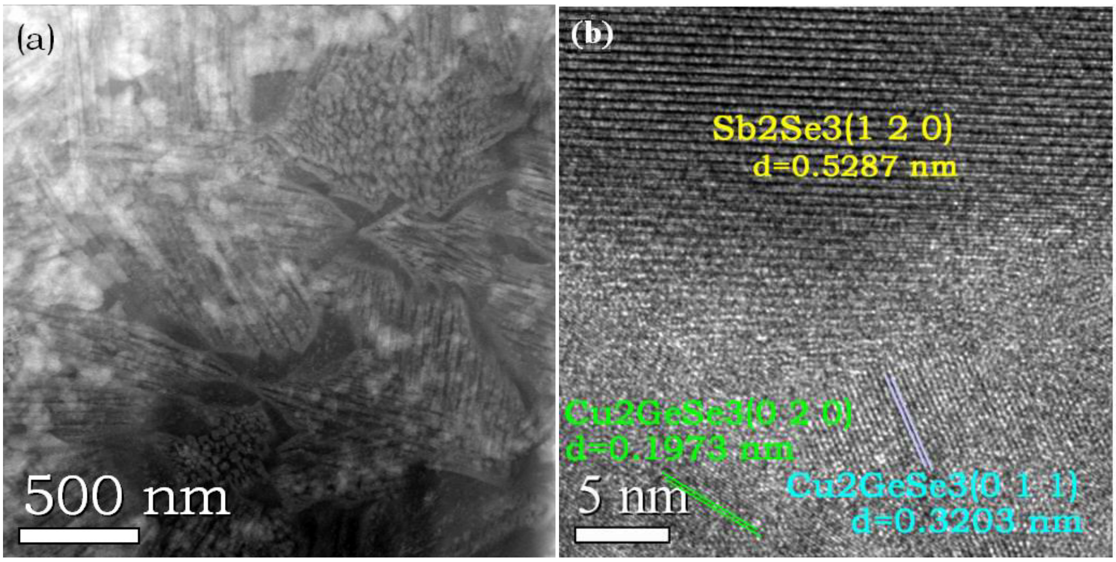

Figure 9. Images HRTEM de la vitrocéramique 40GeSe$_2$-40Sb$_2$Se$_3$-20CuI

Des cristaux Sb_2Se_3 orthorhombique sont bien présents sous forme des aiguilles. Il est aussi constaté que les phases cubiques Cu_2GeSe_3 sont généralement en contact directe avec du Sb_2Se_3.

La conductivité du Sb_2Se_3 et du Cu_2GeSe_3 est respectivement de $10^{-6}\Omega^{-1}\cdot cm^{-1}$ et de $10\Omega^{-1}\cdot cm^{-1}$. Il est donc clair que seule la phase Cu_2GeSe_3 est efficace pour augmenter la conductivité électrique de la vitrocéramique. Cette phase cubique n'est cependant pas efficace pour constituer un réseau interconnecté qui est nécessaire pour obtenir une conduction électrique à travers l'échantillon. Grâce à la nature composite de la vitrocéramique, les cristaux Sb_2Se_3 sous forme des aiguilles sont très efficaces pour constituer un réseau interconnecté. Une fine couche de Cu_2GeSe_3 conductrice sur les Sb_2Se_3 est suffisante pour rendre conducteur ce réseau interconnecté. Par conséquent, le scénario idéal de la cristallisation est le suivant : les Sb_2Se_3 se cristallisent en premiers pour former le réseau interconnecté et en suite les Cu_2GeSe_3 recouvrent progressivement les Sb_2Se_3. La cristallisation ne doit pas être très violente afin de séparer ces deux cristallisations chronologiquement. C'est sans doute la raison pour laquelle un traitement thermique à une température relativement faible est le traitement le plus efficace pour augmenter la conductivité et également pour augmenter le photocourant des vitrocéramiques.

La figure 10 confirme la présence des canaux conducteurs par des mesures de potentiel surfacique. En effet, une calibration avec des échantillons connus montre qu'un potentiel relativement faible représente une phase plus conductrice. On constate que les phases conductrices sont séparées par des phases plutôt isolantes dans le cas de la vitrocéramique 10(a), donnant ainsi un matériau plutôt isolant. Dans le cas de la figure 10(b), les phases conductrices sont connectées et la vitrocéramique présente une bonne conductivité.

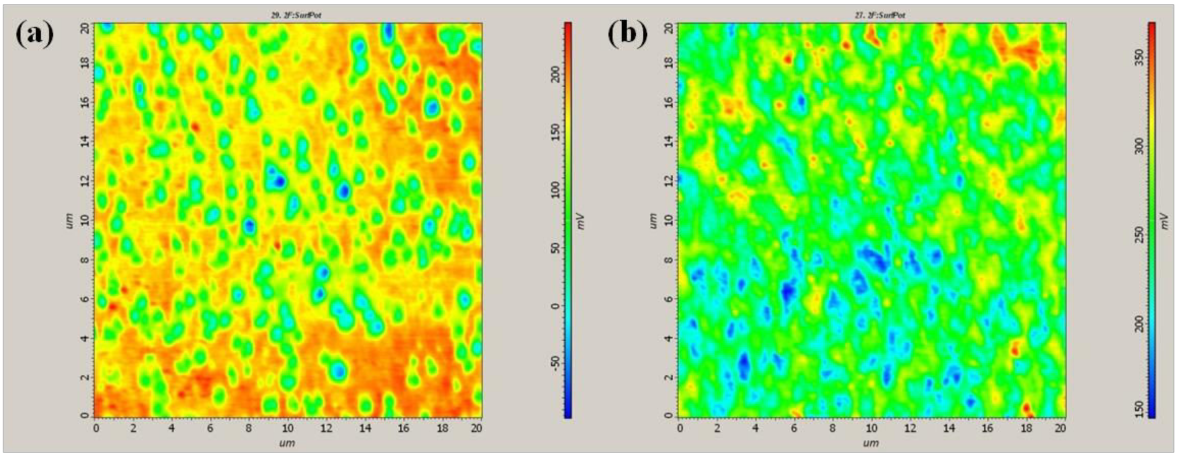

Figure 10. Image en potentiel surfacique de deux vitrocéramiques représentative avec différente conductivité (a) <10^{-8} $\Omega^{-1}\cdot cm^{-1}$; (b) 2.1×10^{-2} $\Omega^{-1}\cdot cm^{-1}$

La distribution des éléments constituant la vitrocéramique a été effectuée grâce à un STEM (Scanning transmission electron microscope) et les résultats sont illustrés sur la figure 11.

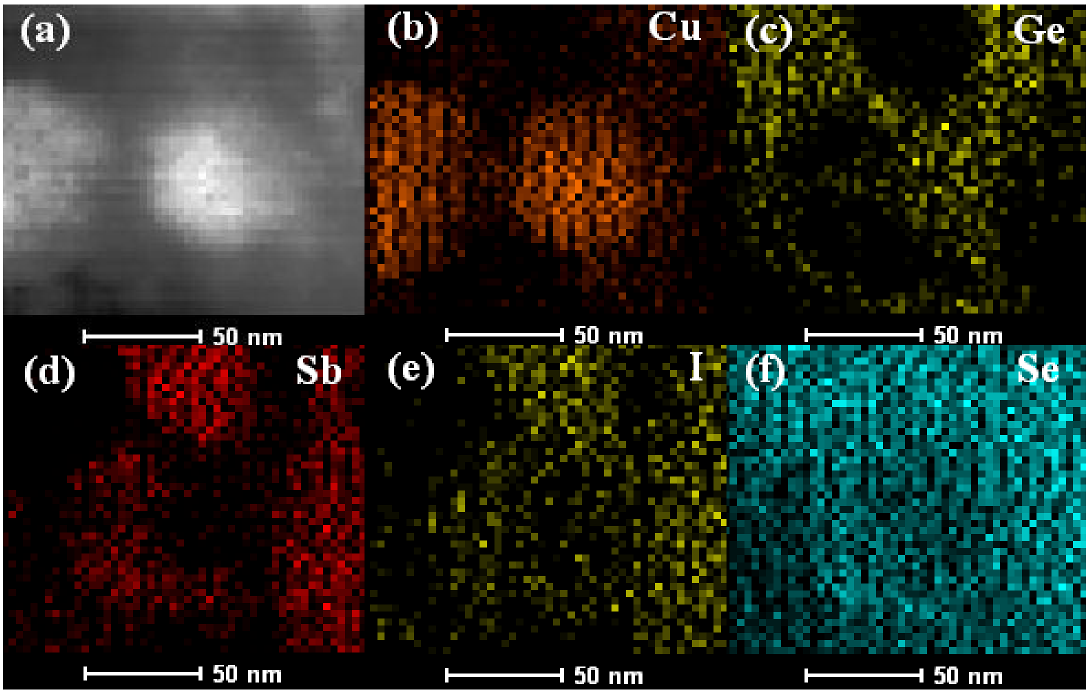

Figure 11. Distribution des éléments dans la vitrocéramique

Nous observons clairement une superposition des éléments Sb et I. Pour comprendre ce phénomène, nous avons examiné les diffractions RX d'une série de vitrocéramique avec différentes concentrations en CuI. Les résultats sont rassemblés à la figure 12. L'agrandissement affiché à droite de cette figure montre que le pic de diffraction situé à 31.2° attribué à Sb_2Se_3 se déplacent progressivement vers les petits angles avec l'introduction du CuI. Cela démontre que l'iode rentre dans la structure du Sb_2Se_3. Ceci est en accord avec le fait que les ions I^- (2.2 Å) sont plus grands que les Se^{2-} (1.9 Å) même s'il est difficile d'identifier des ions dans une structure covalente. Nous avons même constaté la cristallisation du SbSeI quand le verre de départ contient un taux de CuI supérieur à 30 mol%.

Avec le dopage de l'iode, le Sb_2Se_3 est changé du type p en type n. Nous pouvons ainsi prévoir la création des jonctions p-n à l'intérieur de la vitrocéramique avec le Sb_2Se_3 du type n, recouvert des Cu_2GeSe_3 du type p. Ceci sera démontré expérimentalement.

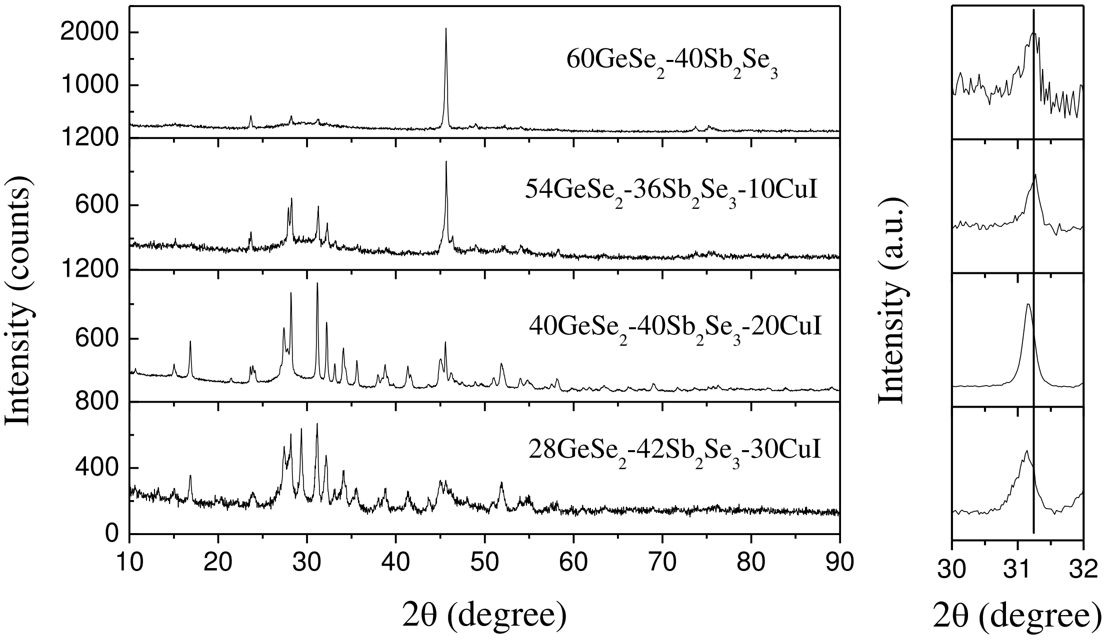

Figure 12. Diffraction aux rayons X de vitrocéramiques avec un taux différent en CuI

5 Caractérisations électroniques et électriques

Les caractéristiques I – V (courent – potentiel) d'une vitrocéramique ont été mesurées avec le schéma de mesure illustré sur la figure 13(a). Les contacts de mesure ont été préalablement vérifiés et ils sont bien ohmiques. Avec ces mesures, il est ainsi clair que la vitrocéramique contient des jonctions p-n. En effet, nous avons observé beaucoup de jonctions créées par des contacts entre des Sb_2Se_3 dopé (type) et des Cu_2GeSe_3 (type p). La vitrocéramique massive contient donc un grand nombre des jonctions p-n orientées aléatoirement. Cette structure peut être simplifiée électroniquement comme l'illustre la figure 13 (b), permettant d'expliquer le comportement I – V de la vitrocéramique.

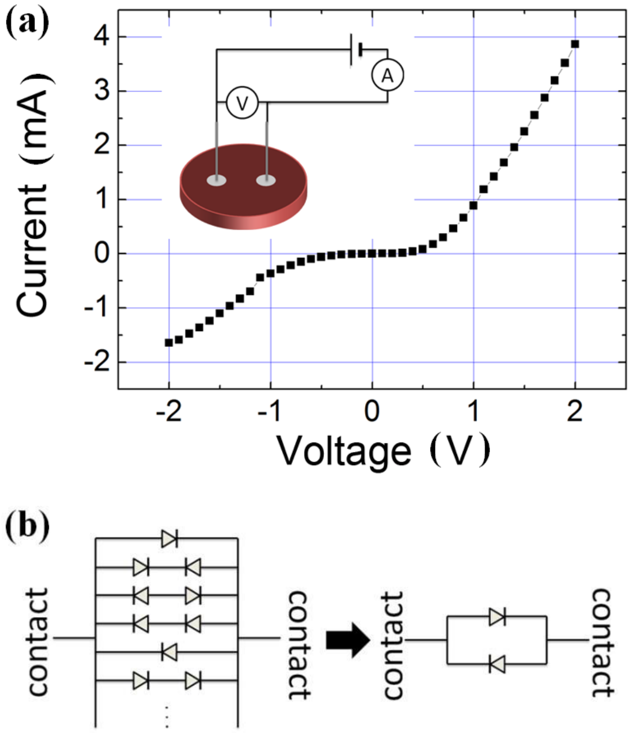

Figure 13. Coubre I-V d'une vitrocéramique et simplification des jonctions p-n

L'existence de nano-jonctions est évidemment très favorable pour la séparation des charges. C'est probablement l'une des raisons pour lesquelles ces matériaux composites présentent une très longue durée de vie des porteurs de charge minoritaire d'environ 16 µs (comme le montre la Figure 14), par rapport à des CIGS, similaires à nos matériaux en constituants et bien étudiés avec une durée de vie généralement plus courts que 0,1 µs. L'inhomogénéité de la durée de vie est associée au caractère composite du matériau avec des canaux conducteurs distribués de façon aléatoire comme précédemment mesurés

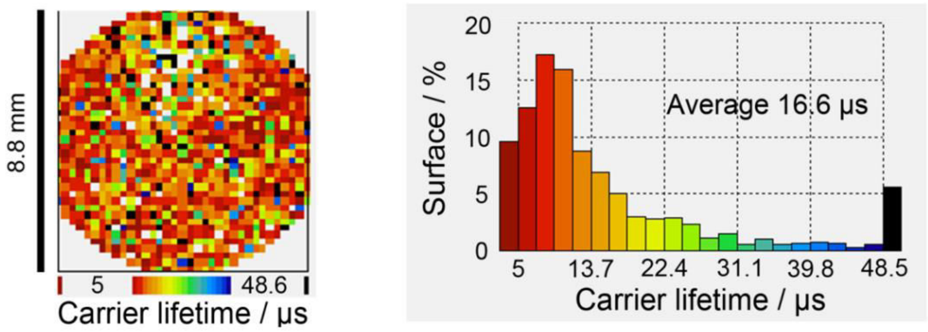

Figure 14. Distribution spatiale de la durée de vie des porteurs de charge minoritaire sur la surface d'une vitrocéramique

6 Mécanisme de photo-génération de porteurs de charge

Les mesures de photocourant ont été effectuées pour le Sb_2Se_3, le Cu_2GeSe_3 séparément et la vitrocéramique contenant ces deux phases cristallisées. Ces mesures donnent un photocourant intense de 74 uA/cm^2 (pour une tension de polarisation de - 0,6 V par rapport à l'électrode de référence Ag/AgCl) avec la vitrocéramique (figure 15). Avec les mêmes conditions de mesure, les deux phases cristallisées donnent individuellement un photocourant négligeable, inférieur à 1 µA/cm^2, comme le montre cette même figure. Ces résultats soulignent l'importance de la coexistence de ces deux phases cristallines pour générer un fort courent photoélectrique. Il semble donc que la structure microscopique, plutôt que le matériau lui-même, joue un rôle décisif dans la photo-génération, la séparation et le transport de porteurs de charge.

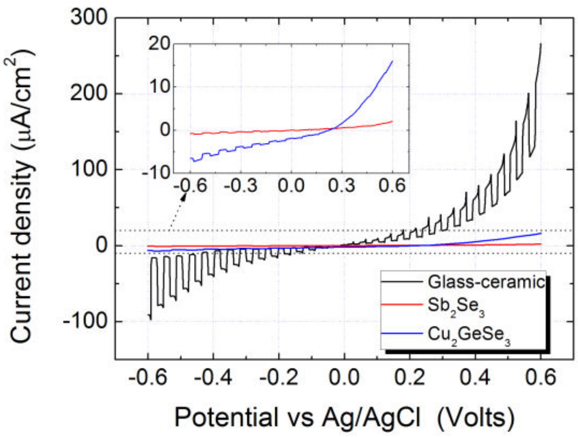

Figure 15. Photocourant des Sb_2Se_3, Cu_2GeSe_3 et de la vitrocéramique contenant ces deux cristaux

Sur la base de différentes mesures et analyses présentées dans ce travail, il peut être constaté qu'il y a trois facteurs clés qui déterminent la photoconductivité d'une vitrocéramique. Le premier facteur est l'existence des phases absorbant fortement la lumière visible, ce qui est le cas ici avec Sb_2Se_3 et Cu_2GeSe_3 qui ont un gap électronique direct. Le deuxième facteur est la formation des hétérojonctions entre Sb_2Se_3 et Cu_2GeSe_3, ce qui peut conduire à une séparation plus efficace des porteurs de charge. Un dernier facteur d'importance est la formation des canaux conducteurs dans la vitrocéramique, ce qui entraîne une amélioration évidente de la conductivité, favorisant ainsi la mobilité de porteurs de charge photo-générés.

Par conséquent, le mécanisme vraisemblable expliquant l'excellente propriété photoélectrique de ces vitrocéramiques est proposé schématiquement à la figure 16. Il est composé de trois étapes clés : Les photons sont efficacement absorbés par Sb_2Se_3 et Cu_2GeSe_3, puis l'hétérojonction formée par Sb_2Se_3 (type n) et Cu_2GeSe_3 (type p) améliore nettement la séparation des charges. Ces charges sont efficacement collectées par le réseau formé de cristaux Sb_2Se_3 interconnectés, sous forme des aiguilles, couverts par la phase conductrice Cu_2GeSe_3. Ce réseau crée des canaux conducteurs, comme en témoigne l'image du potentiel de surface avec des canaux conducteurs. Par conséquent, les porteurs de charge peuvent être transportés efficacement vers des contacts extérieurs.

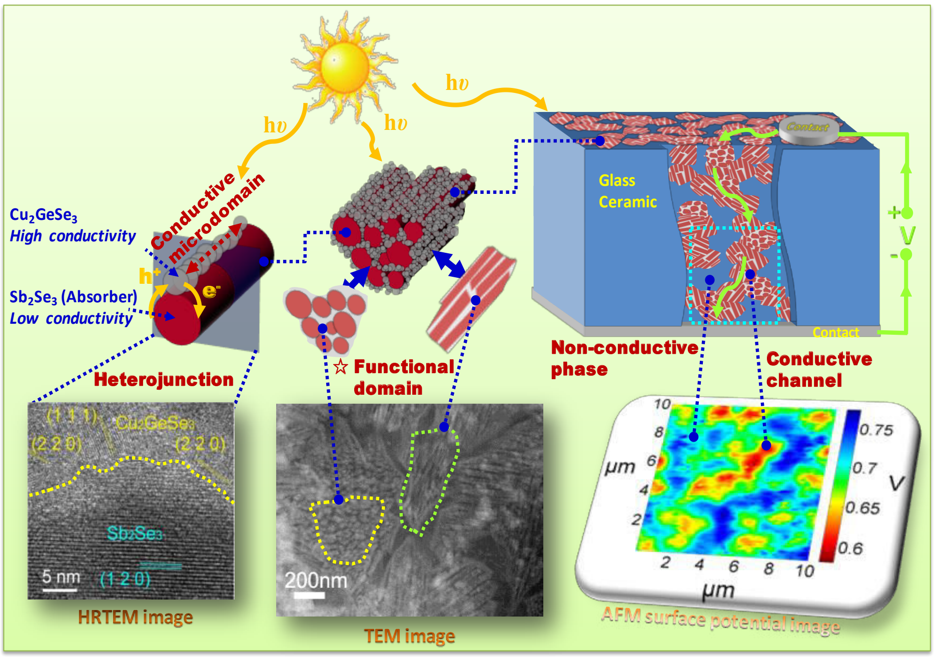

Figure 16. Mécanisme de la photo-génération, de la séparation et du transport des charges dans les vitrocéramiques contenant des hétérojonctions

7 Testes de photocatalyse avec les vitrocéramiques de chalcogénures

La photocatalyse est basée sur l'utilisation des charges photogénérées qui peuvent ainsi oxyder ou réduire des espèces chimiques, en produisant des combustibles chimiques (hydrogène par exemple) ou en décomposant des polluants organiques.

Une représentation schématique du montage pour les testes photocatalytiques est sur la figure 17. Une lampe à halogène de 35 W avec un filtre UV (420 nm) est utilisée comme source de lumière visible.

Le méthyle orange (MO), un polluent organique bien connu est choisi pour ces testes de photocatalyse. La procédure est la suivante : une quantité précise de vitrocéramique sous forme de poudres est dispersée dans un volume précis d'une solution contenant du MO. Le mélange est agité pendant la réaction photocatalytique. De temps en temps, un petit volume de la solution est prélevé pour une analyse spectroscopique. L'intensité de l'absorption centrée vers 464 nm est utilisée pour suivre la décomposition progressive du MO, comme l'illustre la figure 18.

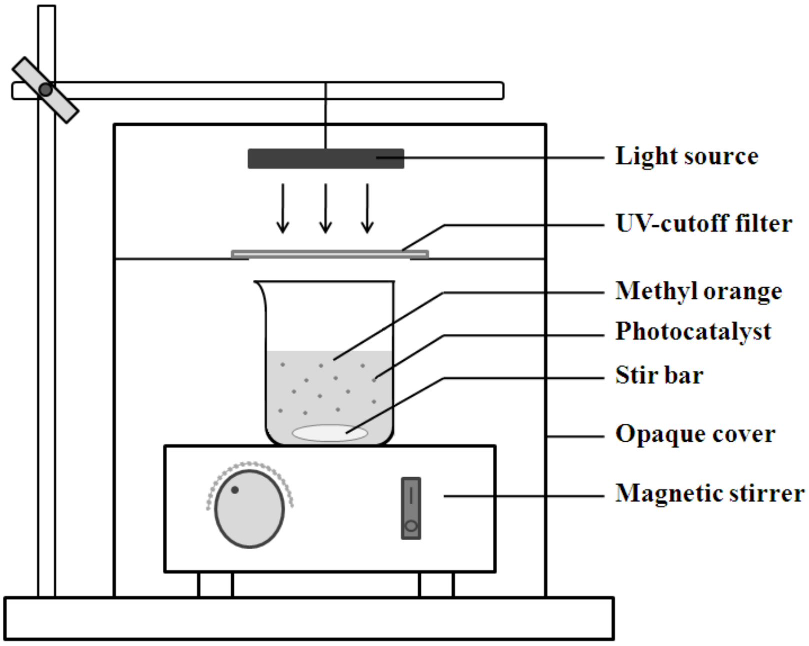

Figure 17. Montage de la photocatalyse

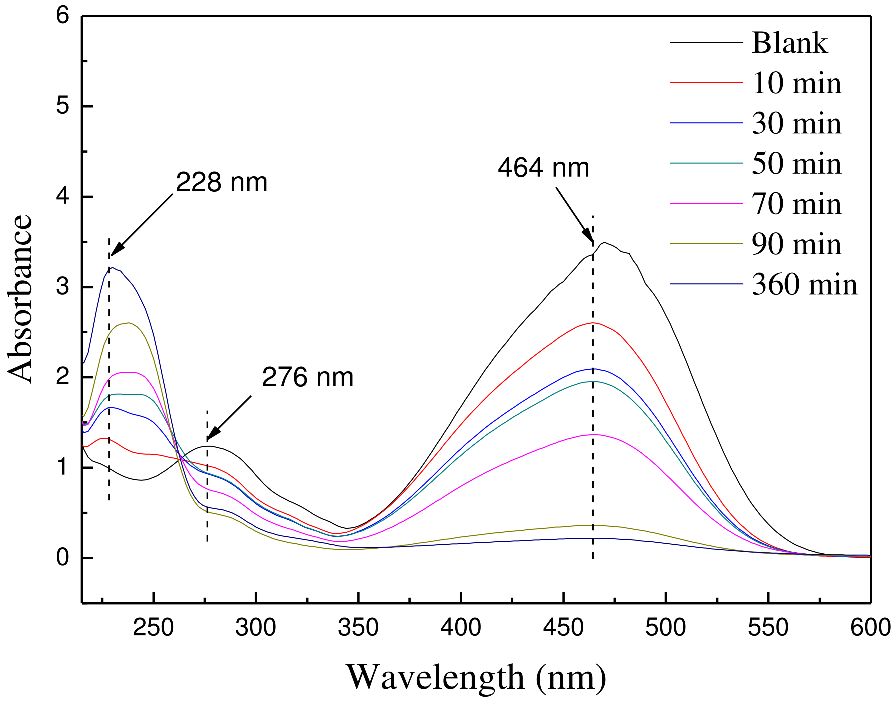

Figure 18. Spectres d'absorption du méthyle orange pour le suivi de la décomposition photocatalytique sous lumière visible

La figure 19 montre la cinétique de décomposition du MO en fonction du temps, C_0 et C_t étant respectivement la concentration du MO initiale et au temps de réaction t. Un photo-catalyseur bien connu, le TiO_2 P25 avec une taille moyenne de l'ordre de 25 nm, est choisi pour comparaison. On peut constater une efficacité cinq fois supérieure de la vitrocéramique pour cette réaction photocatalytique.

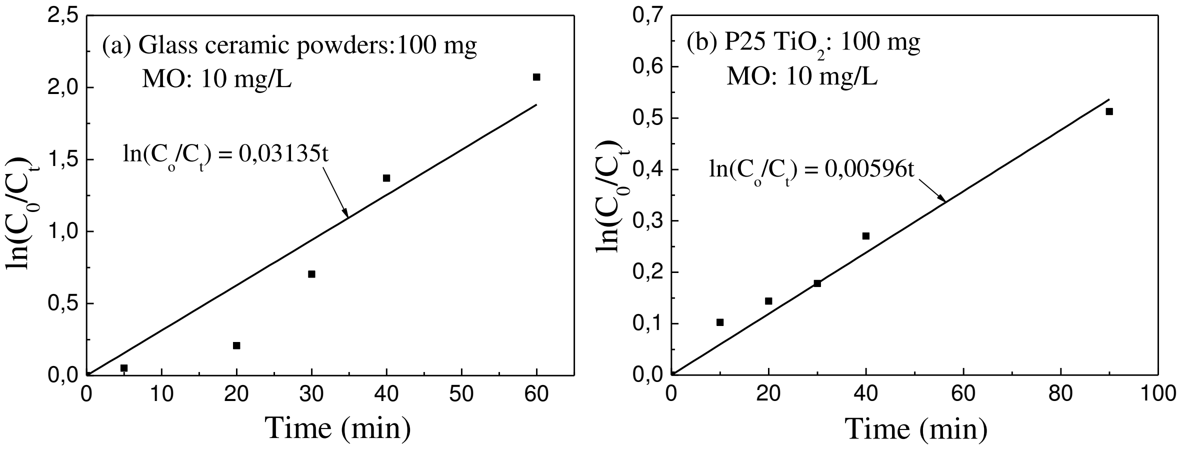

Figure 19. Cinétique de la photo-décomposition du méthyle orange avec la vitrocéramique de chalcogénure et un produit commercial, TiO_2 P25 comme catalyseurs

8 Conclusions

Ce premier travail a permis d'établir des relations entre la composition, la microstructure et les propretés photoélectriques des vitrocéramiques dans le système $GeSe_2$ - Sb_2Se_3 - CuI. Il a été démontré que les excellentes propriétés de certaines vitrocéramiques sont attribuables à une microstructure inédite contenant des heterojunctions p-n formées par des cristaux de Sb_2Se_3 dopé par l'iode (semi-conducteur du type n) et des cristaux Cu_2GeSe_3 (type p). Ces deux cristaux possèdent un gap électronique direct avec une fore absorption de la lumière visible. Ces jonctions favorisent la séparation de charges photogénérées, conduisant à une durée de vie exceptionnellement longue (environ 16 µs) de ces charges. En plus, les cristaux Sb_2Se_3 orthorhombique sont sous forme d'aiguilles, très efficaces pour former un réseau tridimensionnel interconnecté. Ce réseau est rendu conducteur grâce à la croissance de la phase cubique Cu_2GeSe_3, ayant une bonne conductivité, sur les Sb_2Se_3 nettement moins conducteurs. Cette structure peut donc transporter facilement les charges.

Les matériaux/structures permettant d'absorber efficacement la lumière visible, de séparer et de transporter les charges photogénérées, sont recherchés pour exploiter l'énergie solaire par effet photovoltaïque ou par photocatalyse. Cette étude préliminaire a permis de démontrer l'efficacité de ces nouveaux matériaux/structures pour la photocatalyse. D'autres travaux sont indispensables pour encore mieux comprendre ces matériaux et pour fabriquer des dispositifs afin de démontrer expérimentalement leur efficacité pour convertir de l'énergie solaire.

General Introduction

Energy crisis and environmental issues are two big challenges in today's world. As the only source of all renewable energies, solar energy has received much attention due to its acceptable energy density on the Earth and has occupied a central position among the renewable energies. Photovoltaic conversion and photochemical conversion of solar energy, which are all based on quantum processes of semiconductors, are two effective ways to convert solar energy into electricity or chemical fuels.

Photovoltaic solar cells are the most used technique to convert solar energy into electricity, which can be classified into three main groups: silicon solar cells (single crystalline, polycrystalline, amorphous), organic solar cells (such as polymer solar cells, dye-sensitized solar cells) and compound solar cells (such as CdTe, GaAs and CIGS). Silicon solar cells are the oldest and also the most matured technology in solar cell market. Crystalline silicon solar cells have already achieved efficiencies close to the Shockley–Queisser limit, corresponding to a maximum efficiency of about 30%. Therefore, multi-junction structure, which is able to absorb a wider range of the solar spectrum, has been proposed for further increasing the conversion efficiency. The GaInP/GaAs/GaInNAs three-junction system has achieved the highest conversion efficiency of 43.5%. Another important research direction of solar cells is thin film solar cell due to its promising advantages compared to crystalline silicon solar cells, such as flexibility, lightweight, lower production cost. To date, most of the explorations of new photovoltaic materials are based on thin film solar cells. The best efficiency of CIGS (Cu-In-Ga-S(Se)) thin film solar cells has reached 20.3%, whereas the two relatively new thin film solar cells, dye-sensitized solar cells and organic photovoltaic cells, are making rapid progress in laboratory efficiencies. During the recent years, looking for new low-cost and high-efficient alternative materials has become an important issue for solar cell research.

Semiconductor photocatalysis technology provides a relatively simple method for photochemical conversion of solar energy. This technology can also be very useful for environmental remediation through photocatalytic decomposition of organic pollutants. Such technology is based on the use of the photo-generated charge carriers from semiconductors. Consequently, efficient generation and separation of photo-generated carriers are the keys for efficient semiconductor photocatalytic reaction. For an example, most of current studies are concentrated on the modification of TiO_2, which can only absorb 3-4% of the solar energy. Therefore, the development of new photocatalysts with high quantum efficiency and high activity has become a hot research topic. New narrow band-gap semiconductors have been rapidly developed during the recent years. The objective is to obtain high absorption of photons in the visible region as well as relatively high photocatalytic activity. Examples of studied materials are multiple oxide semiconductors (such as $InVO_4$, Bi_2GaNbO_7) and nitride semiconductors (such as g-C_3N_4). At the same time, a structure with nano-heterojunction has also been proposed to inhibit the recombination of photo-generated electron-hole pairs, which is an important issue in narrow band-gap semiconductors. Especially during the recent years, fabricating nano-heterojunction in narrow band-gap semiconductors has become a rising strategy for developing highly efficient semiconductor composites due to its comprehensive advantages of visible-light response and highly separation efficiency for photo-generated carriers.

It is more and more difficult to find a single material to achieve high performance in photovoltaic or photocatalytic applications. Therefore, the development of composite structure has become particularly interesting in order to address separately different issues (strong absorption of solar spectrum, efficient charge generation and separation, open circuit voltage, appropriate potential…) with different components/structures.

The objective of this work is to explore a totally new photoelectric material with unique microstructure by controlling the growth of nanocrystals in the $GeSe_2$-Ga_2Se_3-CuI glass ceramic system. The microstructure of the glass ceramic is mainly determined by the material composition and the crystallizing process of the precursor glass. Consequently emphasis will be put on the establishment of the relationship between the synthesis (composition and process), the microstructure (crystalline phases and composite structure) and the properties (photoelectric and photocatalytic activities) of the glass ceramic. The objective is to understand the mechanism of charge generation, separation and transport in order to design appropriate structures for efficient photon-electron/hole conversion.

The first chapter of this dissertation is on the-state-of-the-art concerning the exploitation of solar energy. The purpose is to situate this work in this context and to explain the motivation. The $GeSe_2$-Sb_2Se_3-CuI system has been selected on the base of previous studies devoted to the development of infrared transmitting glass ceramics. It was discovered that these materials have unusual optical properties, suggesting the existence of high concentration of free charge carrier. This kind of materials is of course interesting for photovoltaic or photocatalytic applications.

Chapter 1

Conversion of Solar Energy

1 Introduction

With the development of human civilization, the energy consumption is rising tremendously year by year. In the present scenario, fossil fuels such as coal, oil and gas, are playing lead role to meet the energy demand. However, as the global fossil resources are limited, it is gradually becoming difficult to solve such a contradiction between supply and demand of human being. Furthermore, fossil fuels have been regarded as the largest greenhouse gas emitters in the world, contributing 3/4 of all carbon dioxide, methane and other greenhouse gas emissions. Burning coal, petroleum and other fossil fuels at extremely high temperatures (combustion) is the primary means by which electricity is produced, but it leads also to high concentration of pollutants in our air and water. The combined effects of the depletion of fossil fuels and the gradually emerging concern about environmental degradation have forced humanity to increase the use of renewable energy resources in the 21st century. Nowadays, looking for new, non-polluting and renewable energy resources have become a worldwide issue.

Renewable energy sources include solar energy, biomass energy, wind energy, biogas, etc. These energy sources are directly or indirectly derived from solar radiation. Biomass energy is produced by plants as a result of photosynthesis generated by the sun; wind energy is also indirectly derived from the heat generated by the sun. Among these renewable energy sources, solar energy has received much attention in solving the environmental and energy crisis due to its clean and inexhaustible feature, and thus occupies a central position as renewable energy. It is predicted that by 2100 solar energy will account for 70% in the energy consumption structure of the world (as shown in Figure 1-1) [1].

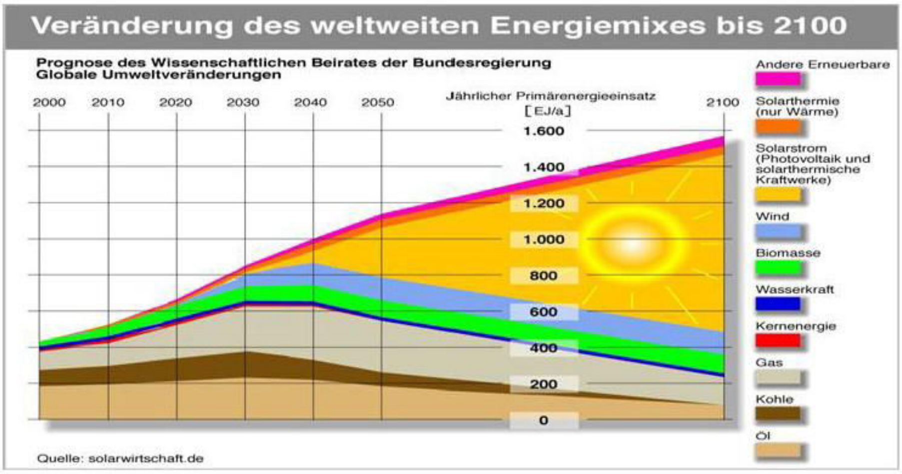

Figure 1-1 World Marketed distribution of energy use by fuel type, -2100 (EJ/a)

The Sun releases an enormous amount of radiation energy to its surroundings: 174 PW (1 PW = 10^{15} W) at the upper atmosphere of the Earth. When the energy arrives at the surface of the Earth, it has been attenuated twice by both the atmosphere (6% by reflection and 16% by absorption) and the clouds (20% by reflection and 3% by absorption), as shown in Figure 1-2. Another 51% (89 PW) of the total incoming solar radiation reaches the land and the oceans.

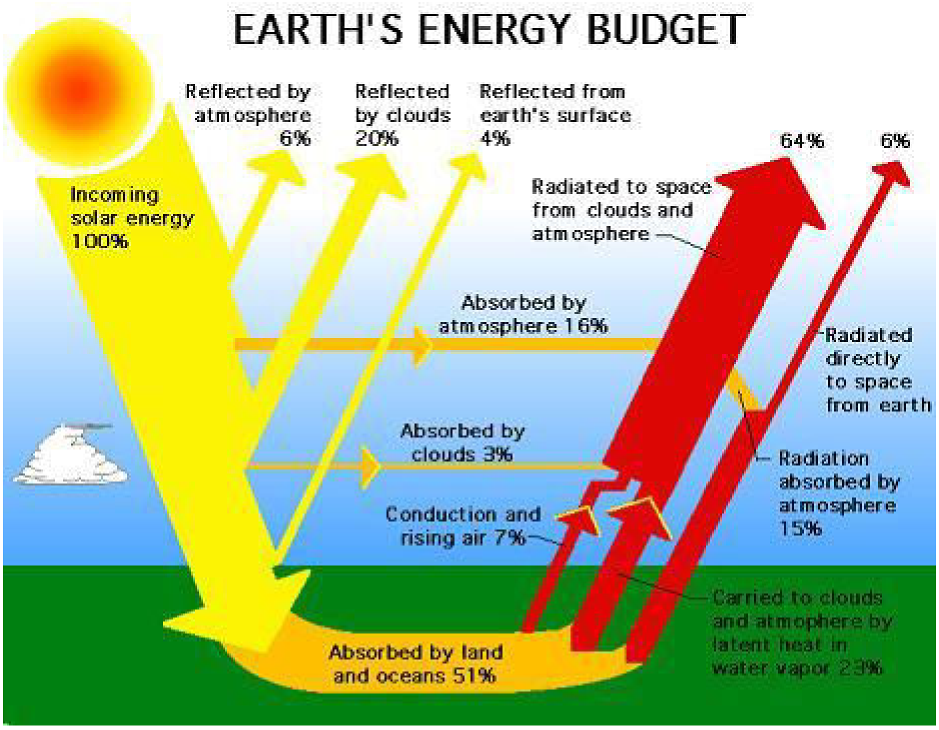

Figure 1-2 The Earth's energy budget from the sun [2]

It is evident that, despite the attenuation, the total amount of solar energy available on the Earth is still of an enormous amount, but owing to its low-density and intermittency, it needs to be transformed and stored efficiently. The commonly used techniques for transforming solar energy are photothermal conversion, photochemical conversion and photovoltaic conversion. For the photothermal conversion, the solar energy is transformed into heat which may be subsequently used directly, stored or transformed into mechanical, electrical or chemical work. While for the photochemical conversion and photovoltaic conversion, they have a similar mechanism. The absorbers based on quantum processes transform part of the solar energy directly into electrical energy (as it happens in a photovoltaic cell) or chemical energy (as it happens in case of photocatalytic water splitting into oxygen and hydrogen).

2 Solar energy conversion

2.1 Photothermal conversion

Photothermal conversion of the solar energy can be divided into different applications according to the working temperature. Low temperature thermal application (less than 80°C) mainly includes heating, water heating and air conditioning, etc. The temperature zone of medium temperature application is typically from 80 °C to 250 °C, and the main applications are solar cooling, solar boiler and solar desalination. High temperature thermal application mainly refers to the use of high temperature (over 250 °C) for electric power generation as an example. Figure 1-3 summarizes the current major solar energy utilization with photothermal conversion [3].

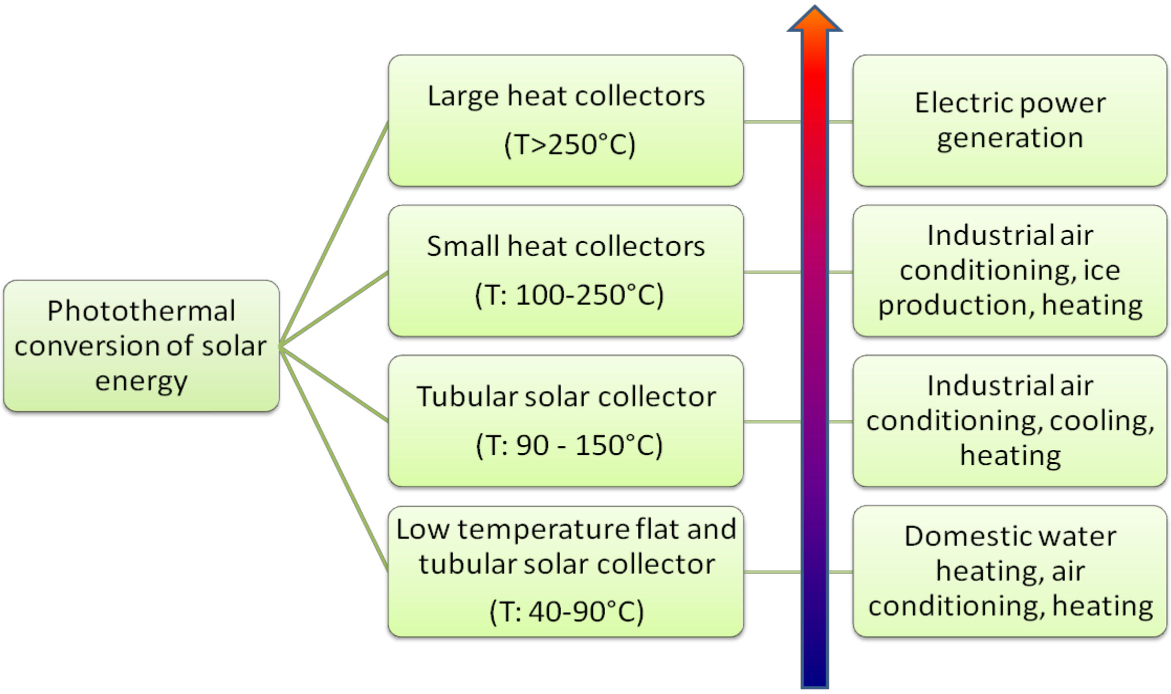

Figure 1-3 Solar thermal applications

Currently, low temperature thermal applications are mainly concentrated in solar water heating systems for domestic use. These systems account for more than 20% of the share in the European market (as shown in Figure 1-4). During the past decade, the growth rate of the European solar water heater has been stable at around 18%/year. The European Solar Energy Council has predicted that by 2020 the application of solar water heaters will be up to 1.4 billion m^2 in Europe.

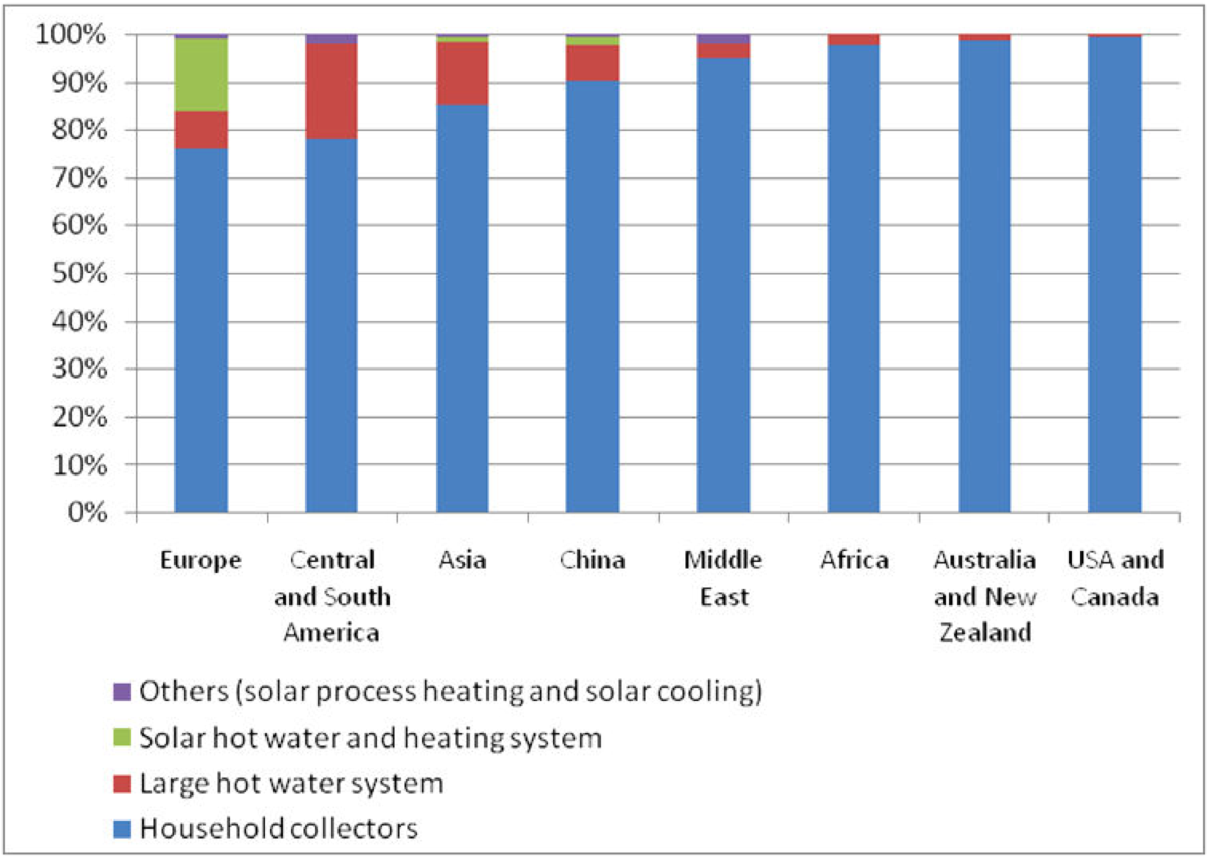

Figure 1-4 Solar thermal utilization forms in the world [4]

The solar energy has low flux density (about 1353W/m^2 at atmospheric peripheral, and less than 1000W/m^2 at the ground), low energy grade and intermittent changes in circadian. Therefore, the use of concentrating technology can improve the conversion temperature and get high quality heat, allowing mid-high temperature thermal applications of solar energy. In the mid-high temperature solar energy utilization, the current research directions mainly include the medium temperature solar industrial heating, solar refrigeration and air conditioning and high temperature solar thermal power technology. There are typically four types of concentrating systems: trough, tower, dish and Fresnel reflection (Figure 1-5). Among them, the trough and tower thermal power technology has achieved commercial operation. The dish thermal power system is still in the demonstration phase due to the high cost of the Stirling engine and its high technical complexity. The maximum consumption of the medium temperature solar energy is mainly in industrial sectors to meet the thermal requirements for food processing, plastics processing, glass processing, chemical industry, paper industry, wood processing, textile industry and other industries.

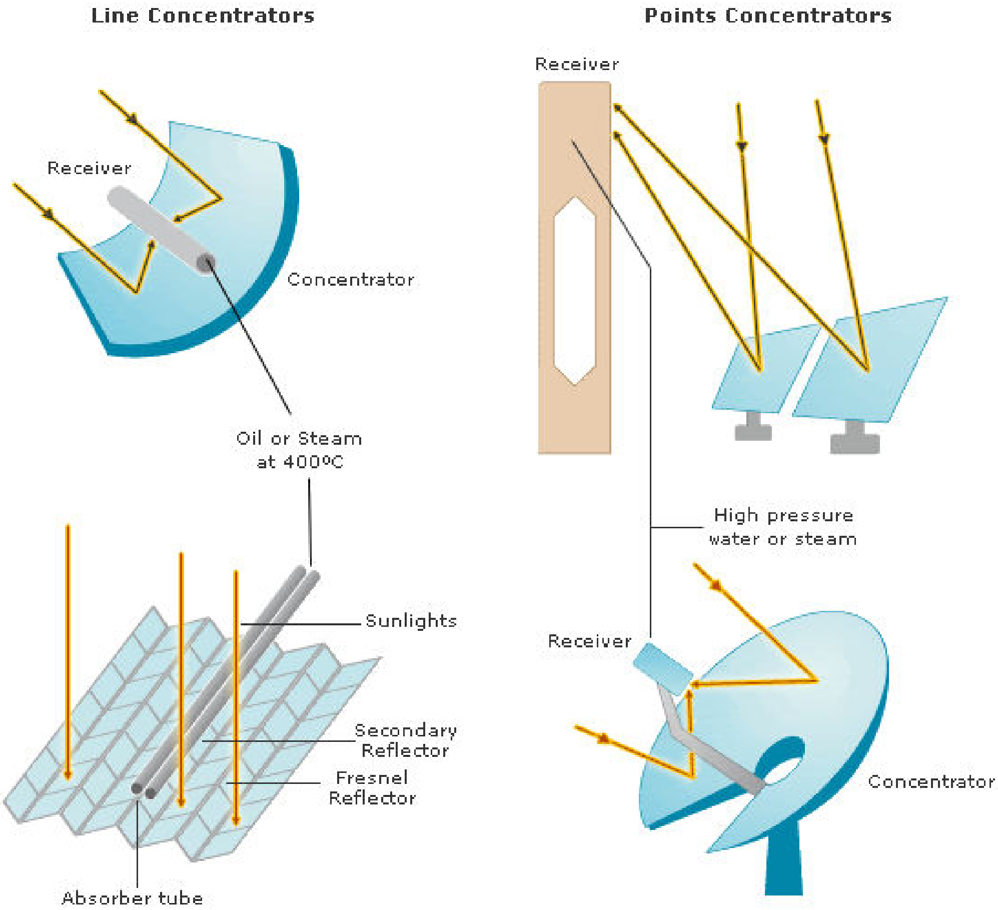

Figure 1-5 Typical concentrating technologies [5]

Solar thermal power generation is an important direction of solar energy utilization. Compared with silicon, solar thermal power generation can significantly reduce the cost of solar power and achieve controllable solar thermal power generation through the energy storage materials. The energy conversion process is as following: the solar radiation is first converted into heat, and then the heat energy is converted into mechanical energy and finally the mechanical energy converted into electrical energy. Currently, the large-scale solar thermal power generation is based on central power tower. Tower solar collector system (as shown in Figure 1-6) is an array of heliostats on the ground with each heliostat tracking the sun on two axes to continuously reflect the solar radiation onto the tower-top receiver. There are various dual-axis tracking modes, such as azimuth-elevation, radial-pitch-roll, azimuth-pitch-roll, oriented polar and receiver [6]. Tower collector concept was first raised by Soviet scientists in the 1950s. In 1965, the Italian scientist Giovanni designed and manufactured the first tower solar collector, and the mirror farm consisted of 120 circular mirrors, which can reflect the solar radiation to the steamer in the tower and generate the superheated steam with a temperature of 500 °C and a pressure of 10MPa [7]. In 1982, the United States built a

10MWe massive solar tower power plant called Solar One (as shown in Figure 1-7). The receiver consists of 24 panels (receiver diameter: 7 m), six of which are for preheating water and eighteen for producing steam. Since 1994, the European Framework IV, V, VI plan continuously supported tower concentrator technology research, such as Solgas plan, Colón Solar plans. Nowadays, concentrated solar power (CSP) is being widely commercialized, with about 1.17 GW of CSP capacities in 2011, with 582 MW of them are located in Spain and the 507 megawatts of capacity in the United States. About 17.54 GW of CSP projects are under development worldwide, and the United States leads with about 8.67 GW. Spain ranks second with 4.46 GW in development, followed by China with 2.5 GW [8]. Figure 1-8 projects CSP electricity production by 2050.

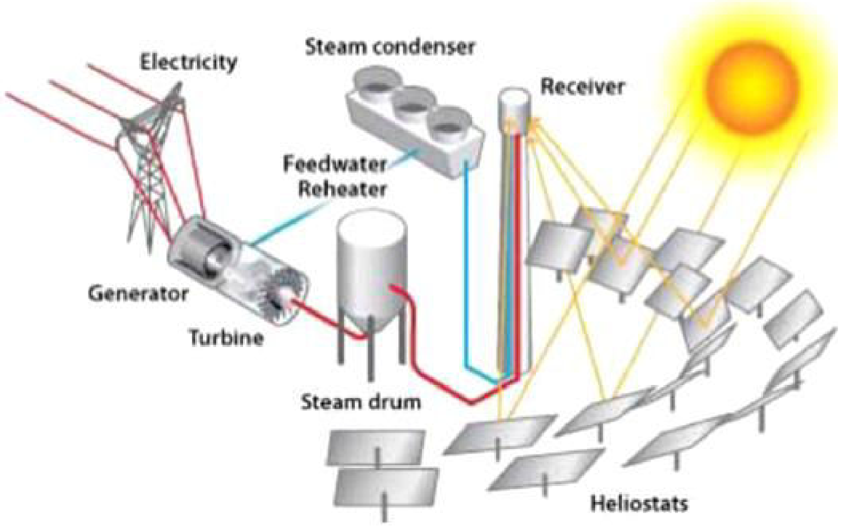

Figure 1-6 Central receiver power tower system [9]

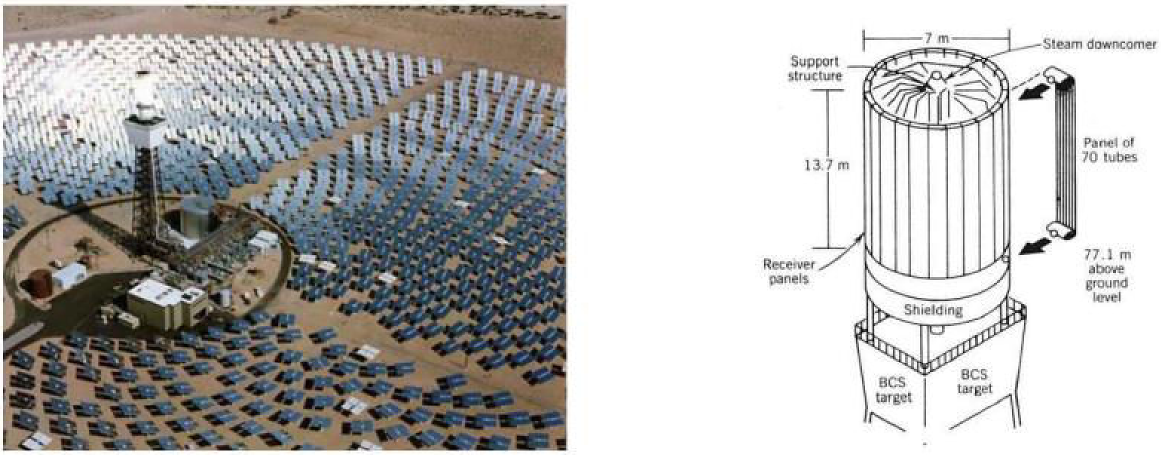

Figure 1-7 System and external receiver utilized at solar one facility in Barstow, California, USA [9, 10]

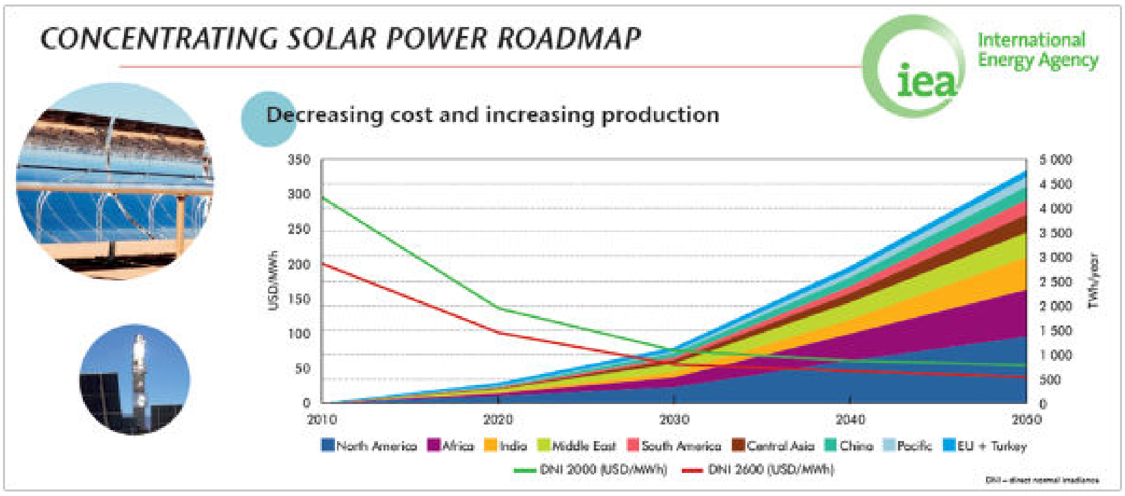

Figure 1-8 Prediction of concentrated solar power production by region [11]

Another solar thermal utilization technology is the use of phase change materials in the residential walls. The phase change materials have the following advantages: Firstly, the phase change process is generally isothermal or approximately isothermal process. This feature is useful to maintain the temperature in a small range, and thus people will feel comfortable. Secondly, the phase change materials can have a high latent heat, so a small amount of material can store large amounts of heat. Using phase change materials to build the walls can significantly enhance the regenerative capacity of the wall, increasing the building's thermal inertia index, thus improving the indoor environment of thermal comfort [12]. Take the heating for example, when the indoor temperature is higher than the phase transition temperature, the phase change materials melt and absorb excess heat in the room; at night when the room temperature is lower than the phase transition point, the phase change materials solidify and slowly release the stored heat into the room to increase the indoor temperature. Compared to the classic building materials (such as concrete, brick, etc.), the phase change materials have higher thermal storage density and lighter weight, and can be therefore large-scale used in lightweight buildings to improve its thermal performance and indoor thermal environment [13,14].

2.2 Photochemical conversion

Since 1972, Fujishima and Honda first reported the possibility of electrolyzing water into hydrogen using solar illuminated TiO_2 semiconductor electrode. Hydrogen production from water photolysis, as a new way to utilize renewable solar energy, has attracted more and more attentions [15]. Figure 1-9 shows the main processes of photocatalytic water splitting.

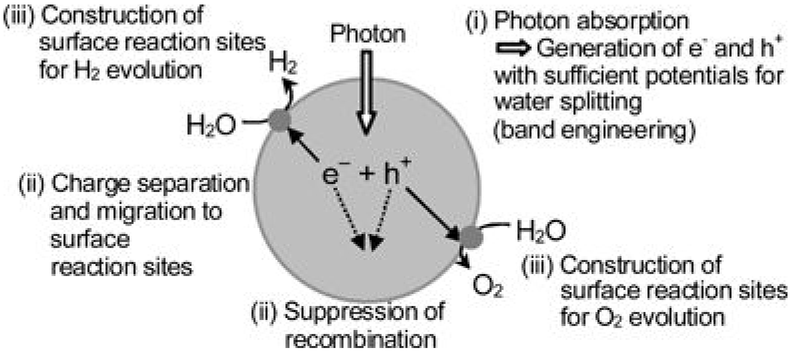

Figure 1-9 Main processes of photocatalytic water splitting [16]

(1) Photon absorption and charge generation. In single-junction absorbers, photons with energies below the semiconductor bandgap cannot be absorbed or converted. Photons with energies exceeding the bandgap are absorbed at rates dependent on the allowed transitions in the semiconductor. Direct bandgap materials absorb more efficiently than indirect bandgap materials. Photo-generated electron-hole pairs rapidly thermalize (usually within picoseconds) to band-edge energy levels, losing excessive energy to heat. High bandgap semiconductors generate little photocurrent due to poor absorption, while low bandgap semiconductors can suffer from low conversion efficiency due to high thermalization losses.

(2) Charge separation and migration. While at band-edge energy states, the electron-hole pairs can often survive for several microseconds before recombination. During this time, they must be separated and migrate to electrochemical interfaces. This separation is assisted by the electric fields set up by charge distributions in the semiconductor and at the solid/liquid interface. Defects in the bulk and at the interface can adversely affect the separation fields, and also result in poor mobility for charge migration. If thick absorption layers are needed (for example, in indirect semiconductors) the charge migration losses can be severe.

(3) Construction of surface reaction sites. Ideally, charge is extracted via the water splitting half-reaction at the solid/liquid interface. The extraction process can be slowed or completely inhibited by poor energetic alignment or poor surface kinetics at the photoelectrode or counter electrode surfaces. Moreover, parasitic or corrosion reactions competing with the water-splitting reactions can result in substantial losses. Surface treatments can be employed to kinetically and/or energetically favor water splitting over the parasitic processes, but such treatments could also block sunlight. Surface incorporation of nanoparticle catalysts is one approach. Since photoelectrochemical water splitting is a low-current density process (typically operating below 20 $mA \cdot cm^{-2}$), non-precious-metal catalysts are necessary. In

addition, nanostructure of electrode surfaces can increase effective surface area for enhanced charge extraction, although this can also lead to higher surface recombination loss.

The positions of the conduction band and valence band edges of the semiconductor are important as they determine whether spontaneous water splitting will occur and whether the material will be stable in a photoelectrochemical (PEC) cell. Much higher hydrogen production efficiency can be achieved if spontaneous water splitting occurs, without the need to apply an electrical bias. A semiconductor capable of spontaneous water splitting has a bandgap ≥ 2 eV [17] with conduction band energy more negative than that of the H^+/H_2 redox potential, and valence band energy more positive than that of the O_2/H_2O redox potential as shown in Figure 1-10 [18]. Under these conditions, charge transfer between the semiconductor and the electrolyte is energetically favorable. Most metal oxides have a valence band edge at a similar energy, well below the O_2/H_2O potential. Therefore, to have a conduction band edge above the H^+/H_2 potential, the material will have a wide band-gap (over 3 eV). Narrower bandgap materials with band edges that overlap the water splitting redox potentials (such as CdS and CdSe) are unstable. Maeda and Domen [18] suggest that oxynitride and oxysulphide materials may be more suitable for spontaneous water splitting than metal oxides, as their valence band edges are closer to the O_2/H_2O potential, and those with a suitable band-gap around 2 eV are able to have band edges that overlap the water splitting potentials.

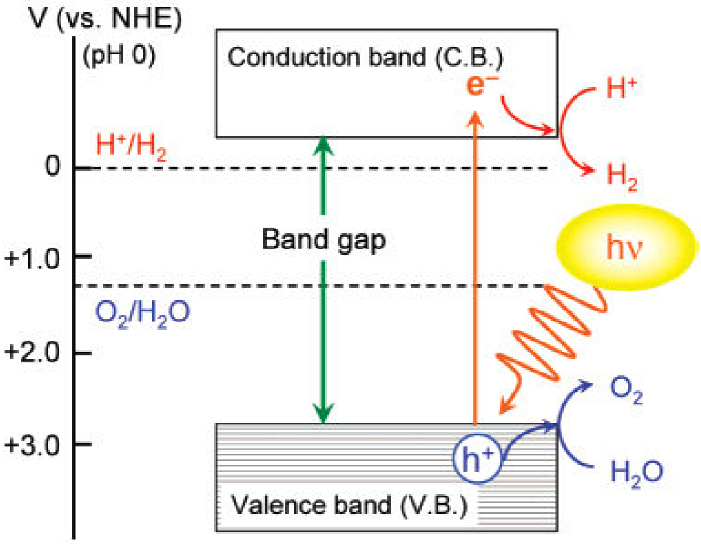

Figure 1-10 Principle of water splitting using semiconductor photocatalysts

Figure 1-11 shows a typical setup for PEC water splitting. In this system, a light-sensitive semiconductor photoelectrode is immersed in an aqueous solution, with electrical wiring connected to a metallic counter-electrode. With the excitation of light, photo-generated electron-hole pairs in the semiconductor interact electrochemically with ionic species in solution at the solid/liquid interfaces. Photo-generated holes drive the oxygen evolution reaction at the anode surface, while photo-generated electrons drive the hydrogen evolution reaction at the cathode surface.

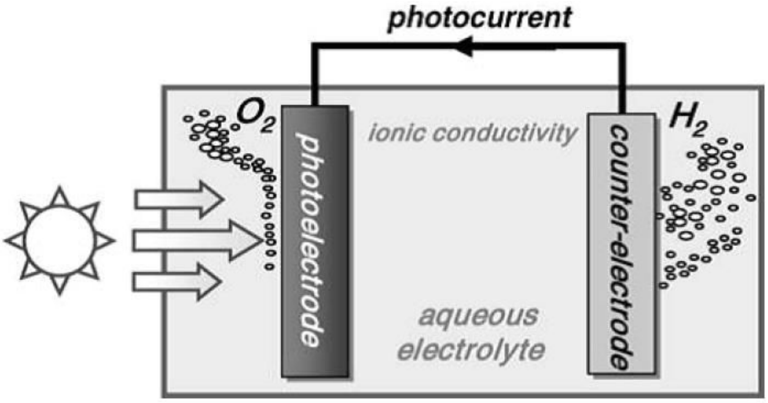

Figure 1-11 typical setup for PEC water splitting

In addition, the photo-generated electrons can also react with the adsorbed O_2 on the semiconductor surface and form various active substances, such as $\cdot O_2^-$, $\cdot HO_2$, H_2O_2, $\cdot OH$, etc (formula 1.1-1.5). Meanwhile, the photo-generated holes will react with the adsorbed H_2O or OH^- ions on the semiconductor surface and generate hydroxyl radicals $\cdot OH$ (formula 1.6, 1.7). These active substances can decompose most organic compounds (formula 1.8). In addition, for the most used photocatalyst such as anatase TiO_2, since the electric potential of its photo-generated hole is greater than 3.0 eV, which is higher than that of chlorine, ozone and permanganate, thus showing strong oxidation. Therefore, such photo-generated holes provide another way to decompose the organic pollutants (formula 1.9) [19].

$$e^- + O_2 \rightarrow \cdot O_2^- \tag{1.1}$$

$$\cdot O_2^- + H_2O \rightarrow \cdot HO_2 + OH^- \tag{1.2}$$

$$2\cdot HO_2 \rightarrow H_2O_2 + O_2 \tag{1.3}$$

$$e^- + \cdot HO_2 + H_2O \rightarrow H_2O_2 + OH^- \tag{1.4}$$

$$e^- + H_2O_2 \rightarrow \cdot OH + OH^- \tag{1.5}$$

$$h^+ + H_2O \rightarrow \cdot OH + H^+ \tag{1.6}$$

$$h^+ + OH^- \rightarrow \cdot OH \tag{1.7}$$

$$\text{Organic pollutants} + (\cdot HO, \cdot O_2^-, \cdot HO_2) \rightarrow \text{Products} \tag{1.8}$$

$$\text{Organic pollutants} + h^+ \rightarrow \text{Products} \tag{1.9}$$

2.3 Photovoltaic conversion

Solar photovoltaic system usually consists of collector panels, controller, inverter, battery and other devices (as shown in Figure 1-12). The collector panels include a number of small series / parallel unities, depending on the requirements for the output current and voltage; the controller is usually used to control the stability of the output parameters, in order to maximize the use efficiency of obtained solar energy; the inverter is used to transform the DC power into AC power for subsequent use; the battery is typically used to store excess power.

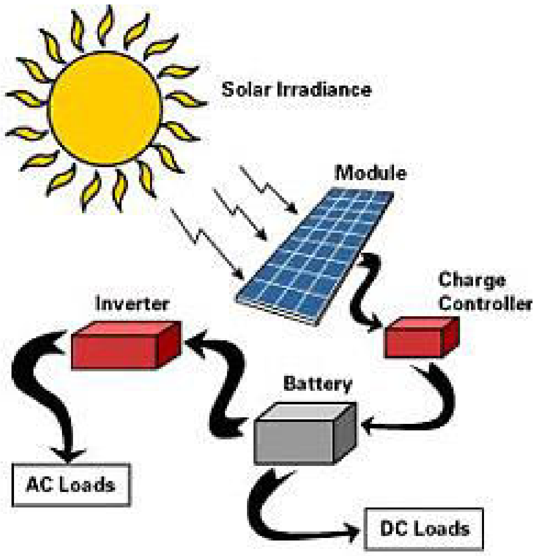

Figure 1-12 Solar energy photoelectric conversion system [20]

Solar cells are the core devices of solar photovoltaic system, and already have a development history of nearly two hundred years. The first event to be noted in the history of solar cells was the discovery of selenium made by Berzelius in 1817 [21]. Incidentally, he was also the first to prepare elemental silicon a few years later. However it was over two decades before Alexandre-Edmond Becquerel, a French physicist, observed the photovoltaic effect in 1839. In 1873, Willoughby Smith reported the photoconductivity of selenium [22]. This has inspired W.G.Adams and R.E. Day to make the first selenium cell in 1877. However, the typical cell efficiency was less than 1%, and therefore unrealistic for large-scale power production. In 1904, Hallwachs found a new material of the combination of copper with cuprous oxide demonstrating photosensitive property. The science of photovoltaics also evolved with Milikan's experimental proof of the photovoltaic effect in 1916 and Albert Einstein's Nobel Prize of 1921 for his contribution to explaining this effect [23]. In 1954, Bell labs researchers D.M. Chapin, C.S. Fuller and G.L. Pearson, reported the monocrystalline silicon solar cells with efficiency of 4.5%, which reached 6% a few months later [24]. Such cells were applied to America's second satellite, Vanguard 1 in 1958 [25]. The most significant market growth for PV has come since 1995, and the world's solar cell production capacity has reached 37.2 GW in 2011 [26].

Solar cells convert solar energy into electrical energy based on the "photovoltaic effect". As shown in Figure 1-13, when the semiconductor p-n junction is exposed to the sunlight, the electrons in the valence band are excited to the conduction band, resulting in generation of holes in the valence band and electrons in the conduction band, thus forming an electron-hole pair (left part in Figure 1-13). The formed electron-hole pairs are separated by the p-n junction electric field and a current proportional to the number of electron-hole pairs created flows through an external circuit (right part in Figure 1-13). If the photon energy is less than E_g, it doesn't carry enough energy to break a covalent bond and free an electron for conduction. Since electrons cannot occupy the forbidden states between the valence and conduction bands, a photon with energy less than E_g cannot be absorbed and will pass through the sample. Only photons which energy is greater than the semiconductor band gap (E_g) can be absorbed, and release excess energy in the form of heat.

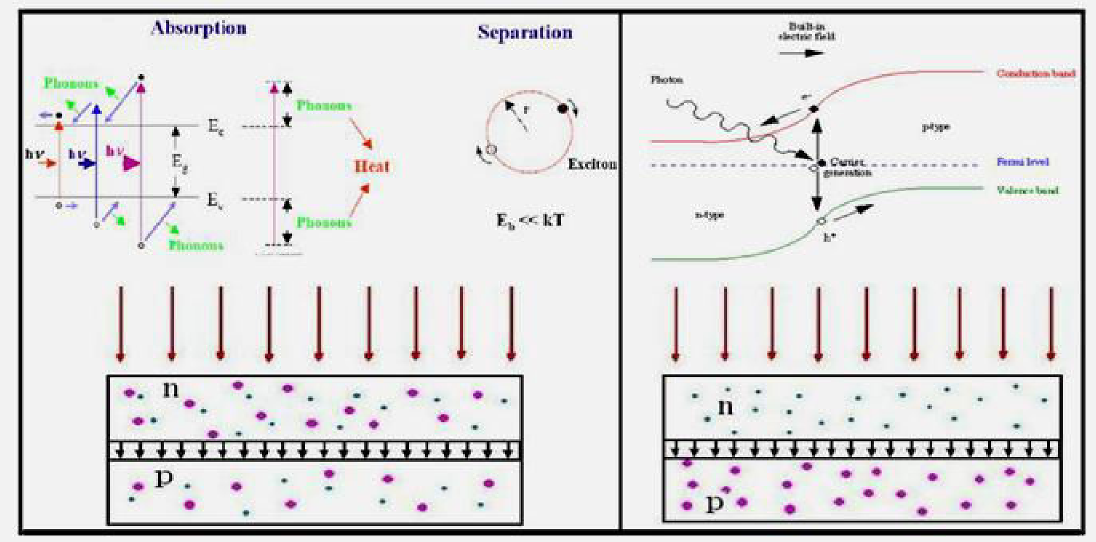

Figure 1-13 Working principle of semiconductor based solar cell

Solar cells can be classified into silicon solar cells, organic solar cells and compound solar cells. Silicon solar cells include monocrystalline silicon solar cells, polycrystalline silicon solar cells and amorphous silicon solar cells; organic solar cells include polymer solar cells (OPV) and dye-sensitized solar cells (DSC or DSSC); compound solar cells include cadmium telluride (CdTe) thin film solar cells, copper indium gallium selenide ($CuIn_xGa_{(1-x)}Se_2$, CIGS) thin film solar cells, gallium arsenide (GaAs, group III-V) film solar cells.

Figure 1-14 shows the best efficiencies of different research solar cells for last decades. Crystalline silicon solar cells have already achieved efficiencies close to the Shockley–Queisser limit, whereas other kinds of solar cells still have room for improvement although the crystalline silicon solar cells are the main solar cell in the market. The optimum bandgap for terrestrial solar cells is around 1.2 eV. Under standard AM1.5 conditions, the maximum efficiency is around 30% for single solar cells with bandgaps in the range of 1.2–1.4 eV. Suitable absorber materials that have bandgaps in this range include CdTe (1.44 eV), whereas the bandgap of CIS ($CuInSe_2$) is too low (1.02 eV) so that gallium is added to create a solid solution $Cu(In,Ga)Se_2$ (CIGS) with higher bandgap close to the optimum value. For CdTe thin film solar cells, among the new efficiency record holders, GE Research is now on top with an 18.3% efficient cell (in 2013), a full percentage point higher than the 17.3% achieved by First Solar in 2011 [27].The best efficiency of CIGS thin film solar cells reached 20.3% [28]. The range of solar cells continues to expand, with two relatively new entries—dye-sensitized solar cells (DSC) and organic photovoltaic cells (OPV)—making rapid progress in laboratory efficiencies. The DSCs and organic solar cells are late starters, but both of these low-cost technologies have reached efficiencies that make them commercially interesting if scale-up and acceptable lifetimes can be demonstrated.

Among all of these solar cells, multijunction cells have achieved much higher efficiencies. The two main reasons are: (1) the highest theoretical efficiencies may be achieved if multiple semiconductor materials (with a range of bandgaps) are chosen to match the spectral distribution of the Sun; (2) the compound semiconductors used in these cells are mostly direct-gap materials and can be grown with near-perfect quality in mass production. The multijunction approach has been described extensively in the literature [29,30].

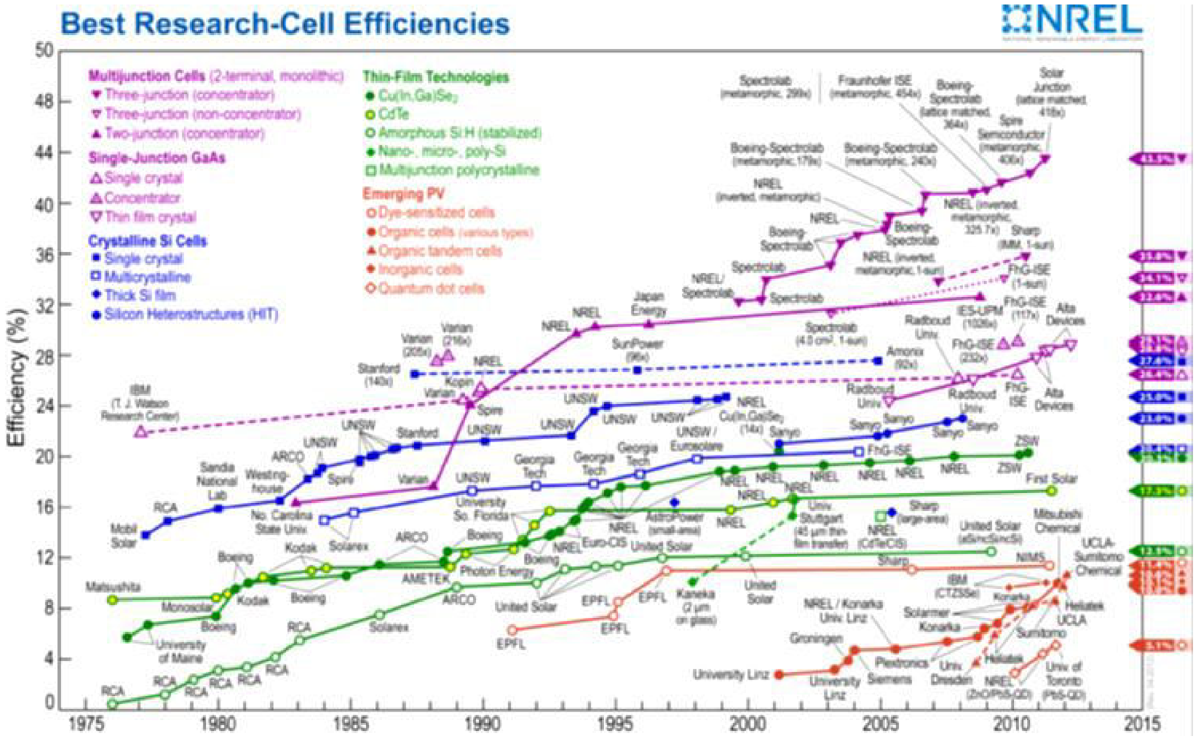

Figure 1-14 Efficiencies of best research solar cells [31]

3 Solar cells

3.1 Classification of solar cells

3.1.1 Crystalline silicon solar cells

In pure silicon crystal, the four valence electrons of a silicon atom are tied with strong covalent bonds to four adjacent silicon atoms. Therefore at zero temperature, silicon is a perfect insulator. Doping is used to make silicon more conductive. By doping silicon with a small number of five-valent atoms (phosphorous, arsenic, or antimony), silicon gets an extra electron to share. This is called an n-type semiconductor. In contrast, doping silicon with an atom of three electrons in its valence, the silicon essentially “loses” an electron to share and this creates a “hole”. This is called a p-type semiconductor. These two types of silicon are put into contact with each other and a p-n junction is formed at the boundary between them. Once the solar cell is exposed to sunlight, an electron-hole pair is generated, and the cell starts converting solar energy into electricity by photovoltaic effect of silicon p-n junction (as shown in Figure 1-15, Figure 1-16).

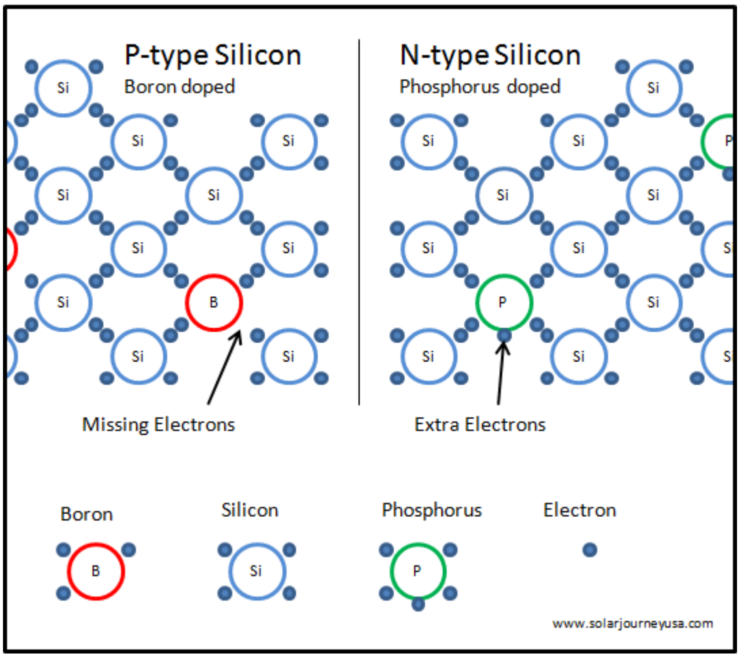

Figure 1-15 Schematic presentation of silicon doping [32]

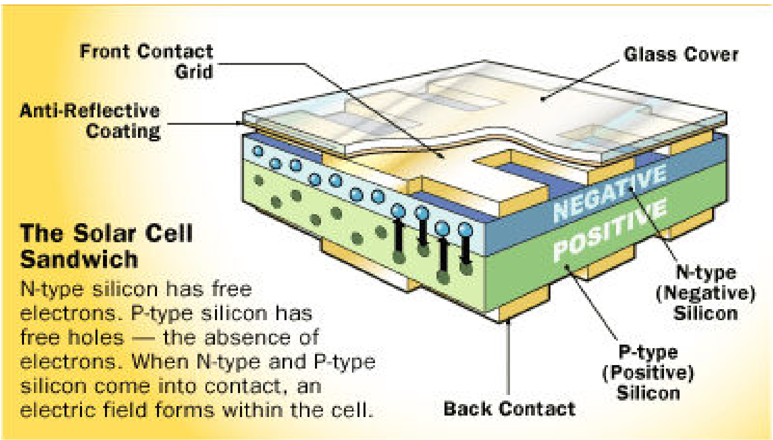

Figure 1-16 principal of crystalline silicon solar cells (©2006 HowStuffWorks) [33]

Several issues affect the efficiency of silicon solar cells [34] (as shown in Figure 1-17): (1) The energy of the photons hitting the solar cell is less than the band gap, so the light cannot be converted into electricity and is lost. (2) The energy of the incoming photons is greater than the band gap, so the excess energy is lost as heat. (3) The Fermi levels of both n-type and p-type silicon are always inside the band gap of silicon so the open-circuit voltage is smaller than the band gap. (4) The series and shunt resistors generated from the contacts and lattice defects in the silicon consume some of the electricity that is generated. (5) Electron-hole pair recombination instead of conversion to electricity.

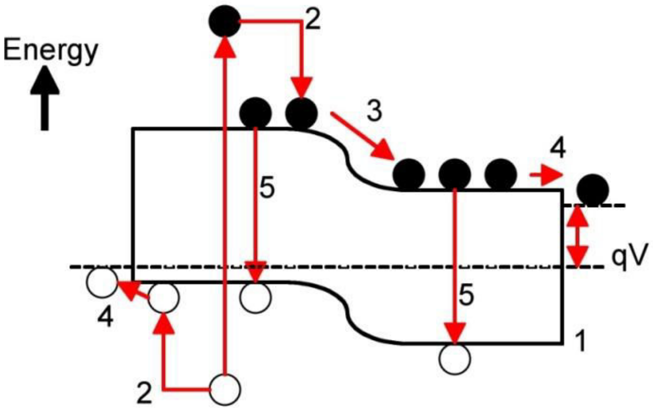

Figure 1-17 Illustration of energy loss in a p-n junction silicon solar cell: (1) unabsorbed light, (2) excess energy loss as heat, (3) Fermi level mismatch with band gap, (4) transfer loss, and (5) electron-hole recombination

Crystalline silicon solar cells, including monocrystalline and polycrystalline cells, are the most widely used of all solar cells due to their relatively high efficiency, high stability and high service life. Figure 1-18 shows the typical production process for crystalline silicon solar cells [35]. The cost of fabricating monocrystalline silicon solar cells is essentially due to the purification process and single crystal growth. To purify silicon, quartzite gravel, high purity silica, is melted and reduced using a carbon bed at a temperature above 1800 °C; this process makes the silicon 98-99% pure and is called metallurgical grade silicon (MGS). MGS is then ground and reacted with hydrochloric acid at 300 °C to make trichlorosilane (TCS). The TCS is heated to 1100 °C in a hydrogen atmosphere to make electronic grade silicon (EGS); this final process makes the silicon 99.9999999% pure. Then a process known as the Czochralski process is used for single crystal silicon production. In this process, a small single crystalline silicon seed is inserted into molten EGS at a temperature above 1700 °C. The seed is continually rotated and slowly drawn out of the melted silicon, which allows the silicon atoms to attach to the seed and arrange in a single crystal lattice; this forms a uniform single crystalline ingot of silicon. Silicon wafers are sliced from the ingot, with a thickness of about 0.2mm. And then these wafers are chemically and mechanically polished. In the production process of solar cells, the first step is to produce a textured structure and then to dope silicon through diffusion, thus forming a p-n junction on the surface of silicon. This step is a key step to produce crystalline silicon solar cells. Next step is the deposition of anti-reflective film to further improve light absorption of cell and finally the screen printing method is used to form silver or aluminum contact on the cell surface. And then the cell is sintered, leading to the formation of alloys between the metal electrodes and silicon to achieve ohmic contact.

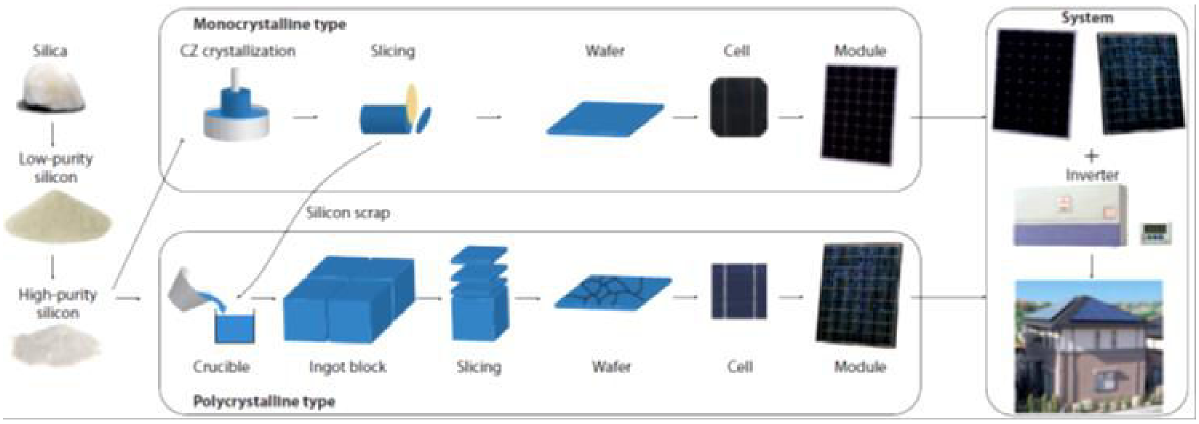

Figure 1-18 Production process for crystalline silicon solar cells (© 2010 Sharp)

Compared to monocrystalline silicon solar cells, polycrystalline cells are much less expensive to manufacture but also less efficient. Polycrystalline silicon is made by pouring molten silicon in a mold and allowing it to cool. This process is called casting. The resulting silicon has no overall lattice structure, but the ingot thus produced has large column grains of crystallinity. The ingot is still sliced and treated as the single crystalline silicon ingot except that the bottom and top of the ingot are removed before slicing due to poor crystallinity at the edges. The casting process is much cheaper and simpler than the Czochralski method used for single crystal growth.

The efficiency of crystalline silicon solar cells is related to the solar cell structure [36]. Representative examples of high-efficiency monocrystalline silicon solar cells are the passivated emitter rear localized (PERL) cell, the heterojunction with intrinsic thin layer (HIT) cell, the back contact-back junction (BC-BJ) cell and metal wrap through (MWT) cell (as shown in Figure 1-19). The PERL cell is a research PV cell with front and rear surface passivation layers, an inverted-pyramid light-trapping surface, a rear localized p+ layer (BSF), a double-layer anti-reflection coating (ARC) and a p-type float zone (FZ) monocrystalline silicon substrate. A PERL cell efficiency of 25.0% was reported by researchers from the University of New South Wales (UNSW) in 2009 [36]. The HIT cell has a unique heterojunction structure consisting of very thin, amorphous p- and n-doped layers and intrinsic amorphous layers on the front and rear surfaces of a Czochralski-grown (CZ) n-type monocrystalline-silicon substrate. The best efficiency of this cell is 23.0% [37]. The BC-BJ cell has front and rear surface passivation layers, a random-pyramid light-trapping surface, front surface field (FSF), interdigitated n- and p-doped regions on the back surface, n and p contact gridlines on n- and p-doped regions, a single-layer ARC and a CZ n-type single crystalline silicon substrate. The best conversion efficiency reported so far for a large-area industrial BC-BJ cell is 23.4% [38]. The MWT cell requires only a relatively small number of through-holes to direct photo-generated electrons to the back surface through the metal electrodes and n-doped emitters, and produce higher collection photocurrents due to the absence of a bus bar (main electrode) on the front surface as in conventional cells. The best efficiency of this cell has reached 18.3% [39].

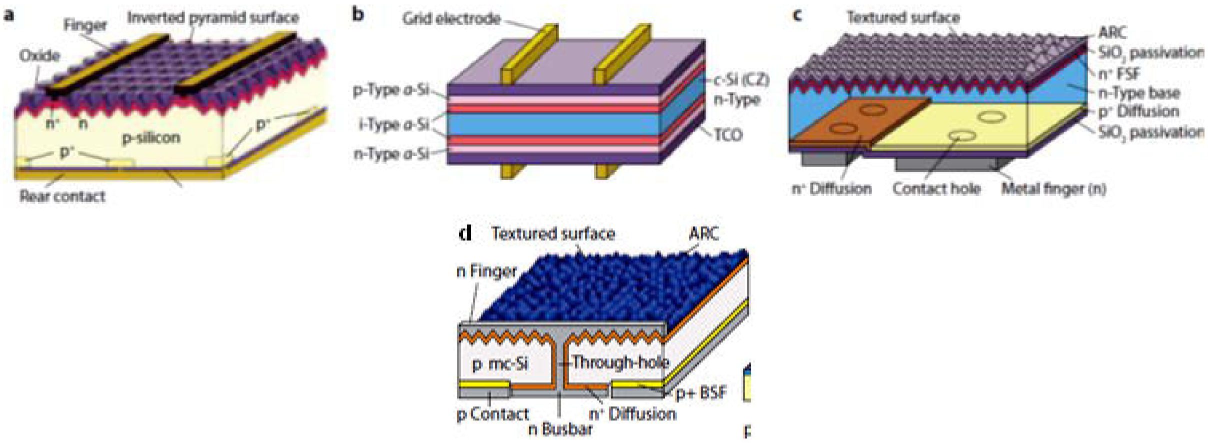

Figure 1-19 Schematics of various crystalline solar cell structures
(a) PERL cell; (b) HIT cell; (c) BC-BJ cell; (d) MWT cell

3.1.2 Amorphous silicon solar cells

Unlike crystal silicon, in which atomic arrangements are regular, amorphous silicon features irregular atomic arrangements. As a result, the reciprocal action between photons and silicon atoms occurs more frequently in amorphous silicon than in crystal silicon, allowing much more light to be absorbed. Thus, an ultra-thin amorphous silicon film of less than 1μm can be produced and used for power generation. Also, by utilizing metal or plastics as substrate, flexible solar cells can be produced. Amorphous silicon layer uses silane (SiH_4) as its source gas and is fabricated using a CVD method [40]. The fundamental photodiode inside an amorphous silicon solar cell has three layers deposited in either the p-i-n or the n-i-p sequence. The three layers are a very thin (typically 20 nm) p-type layer, a much thicker (typically a few hundred nanometer) undoped intrinsic layer, and a very thin n-type layer, as shown in Figure 1-20. This p-i-n junction corresponds to the p-n junction of a crystalline silicon solar cell. In the process of this junction formation, a number of cells are connected in series on a substrate at one time. The sunlight can enter through the transparent substrate, which is usually glass or a transparent plastic. The insulating substrate needs a conducting layer, which is typically a “transparent conducting oxide” (TCO) such as SnO_2. The amorphous silicon photodiode layers (p-i-n junction) are then deposited onto the TCO, starting with a p-type layer. Finally, a back contact (containing reflector) is deposited onto the photodiode. The reflector acts as an electrode to the *n*-type photodiode layer.

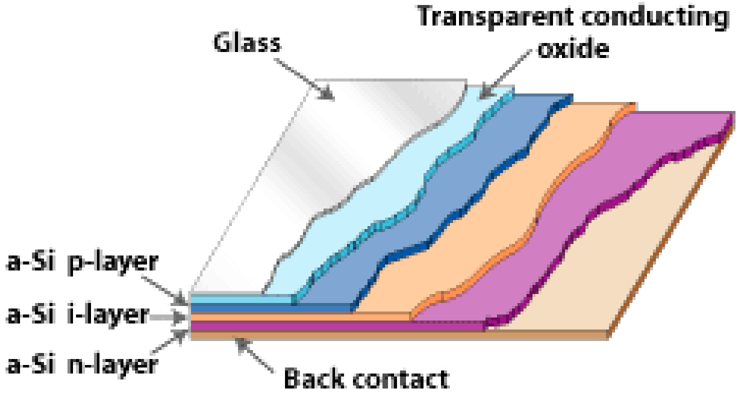

Figure 1-20 A typical structure of amorphous silicon solar cell [41]

However, the poor crystallinity and the existence of dangling bonds in amorphous silicon will lead to short carrier diffusion length and instability upon prolonged illumination [42]. Moreover, the optical threshold of amorphous silicon is rather high (1.7–1.8 eV) and the material suffers from light induced degradation [43]. Therefore, short life cycle and low efficiency have become the big problems for amorphous silicon solar cells. The conversion efficiency of amorphous silicon solar cells is much lower than that of the crystalline silicon solar cells. The best conversion efficiency of this cell achieves 12.5% in laboratory-scale, while industrial conversion efficiency is not more than 10% [44].

3.1.3 Polymer solar cells

As shown in Figure 1-21, the photovoltaic energy conversion process of polymer solar cells can be divided into four steps: light absorption, exciton diffusion, charge transfer, and charge collection [45,46]. The horizontal lines on the right and left of each illustration correspond to the Fermi energies (E_F) of the cathode and anode contacts, respectively. The boxes correspond to the acceptor (left) and donor (right) energy gaps, respectively. Here, LUMO is the lowest unoccupied molecular orbital, and HOMO is the highest occupied molecular orbital of the organic film. Red dots are electrons and red circles are holes, with dashed lines drawn between them to represent excitons. Also, the dip in the energy levels in the vicinity of the exciton qualitatively depicts its binding energy (0.5–1 eV), placing this quasi-particle at an energy somewhat below that of the HOMO–LUMO gap energy. η_A is the absorption efficiency of light within the active region of the solar cell, η_{ED} is the exciton diffusion efficiency to a dissociation site, η_{CC} is the charge collection efficiency, and η_{CT} is the charge transfer efficiency.

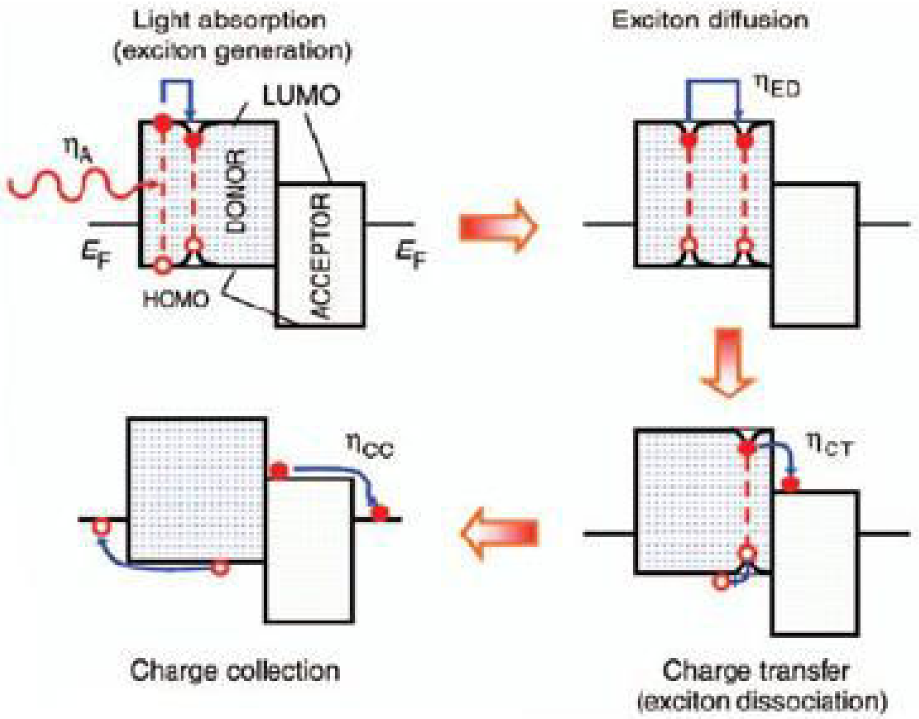

Figure 1-21 Mechanism for polymer solar cells [45]

(1) Light absorption (exciton generation): The active polymer layer absorbs incident photons and then the electrons from the polymer highest occupied molecular orbital (HOMO) are excited to the lowest unoccupied molecular orbital (LUMO), forming the excitons. This process occurs in 10^{-13}-10^{-9} seconds. The active polymer layer is a major factor that determines the efficiency of polymer solar cells. The currently best active layer material can absorb up to 40% of the sunlight, thus wasting the majority of the solar energy. Therefore, in order to improve the energy conversion efficiency of the final device, the first thing need to be done is to make the active polymer layer more absorbents. For an efficient collection of photons, the absorption spectrum of the organic active layer should match the solar emission spectrum and the layer should be sufficiently thick to absorb the entire incident light. A better overlap with the solar emission spectrum is obtained by lowering the band gap of the organic material, but this will ultimately have some negative effects on the open-circuit voltage. Increasing the layer thickness is positive for light absorption, but will slowdown the charge transport and also increase the internal resistance of the device [47, 48].

(2) Exciton diffusion: Creation of charges is one of the key steps in the conversion of sunlight into electrical energy. However, the exciton is separated into charges (i.e. electrons and holes), only at the interface of electron donor/acceptor material. Therefore, when the exciton is generated far from the electron donor/acceptor interface, the exciton must diffuse to the electron donor/acceptor interface before further charge separation. But exciton diffusion is in competition with other decay processes such as luminescence or non-radiative recombination to the ground state. For an efficient solar cell, all excitons have to reach the electron donor/acceptor interface within exponential lifetime, which determines the distance an exciton is able to cross. This distance is generally limited to 10 nm. Therefore, the morphology of electron donor/acceptor is essential [46].

(3) Charge transfer (exciton dissociation): In this step, an electron is transferred from the electron donor to the electron acceptor driven by the energy difference (offset) between the LUMOs of the donor and acceptor. It appears that a minimum energy difference of 0.3 eV is required to induce the exciton splitting and charge dissociation. In the photo-induced electron transfer process, an exciton at the donor/acceptor interface decays by creation of the charge-separated state consisting of the radical cation of the donor and the radical anion of the acceptor. For an efficient charge generation, it is essential that the charge-separated state is the thermodynamically and kinetically most favourite pathway for the exciton. Therefore, it is important that the energy of the absorbed photon is used for generation of the charge separated state and is not lost via competitive processes like fluorescence or non-radiative decay. In addition, it is of importance that the charge-separated state is stabilized, so that the photo-generated charges can migrate to one of the electrodes [49, 50].

(4) Charge collection: In this step, charges transfer to the respective electrodes, and the collection of charges at the electrodes is regularly accomplished by a transparent conductive oxide (TCO) such as ITO on one side and a metal contact on the other side. The effectiveness of the charge collection is mainly affected by the energy level matching between electron donor material and electron acceptor material, as well as the contact situation [51, 52].

In 1986, Tang firstly introduced a double-layer structure of a p- and n-type organic semiconductor with power conversion efficiency of about 1%. Since then, polymer solar cells have undergone a gradual evolution that has led to energy conversion efficiencies of about 10% [31]. To date, two main approaches have been explored in the effort to develop viable devices: the donor–acceptor bilayer [53], commonly achieved by vacuum deposition of molecular components, and the so-called bulk heterojunction (BHJ) [54], which is represented in the ideal case as a bicontinuous composite of donor and acceptor phases, thereby maximizing the all-important interfacial area between the donors and acceptors (as shown in Figure 1-22). Polymer solar cells have certain disadvantages including their low efficiency and short lifetime. Nevertheless, their numerous benefits such as low-cost, lightweight, and flexibility, can justify the current international investment and research in developing new polymeric materials, new combinations and structures to enhance efficiency and to achieve low-cost and large-scale production within the next years.

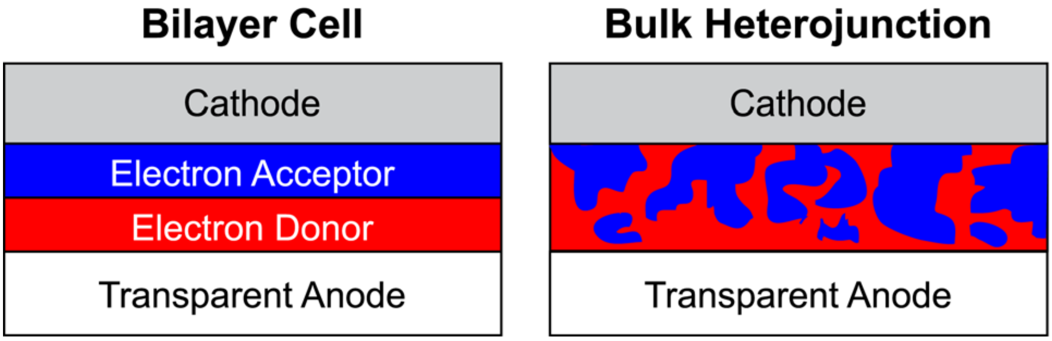

Figure 1-22 Two kinds of structure of polymer solar cells

3.1.4 Dye-sensitized solar cells

Dye-sensitized solar cell generally consists of five main parts, namely the transparent conductive substrate, the nano-crystalline semiconductor thin film, the photosensitizing dye, the electrolyte and the counter electrode, as shown in Figure 1-23. The core part is the porous semiconductor film with thickness of about 10μm and a porosity of 50-60%, which is composed of nano TiO_2 particles with the diameter of about 10-30 nm. The nano-TiO_2 particles link each other and form a network structure by sintering, which not only provides a huge surface area, but also has good inter-particle electron conductivity. Usually, the porous TiO_2 film is supported on the transparent conductive substrate such as FTO glass substrate, and sensitized with a molecular dye chemisorbed on its surface. An electrolytic solution containing iodide and triiodide ions is used as a redox mediator to reduce the oxidized dye molecules. A platinum-coated glass substrate placed parallel to the working electrode with a face-to-face configuration acts as counter electrode.

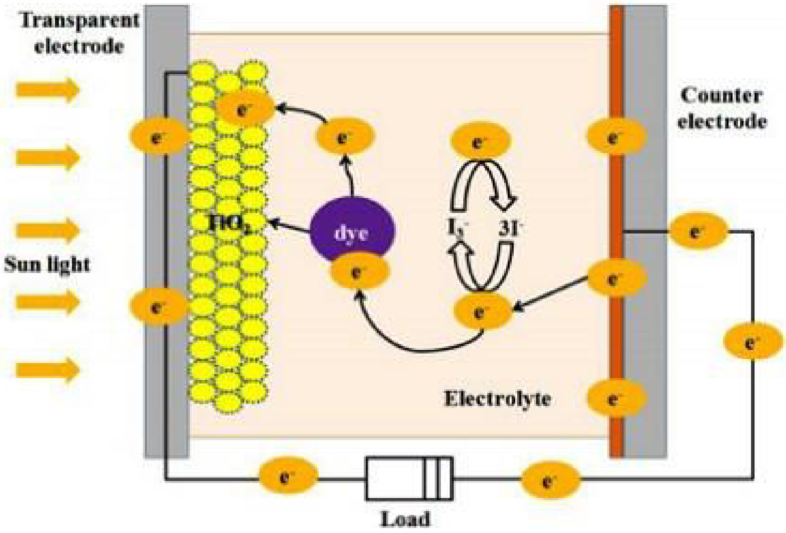

Figure 1-23 Schematic diagram of dye-sensitized solar cells (DSSC) [55]

The sunlight irradiates from the working electrode side, passes through the transparent electrode, reaches the photoanode and is finally absorbed by the dye molecules. The optical absorption occurring in dye molecules involves an electron transit process from the HOMO to the LUMO. The photo-generated electrons then transfer from the dye molecules to the TiO_2 and diffuse to the transparent conducting film of the collector electrode, which is connected to the external circuit. Within a circle process, the oxidized dye molecules are reduced by the electrons in electrolyte and, simultaneously, the electrolyte is regenerated by the electrons injected from the counter electrode. The electron transfer process in DSSC can be summarized as follows:

(1) The dye, upon absorption of a photon (*hv*), goes from ground state(S) to an electronically excited state(S*)

$$S+h\nu\rightarrow S^* \tag{1.10}$$

(2) The excited state(S*) lies energetically above the conduction band (CB) edge of the TiO_2 nanoparticles and injects an electron into the TiO_2 conduction band

$$S^*+TiO_2\rightarrow S^++e^-_{cb}(TiO_2) \tag{1.11}$$

(3) The oxidation of iodide

$$2S^++3I^-\rightarrow 2S+I_3^- \tag{1.12}$$

(4) The injected electrons give a current flow and provide for the reduction of iodine at the counter-electrode

$$I_3^- + 2e^- \rightarrow 3I^- \qquad (1.13)$$

Compared with existing solar cells based on silicone technology, DSSC has big advantages in manufacturing cost and productivity of large devices because high vacuum and high temperature are not necessary for production. In addition, the DSSC will also work in low light conditions (i.e. cloudy skies and indirect sunlight), and it has been suggested that with the use of DSSC, indoors-light from the various lighting sources could even be absorbed [56]. The major disadvantage is that the liquid electrolyte used in DSSC is temperature-sensitive. The electrolyte can freeze at low temperatures cutting power production and causing physical damage. Sealing the panels becomes a difficult task, when the liquid expands at higher temperatures. The use of a liquid electrolyte causes some serious additional problems such as potential instability, limitation of maximum operation temperature, danger of evaporation and extra cost for forming an electrical series connection[57]. Moreover, compared with the first and second generation solar cells based on conventional semiconductor materials with conversion efficiencies of ~20 – 30%, current dye-sensitized solar cells still demonstrate efficiencies relatively low. To date, the world's highest level for dye-sensitized solar cells is about 11.4% [31].

3.1.5 Compound solar cells

Compound solar cells include gallium arsenide (GaAs) thin film solar cell, cadmium telluride (CdTe) thin film solar cells, copper indium gallium selenide (CIGS) thin film solar cells.

GaAs is a direct bandgap semiconductor with a bandgap of 1.45 eV, thus is regarded as an ideal photovoltaic semiconductor materials. The first GaAs solar cells having efficiencies in excess of 6% were already reported in 1956 [58]. Since then, researchers began to study homojunction GaAs solar cells. However, the cost/efficiency ratio of this cell was high compared with silicon-based solar cells, thereby inhibiting the development of GaAs solar cells. In the early 1970s, multi-junction structure attracted attentions of scientists. Such structured GaAs solar cells consist of several stacked p-n junctions (as shown in Figure 1-24).

Each junction is tuned to a separate range of light wavelengths, so that the multiple p-n junctions are able to absorb a wider range of the solar spectrum (as shown in Figure 1-25), allowing for increased conversion efficiency over the solar spectrum. Progress in the development of multi-junction efficiency has shown promising results [59]. From the 16% in the 1980s to the current record of 43.5%, it is expected that within the coming years, multi-junction solar cell for commercial use would reach efficiencies of 50% [32]. However, this kinds of solar cells are complex and expensive to fabricate, requiring additional tunnel layers between p-n junctions.

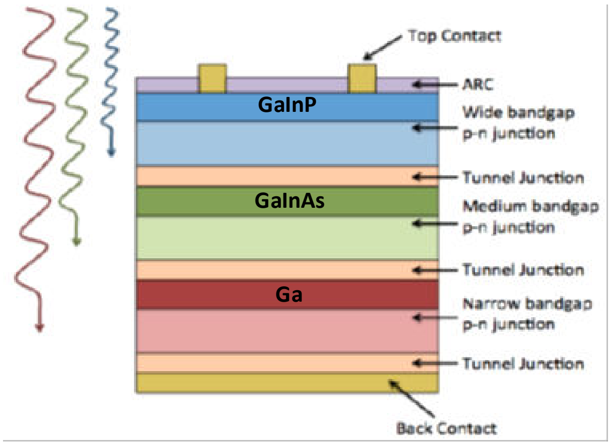

Figure 1-24 Schematic of multi-junction GaAs solar cells

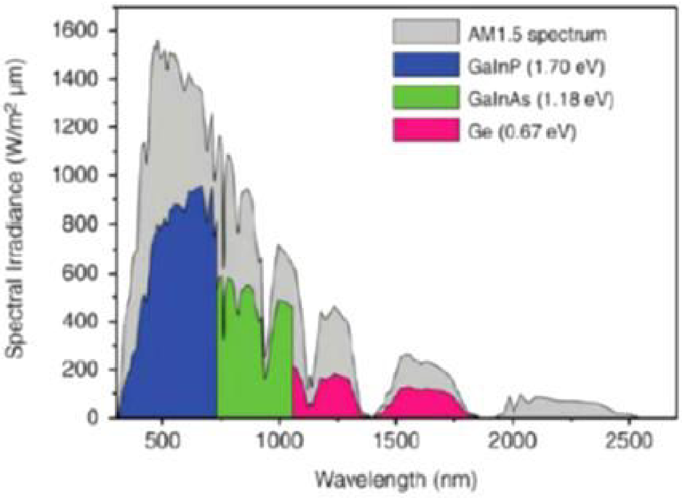

Figure 1-25 Absorption spectrum of the multiple p-n junctions (GaInP/GaInAs/Ge) [59]

CdTe is a strong candidate for thin film solar cell applications due to its high efficiency and low cost. CdTe has a direct band gap (E_g = 1.45 eV) which is very close to optimum bandgap (E_g = 1.5 eV) for solar cell. It has a high absorption coefficient of 5×10^5/cm, which indicates that efficient collection of photons with energy greater than the band gap (E_g) is possible within a very thin CdTe absorber layer [60]. The theoretical efficiency of CdTe thin-film solar cells is expected to be 28%–30% [61]. CdTe solar cells can be manufactured quickly and inexpensively, providing a lower-cost alternative to conventional silicon-based technologies. The typical structure of CdTe solar cell is shown in Figure 1-26 [62]. The core part of CdTe solar cell is a CdTe/CdS junction, in which top layer is CdS and the bottom layer is CdTe. CdTe solar cells are completed by adding a high-quality transparent conductive oxide (TCO)—usually fluorine-doped tin oxide (SnO_2:F)—and a back electrical contact—typically a metal or carbon paste with copper (Cu). The disadvantage to use Cu as the back contact is the gradual diffusion of Cu atoms into the CdTe and CdS layers, which creates defects and promotes Cu accumulation at the CdTe/CdS junction. Between TCO and CdS layer, there is a very thin resistive buffer layer such as Zn_2SnO_4. By incorporating this buffer layer, the CdS layer thickness can be further reduced down to <50 nm, which can significantly improve the blue response and conversion efficiency of the CdTe solar cell [63]. The record efficiency for a laboratory CdTe solar cell is 18.7% to date [64], which is well above current commercial CdTe modules. However, Tellurium is a rare metalloid, while Cadmium is toxic if breathed in fine dust or fumes. Therefore the application of CdTe solar cell is limited.

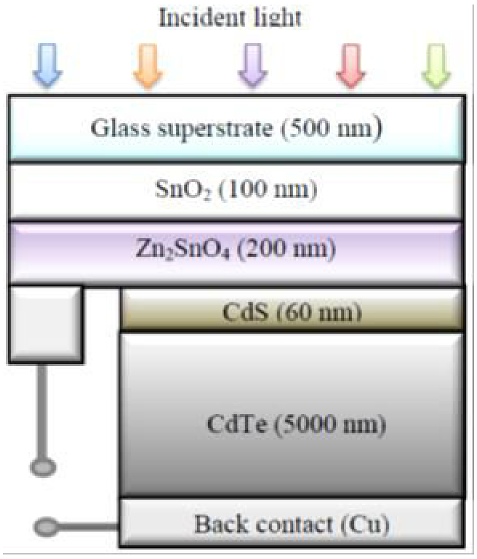

Figure 1-26 Schematic of CdTe solar cells (Zn_2SnO_4 as a buffer layer)

The structure of CIGS solar cells is shown in Figure 1-27. Soda lime glass is commonly used as a substrate. Furthermore, many companies are also looking at lighter and more flexible substrates such as polyimide or metal foils [65]. A molybdenum layer, which serves as the back contact, is deposited on the glass substrate to reflect most unabsorbed light back into the absorber. Then a p-type CIGS absorber layer is grown on the molybdenum layer, followed by the deposition of a thin n-type buffer layer such as CdS. Next, the buffer is overlaid with a thin, intrinsic ZnO layer (i-ZnO) to protect the CdS and the absorber layer from sputtering damage while depositing the ZnO:Al layer. Finally, a thicker Al doped ZnO layer, serving as a transparent window layer, is deposited on the top of the ZnO layer to collect and move electrons out of the cell while absorbing as little light as possible.

CIGS solar cells have many advantages as follows: (1) Compared to silicon solar cells, CIGS layer can be deposited in a polycrystalline form directly onto molybdenum coated glass sheets, steel bands, especially flexible substrates. Moreover, the CIGS solar cells show a better resistance to heat than silicon solar cells. (2) Compared to CdTe solar cells, CIGS solar cells have much lower level of cadmium, in the form of cadmium sulfide. In some designs, zinc is used instead of cadmium. (3) CIGS has an exceptionally high absorption coefficient of more than 10^5/cm for 1.5 eV and higher energy photons [66]. CIGS solar cells with record conversion efficiency of 20.3% to date have been reported by Zentrum für Sonnenenergie und Wasserstoff Forschung (ZSW) [31], which is also a record efficiency of thin film solar cells. However, the efficiency of CIGS solar cells is still lower than crystalline silicon solar cells, for which record efficiency lies at 25% [31]. In addition, the cost of fabricating the CIGS solar cells makes it difficult to be competitive with current grid prices. It may take several more years to solve the manufacturing problems and to bring the production costs in line with the cost of other solar cells.

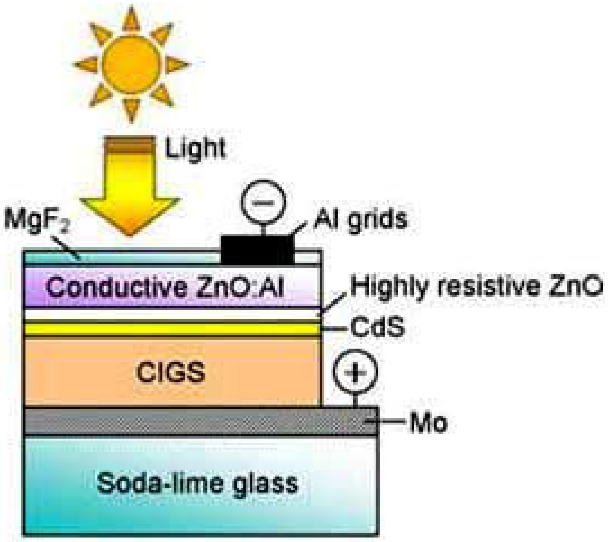

Figure 1-27 Schematic of CIGS solar cells

In summary, Silicon is the oldest technology and up to now it is also the most diffused in solar cell market (exceeding 80% in 2011 [67]). However, the record efficiency of silicon solar cell is 25.0%, approaching the theoretical efficiency limit of 30% [68]. Its main drawback is the low scalability, which results in modules with low efficiency or very high cost. The single junction record efficiency of 29.1% is held by GaAs, however it is mainly used for space application due to the high production cost. Although multi-junction cells achieve the best conversion efficiency of 43.5%, its structures are extremely complex and expensive. The DSC and OPV are late starters, their efficiencies need further development. While CIGS is one of the most promising thin film technologies due to its high efficiency and relatively low production cost. CIGS holds the thin film efficiency record and it is also suitable for flexible modules production. CIGS solar cells on flexible substrates offer several advantages for their manufacturing as well as applications compared to solar cells on rigid glass substrates. They are lightweight, can be applied on uneven surfaces and can be rolled-up when not in use. Flexible and lightweight CIGS modules open up new application possibilities for terrestrial and space applications. Recently, the world efficiency record has reached 20.3%, thus demonstrating the potential for futur development [31].

The photoelectric materials studied in this thesis have some similitude with the CIGS compounds. This is the reason why special attention has been paid to the state-of-the-art of the CIGS solar cells.

3.2 Development of CIGS solar cells

3.2.1 History of CIGS solar cells

In 1953, $CuInSe_2$ material was synthesized for the first time by Hahn and co-workers [69].

In 1974, the first $CuInSe_2$ solar cells with an efficiency of 12% have fabricated by evaporating n-type CdS onto p-type single crystals of $CuInSe_2$ by Wagner and co-workers [70].

In 1976, the first thin-film $CuInSe_2$/CdS devices were fabricated by Kazmerski and co-workers, using films deposited by evaporating $CuInSe_2$ powder in excess of Se vapor [71].

In 1981, the first high-efficiency all thin film solar cell based on the system *n*-ZnCdS/*p*-$CuInSe_2$ was prepared by Mickelsen and co-workers from Boeing, realizing a conversion efficiency of about 9.4% and in 1985 they reached the efficiency of 11.4% [72, 73].

In 1988, by using a different process based on selenization of stacked metal layers, Arco Solar achieved cell efficiencies as high as 14.1% [74].

Since the late 1980s, in order to make full use of the solar spectrum, the gallium element was introduced into the $CuInSe_2$ absorber layer (has a bandgap of 1.04 eV) to increase the band gap (an indium to gallium ratio of 20–40% will result in a bandgap of approximately 1.1–1.2 eV) and to get a better match with the solar spectrum, leading to an important increase in photoelectric conversion efficiency [75].

In 1994, the so-called three-stage process, introduced by NREL [76], is obtained by starting the deposition with an $(In,Ga)_xSe_y$ precursor, followed by the co-deposition of Cu and Se until Cu-rich overall composition is reached, and finally the overall Cu concentration is readjusted by subsequent deposition of In, Ga and Se. The obtained conversion efficiency reached 16.4%. This method leads, up to now, to the most efficient solar cells.

From then on, it was possible to fabricate thin film solar cells based on the $CdS/CuInGaSe_2$ system with an efficiency of 18.8% in 1999 [77], of 19.2% in 2003 [78] and of 20.3% in 2011 [31]. This last result is also the highest value for energy conversion efficiency in an all thin film photovoltaic device.

3.2.2 Research progress on CIGS absorber layer

Nowadays, the aim of CIGS solar cells is to achieve high conversion efficiency and low production cost. As the core part of CIGS solar cells, the CIGS absorber layer still attracts attention from the scientific community and the most significant progresses are achieved in the two following domains:

(1) Material research on CIGS absorber layer

$Cu(In,Ga)(Se,S)_2$ alloys from the I–III–VI group of the periodic table are used as absorber layers, including a wide range of band gaps. $CuInSe_2$ has a relatively narrow band gap of 1.04 eV which can be better adjusted to the solar spectrum by replacing part of In with Ga and part of Se with S. The band gap can be adjusted from 1.04 eV ($CuInSe_2$) to 1.53 eV ($CuInS_2$) and to 1.7 eV ($CuGaSe_2$) [79, 80]. Hence one can change the bandgap throughout the absorber material in the solar cell and make a graded CIGS solar cell. This kinds of cell have two main advantages: i) Increasing the bandgap towards the back of the cell (*back grading*) can create an electrical field which pulls the electrons towards the space charge region so that they can contribute to the light current. ii) Increasing the bandgap towards the front of the absorber layer (*front grading*) will reduce the recombination losses in the space charge region and thus increase the cell efficiency [81]. A graded CIGS solar cell has achieved an efficiency of 19.9% [82]. Most recently, the multilayer CIGS solar cells with Cu gradients in the absorber layer have been studied. The results show that with the Cu and Ga distribution stepped simultaneously in the multilayer cells, the improvement of efficiency could be approximately 3.5% due to the enhanced charge carrier collection for longer-wavelength photons, and to the reduced recombination at the heterojunction and back regions of the cell [83].

The use of rare materials such as In and Ga increases the production cost of the entire device and it is therefore necessary to find new alternative materials for In and Ga elements. Zn and Sn were mostly used to substitute In and Ga, forming $Cu_2ZnSn(Se, S)_4$ (CZTS) absorber layer, while the structure of the solar cells was very similar to the CIGS solar cells standard structure having CdS as buffer layer, ZnO as front and Mo as back contact. The band gap of Cu_2ZnSnS_4 is around 1.5eV, while for $Cu_2ZnSnSe_4$ the gap stays around 1 eV [84, 85, 86]. The band gap of CZTS is affected by the deposition methods, crystallization procedure as well as presence of secondary phases, such as Zn(Se, S), Cu(Se, S), CuSn(Se, S). The best solar cells show a Zn-rich and Cu-poor composition, which provides a Zn(Se, S) secondary phase. As Zn(Se, S) has a wide band gap and low conductivity, it would not affect the open-circuit voltage, and could lead to the high series resistance observed in all solar cells [87]. The efficiency of CZTS solar cells was obviously increased to 5.45% in 2003 [88] and then to 6.7% in 2008 [89] by optimization of the sulfurization process. In 2010, the efficiency of 9.6% was reached by inserting a selenization step [90]. In August 2012, IBM announced they have developed a world-record setting CZTS solar cell with conversion efficiency of 11.1% [91]. However, the efficiency of CZTS solar cell is still lower than that of CIGS solar cell.

(2) Production process research on CIGS absorber layer

The absorber deposition methods mainly include vacuum-based and non-vacuum based methods [92, 93]. The most widely used and successful vacuum-based method is the ‘co-evaporation’, in which all the four elements of Cu, In, Ga and Se are simultaneously delivered to the Mo coated substrate, forming the absorber layer in a single step. The Zentrum für Sonnenenergie und Wasserstoff forschung (ZSW, Germany) and the National Renewable

Energy Laboratory (NREL,USA) used a high-temperature (> 550 ^{o}C) three-stage co-evaporation process to fabricate CIGS absorber layer on glass substrates and achieved high efficiencies of about 20% [93, 82], while the Swiss Federal Laboratories for Materials Science and Technology (Empa, Switzerland) obtained CIGS solar cell with 20.4% efficiency through a low-temperature (< 450 ^{o}C) multi-stage co-evaporation process to prepare the absorber layer using flexible substrates [94]. An alternative vacuum-based method is the sputtering of metal precursors and subsequent selenization followed by sulfurization. Solar Frontier achieved 19.7% efficiency by using such a method [95]. To date, the record efficiency CIGS solar cells are all processed using absorber layers grown via vacuum-based methods.

However, the high vacuum process used in this method increases the fabrication costs. The co-evaporation generally requires a high degree of control and large area coatings with uniform properties are difficult to achieve. Moreover, some of the processes use toxic gases, such as selenium vapor or an H_2Se atmosphere, in order to convert the deposited film of the Cu-In-Ga alloy or the oxide thereof into the final solar responsive form [96]. Hence, the cheap and convenient non-vacuum based methods have attracted wide attentions of scientists [97]. The various non-vacuum based approaches to fabricate CIGS absorber layer may be grouped into two main categories: preparing from well-dispersed solutions containing CIGS nanoparticles/precursors and preparing through electrodeposition.

The well-dispersed solutions prepared from CIGS nano particles are usually called CIGS inks. The CIGS nano particles (or quantum dots) are commonly synthesized by using hot-injection or solvo-thermal routes [98, 99], which are generally rinsed and modified to improve the dispersibility in certain nonpolar solvents, thus getting stable CIGS inks. Next, CIGS inks are coated on the substrate using liquid deposition techniques (such as dip-coating, spin-coating etc.) under ambient condition and then solidified and crystallized at relatively low temperature, which is suitable for coating on flexible substrates [100]. For ink-based methods, highest efficiency of 17.1% was achieved by Nanosolar in 2012 [101]. In addition, the CIGS absorber layer can also be prepared by direct coating of a homogeneous solution containing a dissolved metal precursor (Cu, In, Ga organics, salts, chalcogenides etc.) in an organic solvent. The solvent is a key factor that influences the stability of the solution. Many factors are considered in selecting a suitable solvent, including the boiling point, vapor pressure, polarity, reactivity, surface tension, toxicity and cost [102, 103]. In 2013, IBM achieved a conversion efficiency of 15.2% by this solution-based method using hydrazine solvent [104].

Electrodeposition is another solution-based method to fabricate CIGS absorber layer, which have advantages of low instrumental and materials cost, high deposition speed, efficient utilization of raw materials and feasibility in making large area films. This deposition technique can be divided into one-step method and two-step method [105,106]. In a one-step deposition, the concentration and pH value of the electrolyte must be adjusted, so the electrode potentials of all the individual elements may come closer to each other. Therefore, one-step electrodeposition of CIGS layers is rather difficult due to the large difference in the values of equilibrium reduction potential for each constituent. Many works have been carried out to find out the best concentration of electrolyte for obtaining the stoichiometry, as well as the appropriate deposition potential in one-step electrodeposition of CIGS layer [107]. While the two-step method can be employed via stacked layer structure deposition of pure elements, binary or ternary compounds, followed by a selenization treatment [108, 109]. As the as-deposited CIGS layers are poorly crystalline and may contain Cu-Se second phases, the high temperature post-annealing is carried out in a Se-rich environment to avoid micro cracks and defects in the layer. The layer morphology and the resulting conversion efficiency depend on the relative ratio of the component elements in the fabricated layer [85].

4 Photocatalytic materials

4.1 State-of-the-art and research directions

From the photocatalytic mechanism analyzed in section 2.2, it is obvious that the efficient generation, separation and migration of photo-generated charge carriers (electrons and holes) is necessary for the semiconductor photocatalytic reaction. Based on this understanding, the current semiconductor photocatalysis research is mainly carried out to address the two following issues:

(1) How to efficiently capture the photo-generated charge carriers? The high specific surface area of photocatalytic material can enhance the adsorption of O_2 and H_2O, thereby increasing the yield of active groups to obtain a higher photocatalytic activity. Furthermore, the high specific surface area of the photocatalyst is also beneficial for increasing the contact area with the organic contaminants, thus improving the photocatalytic oxidation reaction rate. Therefore, photocatalytic materials with high specific surface area have become an important research direction.

(2) How to efficiently produce the photo-generated charge carriers and to promote their efficient separation and migration? For example, the most commonly used TiO_2 photocatalyst, has a band gap of about 3.2 eV (for anatase phase), thus deciding that only the UV light with a wavelength less than 387.5 nm, representing only a small part (3-5%) of solar irradiation, can excite electrons in the valence band . Therefore, the enhancement of visible photocatalytic activity has become a hot research topic. In addition, studies have shown that for a pure photocatalyst, the recombination process of photo-generated charge carriers is faster than its separation process, and only the electrons and holes yielded from effective separation of photo-generated carriers will further react and form active substances, leading to the decomposition of organic pollutants. Therefore, inhibiting the recombination of photo-generated electrons and holes becomes an effective way to improve the photocatalytic activity.

4.1.1 Research on porous photocatalytic materials

Currently, in order to increase the specific surface area of the photocatalytic material, the photocatalytic materials are mainly prepared in the forms of nano powder, porous film and a porous bulk material.

(1) Photocatalytic nano powder

Photocatalytic nano powder has a large specific surface area and its preparation method can be divided into gas and liquid methods. The most typical example of gas preparation is the commercial P25 type TiO_2 nano powder produced by Degussa Company through oxidation of $TiCl_4$ gas [110]. The most studied method is still a liquid phase method. In this method, the particle size of photocatalyst is mainly determined by the two following parameters: one is an aggregation of nano powder in common drying process; the other one is the growth of nanoparticles during the heat treatment.

By means of freeze-drying or supercritical fluid extraction, one can effectively eliminate the water capillary force to overcome the gel collapse during the drying process, thus preventing the aggregation. Stallings et al. [111] added water and surfactant into the supercritical CO_2, forming a micro emulsion. Therefore the reaction can be controlled in the droplets to avoid further crystal growth; furthermore, the nanoparticle aggregation in the drying process can be avoided by using supercritical CO_2. The as-prepared TiO_2 microspheres have a specific surface area of 275~475 m^2/g.

Hydrothermal method has become another effective route to prepare nanoparticles because it allows avoiding subsequent high temperature crystallization treatment. Cheng et al. [112] diluted $TiCl_4$ into ice-water to obtain a gel and prepared TiO_2 nano powders with an average particle size of 8~20 nm under hydrothermal conditions. The organic solvent can effectively reduce the interaction between particles due to its weak polar and small surface tension. Thus, Wang et al. [113] used the organic solvents to replace the traditionally used water solvent in the hydrothermal reaction and prepared TiO_2 nano powders with an average particle diameter of only a few nanometers under solvothermal conditions. While Kominami et al. [114] diluted a titanium alkoxide into an organic solvent, and then injected into the tube, which was subsequently put into the autoclave. Between the tube and the inner wall of the autoclave, there were a certain amount of water or its mixed solvents. Therefore, the formed water vapor could promote the hydrolysis of titanium alkoxide with water dissolved in organic solvent from water vapor, resulting in the formation of crystalline nano TiO_2 in the organic solvent.

(2) Photocatalytic porous film

Currently, there are mainly two ways to fabricate photocatalytic porous film: First one is increasing the roughness of the film by controlling the particle size in the film to obtain pores between the particles; Second technique is to use a template to form the film, followed by the removal of the template, leading to a porous film.

Doherty et al. [115] prepared a porous TiO_2 film with large specific surface area by controlling the particle size through traditional sol-gel method. O'Regan [116] prepared a three-dimensional network of the porous TiO_2 films on conductive glass with roughness factor of 1000 by hydrothermal method film. Zhang et al. [117] prepared a mechanically stable mesoporous nanocrystalline titania thick films by hydrothermal treatment of an aqueous mixed paste containing nanocrystalline TiO_2 powder and Ti alkoxide. The Ti monomers were converted into crystalline TiO_2, which acted as a “glue” to chemically connect the TiO_2 particles.

The template method is most commonly used to fabricate the porous photocatalytic film. Many works have been reported on the preparation of porous TiO_2 thin film by using block copolymers surfactant, latex spheres, polystyrene particles, polyethylene glycol, colloidal crystals and monomer droplets as templates [118, 119]. These templates are eliminated from TiO_2 thin film via an annealing step in a typical procedure, accompanied with the crystallization of amorphous TiO_2 colloidal particles, thereby forming the porous crystalline TiO_2 thin film. In addition, the template can also be removed by etching effect using appropriate solvents. For example, Kotani et al. [120] put the poly(ethylene glycol) (PEG) in SiO_2-TiO_2 gel film with hot water treatment, so the PEG could be removed from the film and pores are obtained in the film.

(3) Photocatalytic porous bulk materials

At present, there are two types of method to prepare photocatalytic porous bulk materials. One is to directly load the nano photocatalyst on the porous carrier. Owing to the high adsorption ability of the porous carrier, the mass transfer rate and the photocatalytic efficiency could be increased. The common porous carriers are some minerals such as carbon, zeolite, clay and montmorillonite [121, 122], as well as some artificial porous material such as honeycomb ceramics, molecular sieves, porous SiO_2 and Al_2O_3 etc [123]. Another technique is to prepare the aerogel materials. Dagan et al. [124, 125] prepared TiO_2 aerogel with specific surface area close to 500 m^2/g, and both surface and the interior of TiO_2 aerogel could absorb the light due to the relatively high transmittance of the bulk aerogel.

4.1.2 Research on photocatalytic materials with high quantum efficiency

Improving the quantum efficiency of photocatalytic materials was mainly realized by changing the energy band structure, leading to more absorption of visible light or to the more efficient separation and migration of photo-generated carriers. The current improving methods are mainly divided into metal ion doping, nonmetal ion doping, noble metal deposition, organic dye sensitization and use of semiconductor composite.

(1) Metal ion doping

Metal ion doping is to introduce transition metal or rare earth metal into the TiO_2 lattice structure by physical or chemical method, which leads to the formation of defects or a change in the lattice type. Therefore, doping metal iron in TiO_2 can change the energy band structure (as shown in Figure 1-28), such as a shift of the energy level [126], narrowing of the band gap [127] and the creation of a doping level [128]. The objective is to promote the transfer of photo-generated electrons and holes, to adjust their distribution state and to facilitate photo-generated carrier separation.

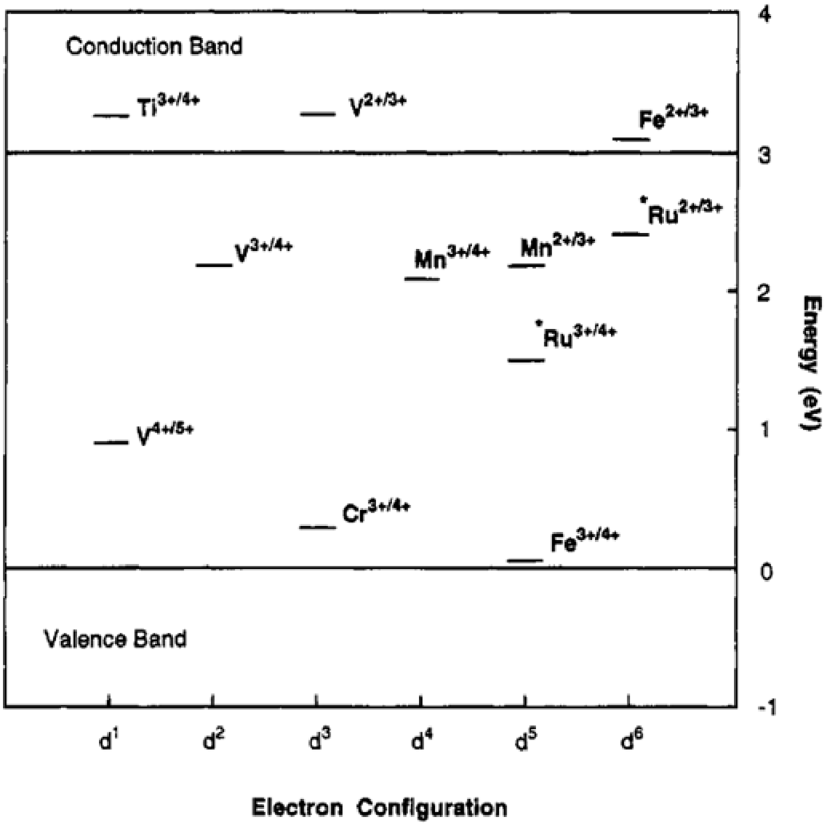

Figure 1-28 Energy levels of impurity metal ions in TiO_2 [129]

Xu et al. [130] have studied the La^{3+}, Ce^{3+}, Er^{3+}, Pr^{3+}, Gd^{3+}, Nd^{3+}, Sm^{3+} and other lanthanide rare earth ions doped TiO_2, and found that the absorption wavelength of doped TiO_2 was "red shifted", in the order of : Gd^{3+}> Nd^{3+}> La^{3+}> Pr^{3+}(Er^{3+})> Ce^{3+}> Sm^{3+}, Gd^{3+} with a higher visible photocatalytic activity. In addition, the photocatalytic activity was also determined by the doping concentration and the optimum doping concentration was about 0.5%. Serpone et al. [131] used transition metal ions M (M is Cr^{3+}, Fe^{3+}, V^{5+}) as dopant-ions to prepare M/TiO_2 photocatalytic materials, forming doping level within the band gap of TiO_2, thus extending the absorption wavelength of TiO_2 to the visible range of 410-620 nm (3.0 eV-2.0 eV). Yamashita et al. [132] doped TiO_2 with V^{5+}, Mn^{3+}, Fe^{3+}, Co^{2+}, Ni^{2+}, Cr^{3+} and other transition metal ions, effectively expanding the absorption wavelength of photocatalytic material to the visible light. Choi et al. [129] studied 21 kinds of metal ions doped TiO_2 and found that 0.1-0.5% of Fe^{3+}, Mo^{5+}, Ru^{3+}, Os^{4+}, Re^{5+}, V^{5+} and Rh^{3+} could greatly improve the photocatalytic activity of TiO_2. In contrast, doping Co^{3+} or Al^{3+} reduced the photocatalytic activity of TiO_2 likely because they became the electron and hole recombination centers.

(2) Nonmetal ion doping

Nonmetal ion doping is to introduce ions such as N, C, S and F into the oxygen lattice. The orbital hybridization of the p orbital of these ions with the O 2p orbital can lead to the shift of the valence band and to the decrease of band gap, so that the material can absorb the visible light.

As early as 1986, Sato et al. [133] have discovered that N-doped TiO_2 exhibited photocatalytic activity under the visible light illumination. However, this result failed to attract attentions. Only in 2001, Asahi et al. [134] reported N-doped TiO_2 photocatalytic materials on ‘Science’ journal and the nonmetal ion doped TiO_2 became a hot research topic. Khan et al. [135] prepared C-doped TiO_2 thin films by burning metal titanium sheet. The absorption edge of obtained TiO_2 film red shifted to 535 nm, thus achieving photoelectric conversion efficiency of 8.35% when electrolyzing water under visible light irradiation. Umebayashi et al. [136] prepared S-doped TiO_2 powder using the oxidation annealing of TiS_2. The remaining S could occupy the position of O atom in TiO_2 lattice, forming a Ti-S bond. The orbital hybridization of S 3p orbital with the O 2p orbital can lead to narrowing of the band gap and to ‘red shift’ of absorption edge. Yamaki et al. [137] prepared F-doped TiO_2 by ion implantation method and believed that the F atoms replaced the O atoms in the lattice, forming the hole-type defects in the crystal, thus leading to enhanced absorption of visible light. In addition, Yu et al. [138] considered that the F doping could not only enhance the absorption of visible light, but also improve the crystallinity of anatase TiO_2, suppress the formation of brookite phase, and prevent the transformation from anatase to rutile phase.

(3) Noble metal deposition

With the deposition of appropriate amount of noble metal (Pt, Ag, Pd, Au, etc.) on the surface of TiO_2, the photo-generated electrons will be transferred from TiO_2 (with high Fermi level) to noble metal (with low Fermi level), forming Schottky barrier, which can effectively capture electrons [139], thereby limiting the recombination of electrons and holes (as shown in Figure 1-29).

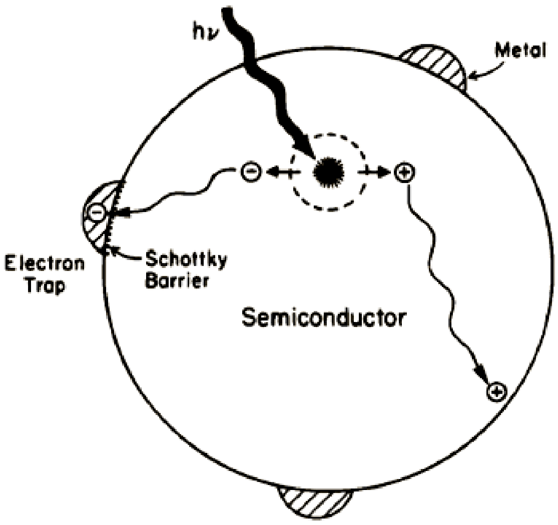

Figure 1-29 Schematic diagram of photoexcitation in metal-modified semiconductor

Noble metal deposition can not only promote electrons and holes separation, but also extend the absorption wavelength range to visible light region. Sasaki et al. [140] deposited Pt on TiO_2 thin films by pulse laser deposition and obtained Pt/TiO_2 photocatalytic material with a band gap of 2.3 eV, exhibiting high visible photocatalytic activity. Noble metals deposited on TiO_2 surface are generally in the form of nanoscale clusters and its coverage on the TiO_2 surface tend to be small. This is because the excessive deposition of noble metal will reduce the contact area between TiO_2 and organic pollutants. It was reported that the photocatalytic activity of Pt/TiO_2 with Pt loading amount of 0.2% was 4 times higher than pure TiO_2; while when the Pt loading amount reached 0.5%, the photocatalytic activity of Pt/TiO_2 was lower than pure TiO_2 [141].

(4) Organic dye sensitization

The organic dye sensitization is to modify TiO_2 material with organic photoactive substances such as chlorophyll, phthalocyanine, eosin, porphyrin, ruthenium complexes [142, 143], which can absorb photons and form excited state under the visible light. The photo-generated electrons are then transferred from the excited dye molecules to the TiO_2, so that the excitation wavelength of the light can be expanded into the visible light range (as shown in Figure 1-30). However, in the photocatalytic reaction, the photosensitized TiO_2 may lead to decomposition of the conjugated structure or chromophore in dye molecule, even highly mineralizing the dye to CO_2 and H_2O. In addition, most used sensitizers have weak absorption in the near infrared region, which cannot be well matched to the solar spectrum. Therefore, the selection of dye is important to get a better performance.

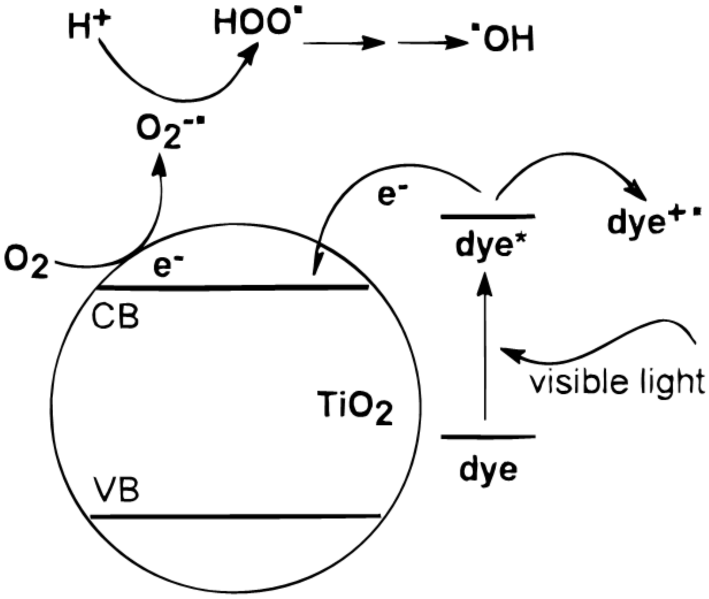

Figure 1-30 Schematic diagram of dye sensitization mechanism of TiO_2 [144]

(5) Semiconductor composite

Semiconductor composite is composed of various semiconductors with different energy band structure. Figure 1-31 shows the energy band structure of common semiconductors. With semiconductor composite, the energy band overlap can occur, leading to the separation and migration of the photo-generated carriers within these semiconductors, thereby effectively inhibiting recombination of photo-generated electrons and holes. Figure 1-32 describes photo excitation process of semiconductor composite by taking TiO_2-CdS system as an example. Currently, the compound semiconductors, such as TiO_2-CdS [145], TiO_2-CdSe [146], TiO_2-SnO_2 [147], TiO_2-ZnO [148], TiO_2-WO_3 [149] have shown higher photocatalytic activity than pure TiO_2. In addition, the combination of TiO_2 with some narrow-bandgap semiconductors (such as CdS, CdSe, WS_2, etc. [145, 146, 150]), can lead to a visible photocatalytic activity.

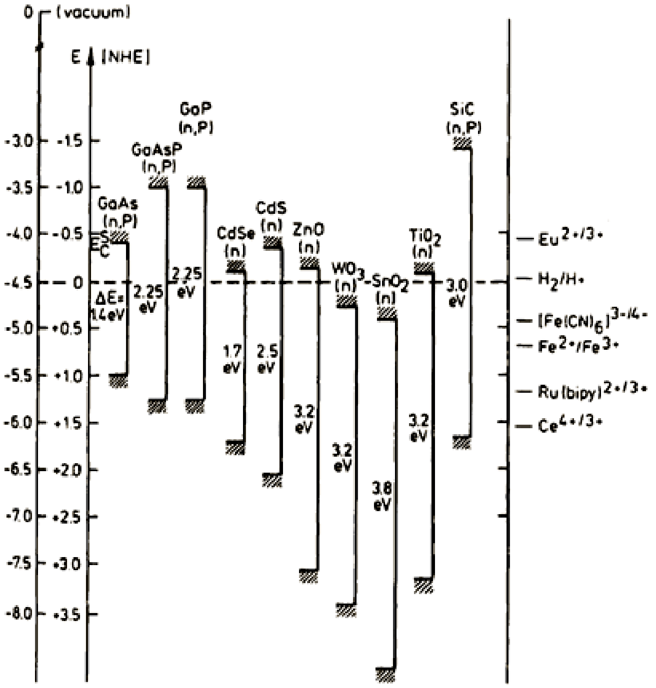

Figure 1-31 Scheme of band edge position of several semiconductors (pH=1) [151]

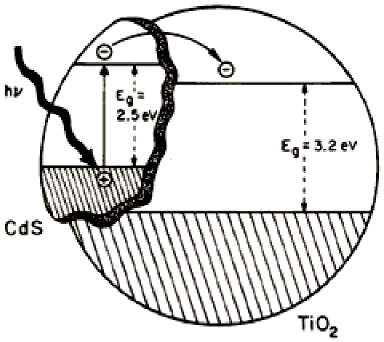

Figure 1-32 Schematic diagram of photoexcitation in TiO_2-CdS compound semiconductor

4.2 Research progress on narrow gap semiconductors photocatalytic materials

4.2.1 Sulfide semiconductor

The studies have suggested that in order to effectively expand the absorption wavelength range to visible light region, the band gap of the narrow band gap semiconductor must be small enough to produce full absorption of visible light (typically smaller than 1.6 eV); Meanwhile, the conduction band potential of narrow gap semiconductors should be higher than that of pure TiO_2 to ensure the migration of photo-generated electrons [150]. Bessekhouad et al. [152] prepared CdS and TiO_2 mixed precipitation followed by the calcination at 400 °C and obtained CdS/TiO_2 composite. After two hours of visible light illumination, the photocatalytic degradation rate of 4-hydroxybenzoic acid over CdS/TiO_2 was about 60% and this rate was only about 10% with the prue CdS. Ho et al. [150] reported that nanoclusters of MoS_2 and WS_2 were coupled to TiO_2 by an in-situ photoreduction deposition method by taking advantage of the reducing power of the photo-generated electrons from TiO_2 particles. Quantum size effects altered the energy levels of the conduction and valence band edges in the coupled semiconductor systems, which favored the interparticle electron transfer (as shown in Figure 1-33). In addition, the coupled systems were believed to act in a cooperative manner by increasing the degree of charge carrier separation, which effectively reduces recombination.

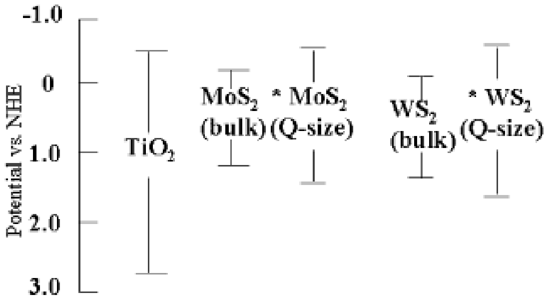

Figure 1-33 Energy levels of the conduction and valence band edges versus normal hydrogen electrode (NHE) for pure TiO_2, WS_2 and MoS_2 with various sizes at pH 7 [150]

4.2.2 Multiple oxide semiconductor

The only common semiconductors, with small band gap making possible the full use of sunlight in the visible region (400-700 nm) and at the same time with a conduction band potential higher than that of TiO_2, are CdS, GaP, GaAsP, and SiC. Therefore, the selection of the narrow band gap semiconductor for combining with TiO_2 is relatively limited. The synthesis of new narrow band gap semiconductors becomes very important and necessary. Of course, these new narrow band gap semiconductors can not only be used to prepare visible-light compound photocatalysts, but also directly serve as photocatalysts due to their strong visible photocatalytic activity.

Currently, many multiple oxide semiconductors such as TaON (2.5 eV) [153], $BiVO_4$ (2.4 eV) [154], $InVO_4$ (2.0 eV) [155] etc. were prepared and used for decomposing the organic matter or water under visible light irradiation. Furthermore, Ishikawa et al. [156]

mixed Sm_2S_2, Sm_2O_3 and TiO_2 together, and then performed a calcination at 1000 °C under vacuum, obtaining the quaternary oxide semiconductor of $Sm_2Ti_2S_2O_5$ with narrow band gap of 2.1 eV. Yamasita et al. [153] calcinated MTa_2O_7 (M = Ca, Sr, Ba) in NH_3 gas at 850 °C and obtained the quaternary narrow band gap semiconductor of $MTaO_2N$ (M = Ca, Sr, Ba, corresponding to the band gap of 2.5 eV, 2.1 eV, 2.0 eV). In recent years, Zou and co-workers are very active in this research field. They prepared many series of multiple metal oxides, such as pyrochlore configuration compound of Bi_2MNbO_7 (M=Al, Ga, In or rare earth element) [157], wolframite configuration compound of $InMO_4$ (M=Nb, Ta, V) [158], perovskite configuration compound of $MIn_{0.5}Nb_{0.5}O_3$ and $MCo_{1/3}Nb_{2/3}O_3$ (M=Ca, Sr, Ba) [159]. Table 1-1 shows a part of Zou's research on the preparation and properties of new narrow band gap semiconductors. It can be seen from the table that the prepared new narrow band gap semiconductors are ternary or multiple oxides, the band gaps are about 2.0-3.0 eV (620 nm to 410 nm). This absorption range of 410-620 nm covers most visible light.

Table 1-1 The photocatalytic activities of various narrow band gap semiconductors under visible light

No	Semiconductors	Band gap (eV) or Wavelength	Activity characterizations	Irradiation conditions	Efficiency
1	$In_{1-x}Ni_xTaO_4$ (x=0-0.2) [160]	2.3	Decomposing water for H_2	λ>420 nm	Quantum yield 0.66 %
2	$InMO_4$ (M=Nb, Ta, V) [155]	Nb: 2.5 Ta: 2.6 V: 2.0	Decomposing water for H_2	λ>420 nm irradiation for 50 h	Nb: 4.0μmol/(gh) Ta: 3.5μmol/(gh) V: 7.0μmol/(gh)
3	$MCo_{1/3}Nb_{2/3}O_3$ (M=Ca, Sr, Ba) [161]	Ca: 2.80 Sr: 2.46 Ba: 2.46	Decomposing methyl alcohol for H_2	λ>420 nm irradiation for ~13 h	Ca: 0.44μmol/h Sr: 0.17μmol/h Ba: 1.40μmol/h
4	MIn_2O_4 (M=Ca, Sr, Ba) [162]	Maximum response wavelengh 480nm	Decomposing 15.3mg/L of methylthion chloride	λ>420 nm irradiation for 2 h	Ca: 60 % Sr: 42 % Ba: 30 %
5	$M_{2.5}VMoO_8$ (M=Mg, Zn) [163]	Maximum response wavelengh 530nm	Decomposing $AgNO_3$ solution for O_2	λ>420 nm irradiation for ~24 h	Mg: ~3μmol/h Zn: ~6μmol/h
6	Bi_2MNbO_7 (M=Al, Ga, In) [164,165]	Al: 2.9 Ga:2.75 In: 2.7	Decomposing methyl alcohol for H_2	irradiation for 10 h	Al: 0.71mmol/(gh) Ga: 0.3 mmol/(gh) In: 0.18 mmol/(gh)
7	$M_3V_2O_8$ (M=Mg, Ni, Zn) [166]	Mg: 3.02 Ni: 2.25 Zn: 2.92	Decomposing $AgNO_3$ solution for O_2	λ>420 nm irradiation for 5 h	Quantum yield Mg: 0.23 % Ni: 0 % Zn: 0.64 %

In summary, the synthesis of new narrow band gap semiconductors has been developing rapidly in recent years. However, the studies are mainly concentrated on the photocatalytic decomposition of water and rarely focused on the visible photocatalytic degradation of organic compounds. In addition, the current new narrow gap semiconductors are mainly prepared by high temperature solid phase method, resulting in very small specific surface area, with therefore limited photocatalytic activity.

4.2.3 Nitride semiconductor

Most recently, a polymeric semiconductor on the basis of a defective graphitic carbon nitride (g-C_3N_4) has stimulated intensive interest in photocatalytic applications (as shown in Figure 1-34) [167]. The simple polymer-like semiconductor, made only from carbon, nitrogen and some minor hydrogen content, can function as a metal-free photocatalyst for the extraction of hydrogen from water or for degrading organic pollutants. Among all the allotropes of carbon nitrides, g-C_3N_4 is regarded as the most stable at ambient conditions and has the smallest direct band gap (2.7 eV) due to the sp^2 hybridization of carbon and nitrogen that forms the π conjugated graphitic planes. Unfortunately, its practical applications are mainly limited by the rapid recombination of photo-generated electron-hole pairs which often results in a low quantum yield and poor photocatalytic activity. To date, a number of methods have been developed to enhance the photocatalytic activity of g-C_3N_4, such as doping [168], and coupling with grapheme [169] or other semiconductors [170]. Considering the matched band potential between g-C_3N_4 (the calculated CB and VB edge potentials of g-C_3N_4 are -1.12 and 1.57 eV) and the most studied photocatalyst (TiO_2), it is feasible to combine g-C_3N_4 with TiO_2, and the photo-generated electrons can migrate effectively from the CB of g-C_3N_4 to that of TiO_2. In this way, a highly efficient photocatalyst with improved quantum efficiency in visible light can be obtained [171].

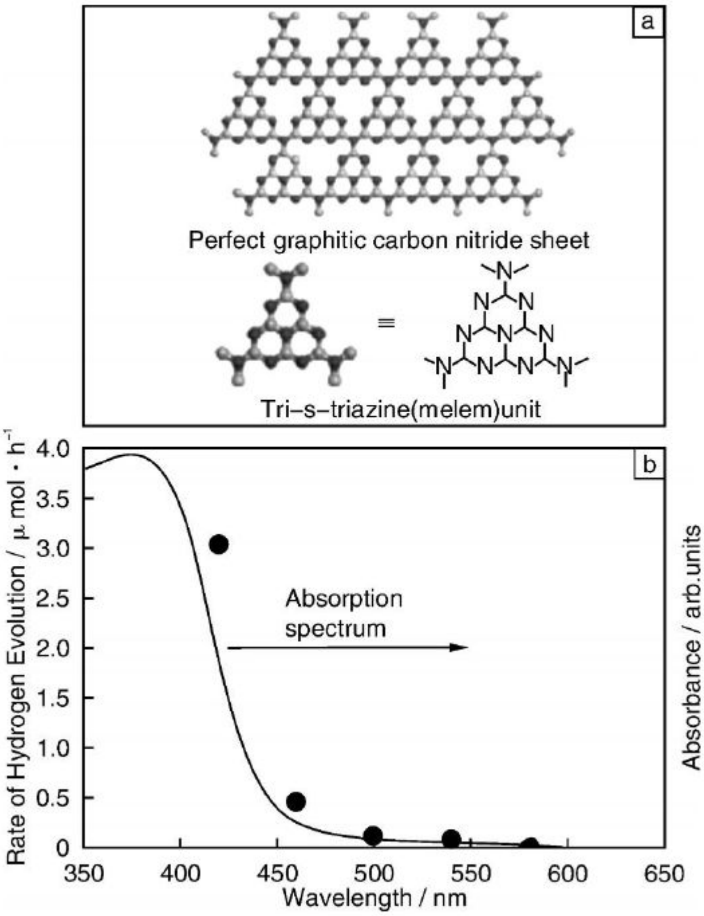

Figure 1-34 (a) Crystal structure of g-C_3N_4 and (b) relationship of the photocatalytic hydrogen production activity and the wavelength

5 Conclusions

With the increasing scarcity of fossil energy and the global environment concerns the development of renewable energy is an increasing global societal issue. Solar energy attracts more and more attentions due to its total renewability and acceptable energy density on the Earth. To date, Photovoltaic solar cells are the most used technique to convert solar energy into electricity. .Silicon solar cells are the oldest and also the most matured technology in solar cell market. The performance/cost ration of these cells is still low compared to other traditional technologies. The single junction record efficiency of 29.1% is held by GaAs which is however mainly used for space application due to the high production cost. Although multi-junction cells can achieve high conversion efficiency of 43.5%, its multi-junction structures are extremely complex and expensive. The dye-sensitized cells (DSC) and the organic photovoltaic cells (OPV) are late starters and their efficiencies need to be further improved. Cu-In-Ga-S(Se) (CIGS) cells are based on one of the most promising thin film technologies due to its high efficiency and can be used for flexible modules production. The use of rare raw materials such as In and Ga increases the production cost of the entire device. In recent years, looking for new low-cost and high-efficient alternative materials has become an important issue for solar cell research. Photocatalytic reaction is another technique for converting solar energy with still low quantum efficiency. Most studies have been concentrated on TiO_2 which can only absorb 3-4% of the solar energy. The development of new materials with visible-light sensitivity is the key for converting efficiently solar energy to chemical energy. Currently, the use of narrow band gap semiconductors is relatively very limited with low efficiency. Therefore, research on new narrow band gap semiconductors attracts more and more attentions. Based on the analysis of the previous works, we propose to investigate the $GeSe_2$-Sb_2Se_3-CuI glass ceramics with narrow and tunable band-gap. The objective is to develop a totally new material for converting efficiently the solar energy into electrical or chemical energy.

References

[1] M. Rogol, Refining benchmarks and forecasts, Photon International, 1 (2008) 84-94.

[2] http://www.nasa.gov/images/content/57911main_Earth_Energy_Budget.jpg

[3] M. Lin, On Fresnel Reflector Solar Collectors with Cavit Receiver, thesis, Shanghai Jiao Tong University, 2013.

[4] Y. Liu, Reasearch of Integrated Design and Application of Residence and Solar Thermal System in Shandong Province, thesis, Shangdong Jianzhu University, 2013.

[5] http://www.dailykos.com/story/2008/10/15/628465/-The-power-of-concentration-CSP.

[6] M. Guo, Z. Wang, W. Liang, X. Zhang, C. Zang, Z. Lu, X. Wei, Tracking formulas and strategies for a receiver oriented dual-axis tracking toroidal heliostat, Solar Energy, 84 (2010) 939-947.

[7] J. Pye, Concentrating Solar Power Systems, Australian National University Solar Thermal Group, 2010.

[8] H.A. Siddiqui, Cheaper Options of Solar Power, Technology Times, April 16, 2012.

[9] http://www.solar-energy-at-home.com/concentrating-solar-power.html.

[10] http://www.powerfromthesun.net/Book/chapter10/chapter10.html.

[11] http://www.iea.org/publications/freepublications/publication/name,3903,en.html

[12] F. Kuznik, J. Virgone, J.-J. Roux, Energetic efficiency of room wall containing PCM wallboard: A full-scale experimental investigation, Energy and Buildings, 40 (2008) 148-156.

[13] A.M. Khudhair, M.M. Farid, A review on energy conservation in building applications with thermal storage by latent heat using phase change materials, Energy Conversion and Management, 45 (2004) 263-275.

[14] B. He, F. Setterwall, Technical grade paraffin waxes as phase change materials for cool thermal storage and cool storage systems capital cost estimation, Energy Conversion and Management, 43 (2002) 1709-1723.

[15] A. Fujishima, K. Honda, Electrochemical photolysis of water at a semiconductor electrode, Nature, 238 (1972) 37-38.

[16] A. Kudo, Y. Miseki, Heterogeneous photocatalyst materials for water splitting, Chemical Society Reviews, 38 (2009) 253-278.

[17] S. Choudhary, S. Upadhyay, P. Kumar, N. Singh, V.R. Satsangi, R. Shrivastav, S. Dass, Nanostructured bilayered thin films in photoelectrochemical water splitting – A review, International Journal of Hydrogen Energy, 37 (2012) 18713-18730.

[18] K. Maeda, K. Domen, New Non-Oxide Photocatalysts designed for overall water splitting under visible light, The Journal of Physical Chemistry C, 111 (2007) 7851-7861.

[19] Y. Xu, C.H. Langford, A comparison of acetophenone photoxidation in aqueous media via direct photolysis and TiO_2 photocatalysis. Journal of Advanced Oxidation Technologies, 2 (1997) 408-414.

[20] http://www.artinaid.com/2013/04/uses-of-solar-energy/.

[21] M. Wolf, Historical development of solar cells, Proceedings of the 25th Power Sources Symposium, May 23-25, 1972.

[22] W. Smith, Effect of light on selenium during the passage of an electric current, Nature, 7 (1873) 303.

[23] http://mirror.nobel.ki.se/laureates/physics-1921-press.html.

[24] D.M. Chapin, C.S. Fuller, G.L. Pearson, A new silicon p-n junction photocell for converting solar radiation into electrical power, Journal of Applied Physics, 25 (1954) 676-677.

[25] M. Williamson, Watts in space, Institution of Electrical Engineers, UK, Review, 45 (1999) 19-23.

[26] http://beforeitsnews.com/environment/2012/03/worldwide-solar-cell-production-in-2011-37-2-gw-up-36-1954658.html.

[27] http://www.linkedin.com/groups/Best-research-cell-efficiencies-CdTe-2121068.S.208450756.

[28] S. Kodigala, Cu($ln_{1-x}Ga_x$)Se_2 based thin film solar cells, Academic Press, (2010)

[29] W. Guter, J. Schöne, S.P. Philipps, M. Steiner, G. Siefer, A. Wekkeli, E. Welser, E. Oliva, A.W. Bett, F. Dimroth, Current-matched triple-junction solar cell reaching 41.1% conversion efficiency under concentrated sunlight, Applied Physics Letters, 94 (2009) 223504.

[30] R.R. King, D.C. Law, K.M. Edmondson, C.M. Fetzer, G.S. Kinsey, H. Yoon, R.A. Sherif, N.H. Karam, 40% efficient metamorphic GaInP / GaInAs / Ge multijunction solar cells, Applied Physics Letters, 90 (2007) 183516.

[31] S. Kurtz, Opportunities and challenges for development of a mature concentrating Photovoltaic Power Industry (Revision), Technical Report, (2012) 32.

[32] http://solarjourneyusa.com/bandgaps.php.

[33] http://www.comerfordsolar.com/basics.html.

[34] M. Pagliaro, G. Palmisano, R. Ciriminna, Flexible solar cells, John Wiley, New York (2008).

[35] T. Saga, Advances in crystalline silicon solar cell technology for industrial mass production, NPG Asia Materials, 2 (2010) 96-102.

[36] M.A. Green, The path to 25% silicon solar cell efficiency: History of silicon cell evolution, Progress in Photovoltaics: Research and Applications, 17 (2009) 183-189.

[37] M. Taguchi, Y. Tsunomura, H. Inoue, S. Taira, T. Nakashima, T. Baba, H. Sakata, E. Maruyama, High efficiency HIT solar cell on thin (< 100 μm) silicon wafer, in: Proceedings of the 24th European Photovoltaic Solar Energy Conference, (2009) 1690-1693.

[38] R.M. Swanson, Device physics for backside-contact solar cells, in: Proceeding of the 33rd IEEE Photovoltaic Specialists Conference, keynote session, May 2008.

[39] S. Inoue, T. Sakamoto, M. Komoda, H. Ohwada, K. Fukui, K. Shirasawa, High efficiency multicrystalline silicon back-contact solar cells, in: Proceeding of the 23rd European Photovoltaic Solar Energy Conference, 988 (2008).

[40] X. Deng, E. Schiff, Amorphous silicon based solar cells, John Wiley & Sons, Chichester, 2003.

[41] http://www.daviddarling.info/encyclopedia/S/AE_silicon.html.

[42] H. Huang, L. Lu, J. Wang, J. Yang, S.-F. Leung, Y. Wang, D. Chen, X. Chen, G. Shen, D. Li, Z. Fan, Performance enhancement of thin-film amorphous silicon solar cells with low cost nanodent plasmonic substrates, Energy & Environmental Science, 6 (2013) 2965-2971.

[43] Y.Y. Cheng, B. Fuckel, R.W. MacQueen, T. Khoury, R.G.C.R. Clady, T.F. Schulze, N.J. Ekins-Daukes, M.J. Crossley, B. Stannowski, K. Lips, T.W. Schmidt, Improving the light-harvesting of amorphous silicon solar cells with photochemical upconversion, Energy & Environmental Science, 5 (2012) 6953-6959.

[44] http://www1.eere.energy.gov/solar/sunshot/pv_asi.html.

[45] S.R. Forrest, The limits to organic photovoltaic cell efficiency, MRS Bulletin, 30 (2005) 28-32.

[46] B.C. Thompson, J.M.J. Fréchet, Polymer–fullerene composite solar cells, Angewandte Chemie International Edition, 47 (2008) 58-77.

[47] A.J. Heeger, Semiconducting polymers: the third generation, Chemical Society Reviews, 39 (2010) 2354-2371.

[48] A. Pivrikas, N.S. Sariciftci, G. Juška, R. Österbacka, A review of charge transport and recombination in polymer/fullerene organic solar cells, Progress in Photovoltaics: Research and Applications, 15 (2007) 677-696.

[49] C.J. Brabec, C. Winder, N.S. Sariciftci, J.C. Hummelen, A. Dhanabalan, P.A. van Hal, R.A.J. Janssen, A low-bandgap semiconducting polymer for photovoltaic devices and infrared emitting diodes, Advanced Functional Materials, 12 (2002) 709-712.

[50] C.J. Brabec, N.S. Sariciftci, J.C. Hummelen, Plastic solar cells, Advanced Functional Materials, 11 (2001) 15-26.

[51] B.P. Rand, J. Li, J. Xue, R.J. Holmes, M.E. Thompson, S.R. Forrest, Organic double-heterostructure photovoltaic cells employing thick tris(acetylacetonato)ruthenium(III) exciton-blocking layers, Advanced Materials, 17 (2005) 2714-2718.

[52] H.R. Wu, Q.L. Song, M.L. Wang, F.Y. Li, H. Yang, Y. Wu, C.H. Huang, X.M. Ding, X.Y. Hou, Stable small-molecule organic solar cells with 1,3,5-tris(2-N-phenyl-benzimidazolyl) benzene as an organic buffer, Thin Solid Films, 515 (2007) 8050-8053.

[53] J. Xue, S. Uchida, B.P. Rand, S.R. Forrest, 4.2% efficient organic photovoltaic cells with low series resistances, Applied Physics Letters, 84 (2004) 3013-3015.

[54] J.J.M. Halls, C.A. Walsh, N.C. Greenham, E.A. Marseglia, R.H. Friend, S.C. Moratti, A.B. Holmes, Efficient photodiodes from interpenetrating polymer networks, Nature, 376 (1995) 498-500.

[55] http://theenergycollective.com/namarchetti/85100/are-dye-sensitized-cells-future-solar.

[56] B. O'Regan, M. Gratzel, A low-cost, high-efficiency solar cell based on dye-sensitized colloidal TiO_2 films, Nature, 353 (1991) 737-740.

[57] A. Shah, P. Torres, R. Tscharner, N. Wyrsch, H. Keppner, Photovoltaic technology: The case for thin-film solar cells, Science, 285 (1999) 692-698.

[58] F. Seitz, J. S. Koehler, Displacement of atoms duringi, Solid State Physics (Academic, New York), 2 (1956) 305.

[59] N. Yastrebova, High-efficiency multi-junction solar cells: Current status and future potential. University of Ottawa. Ottawa, Canada. April 2007

[60] M. Hadrich, C. Kraft, C Loffler, H. Metzner, U. Reislohner, W. Witthuhn, Pathways to thin absorbers in CdTe solar cells, Thin Solid Films, 517 (2009) 2282-2285.

[61] A. Bosio, N. Romeo, S. Mazzamuto, V. Canevari, Polycrystalline CdTe thin films for photovoltaic applications, Progress in Crystal Growth and Characterization of Materials, 52 (2006) 247-279.

---

[62] M. Gloeckler, A.L. Fahrenbruch, J.R. Sites, Numerical modeling of CIGS and CdTe solar cells: setting the baseline, Proceedings of 3rd World Conference on Photovoltaic Energy Conversion, 491 (2003) 491-494.

[63] A. Morales-Acevedo, Thin film CdS/CdTe solar cells: Research perspectives, Solar Energy, 80 (2006) 675-681.

[64] M.A. Green, K. Emery, Y. Hishikawa, W. Warta, E.D. Dunlop, Solar cell efficiency tables (version 41), Progress in Photovoltaics: Research and Applications, 21 (2013) 1-11.

[65] N.G. Dhere, Toward GW/year of CIGS production within the next decade, Solar Energy Materials and Solar Cells, 91 (2007) 1376-1382.

[66] B.J. Stanbery, Copper indium selenides and related materials for photovoltaic devices, Critical Reviews in Solid State and Materials Sciences, 27 (2002) 73-117.

[67] Photovoltaics Report, Fraunhofer institute for solar energy systems ise, Freiburg, December 2012.

[68] P.S. Vasekar, A.H. Jahagirdar, N.G. Dhere, Photovoltaic characterization of Copper–Indium–Gallium Sulfide ($CIGS_2$) solar cells for lower absorber thicknesses, Thin Solid Films, 518 (2010) 1788-1790.

[69] H. Hahn, G. Frank, W. Klingler, A.-D. Meyer, G. Störger, Untersuchungen über ternäre Chalkogenide. V. Über einige ternäre Chalkogenide mit Chalkopyritstruktur, Zeitschrift für anorganische und allgemeine Chemie, 271 (1953) 153-170.

[70] S. Wagner, J.L. Shay, P. Migliorato, H.M. Kasper, $CuInSe_2$/CdS Heterojunction Photovoltaic Detectors, Applied Physics Letters, 25 (1974) 434–435.

[71] L.L. Kazmerski, F.R. White, G.K. Morgan, Thin-film $CuInSe_2$/CdS heterojunction solar cells, Applied Physics Letters, 29 (1976) 268–270.

[72] R.A. Mickelsen, W.S. Chen, Polycrystalline thin-film $CuInSe_2$ solar cells, in Proceedings 16th IEEE Photovoltaic Specialists Conference, (1982) 781–785.

[73] W. Devaney, R. Michelsen, W. Chen, Paper presented at 18th IEEE Photovoltaic Specialists Conference, IEEE Publishing, NY, (1985) 173.

[74] K. Mitchell, C. Eberspacher, J. Ermer, D. Pier, Single and tandem junction $CuInSe_2$ cell and module technology, in proceedings 20th IEEE Photovoltaic Specialists Conference, 2 (1988) 1384–1389.

---

[75] R. Potter, Enhanced photocurrent ZnO/CdS/$CuInSe_2$ solar cells, Solar Cells, 16 (1986) 521-527.

[76] A.M. Gabor, J.R. Tuttle, D.S. Albin, M.A. Contreras, R. Noufi, A.M. Hermann. High-efficiency $CuIn_xGa_{1-x}Se_2$ solar cells made from $(In_x,Ga_{1-x})_2Se_3$ precursor films, Applied Physics Letters, 65 (1994) 198–200.

[77] M.A. Contreras, B. Egaas, K. Ramanathan, J. Hiltner, A. Swartzlander, F. Hasoon, R. Noufi, Progress toward 20% efficiency in Cu(In,Ga)Se_2 polycrystalline thin-film solar cells, Progress in Photovoltaics: Research and Applications, 7 (1999) 311-316.

[78] K. Ramanathan, M.A. Contreras, C.L. Perkins, S. Asher, F.S. Hasoon, J. Keane, D. Young, M. Romero, W. Metzger, R. Noufi, J. Ward, A. Duda, Properties of 19.2% efficiency ZnO/CdS/$CuInGaSe_2$ thin-film solar cells, Progress in Photovoltaics: Research and Applications, 11 (2003) 225-230.

[79] S.-H. Wei, S.B. Zhang, A. Zunger, Effects of Ga addition to $CuInSe_2$ on its electronic, structural, and defect properties, Applied Physics Letters, 72 (1998) 3199–3201.

[80] M.V. Yakushev, A.V. Mudryi, I.V. Victorov, J. Krustok, E. Mellikov, Energy of excitons in $CuInS_2$ single crystals, Applied Physics Letters, 88 (2006) 011922.

[81] M. Topic, F. Smole, J. Furlan, Band-gap engineering in CdS/Cu(In,Ga)Se_2 solar cells, Journal of Applied Physics, 79 (1996) 8537-8540.

[82] I. Repins, M.A. Contreras, B. Egaas, C. DeHart, J. Scharf, C.L. Perkins, B. To, R. Noufi, 19.9%-efficient ZnO/CdS/$CuInGaSe_2$ solar cell with 81.2% fill factor, Progress in Photovoltaics: Research and Applications, 16 (2008) 235-239.

[83] S. Sharbati, S.-H. Keshmiri, Model for increased efficiency of CIGS solar cells by a stepped distribution of carrier density and Ga in the absorber layer, Science China Physics, Mechanics and Astronomy, 56 (2013) 1533-1541.

[84] A. Redinger, D.M. Berg, P.J. Dale, S. Siebentritt, The Consequences of Kesterite Equilibria for Efficient Solar Cells, Journal of the American Chemical Society, 133 (2011) 3320-3323.

[85] C.J. Hibberd, E. Chassaing, W. Liu, D.B. Mitzi, D. Lincot, A.N. Tiwari, Non-vacuum methods for formation of Cu(In, Ga)(Se, S)$_2$ thin film photovoltaic absorbers, Progress in Photovoltaics: Research and Applications, 18 (2010) 434-452.

[86] A. Weber, R. Mainz, H.W. Schock, On the Sn loss from thin films of the material system Cu–Zn–Sn–S in high vacuum, Journal of Applied Physics, 107 (2010) 013516-013521.

[87] H. Katagiri, K. Saitoh, T. Washio, H. Shinohara, T. Kurumadani, S. Miyajima, Development of thin film solar cell based on Cu_2ZnSnS_4 thin films, Solar Energy Materials and Solar Cells, 65 (2001) 141-148.

[88] H. Katagiri, K. Jimbo, K. Moriya, K. Tsuchida, Solar cell without environmental pollution by using CZTS thin film, in: Proceedings of 3rd World Conference on Photovoltaic Energy Conversion, 2873 (2003) 2874-2879.

[89] H. Katagiri, K. Jimbo, S. Yamada, T. Kamimura, W.S. Maw, T. Fukano, T. Ito, T. Motohiro, Enhanced conversion efficiencies of Cu_2ZnSnS_4-based thin film solar cells by using preferential etching technique, Applied Physics Express, 1 (2008) 041201.

[90] T.K. Todorov, K.B. Reuter, D.B. Mitzi, High-efficiency solar cell with earth-abundant liquid-processed absorber, Advanced Materials, 22 (2010) E156-E159.

[91] T. Todorov, D. Mitzi, Shedding light on new frontiers of solar cell semiconductors, IBM, 22 August 2012.

[92] P. Reinhard, S. Buecheler, A. N. Tiwari, Technological status of $Cu(In,Ga)(Se,S)_2$-based photovoltaics, Solar Energy Materials & Solar Cells, 119 (2013) 287–290.

[93] P. Jackson, D. Hariskos, E. Lotter, S. Paetel, R. Wuerz, R. Menner, W. Wischmann, M. Powalla, New world record efficiency for $Cu(In,Ga)Se_2$ thin-film solar cells beyond 20%, Progress in Photovoltaics: Research and Applications, 19 (2011) 894-897.

[94] M.A. Green, K. Emery, Y. Hishikawa, W. Warta, E.D. Dunlop, Solar cell efficiency tables (version42), Progress in Photovoltaics: Research and Applications, 21 (2013) 827–837.

[95] M. Nakamura, Y. Kouji, Y. Chiba, H. Hakuma, T. Kobayashi, T. Nakada, Achievement of 19.7% efficiency with a small-sized $Cu(InGa)(SeS)_2$ solar cell prepared by sulfurization after selenization process with Zn-based buffer, in: Proceedings of the 39th IEEE Photovoltaic Specialists Conference, Tampa, USA, 2013.

[96] S. Ahn, K. Kim, Y. Chun, K. Yoon, Nucleation and growth of $Cu(In,Ga)Se_2$ nanoparticles in low temperature colloidal process, Thin Solid Films, 515 (2007) 4036-4040.

[97] T. Yamaguchi, Y. Asai, N. Oku, S. Niiyama, T. Imanishi, S. Nakamura, Preparation of Cu(In,Ga)(S,Se)$_2$ thin films by sequential evaporation and annealing in sulfur atmosphere, Solar Energy Materials and Solar Cells, 95 (2011) 274-276.

[98] C.J. Stolle, T.B. Harvey, B.A. Korgel, Nanocrystal photovoltaics: a review of recent progress, Current Opinion in Chemical Engineering, 2 (2013) 160-167.

[99] C. de Mello Donegá, P. Liljeroth, D. Vanmaekelbergh, Physicochemical evaluation of the hot-injection method, a Synthesis Route for Monodisperse Nanocrystals, Small, 1 (2005) 1152-1162.

[100] F. Kessler, D. Rudmann, Technological aspects of flexible CIGS solar cells and modules, Solar Energy, 77 (2004) 685-695.

[101] G. Brown, P. Stone, J. Woodruff, B. Cardozo, D. Jackrel, Device characteristics of a 17.1% efficient solar cell deposited by a non-vacuum printing method on flexible foil, in: Proceedings of the 38th IEEE Photovoltaic Specialists Conference, Austin, USA, (2012) 3280–3233.

[102] D. Lee, Y. Choi, K. Yong, Morphology and crystal phase evolution of doctor-blade coated CuInSe$_2$ thin films, Journal of Crystal Growth, 312 (2010) 3665-3669.

[103] S. Ahn, T.H. Son, A. Cho, J. Gwak, J.H. Yun, K. Shin, S.K. Ahn, S.H. Park, K. Yoon, CuInSe$_2$ thin-film solar cells with 7.72% efficiency prepared via direct coating of a metal salts/alcohol-based precursor solution, ChemSusChem, 5 (2012) 1773-1777.

[104] T.K. Todorov, O. Gunawan, T. Gokmen, D.B. Mitzi, Solution-processed Cu(In,Ga) (S,Se)$_2$ absorber yielding a 15.2% efficient solar cell, Progress in Photovoltaics: Research and Applications, 21 (2013) 82-87.

[105] R.N. Bhattacharya, CIGS-based solar cells prepared from electrodeposited stacked Cu/In/Ga layers, Solar Energy Materials and Solar Cells, 113 (2013) 96-99.

[106] R.N. Bhattacharya, Electrodeposited two-layer Cu–In–Ga–Se/In–Se thin films, Journal of The Electrochemical Society, 157 (2010) D406-D410.

[107] P.H. Quang, N.D. Sang, L.T. Tu, D.T.B. Hop, N.T. Nghi, Effect of electrodeposition potential on the composition and morphology of CIGS absorber thin film, World Journal of Engineering, S3 (2010) 859-860.

[108] R. Friedfeld, R.P. Raffaelle, J.G. Mantovani, Electrodeposition of $CuIn_xGa_{1-x}Se_2$ thin films, Solar Energy Materials and Solar Cells, 58 (1999) 375-385.

[109] M. Ganchev, J. Kois, M. Kaelin, S. Bereznev, E. Tzvetkova, O. Volobujeva, N. Stratieva, A. Tiwari, Preparation of $Cu(In,Ga)Se_2$ layers by selenization of electrodeposited Cu–In–Ga precursors, Thin Solid Films, 511–512 (2006) 325-327.

[110] C. Raillard, V. Héquet, P.L. Cloirec, J. Legrand, Photocatalytic oxidation of volatile organic compounds present in airborne environment adjacent to sewage treatment plants. Water Science & Technology, 49 (2004) 111-114.

[111] W.E. Stallings, H.H. Lamb, Synthesis of nanostructured titania powders via hydrolysis of titanium isopropoxide in supercritical carbon dioxide, Langmuir, 19 (2003) 2989-2994.

[112] H. Cheng, J. Ma, Z. Zhao, L. Qi, Hydrothermal preparation of uniform nanosize rutile and anatase particles, Chemistry of Materials, 7 (1995) 663-671.

[113] C. Wang, Z.-X. Deng, Y. Li, The synthesis of nanocrystalline anatase and rutile titania in mixed organic media, Inorganic Chemistry, 40 (2001) 5210-5214.

[114] H. Kominami, Y. Takada, H. Yamagiwa, Y. Kera, M. Inoue, T. Inui, Synthesis of thermally stable nanocrystalline anatase by high-temperature hydrolysis of titanium alkoxide with water dissolved in organic solvent from gas phase, Journal of Materials Science Letters, 15 (1996) 197-200.

[115] S. Doherty, D. Fitzmaurice, Preparation and characterization of transparent nanocrystalline TiO_2 films possessing well-defined morphologies, The Journal of Physical Chemistry, 100 (1996) 10732-10738.

[116] B. O' Regan, M. Graetzel, A low-cost, high efficiency solar cells based on dye-sensitized colloidal TiO_2, Nature, 353 (1991) 737-739.

[117] D. Zhang, T. Yoshida, H. Minoura, Low-temperature fabrication of efficient porous titania photoelectrodes by hydrothermal crystallization at the solid/gas interface, Advanced Materials, 15 (2003) 814-817.

[118] S.J. Bu, Z.G. Jin, X.X. Liu, L.R. Yang, Z.J. Cheng, Synthesis of TiO_2 porous thin films by polyethylene glycol templating and chemistry of the process, Journal of the European Ceramic Society, 25 (2005) 673-679.

[119] J. Du, Z. Liu, Z. Li, B. Han, Y. Huang, J. Zhang, Synthesis of mesoporous $SrCO_3$ spheres and hollow $CaCO_3$ spheres in room-temperature ionic liquid, Microporous and Mesoporous Materials, 83 (2005) 145-149.

[120] Y. Kotani, A. Matsuda, T. Kogure, M. Tatsumisago, T. Minami, Effects of addition of poly(ethylene glycol) on the formation of anatase nanocrystals in SiO_2–TiO_2 gel films with Hot Water Treatment, Chemistry of Materials, 13 (2001) 2144-2149.

[121] M.A. Aramendía, J.C. Colmenares, S. López-Fernández, A. Marinas, J.M. Marinas, F.J. Urbano, Screening of different zeolite-based catalysts for gas-phase selective photooxidation of propan-2-ol, Catalysis Today, 129 (2007) 102-109.

[122] J. Ménesi, L. Körösi, É. Bazsó, V. Zöllmer, A. Richardt, I. Dékány, Photocatalytic oxidation of organic pollutants on titania–clay composites, Chemosphere, 70 (2008) 538-542.

[123] N. Bouazza, M.A. Lillo-Ródenas, A. Linares-Solano, Enhancement of the photocatalytic activity of pelletized TiO_2 for the oxidation of propene at low concentration, Applied Catalysis B: Environmental, 77 (2008) 284-293.

[124] M. Tomkiewicz, G. Dagan, Z. Zhu, Morphology and photocatalytic activity of TiO_2 Aerogels, Research on Chemical Intermediates, 20 (1994) 701-710.

[125] G. Dagan, M. Tomkiewicz, Preparation and characterization of TiO_2 aerogels for use as photocatalysts, Journal of Non-Crystalline Solids, 175 (1994) 294-302.

[126] F. Yang, N.-N. Yan, S. Huang, Q. Sun, L.-Z. Zhang, Y. Yu, Zn-doped CdS nanoarchitectures prepared by hydrothermal synthesis: Mechanism for enhanced photocatalytic activity and stability under visible light, The Journal of Physical Chemistry C, 116 (2012) 9078-9084.

[127] M. Luo, Y. Liu, J. Hu, H. Liu, J. Li, One-pot synthesis of CdS and Ni-doped CdS hollow spheres with enhanced photocatalytic activity and durability, ACS Applied Materials & Interfaces, 4 (2012) 1813-1821.

[128] Y.-F. Li, D. Xu, J.I. Oh, W. Shen, X. Li, Y. Yu, Mechanistic study of codoped titania with nonmetal and metal ions: A case of C + Mo codoped TiO_2, ACS Catalysis, 2 (2012) 391-398.

---

[129] W.Y. Choi, A. Termin, M.R. Hoffmann, The role of metal ion dopants in quantum-sized TiO_2: correlation between photoreactivity and charge carrier recombination dynamics. The Journal of Physical Chemistry, 98 (1994) 13669-13679.

[130] A.-W. Xu, Y. Gao, H.-Q. Liu, The Preparation, Characterization, and their photocatalytic activities of rare-earth-doped TiO_2 Nanoparticles, Journal of Catalysis, 207 (2002) 151-157.

[131] N. Serpone, D. Lawless, J. Disdier, J.-M. Herrmann, Spectroscopic, photoconductivity, and photocatalytic studies of TiO_2 colloids: Naked and with the lattice doped with Cr^{3+}, Fe^{3+}, and V^{5+} cations, Langmuir, 10 (1994) 643-652.

[132] H. Yamashita, M. Harada, J. Misaka, M. Takeuchi, K. Ikeue, M. Anpo, Degradation of propanol diluted in water under visible light irradiation using metal ion-implanted titanium dioxide photocatalysts, Journal of Photochemistry and Photobiology A: Chemistry, 148 (2002) 257-261.

[133] S. Sato, Photocatalytic activity of NO_x-doped TiO_2 in the visible light region, Chemical Physics Letters, 123 (1986) 126-128.

[134] R. Asahi, T. Morikawa, T. Ohwaki, K. Aoki, Y. Taga, Visible-light photocatalysis in nitrogen-doped titanium oxides, Science, 293 (2001) 269-271.

[135] S.U.M. Khan, M. Al-Shahry, W.B. Ingler, Efficient photochemical water splitting by a chemically modified n-TiO_2, Science, 297 (2002) 2243-2245.

[136] T. Umebayashi, T. Yamaki, H. Itoh, K. Asai, Band gap narrowing of titanium dioxide by sulfur doping, Applied Physics Letters, 81 (2002) 454-456.

[137] T. Yamaki, T. Sumita, S. Yamamoto, Formation of $TiO_{2-x}F_x$ compounds in fluorine-implanted TiO_2, Journal of Material Science Letters, 21 (2002) 33-35.

[138] J.C. Yu, Yu, Ho, Jiang, Zhang, Effects of F- doping on the photocatalytic activity and microstructures of nanocrystalline TiO_2 powders, Chemistry of Materials, 14 (2002) 3808-3816.

[139] A.L. Linsebigler, G. Lu, J.T. Yates, Photocatalysis on TiO_2 surfaces: Principles, mechanisms, and selected results, Chemical Reviews, 95 (1995) 735-758.

---

[140] T. Sasaki, N. Koshizaki, J.-W. Yoon, K.M. Beck, Preparation of Pt/TiO_2 nanocomposite thin films by pulsed laser deposition and their photoelectrochemical behaviors, Journal of Photochemistry and Photobiology A: Chemistry, 145 (2001) 11-16.

[141] W. Zhao, C. Chen, X. Li, J. Zhao, H. Hidaka, N. Serpone, Photodegradation of sulforhodamine-B dye in platinized titania dispersions under visible light irradiation: Influence of platinum as a functional co-catalyst, The Journal of Physical Chemistry B, 106 (2002) 5022-5028.

[142] Y. Ohmori, E. Itoh, K. Miyairi, Photovoltaic properties of phthalocyanine based p-n diode evaporated onto titanium dioxide, Thin Solid Films, 499 (2006) 369-373.

[143] Y. Amao, Y. Yamada, K. Aoki, Preparation and properties of dye-sensitized solar cell using chlorophyll derivative immobilized TiO_2 film electrode, Journal of Photochemistry and Photobiology A: Chemistry, 164 (2004) 47-51.

[144] T. Wu, G. Liu, J. Zhao, H. Hidaka, N. Serpone, Photoassisted degradation of dye pollutants. V. self-photosensitized oxidative transformation of rhodamine B under visible light irradiation in aqueous TiO2 dispersions, The Journal of Physical Chemistry B, 102 (1998) 5845-5851.

[145] T. Hirai, K. Suzuki, I. Komasawa, Preparation and photocatalytic properties of composite CdS nanoparticles–titanium dioxide particles, Journal of Colloid and Interface Science, 244 (2001) 262-265.

[146] W. Ho, J.C. Yu, Sonochemical synthesis and visible light photocatalytic behavior of CdSe and CdSe/TiO_2 nanoparticles, Journal of Molecular Catalysis A: Chemical, 247 (2006) 268-274.

[147] Z. Liu, D.D. Sun, P. Guo, J.O. Leckie, An efficient bicomponent TiO_2/SnO_2 nanofiber photocatalyst fabricated by electrospinning with a side-by-side dual spinneret method, Nano Letters, 7 (2007) 1081-1085.

[148] G. Marcì, V. Augugliaro, M.J. López-Muñoz, C. Martín, L. Palmisano, V. Rives, M. Schiavello, R.J.D. Tilley, A.M. Venezia, Preparation characterization and photocatalytic activity of polycrystalline ZnO/TiO_2 systems. 2. surface, bulk characterization, and 4-nitrophenol photodegradation in liquid−solid regime, The Journal of Physical Chemistry B, 105 (2001) 1033-1040.

[149] J.H. Pan, W.I. Lee, Preparation of highly ordered cubic mesoporous WO_3/TiO_2 films and their photocatalytic properties, Chemistry of Materials, 18 (2006) 847-853.

[150] W. Ho, J.C. Yu, J. Lin, J. Yu, P. Li, Preparation and photocatalytic behavior of MoS_2 and WS_2 nanocluster sensitized TiO_2, Langmuir, 20 (2004) 5865-5869.

[151] A. Hagfeldt, M. Graetzel, Light-induced redox reactions in nanocrystalline systems, Chemical Reviews, 95 (1995) 49-68.

[152] Y. Bessekhouad, D. Robert, J.V. Weber, Bi_2S_3/TiO_2 and CdS/TiO_2 heterojunctions as an available configuration for photocatalytic degradation of organic pollutant. Journal of Photochemistry and Photobiology A, 163 (2004) 569-580.

[153] D. Yamasita, T. Takata, M. Hara, J.N. Kondo, K. Domen, Recent progress of visible-light-driven heterogeneous photocatalysts for overall water splitting, Solid State Ionics, 172 (2004) 591-595.

[154] H. Harada, C. Hosoki, A. Kudo, Overall water splitting by sonophotocatalytic reaction: the role of powdered photocatalyst and an attempt to decompose water using a visible-light sensitive photocatalyst, Journal of Photochemistry and Photobiology A: Chemistry, 141 (2001) 219-224.

[155] J. Ye, Z. Zou, M. Oshikiri, A. Matsushita, M. Shimoda, M. Imai, T. Shishido, A novel hydrogen-evolving photocatalyst $InVO_4$ active under visible light irradiation, Chemical Physics Letters, 356 (2002) 221-226.

[156] A. Ishikawa, T. Takata, J.N. Kondo, M. Hara, H. Kobayashi, K. Domen, Oxysulfide $Sm_2Ti_2S_2O_5$ as a stable photocatalyst for water oxidation and reduction under visible light irradiation ($\lambda \leqslant 650$ nm), Journal of the American Chemical Society, 124 (2002) 13547-13553.

[157] Z. Zou, J. Ye, H. Arakawa, Photocatalytic properties and electronic structure of a novel series of solid photocatalysts, Bi_2RNbO_7 (R = Y, Rare Earth), Topics in Catalysis, 22 (2003) 107-110.

[158] Z. Zou, J. Ye, H. Arakawa, Photophysical and photocatalytic properties of $InMO_4$ (M = Nb^{5+}, Ta^{5+}) under visible light irradiation, Materials Research Bulletin, 36 (2001) 1185-1193.

[159] J. Yin, Z. Zou, J. Ye, Photophysical and photocatalytic properties of $MIn_{0.5}Nb_{0.5}O_3$ (M = Ca, Sr, and Ba), The Journal of Physical Chemistry B, 107 (2002) 61-65.

[160] Z. Zou, J. Ye, K. Sayama, H. Arakawa, Direct splitting of water under visible light irradiation with an oxide semiconductor photocatalyst, Nature, 414 (2001) 625-627.

[161] J. Yin, Z. Zou, J. Ye, A novel series of the new visible-light-driven photocatalysts $MCo_{1/3}Nb_{2/3}O_3$ (M = Ca, Sr, and Ba) with special electronic structures, The Journal of Physical Chemistry B, 107 (2003) 4936-4941.

[162] J. Tang, Z. Zou, J. Ye, Effects of substituting Sr^{2+} and Ba^{2+} for Ca^{2+} on the structural properties and photocatalytic behaviors of $CaIn_2O_4$, Chemistry of Materials, 16 (2004) 1644-1649.

[163] D. Wang, Z. Zou, J. Ye, A novel series of photocatalysts $M_{2.5}VMoO_8$ (M = Mg, Zn) for O_2 evolution under visible light irradiation, Catalysis Today, 93–95 (2004) 891-894.

[164] Z. Zou, H. Arakawa, Direct water splitting into H_2 and O_2 under visible light irradiation with a new series of mixed oxide semiconductor photocatalysts, Journal of Photochemistry and Photobiology A: Chemistry, 158 (2003) 145-162.

[165] Z. Zou, J. Ye, H. Arakawa, Preparation, structural and optical properties of a new class of compounds, Bi_2MNbO_7 (M=Al, Ga, In), Materials Science and Engineering: B, 79 (2001) 83-85.

[166] D. Wang, J. Tang, Z. Zou, J. Ye, Photophysical and photocatalytic properties of a new series of visible-light-driven photocatalysts $M_3V_2O_8$ (M = Mg, Ni, Zn), Chemistry of Materials, 17 (2005) 5177-5182.

[167] X. Wang, K. Maeda, A. Thomas, K. Takanabe, G. Xin, J.M. Carlsson, K. Domen, M. Antonietti, A metal-free polymeric photocatalyst for hydrogen production from water under visible light, Natural Material, 8 (2009) 76-80.

[168] Y. Zhang, T. Mori, J. Ye, M. Antonietti, Phosphorus-doped carbon nitride solid: Enhanced electrical conductivity and photocurrent generation, Journal of the American Chemical Society, 132 (2010) 6294-6295.

[169] Q. Xiang, J. Yu, M. Jaroniec, Preparation and enhanced visible-light photocatalytic H_2-production activity of graphene/C_3N_4 composites, The Journal of Physical Chemistry C, 115 (2011) 7355-7363.

[170] S. Kumar, T. Surendar, A. Baruah, V. Shanker, Synthesis of a novel and stable g-C_3N_4-Ag_3PO_4 hybrid nanocomposite photocatalyst and study of the photocatalytic activity under visible light irradiation, Journal of Materials Chemistry A, 1 (2013) 5333-5340.

[171] B. Chai, T. Peng, J. Mao, K. Li, L. Zan, Graphitic carbon nitride (g-C_3N_4)–Pt-TiO_2 nanocomposite as an efficient photocatalyst for hydrogen production under visible light irradiation, Physical Chemistry Chemical Physics, 14 (2012) 16745-16752.

Chapter 2

Compositions, structure and photoelectric properties of glass ceramics in the $GeSe_2$-Sb_2Se_3-CuI system

1 Introduction

Previous research in our laboratory has been mainly focused on the development of infrared transmitting glasses. Metallic halides have been introduced into the glasses for inducing controllable crystallization and the obtained glass-ceramics can be highly transparent from 1 μm to 16 μm [1-3].

From Figure 2-1, it can be seen that the annealed samples with the composition 62.5GeS_2-12.5Sb_2S_3-25CsCl gradually lose transmission in the visible region with the extension of annealing time. This is due to the fact that nanocrystals are generated in the glass matrix. Since the refraction index of these crystals (CsCl) is very different from that of the base glass, the optical losses due to scattering increase with the increasing number or/and size of the crystals [4].

Indeed, when the incident light meets the particles/crystals, the light direction will change dramatically, leading to light scattering or diffusion. Scattering intensity depends on the particle shape, size and concentration. When the size reaches approximately 1/20 of the incident light's wavelength, the scattering will become significant. If the particles are uniformly spherical, models of light scattering can be divided into three domains based on a dimensionless size parameter, α which is defined as

$$\alpha = 2\pi r/\lambda \tag{2.1}$$

where r is the radius of a particle, λ is the wavelength of incident light. Based on the value of α, these domains are (1) $\alpha \ll 1$: Rayleigh scattering, (2) $\alpha \approx 1$: Mie scattering and (3) $\alpha \gg 1$: Geometric scattering [5].

In our case, the crystal size, observed with scanning electronic microscope, is typically in the range of 50-100 nm (comparable with our working wavelength). The optical loss is essentially due to Mie scattering which is inversely proportional to the wavelength.

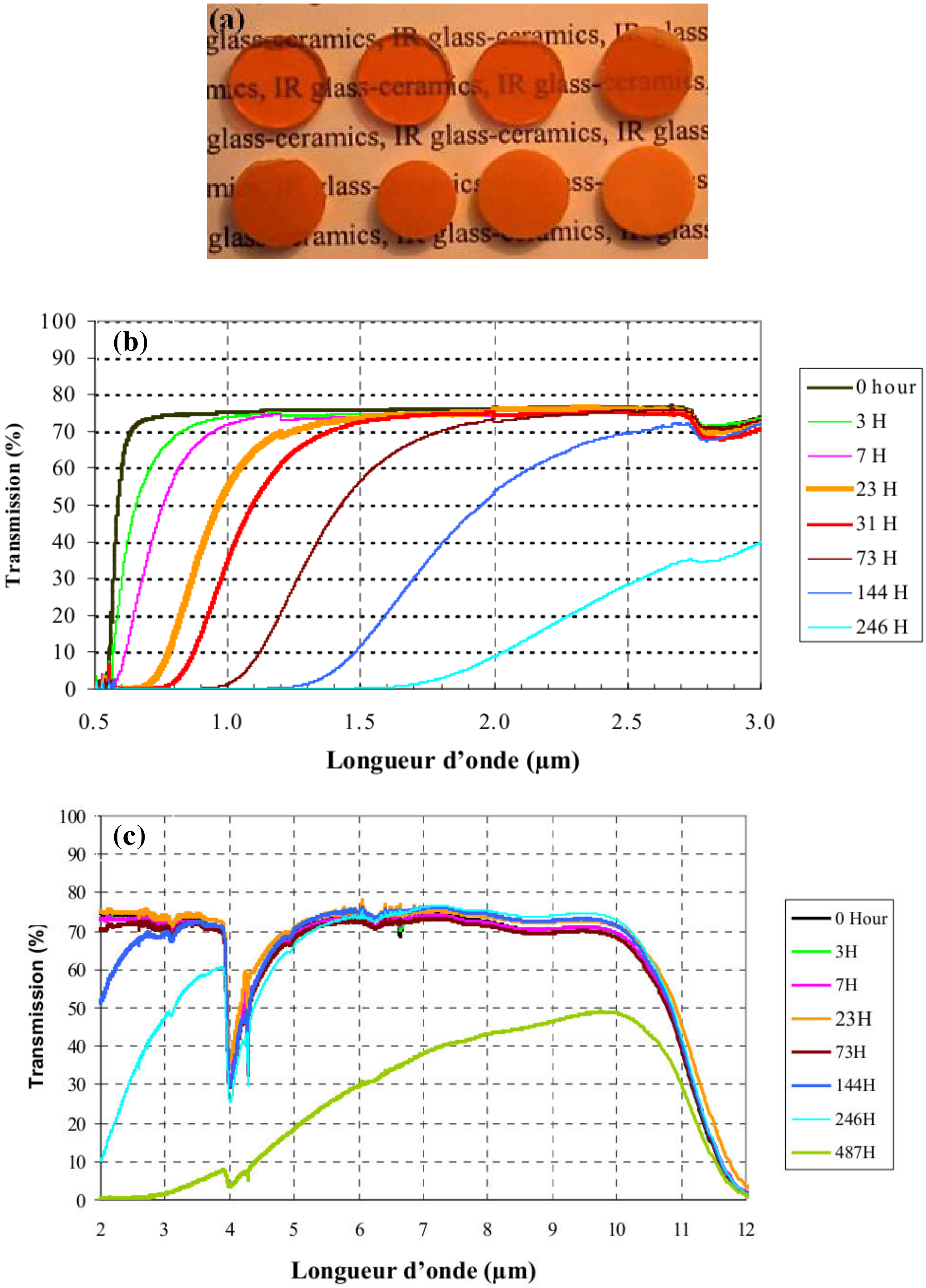

Figure 2-1 Photograph and transmission curves of 62.5GeS_2-12.5Sb_2S_3-25CsCl annealed at 290 °C for different times

(a) photograph; (b) visible and near-infrared transmission; (c) infrared transmission

The main objective of introducing crystals inside the glass matrix is to improve the mechanical strength of the materials. The evolution of mechanical properties of different glass ceramics obtained by annealing the base glass $62.5GeS_2$-$12.5Sb_2S_3$-$25CsCl$ at 290°C is presented in Figure 2-2. It is possible to observe that the tenacity (K_c) stays stable before 40 hours of annealing and then gradually increases. However, the critical load for the crack initiation (P_c) increases continuously with the annealing time. The crystals in the samples are of course responsible for the increasing tenacity and especially the resistance to crack initiation [6]. This resistance can be multiplied by more than 5.

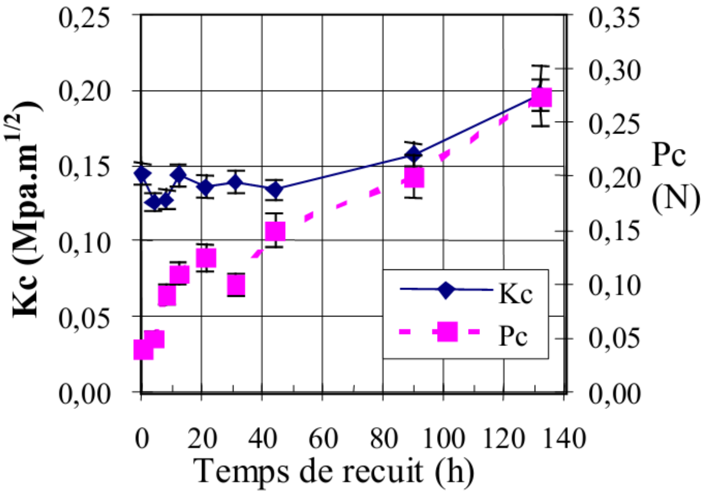

Figure 2-2 Tenacity (K_c) and critical load for crack initiation (P_c) of $62.5GeS_2$-$12.5Sb_2S_3$-25CsCl annealed at 290 °C for different times

During the optimization of glass ceramics, some unusual optical losses have been noted with the $GeSe_2$-Sb_2Se_3-CuI system. The transmission of different glass ceramics, obtained by thermal annealing of the base glass (Figure 2-3) is similar to those observed in III-V type semiconductors GeSb [7]: the transmission decreases with increasing wavelength. The absorption here in the middle infrared region is attributed to the presence of free charge carriers, which can be modeled by the theory of Drude-Zener [8]:

$$\alpha_{FCA} = \left(\frac{e_3}{4\pi^2 c^3 m_0^2 \varepsilon_0}\right)\left(\frac{1}{n({m^*}/{m_0})}\right)\left(\frac{\lambda^2}{\mu}\right)N = S\lambda^2 N \tag{2.2}$$

α_{FCA} is the absorption coefficient of free carriers, m* is the effective mass, μ is the mobility, N is the concentration, n is the refractive index, λ is wavelength and S is a constant. According to the principle of quantum mechanics, there are different values of the exponent of the wavelength, which are determined by the dominant loss mechanism. There are mainly three modes of losses, which are losses by acoustic phonons ($\lambda^{1.5}$), losses based on optical phonon ($\lambda^{2.5}$) and losses due to impurities (λ^3 or $\lambda^{3.5}$). Consequently, the absorption coefficient can be simplified as follows

$$\alpha_{FCA} = S\left(A\lambda^{1.5} + B\lambda^{2.5} + C\lambda^{3}\right) \tag{2.3}$$

A, B and C are corresponding parameters.

The strong transmission decrease in the middle infrared region suggests a relatively high concentration of free charge carriers. Therefore, we have decided to study in detail, the semiconducting properties of the $GeSe_2$-Sb_2Se_3-CuI system.

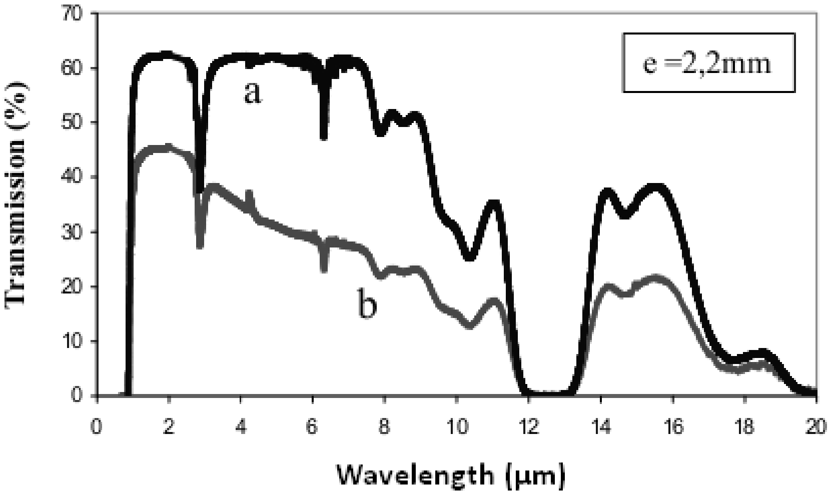

Figure 2-3 Transmission curve of (a) glass $60GeSe_2$-$30Sb_2Se_3$-10CuI and (b) glass ceramic obtained after annealing at 260 °C for 1 h

2 Sample preparation in the $GeSe_2$-Sb_2Se_3-CuI system

2.1 Glass preparation

The glasses are prepared by the melt-quenching process in vacuum sealed silica tube. The base glasses are synthesized using the polycrystalline germanium (99.999%), antimony (99.999%), selenium (99.999%) and CuI (98%) as starting materials. Because the chalcogenide glass is sensitive to oxygen and water during the melting, the synthesis was done in a silica tube shown in Figure 2-4. A vacuum trap filled with liquid nitrogen is used to condense eventual volatile products and to improve the vacuum. The vitreous domain of the $GeSe_2$-Sb_2Se_3-CuI system was determined using a silica tube with 9 mm internal diameter. The tube was cleaned by hydrofluoric acid for one minute to eliminate dust presented on the wall. It was then thoroughly rinsed with distilled water and dried. Appropriate quantities of each material were weighed according to glass composition and loaded into the silica tube which was then sealed under a typical vacuum of around 10^{-5} mbar. The tube containing the mixture was put into a rocking furnace (as shown in Figure 2-5).

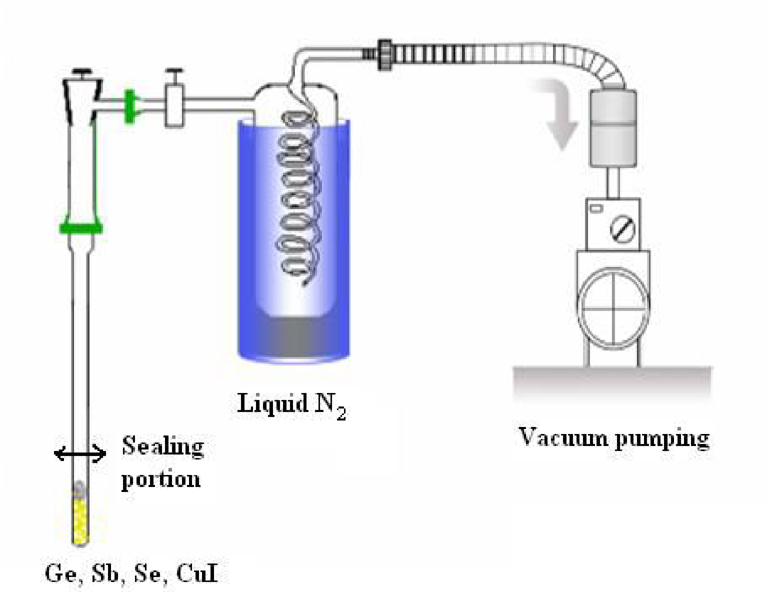

Figure 2-4 Setup used for preparation of chalcogenide glasses

Figure 2-5 Photograph of a rocking furnace

A typical thermal procedure for the synthesis of a chalcogenide glass is shown in Figure 2-6. The silica tube containing all the starting materials was heated to 800 °C at the rate of 1.5°C/min and hold for about 12 h to ensure a thorough reaction and homogenization. Then the furnace was cooled down to 700 °C and the thermal quenching was performed by putting the sealed tube into water at room temperature. The thermal shock in the quenching process generated high mechanical stresses in the glass. In order to reduce these stresses, the tube was annealed at (T_g-10) for 3 h. The glass is then cooled slowly and released from the silica tube.

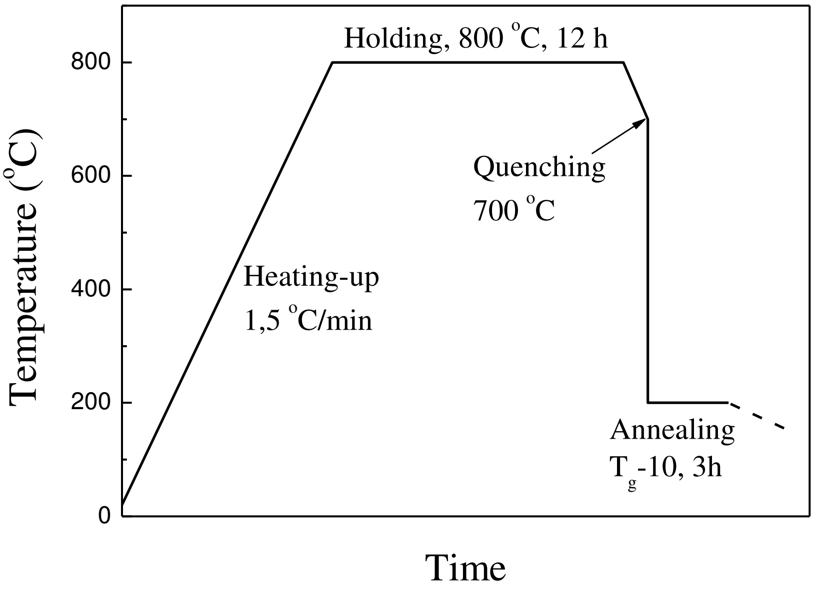

Figure 2-6 Thermal procedure for chalcogenide glass synthesis

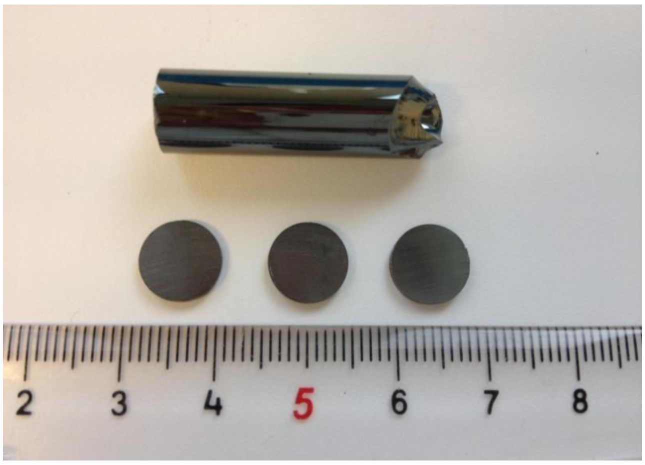

Figure 2-7 Photograph of glass rod and discs

After the annealing, a glass rod of 9 nm was obtained and was sliced into discs with the thickness of about 1.5 mm before polishing for different measurements (Figure 2-7). In this chapter, the $GeSe_2$-Sb_2Se_3-CuI system was studied in detail. The glass-forming domain of this system was determined by synthesizing 10 g of glass and illustrated in Figure 2-8. The five series of glasses illustrated in this figure will be studied in detail. The maximum amount of copper iodide (CuI) introduced into the matrix is up to 30%.

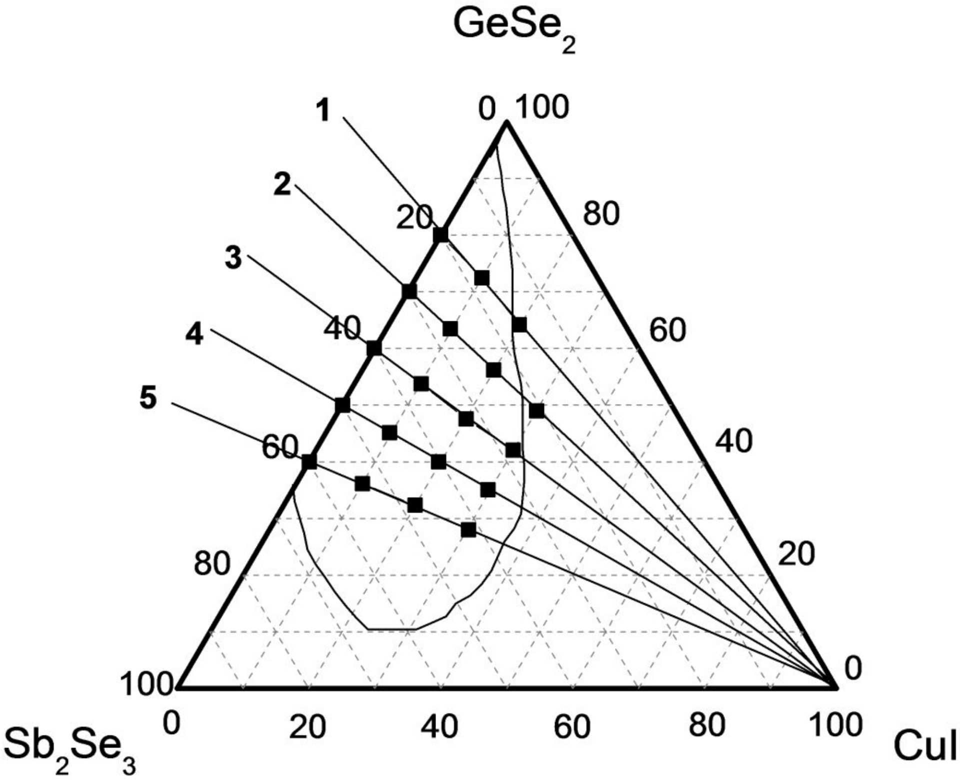

Figure 2-8 Glass-forming region in the ternary diagram of $GeSe_2$-Sb_2Se_3-CuI

2.2 Thermal dynamical consideration of crystallization

Associated with the wide transmission range in the infrared region, chalcogenide glasses have relatively weak chemical bonds, which lead to poor thermomechanical properties [9]. One efficient way to mitigate this weakness is to generate a high number of small crystals. For achieving this objective, it is useful to understand the crystallization mechanism in order to induce controlled crystallization.

The crystallization of a glass is generally governed by a two-step mechanism (Figure 2-9) [10]. One is the nucleation at a temperature near the glass transition temperature. In this temperature region, nuclei are formed in the glass matrix. The other step is the crystal growth around the nuclei.

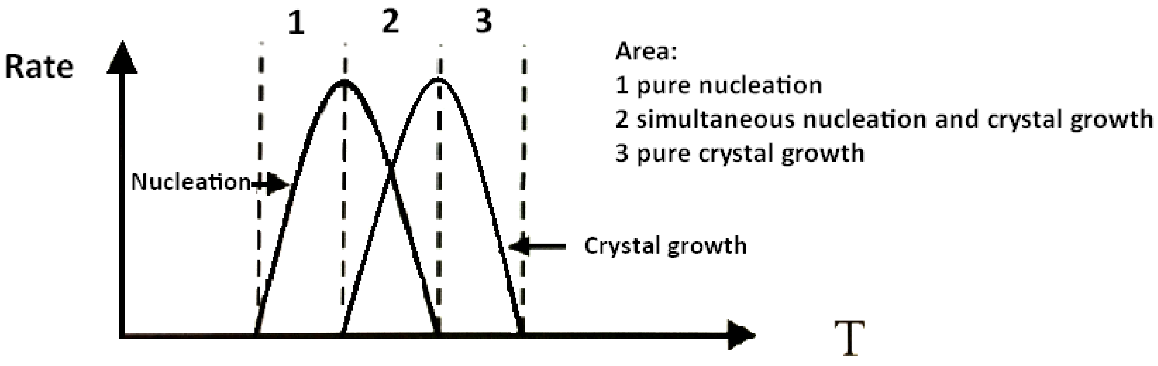

Figure 2-9 Schematic diagram of the crystallization process

2.2.1 Nucleation

Nucleation is the process of generating a new phase from an old one whose free energy has become higher than that of the emerging new phase. The mechanism of nucleation is the subject of many studies [11-15]. Indeed, germination plays a crucial role in controlling the microscopic properties (size, purity, morphology and crystalline structure) that directly affect the physical and chemical properties of the generated macroscopic crystalline material [16-18].

There are two basic types of nucleation during bulk crystallization [19, 20]:

(1) Homogeneous nucleation: nucleation occurring arbitrarily throughout the system with no preferential sites for nucleus formation.

(2) Heterogeneous nucleation: formation of the nuclei of a new phase on the surface of an already existing phase boundary.

The rate of nucleation has been considered from the point of view of the classical model for steady-state thermal nucleation. The model based on quantitative determination of the nucleation rate as a criterion of the glass formation was developed by Turnbull [21]. He expressed the nucleation rate using an expression for the steady-state nucleation rate in terms of the classical theory of homogeneous nucleation. The free energy of phase created between the crystalline phase and the supercooled liquid is expressed by the sum of two expressions, which is the function of volume and the surface area [21, 22]:

$$\Delta G_{total} = \Delta G_{volume} + \Delta G_{surface} \tag{2.4}$$

In fact, the formation of spherical nucleus thermodynamically affects the free energy of the system in two ways [16]: on one hand, it induces the minimization of the free energy per unit of volume transformed; on the other hand, the spontaneous creation of heterogeneous nucleation in an initially homogeneous system requires the formation of high energy interfaces. The total free energy of the spherical regions is

$$\Delta G_{total} = \frac{4}{3}\pi r^3 \Delta G_{volume} + 4\pi r^2 \gamma \tag{2.5}$$

where *r* is the radius of regions, σ is the interfacial energy per surface area unit.

Figure 2-10 shows the evolution of the volume free energy, interfacial energy and overall free energy of the system according to the radius of nucleus [23]. When the temperature decreases below the melting point Tm, the driving force becomes positive. The new phase regions formed with small *r* are again unstable until they attain a certain critical size *r**, at which further growth becomes spontaneous. After having reached the maximum value ΔG* when *r* = *r**, its overall free energy decrease in the system.

The nuclear size *r** with maximal free energy corresponding to ΔG* can be found from condition

$$\frac{d(\Delta G_{total})}{dr} = 0 \tag{2.6}$$

So the value of critical radius *r** is

$$r^* = -\frac{2\gamma}{\Delta G_{volume}} \tag{2.7}$$

Then the value of critical free energy

$$\Delta G^* = \frac{16\pi\gamma^3}{3\Delta G_{volume}^2} \tag{2.8}$$

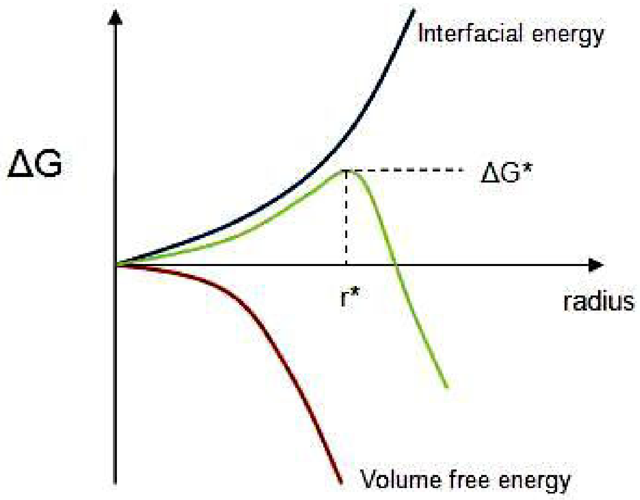

Figure 2-10 Evolution of free energy according to the radius of nucleus when the temperature is below the melting point $T < T_m$

2.2.2 Crystal growth

After the formation of stable nuclei in the parent phase, crystallization proceeds by growth of the new phase. The factors controlling crystal growth processes are (1) the rate of heat transfer at the phase boundary, (2) the rate of diffusion of structural units, (3) the rate of the reaction in which the structural units are incorporated into the crystal lattice. In the typical glass-forming systems, the heat of crystallization is mostly small, so that the crystal growth is mostly controlled by molecular transport or by reactions at interface between crystal and the melt. Theoretical description of the rate of crystal growth is based on more or less idealized models that assume a certain character for interface and for sites on the interface where atoms (molecules) are incorporated or removed. These models can be demonstrated for simple example of the growth of new phase from parent phase, where the composition does not change [10].

For the $GeSe_2$-Sb_2Se_3-CuI glasses studied in this work, we have observed that the nucleation region is quite close to the crystal growth region with overlaps. Therefore, a simplified preparation method is firstly adopted here and the glass ceramics are prepared by directly annealing the glass at crystallization onset temperature T_x. A detailed study of the influence of the nucleation and crystal growth on the properties of the glass ceramic will be conducted in the next chapter.

3 Presentation of characterization techniques

3.1 Photoelectrochemical (PEC) measurement

This measurement method is based on a PEC cell with generally an appropriate liquid electrolyte. The principle of the measurement is the following: a certain bias is applied on the semiconductor which is illuminated with chopped light. The light will generate free charge carriers on the surface of the semiconductor in contact with the electrolyte and will consequently increase the current. The applied bias is generally scanned and the appearance or absence of photocurrent at positive or negative bias can be used for the determination of the type of the semiconductor [24, 25]. The PEC measurements can either use a two-electrode method or a three-electrode method.

3.1.1 Two-electrode method

The two-electrode method (Figure 2-11) uses the semiconductor as working electrode and a metal as counter electrode. It measures the relationship between reverse bias and photocurrent in this bias [26]. However, in the absence of reference electrode, the real bias applied on the semiconductor is unknown. Besides, we cannot record the data until the system become stabilize. For these reasons, this method is generally not used.

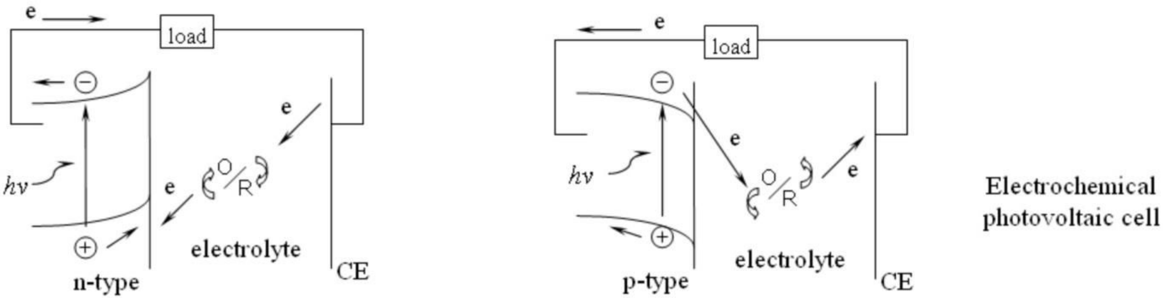

Figure 2-11 Schematic presentation of two-electrode method

3.1.2 Three-electrode method

In this method, a reference electrode is added. The semiconducting glass ceramic studied here is always used as working electrodes. The working electrode has an ohmic electrical contact, created by connecting the back side (without illumination) with a copper wire with the help of conductive glue. Except the working surface of 9 mm in diameter, all edges and the backside electrical contact were sealed by a non-conducting resin as shown in Figure 2-12. The measurement set-up is schematically represented in Figure 2-13. The working electrode was used in association with a platinum counter electrode and Ag/AgCl reference electrode. Aqueous solution of 0.5 M $LiClO_4$ was used as electrolyte. The potential difference is measured between the reference electrode and the working electrode. The current density is measured between the Pt electrode and the working electrode. A potentiostat AUTOLAB METROHM and a chopped white light lamp of 150 W with an intensity of 30 W/cm^2 on the sample were employed to record current-voltage (I-V) characteristics. The result was analyzed by using the NOVA software.

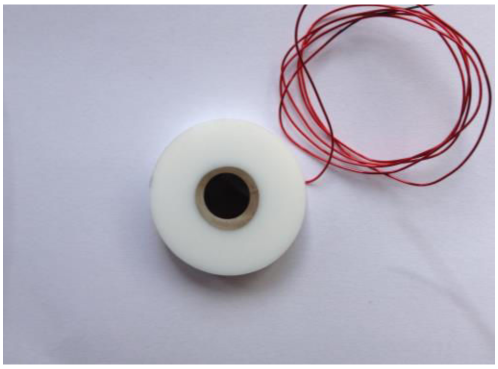

Figure 2-12 Photograph of semiconductor working electrode

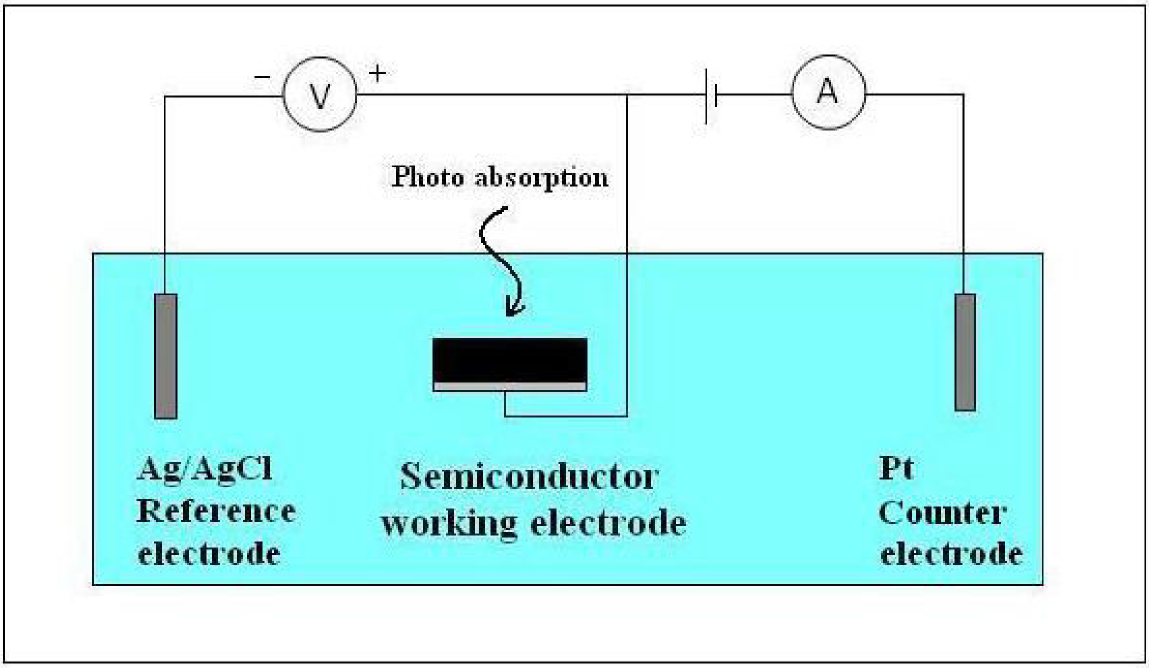

Figure 2-13 Schematic presentation of three-electrode PEC method

The advantage of the three-electrode method is that there is no current flow throw the reference electrode to ensure the stability of the electrodes. Therefore, the measured potential is the applied bias, relative to the reference potential of Ag/AgCl, on the sample. The measurement consists of recoding the current as function of the applied bias under chopped illumination to distinguish the dark and light current.

By putting a chopper between lamp and sample, the dark current and light current can be recorded to calculate the photo current under bias potential. Furthermore, if we can measure the number of photons absorbed by the semiconductor, the quantum efficiency of semiconductor can be calculated as follows [27]

$$\Phi = \frac{\Delta I_{photo}/e}{N_{photon-absorbed}} \tag{2.9}$$

3.2 Other characterizations of glasses and glass ceramics

As described before, glasses used in this study have been prepared by the melt-quenching of the glass contained in a vacuum-sealed silica tube. The characteristic temperatures of the glasses are obtained by thermal analysis which was performed with a differential scanning calorimeter (DSC) by using a sample weight of 8 mg and a heating rate of 10 ^{o}C/min. The temperature reproducibility is typically ±1 ^{o}C. From the thermal analysis, the glass transition temperature T_g and crystallization onset temperature T_x can be graphically obtained as shown in Figure 2-14. The difference $\Delta T = T_x - T_g$ is a good indication of the stability of a glass against the crystallization.

Optical transmission was measured using a polished disc of 9 mm in diameter and typically 1.5 mm in thickness. The measurements in the visible and near-infrared region were done with a double-beam spectrometer with transmission reproducibility of about ±0.5%. In the mid and far infrared region, they were performed by a Fourier transform spectrometer with a transmission precision of ±2%.

X-ray diffraction data were collected by PANalytical's X-ray diffractonmeter with a step width of 0.02^{o} and a counting duration of 13 s/step. A polished disc was generally used for this measurement.

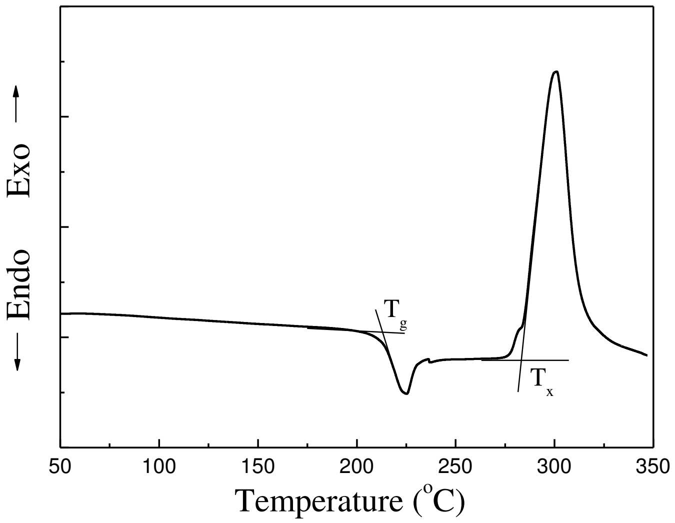

Figure 2-14 Typical DSC curve, showing the characteristic temperatures for a glass

The conductivity type of the as-prepared glass ceramics is measured with a Semilab PN tester PN-100. A semiconductor surface covered by native oxide is typically in depletion conditions regardless of its type. As a consequence the polarity of the surface barrier is characteristic of the conductivity type of the sample under test. Surface barrier polarity can be detected in a non-contact way by measuring the surface photovoltage. During such measurement, a chopped laser light is applied: by the high intensity illumination excess carriers are generated and their presence decreases the surface barrier, i.e. flatband condition is approached. The barrier change due to the illumination is capacitively detected by a probe. Conductivity type is determined by the polarity of the surface barrier change due to illumination.

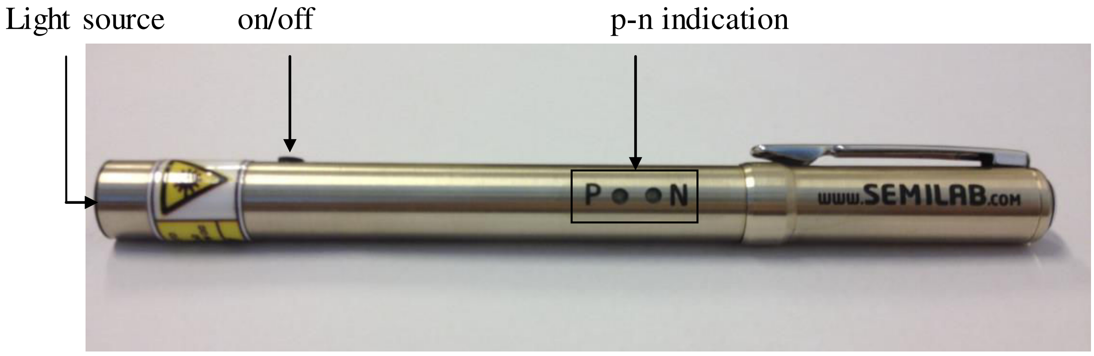

Figure 2-15 Photograph of a Semilab PN tester

Electric conductivity of the samples was measured by the four-point probe method. It is the apparatus typically used to determine bulk resistivity. The principle of this technique is to induce a direct current through the sample with a power source and to measure the potential difference of two other contacts as shown in Figure 2-16.

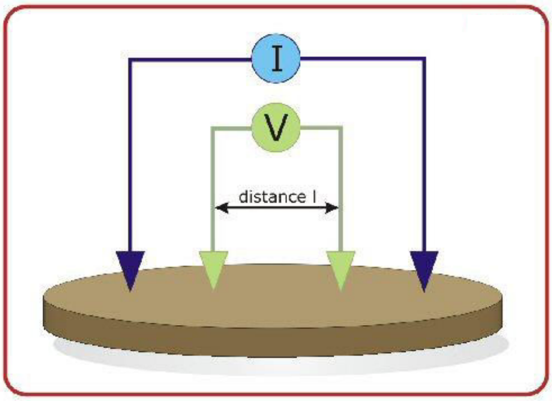

Figure 2-16 Schematic presentation of four-point probe method for resistivity measurement

4 Systematic studies of the $GeSe_2$-Sb_2Se_3-CuI system

In this paragraph, we will perform a systematic screening of glass and glass ceramic compositions in relation with the photo-electro-chemical properties. Optimization and detailed structure studies will be performed in the following chapters.

4.1 Series 1: (1-x)(80$GeSe_2$-20Sb_2Se_3)-100xCuI, x=0, 0.1, 0.2

This series of samples is prepared by introducing various amount of CuI into the base glass of 80$GeSe_2$-20Sb_2Se_3. The DSC curve of this base glass is shown in Figure 2-17, and exhibits its glass transition at ~308 °C (T_g). It can also be seen that the glass is stable against crystallization, as there is not any exothermic peak, which can be attributed to the crystallization phenomenon, up to 450 °C. However, when CuI is introduced into the base glass, the glass transition temperature decreases and three crystallization peaks appear and are shifted towards lower temperatures with the increasing CuI content [3]. From the XRD pattern shown in Figure 2-18, it can be determined that the exothermic peaks at 309 °C and 278 °C are attributed to the crystallization of Cu_2GeSe_3, which is facilitated with increasing CuI content. In addition, the Sb_2Se_3 crystallizes in both 72$GeSe_2$-18Sb_2Se_3-10CuI and 64$GeSe_2$-16Sb_2Se_3-20CuI samples when thermally annealed at higher temperature. The peaks at 393 °C and 390 °C correspond to the crystallization of Sb_2Se_3. The last exothermic peak respectively at 410°C and 379°C for 72$GeSe_2$-18Sb_2Se_3-10CuI and 64$GeSe_2$-16Sb_2Se_3-20CuI samples is attributed respectively to the crystallization of $GeSe_2$ and maybe Sb.

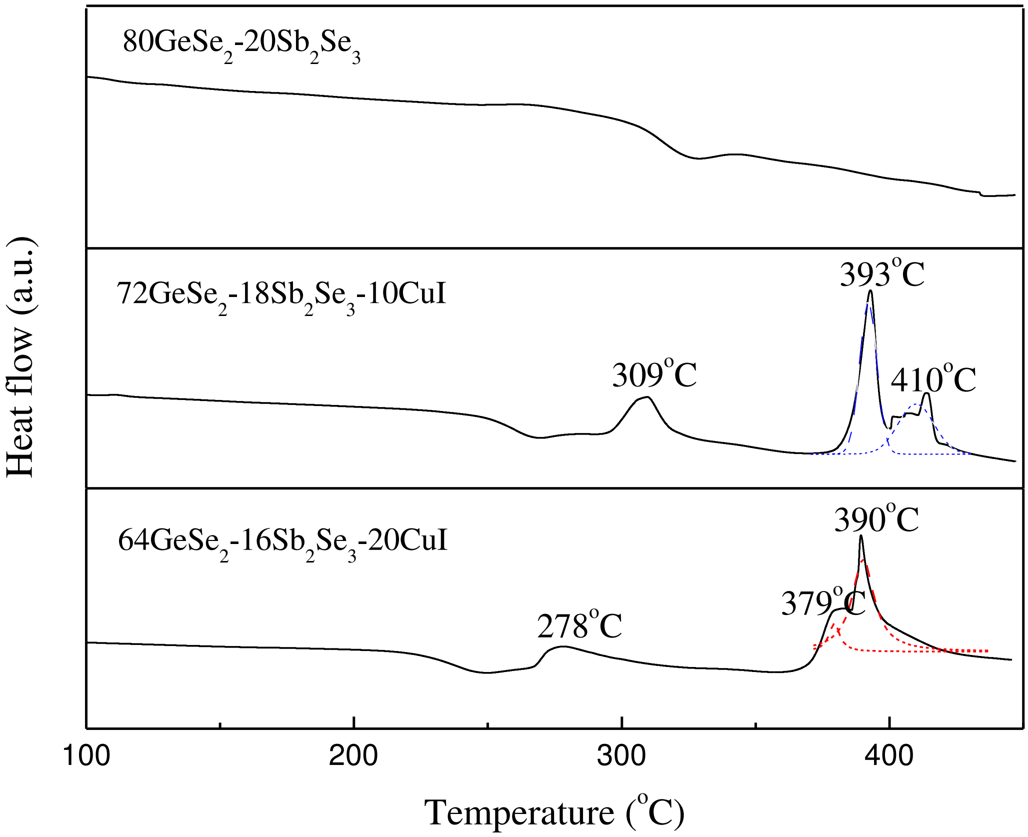

Figure 2-17 DSC curves of various glasses of Series 1

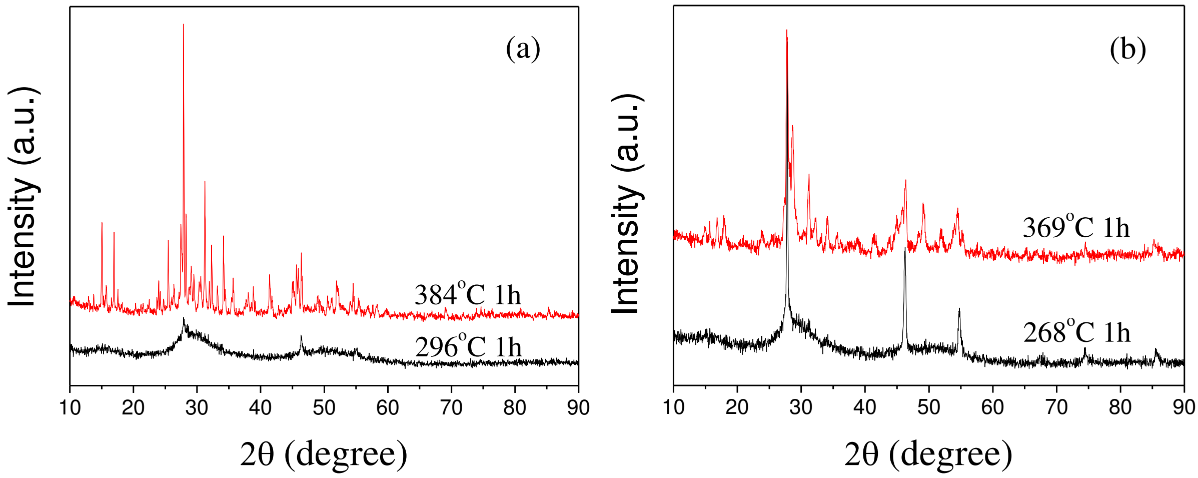

Figure 2-18 XRD patterns of samples annealed at different crystallization temperature for 1 h: (a) 72GeSe$_2$-18Sb$_2$Se$_3$-10CuI; (b) 64GeSe$_2$-16Sb$_2$Se$_3$-20CuI

Figure 2-19 shows the XRD patterns of different glass ceramics which were prepared with different thermal annealing conditions listed in Table 2-1. The diffraction peaks of the glass ceramic obtained from the base glass without CuI consists of two phases, GeSe$_2$ and Sb$_2$Se$_3$. As GeSe$_2$ is more difficult to crystallize [28, 29], the diffraction peak intensity of GeSe$_2$ is lower than that of Sb_2Se_3 although the initial amount of Ge is much higher than Sb. Indeed, $GeSe_2$ is glass former and tends to stay in amorphous state in the $80GeSe_2$-$20Sb_2Se_3$ sample. When introducing CuI into the base glass, the obtained glass easily leads to the generation of Cu_2GeSe_3, resulting in the decrease of $GeSe_2$. Moreover, the formation of Cu_2GeSe_3 makes Sb amount exceed the stoichiometric ratio, according to the Sb:Se atomic ratio of 2:3 in Sb_2Se_3 compound. The excessive Sb element will exist in the form of elemental Sb after further increase of the CuI content, and the phase of $GeSe_2$ disappears at the same time.

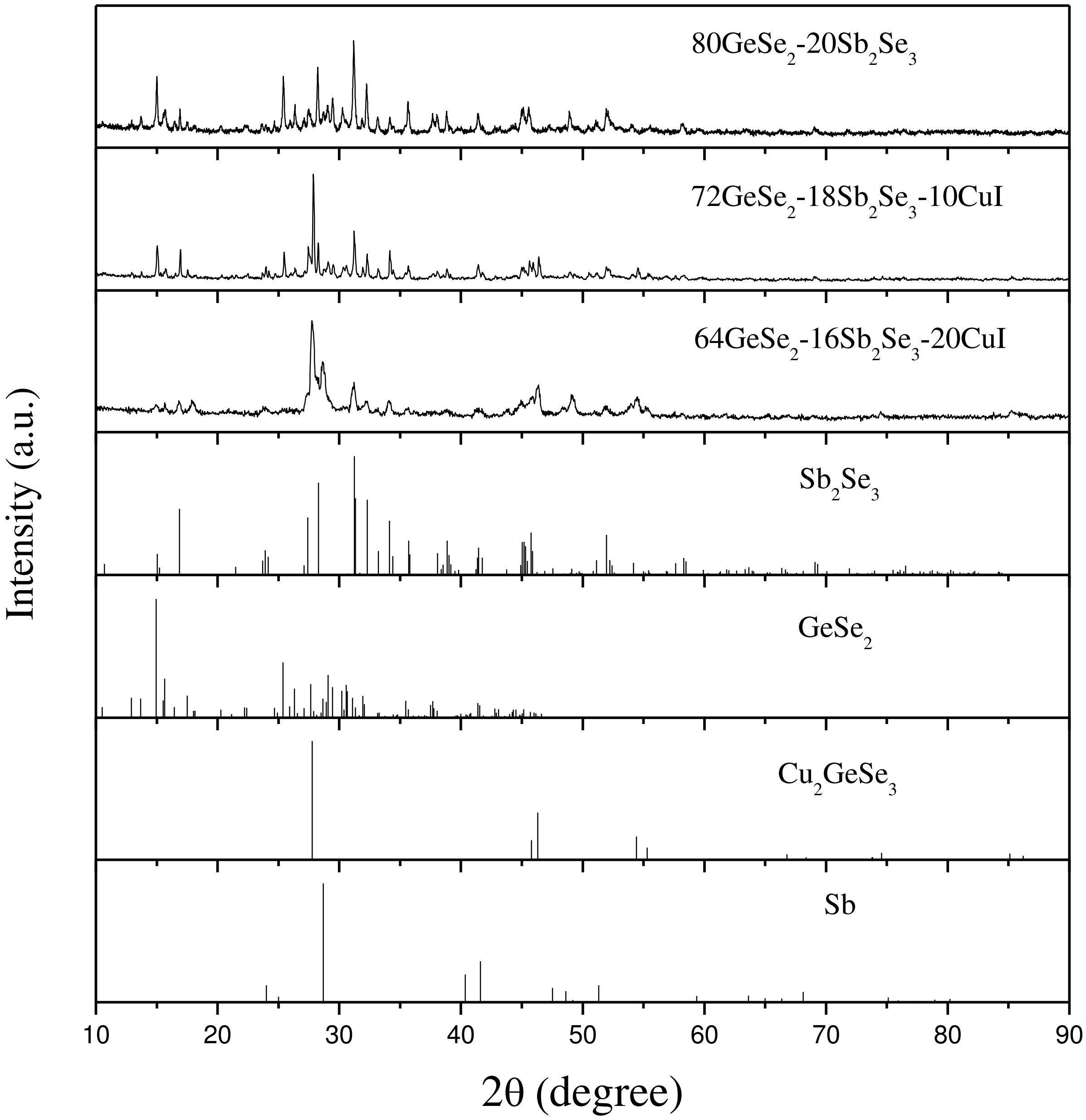

Figure 2-19 XRD patterns of different glass ceramics

The photoelectric properties of the glass ceramics were measured by the three-electrode PEC method. Figure 2-20 shows the dark and light current-voltage characteristics of the glass ceramics. The glass ceramics of $80GeSe_2$-$20Sb_2Se_3$ and $72GeSe_2$-$18Sb_2Se_3$-10CuI all display photocurrent signals with very weak intensity. The photocurrent is here defined as the difference between the current under illumination and the current in the dark at a certain bias voltage. The photocurrent is highly dependent of composition and it disappears with the composition containing 20% of CuI (as shown in Figure 2-20(c)). Furthermore, semiconductor type of the glass ceramics is measured and the results are listed in Table 2-1. Both glass ceramics having photocurrent are p-type semiconductors, and it is difficult to determine the semiconductor type of all glass ceramics with weak or nonexistent photocurrent.

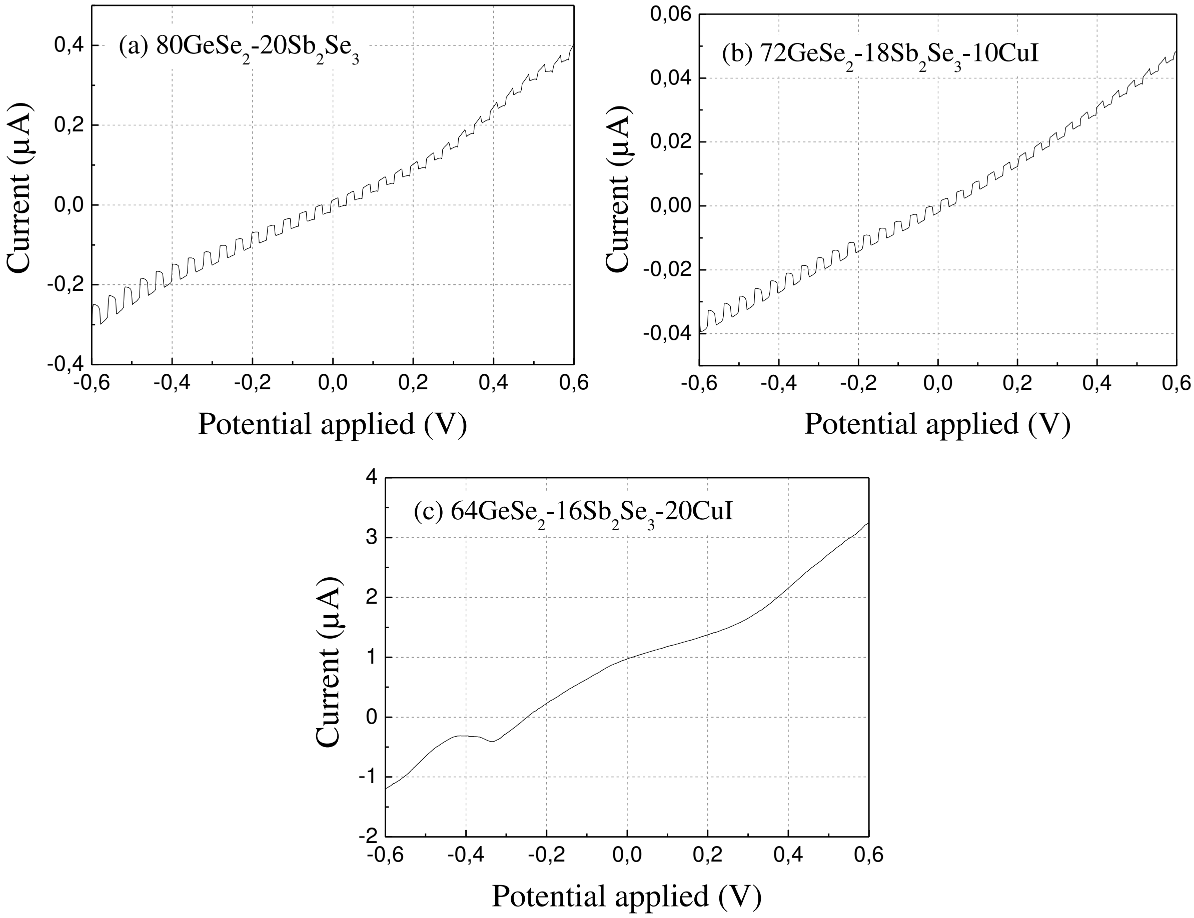

Figure 2-20 Current-voltage characteristics of different glass ceramics in Series 1 under chopped visible light illumination

Table 2-1 Preparation conditions, crystallized phases and photoelectric properties of different glass ceramics in Series 1

Samples	T_x (°C)	Annealing conditions	Crystal phase	Photocurrent I_p at -0.5 V (μA)	Semiconductor type	Conductivity ($\Omega^{-1}\cdot cm^{-1}$)
$80GeSe_2$-$20Sb_2Se$	-	450°C 5h	$GeSe_2$+ Sb_2Se_3	-0.05	P	$<10^{-8}$
$72GeSe_2$-$18Sb_2Se_3$-10CuI	296	296°C 1h	Cu_2GeSe_3	0	-	$<10^{-8}$
	384	384°C 1h	$GeSe_2$+ Sb_2Se_3+ Cu_2GeSe_3	-0.005	P	$<10^{-8}$
$64GeSe_2$-$16Sb_2Se_3$-20CuI	268	268°C 1h	Cu_2GeSe_3	0	-	$<10^{-8}$
	369	369°C 1h	Cu_2GeSe_3 +Sb_2Se_3+ Sb	0	-	$<10^{-8}$

4.2 Series 2: $(1-x)(70GeSe_2-30Sb_2Se_3)-100xCuI$, x = 0, 0.1, 0.2, 0.3

This series of samples is prepared by introducing various amount of CuI into the base glass of $70GeSe_2$-$30Sb_2Se_3$. Figure 2-21 shows the XRD patterns of different glass ceramics prepared with conditions listed in Table 2-2. The diffraction peaks of the glass ceramic obtained from base glass without CuI consists of $GeSe_2$ and Sb_2Se_3 with possibly some selenium. When the introduction of CuI into the base glass, the crystallized phases of the glass ceramics are considerably modified, and the main crystalline phase is Cu_2GeSe_3, with a very small amount of Sb_2Se_3. When increasing CuI content up to 30 mol%, the intensity of the diffraction peaks attributed to Sb_2Se_3 decreases obviously and a new crystalline phase of SbSeI appears due to the presence of a large number of iodine.

Figure 2-22 shows a typical dark and light current-voltage characteristic of the glass ceramics from the Series 2, indicating that no photocurrent is generated. The most likely reason for this result is that all the glass ceramics have poor conductivity (as shown in Table 2-2).

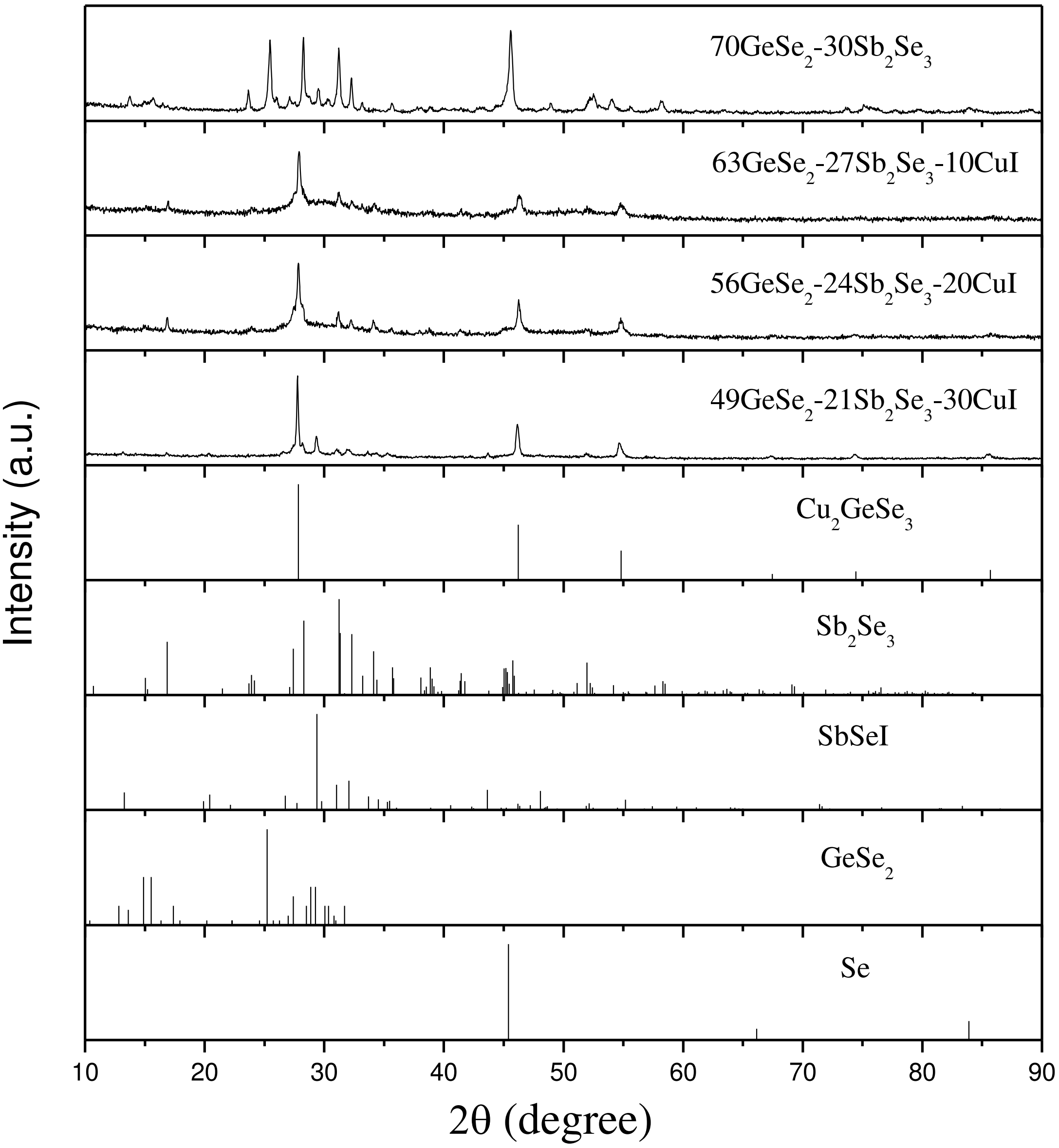

Figure 2-21 XRD patterns of different glass ceramics in Series 2

In this series of glass ceramic, the main crystalline phase is Cu_2GeSe_3, which has relative higher conductivity of about 5 $\Omega^{-1}\cdot cm^{-1}$ at 0 °C [30].This conductive cubic phase is likely not interconnected inside of the glass ceramics and therefore, all the glass ceramics in this series still show high resistance. Even though the signal is weak, it was still possible to measure the type of the semiconductor. It can be seen from Table 2-2 that the $63GeSe_2$-$27Sb_2Se_3$-10CuI glass ceramic is p-type semiconductor, and the conductivity type of the samples is changed from p-type to n-type with the further increase of CuI content.

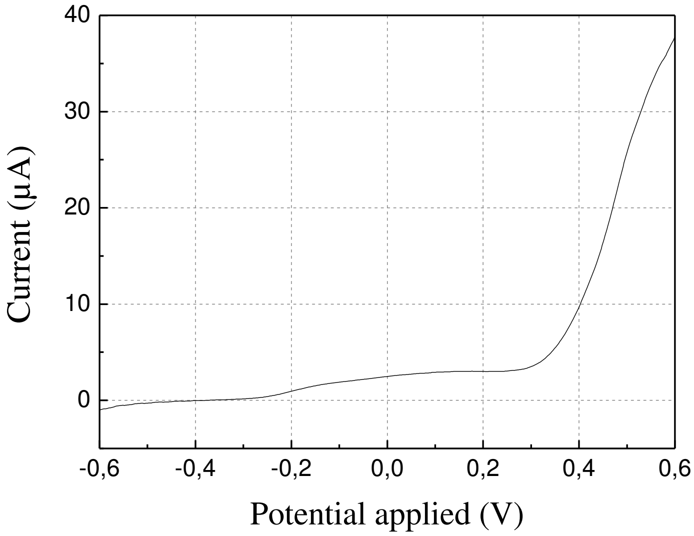

Figure 2-22 Typical current-voltage characteristic of glass ceramics in Series 2 under chopped visible light illumination

Table 2-2 Preparation conditions, crystallized phases and photoelectric properties of different glass ceramics in Series 2

Samples	Annealing condition	Crystal phase	Photocurrent I_p at -0.5 V (μA)	Type	Conductivity ($\Omega^{-1}\cdot cm^{-1}$)
$70GeSe_2$-$30Sb_2Se_3$	420°C 5h	$GeSe_2$+Sb_2Se_3+ Se	0	-	<10^{-8}
$63GeSe_2$-$27Sb_2Se_3$-10CuI	290 °C 5h	Cu_2GeSe_3+ Sb_2Se_3	0	P(w)	<10^{-8}
$56GeSe_2$-$24Sb_2Se_3$-20CuI	274 °C 5h	Cu_2GeSe_3+ Sb_2Se_3	0	N(w)	<10^{-8}
$49GeSe_2$-$21Sb_2Se_3$-30CuI	257 °C 5h	Cu_2GeSe_3+ SbSeI	0	N(w)	<10^{-8}

4.3 Series 3: (1-x)($60GeSe_2$-$40Sb_2Se_3$)-100xCuI, x = 0, 0.1, 0.2, 0.3

This series of samples is prepared by introducing various amount of CuI into the base glass of $60GeSe_2$-$40Sb_2Se_3$. Figure 2-23 shows the XRD patterns of different glass ceramics prepared under the conditions listed in Table 2-3. For the glass ceramic without or with low CuI content (10 mol%), the main crystallized phase seems to be close to elemental Se with however slightly shifted diffraction angle. This is difficult to understand, as selenium is a good glass-former. More detailed studies are necessary to elucidate the mystery of the diffraction peak at around 21° (2θ). The second crystal phase is Sb_2Se_3. With the increase of CuI content, Cu_2GeSe_3 begins to appear in the sample. When further increasing CuI content from 20 mol% to 30 mol%, the excessive iodine leads to the formation of SbSeI.

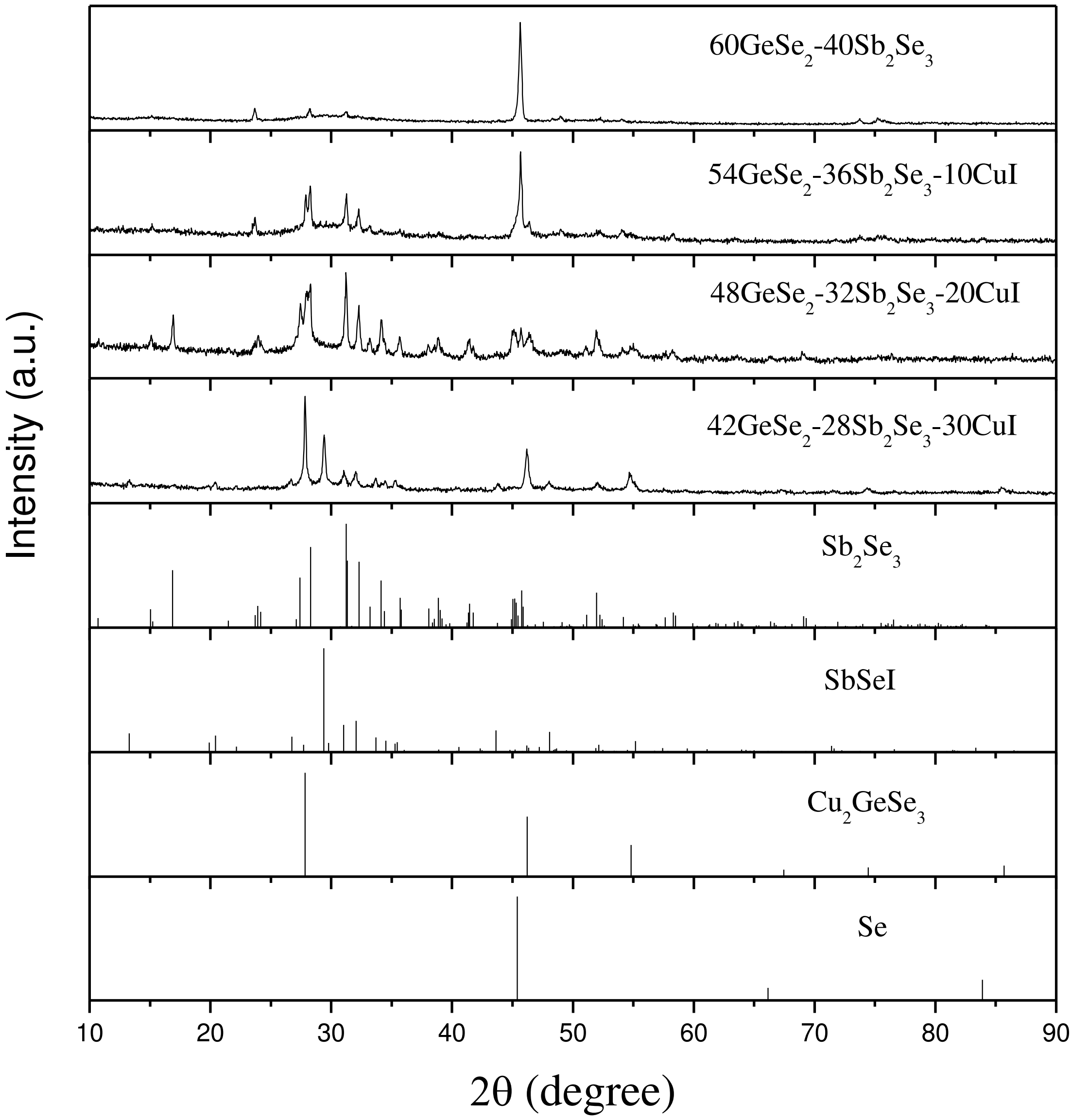

Figure 2-23 XRD patterns of different glass ceramics in Series 3

Figure 2-24 shows current-voltage characteristics of the glass ceramics in Series 3 under chopped visible light illumination. Combining with the XRD result, it can be seen that the most abundant phase (with diffraction peak close to that of selenium) in the glass ceramics of $60GeSe_2$-$40Sb_2Se_3$ and $54GeSe_2$-$36Sb_2Se_3$-10CuI cannot efficiently generate photocurrents. These two samples show p-type semiconductor nature (Table 2-3) in agreement with the fact that selenium is a p-type semiconductor [31, 32]. Moreover, the photocurrent increases with the Cu_2GeSe_3 content. However, the photocurrent intensity is weak for all the samples of this series. The results may be attributed to the poor conductivity of the glass ceramics (as shown in Table 2-3).

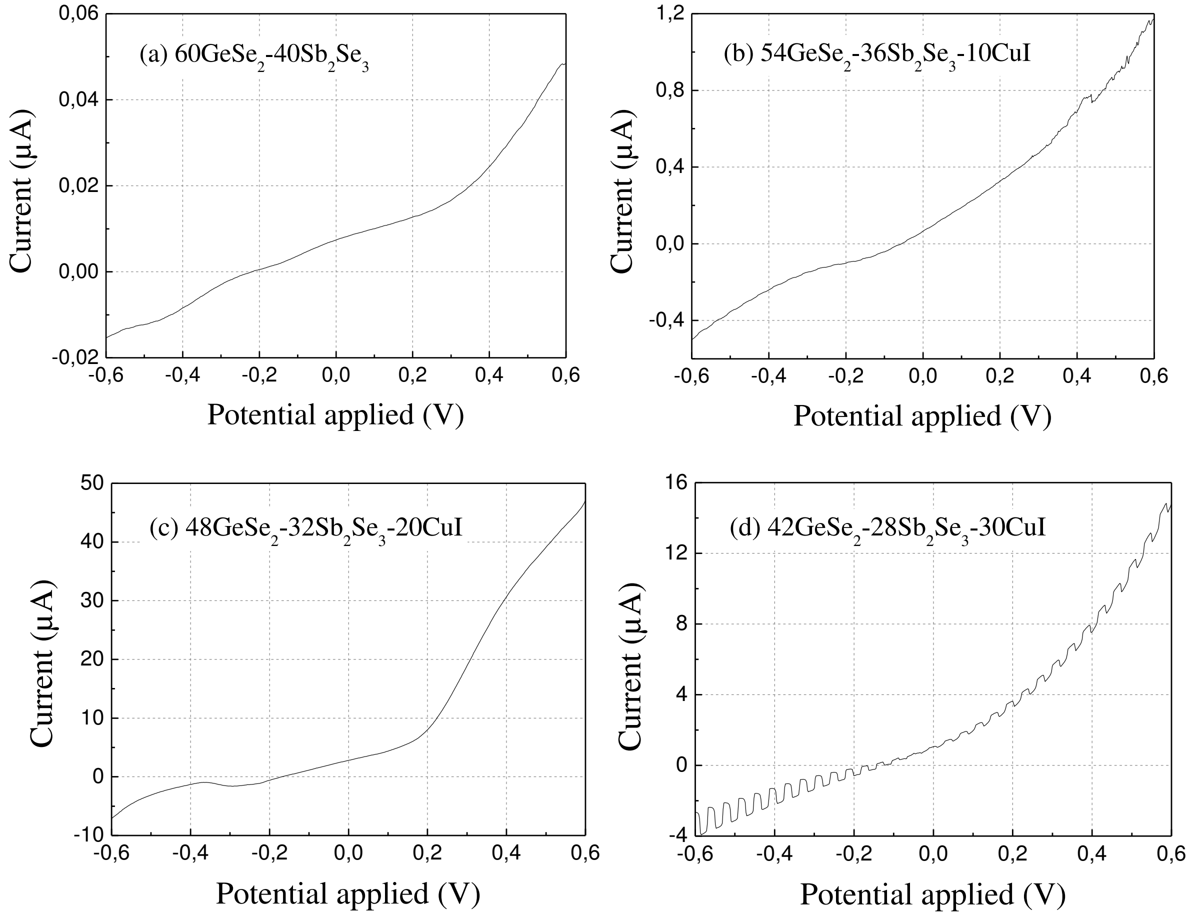

Figure 2-24 Current-voltage characteristics of different glass ceramics in Series 3 under chopped visible light illumination

Table 2-3 Preparation conditions, crystallized phases and photoelectric properties of different glass ceramics in Series 3

Samples	Annealing condition	Crystal phase	Photocurrent I_p at -0.5 V (μA)	Type	Conductivity ($\Omega^{-1}\cdot cm^{-1}$)
$60GeSe_2$-$40Sb_2Se_3$	404°C 1h	Sb_2Se_3+Se	0	P	$<10^{-8}$
$54GeSe_2$-$36Sb_2Se_3$-10CuI	348°C 1h	Sb_2Se_3+Se	0	P	8.4×10^{-8}
$48GeSe_2$-$32Sb_2Se_3$-20CuI	317°C 1h	Cu_2GeSe_3+ Sb_2Se_3+Se	-0.2	P	3.3×10^{-7}
$42GeSe_2$-$28Sb_2Se_3$-30CuI	303°C 1h	Cu_2GeSe_3+ SbSeI	-1.73	P	$<10^{-8}$

4.4 Series 4: (1-x)(50$GeSe_2$-50Sb_2Se_3)-100xCuI, x = 0, 0.1, 0.2, 0.3

This series of samples is prepared by introducing various amount of CuI into the base glass of 50$GeSe_2$-50Sb_2Se_3. The glass ceramics are prepared by annealing the corresponding glass under the conditions detailed in Table 2-4. Figure 2-25 shows the XRD patterns of different glass ceramics. All observed diffraction peaks of the base glass belong to Sb_2Se_3, but the relative intensity of each peak is different from the standard PDF card (No. 01-072-1184). More detailed study is necessary for understanding the reason. It is true that the crystallization of a phase in a quite complex amorphous environment with low mobility of atoms can be very different from the crystallization of a melt with the same composition.

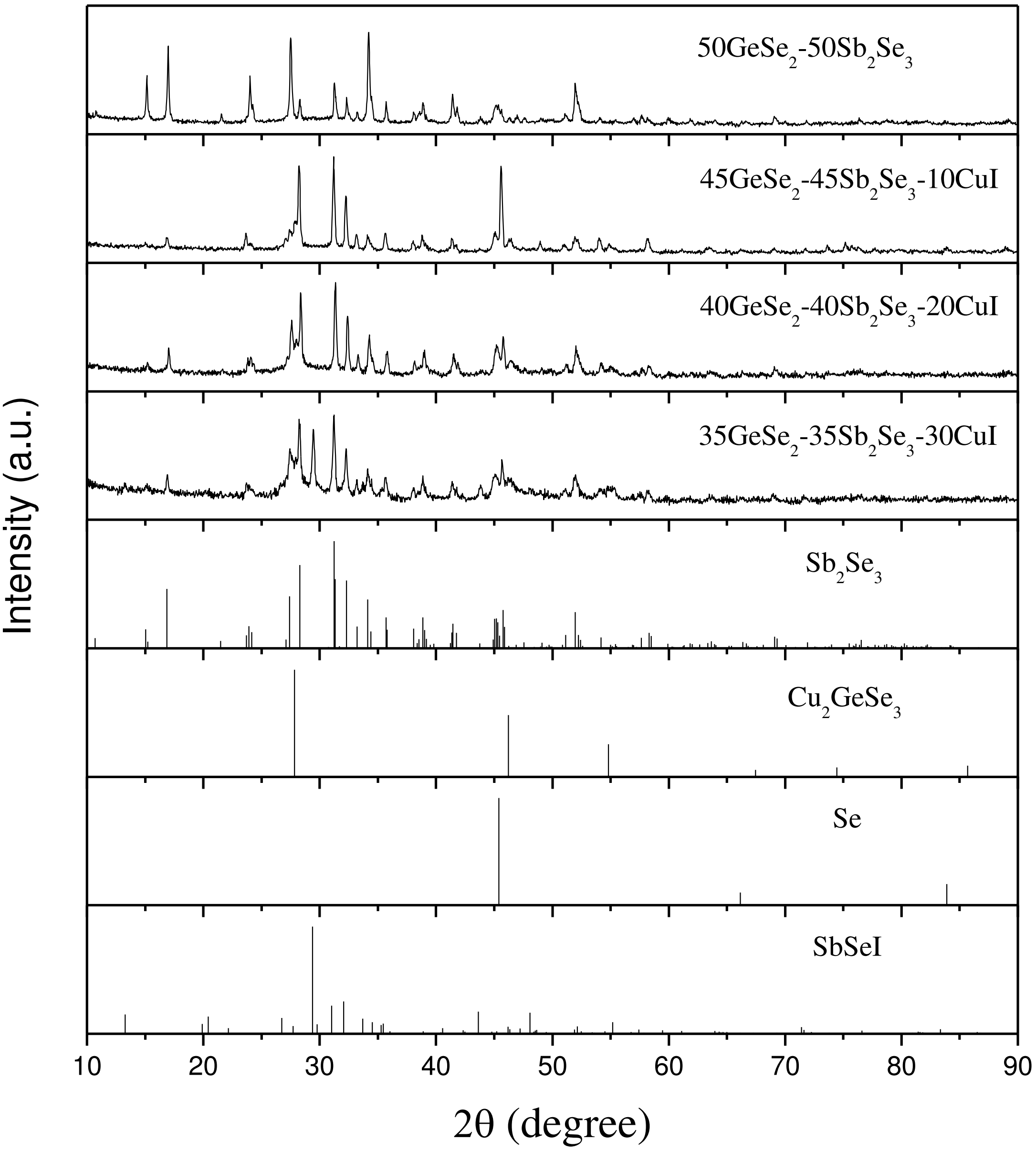

Figure 2-25 XRD patterns of different glass ceramics in Series 4

When introducing CuI into the base glass, the obtained glass ceramics, after annealing with the conditions listed in Table 2-4, contain three crystallized phases: Cu_2GeSe_3, Sb_2Se_3 and something close to elemental selenium. With the increase of CuI content, the intensity of the diffraction peaks attributed to elemental Se decreases obviously and the Cu_2GeSe_3 becomes more important. When further increasing CuI content to 30 mol%, the intensity of the diffraction peaks of Sb_2Se_3 decreases significantly and a new crystalline phase of SbSeI appears due to the presence of a large number of Iodine.

Figure 2-26 shows the dark and light current-voltage characteristics of the glass ceramics. The glass ceramics of $50GeSe_2$-$50Sb_2Se_3$ and $45GeSe_2$-$45Sb_2Se_3$-10CuI cannot generate significant photocurrent. When the content of Cu_2GeSe_3 is increased, the photocurrent is generated and reaches the highest value. For the glass ceramic of $35GeSe_2$-$35Sb_2Se_3$-30CuI, the content of Sb_2Se_3 is decreased since part of antimony exists in the form of SbSeI. The photocurrent generated by this sample is comparable with that of the $40GeSe_2$-$40Sb_2Se_3$-20CuI.

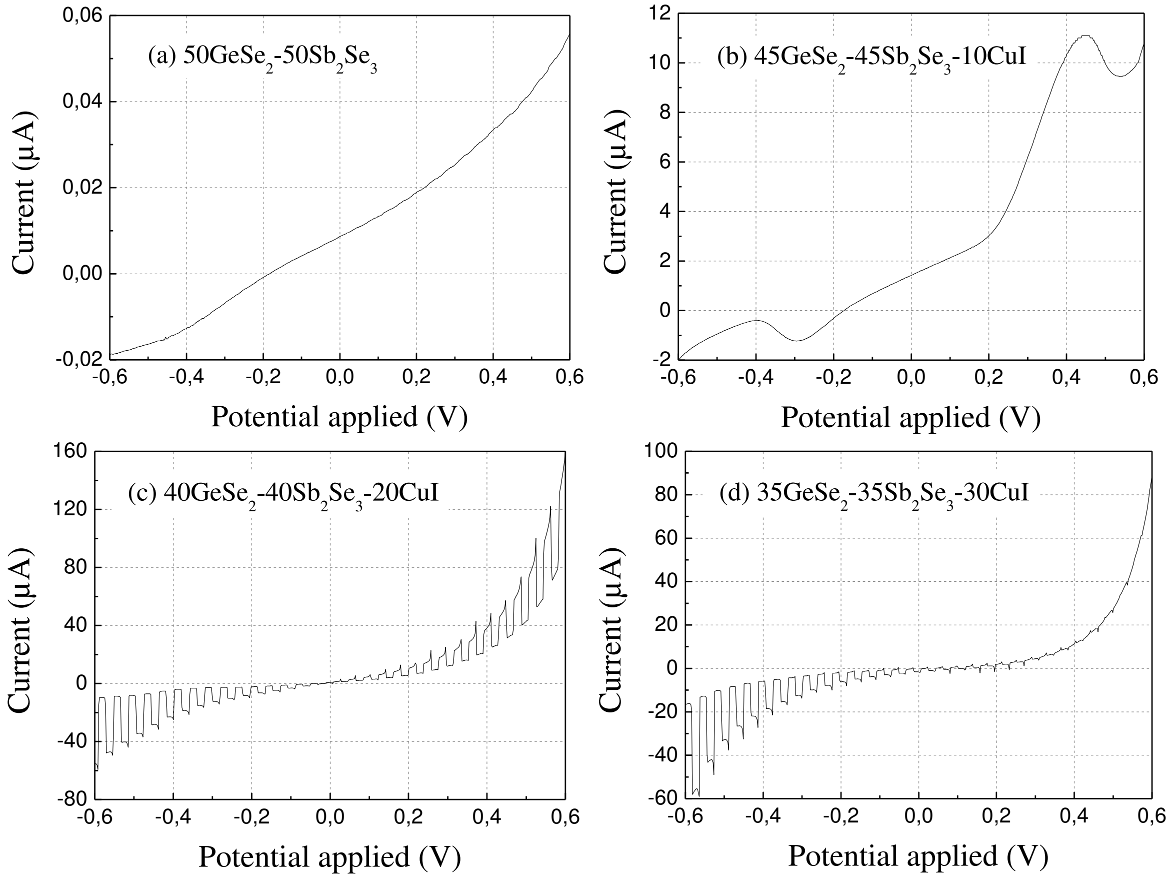

Figure 2-26 Current-voltage characteristics of different glass ceramics in Series 4 under chopped visible light illumination

Compared to samples of other series, the samples in this series show much higher conductivity with the same content of CuI or Cu_2GeSe_3 (as shown in Table 2-4). It indicates that there must be other important parameters, beside of material composition, which affects greatly the conductivity of the glass ceramic. This will be discussed below. Combining the photocurrent and conductivity results of the samples, it can be found that the high photocurrent is based on the high conductivity. Moreover, it can also be seen from Table 2-4 that the conductivity type of the samples in this series is changed from p-type to n-type with the increase of CuI content. It must be mentioned here that the conducting type of the glass ceramics is determined macroscopically by using the PN tester described earlier in this chapter. It is absolutely not in contradiction with the possibility of having simultaneously p-type and n-type semiconducting phases in the same composite materials, as suggested by the Figure 2-26(c).

Table 2-4 Preparation conditions, crystallized phases and photoelectric properties of different glass ceramics in Series 4

Samples	Annealing condition	Crystal phase	Photocurrent I_p at -0.5 V (μA)	Type	Conductivity ($\Omega^{-1}\cdot cm^{-1}$)
$50GeSe_2$-$50Sb_2Se_3$	353°C 1h	Sb_2Se_3	0	P	$<10^{-8}$
$45GeSe_2$-$45Sb_2Se_3$-10CuI	324°C 1h	Cu_2GeSe_3+Sb_2Se_3 + Se	0	P	1.8×10^{-4}
$40GeSe_2$-$40Sb_2Se_3$-20CuI	285°C 1h	Cu_2GeSe_3+Sb_2Se_3	-28.4	N	4.4×10^{-2}
$35GeSe_2$-$35Sb_2Se_3$-30CuI	242°C 1h	Cu_2GeSe_3+Sb_2Se_3 + SbSeI	-23.2	N	5.0×10^{-3}

4.5 Series 5: (1-x)($40GeSe_2$-$60Sb_2Se_3$)-100xCuI, x = 0, 0.1, 0.2, 0.3

The last series of samples is prepared by introducing various amount of CuI into the base glass of $40GeSe_2$-$60Sb_2Se_3$. After different heat treatments detailed in Table 2-5, the XRD patterns of the obtained glass ceramics are shown in Figure 2-27. It can be seen that the base glass of $40GeSe_2$-$60Sb_2Se_3$ is stable. It is difficult to attribute the diffraction peak around 21° to elemental selenium. Beside the fact that selenium is a good glass former, in case of crystallization of a large amount of selenium, the remaining composition would be highly instable against crystallization. The addition of CuI can obviously promote the crystallization in the base glass, leading to the formation of Sb_2Se_3. With higher CuI content, Cu_2GeSe_3

appears in the crystallized phases of the glass ceramics. When the CuI content is 30 mol%, the formation of SbSeI crystals is observed.

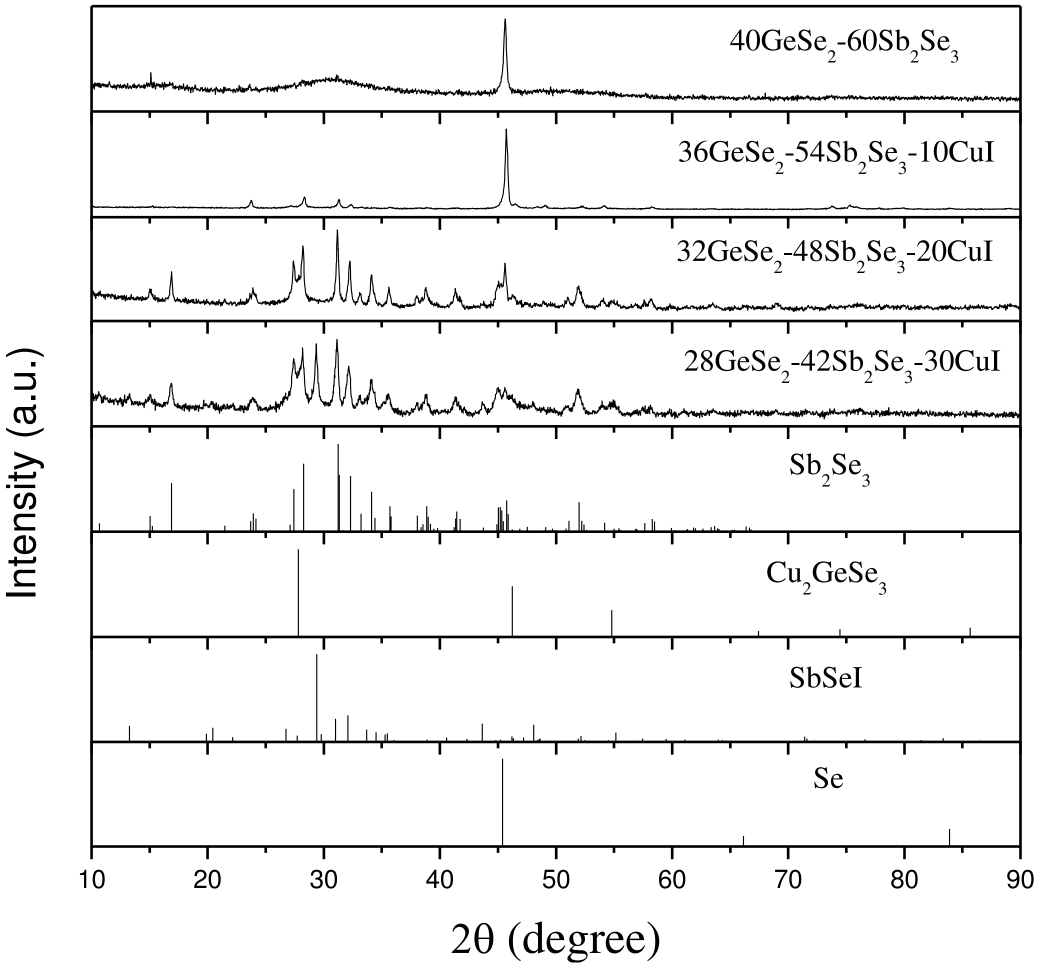

Figure 2-27 XRD patterns of different glass ceramics in Series 5

Figure 2-28 shows the dark and light current-voltage characteristics of the glass ceramics. The glass ceramic of 40GeSe$_2$-60Sb$_2$Se$_3$ cannot generate photocurrent due to its poor crystallinity and low conductivity (as shown in Table 2-5). The photocurrent cannot be detected as well in the glass ceramic of 36GeSe$_2$-54Sb$_2$Se$_3$-10CuI although it contains Sb$_2$Se$_3$ crystals. With the increase of CuI content, the photocurrent is generated in the samples and its intensity first increases and then decreases. Meanwhile, the conductivity type of the samples in this series is changed from p-type to n-type when introducing CuI in the base glass (as shown in Table 2-5).

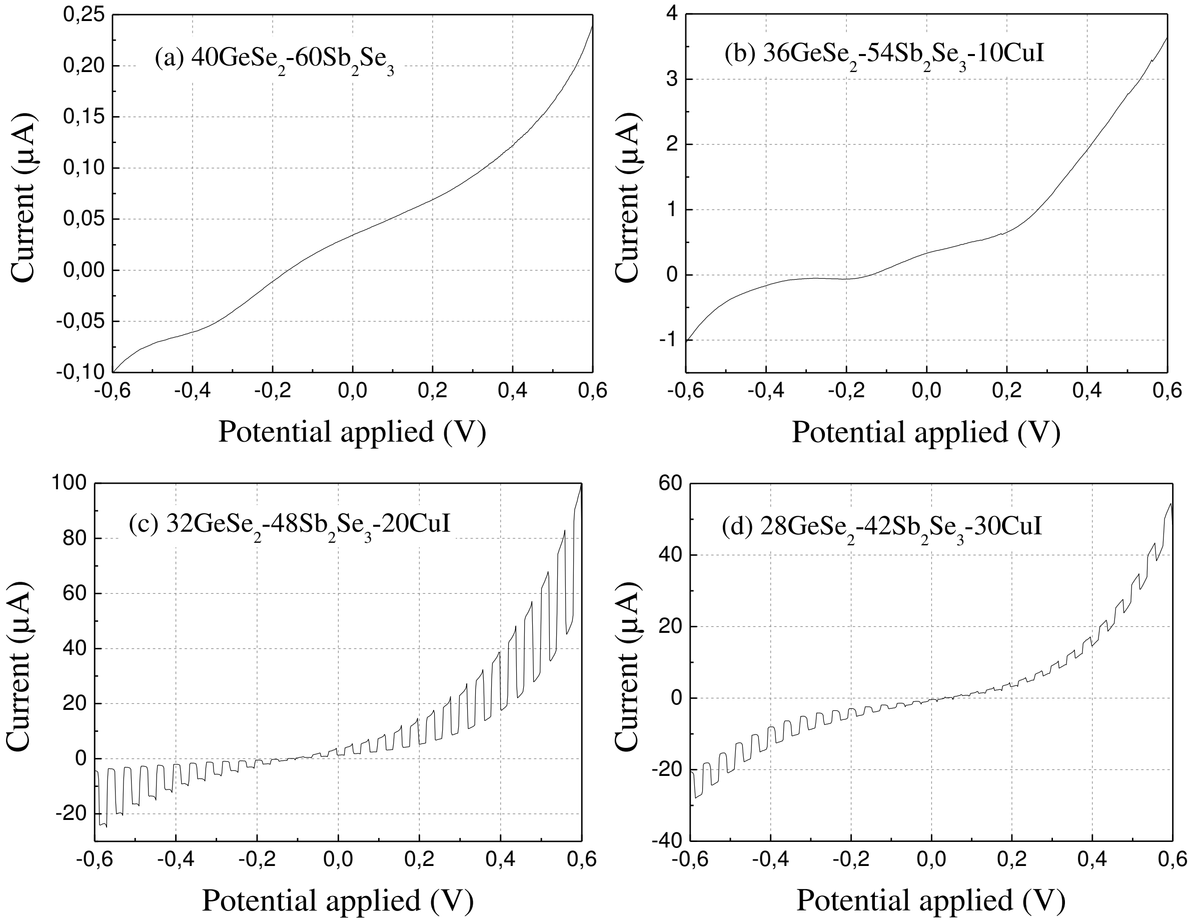

Figure 2-28 Current-voltage characteristics of different glass ceramics in Series 5

Table 2-5 Preparation conditions, crystallized phases and photoelectric properties of different glass ceramics in Series 5

Samples	Annealing condition	Crystal phase	Photocurrent I_p at -0.5 V (µA)	Type	Conductivity ($\Omega^{-1}\cdot cm^{-1}$)
40 GeSe$_2$-60 Sb$_2$Se$_3$	318°C 1h	Se	0	P	<10^{-8}
36 GeSe$_2$-54 Sb$_2$Se$_3$-10 CuI	320°C 1h	Se+Sb$_2$Se$_3$	0	N	4.5×10^{-7}
32 GeSe$_2$-48 Sb$_2$Se$_3$-20 CuI	292°C 1h	Sb$_2$Se$_3$+ Cu$_2$GeSe$_3$	-13.2	N	1.2×10^{-6}
28 GeSe$_2$-42 Sb$_2$Se$_3$-30 CuI	260°C 1h	Sb$_2$Se$_3$+ Cu$_2$GeSe$_3$+ SbSeI	-6.3	N	4.7×10^{-3}

4.6 Discussion

Figure 2-29 shows the XRD patterns of different glass ceramics with the fixed CuI content of 20 mol%. It can be seen that the XRD intensity ratio of Sb_2Se_3 (221) to Cu_2GeSe_3 (111) is increased from 0.46, 0.44, 1.35 to 2.11with the decrease of Ge content and the increase of Sb content. Based on the PEC analysis of all these samples, it can be found that the photocurrent intensity first increased and then decreased with the increase of the XRD intensity ratio of Sb_2Se_3 (221) to Cu_2GeSe_3 (111). It means that increasing the Sb_2Se_3 content in glass ceramic is favorable for the generation of photocurrent. Sb_2Se_3 is a direct band gap semiconductor with an energy gap of 1.2 eV [33]. It has been demonstrated that the maximum efficiency of around 30% for single junction solar cells is predicted for materials with band gaps in the range of 1.2–1.4 eV under standard AM1.5 conditions [34, 35]. Therefore, Sb_2Se_3 can be a suitable absorber material for photovoltaic application. During the PEC measurement, when the glass ceramic working electrode is exposed to the simulated sunlight, Sb_2Se_3 in the glass ceramic can efficiently absorb photons, leading to the formation of electron-hole pairs. This is however not sufficient for generating high photocurrent intensity as demonstrated in the case of $32GeSe_2$-$48Sb_2Se_3$-20CuI glass ceramic containing Sb_2Se_3 crystals but with weak photocurrent.

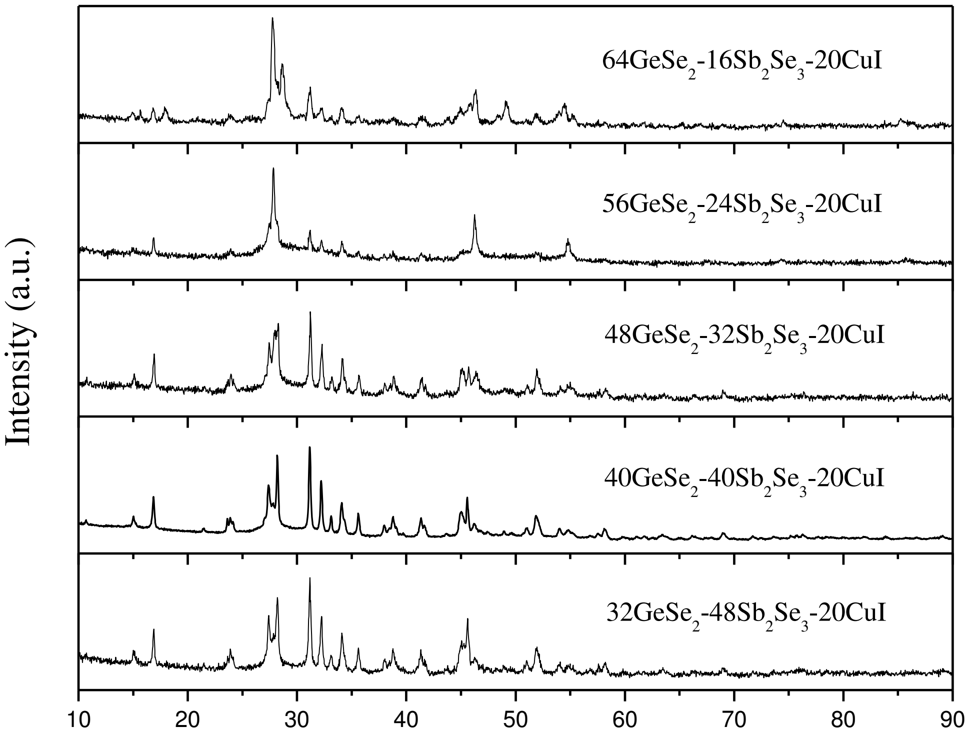

Figure 2-29 XRD patterns of different glass ceramics with 20 mol% CuI

Actually, the photocurrent is generated by the migration of photo-generated charge carriers, which is determined by the conductivity of glass ceramic. The four-point probe resistivity test shows that the conductivity of $48GeSe_2$-$32Sb_2Se_3$-20CuI, $40GeSe_2$-$40Sb_2Se_3$-20CuI and $32GeSe_2$-$48Sb_2Se_3$-20CuI is $3.27\times10^{-7}\ \Omega^{-1}\cdot cm^{-1}$, $3.13\times10^{-2}\ \Omega^{-1}\cdot cm^{-1}$ and $1.18\times10^{-6}\ \Omega^{-1}\cdot cm^{-1}$ respectively, while the conductivities of $64GeSe_2$-$16Sb_2Se_3$-20CuI and $56GeSe_2$-$24Sb_2Se_3$-20CuI cannot be measured here ($<10^{-8}\ \Omega^{-1}\cdot cm^{-1}$). Considering the associated PEC results, it is clear that the high conductivity can promote the migration of photo-generated carriers, leading to the enhancement of photocurrent.

The conductivity of the glass ceramic obviously depends on the material composition and structure. For example, $56GeSe_2$-$24Sb_2Se_3$-20CuI and $40GeSe_2$-$40Sb_2Se_3$-20CuI all contain two crystalline phases of Cu_2GeSe_3 and Sb_2Se_3. Cu_2GeSe_3 exhibits a metallic behavior at room temperature and its conductivity is about $5\ \Omega^{-1}\cdot cm^{-1}$ at 0 °C, whereas the conductivity of Sb_2Se_3 is about $\sim10^{-6}\ \Omega^{-1}\cdot cm^{-1}$ [36]. However, the conductivity of $56GeSe_2$-$24Sb_2Se_3$-20CuI cannot be measured and is much lower than that of $40GeSe_2$-$40Sb_2Se_3$-20CuI although the main crystalline phase of $56GeSe_2$-$24Sb_2Se_3$-20CuI is the electrically conductive Cu_2GeSe_3. The observation of $56GeSe_2$-$24Sb_2Se_3$-20CuI under scanning electron microscope shows that the Cu_2GeSe_3 crystals are fully dispersed in the glass matrix and surrounded by the amorphous phase (as shown in Figure 2-30(a)). Therefore, the insulating glass phase between Cu_2GeSe_3 crystals leads to the poor conductivity of the glass ceramic.

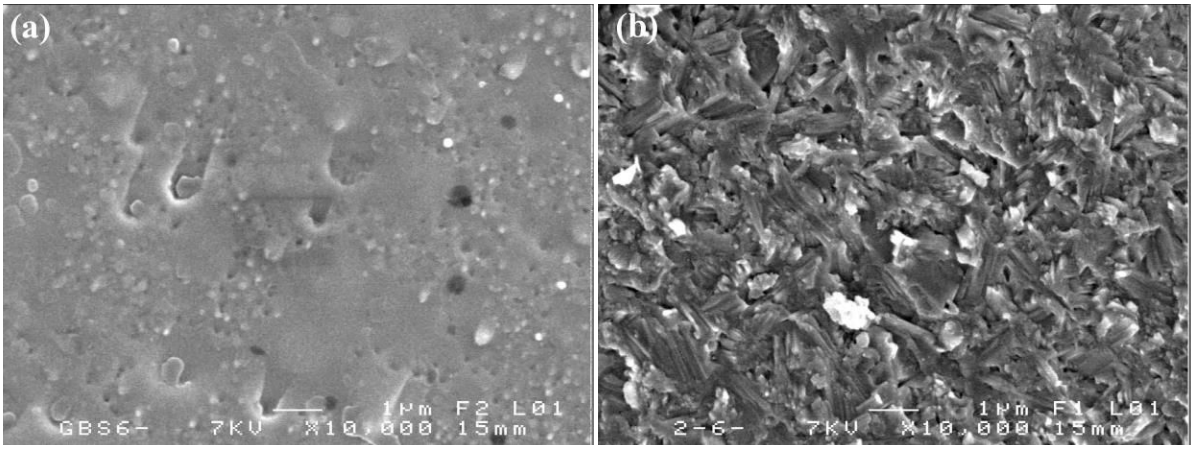

Figure 2-30 SEM images of the different glass ceramics: (a) $56GeSe_2$-$24Sb_2Se_3$-20CuI; (b) $40GeSe_2$-$40Sb_2Se_3$-20CuI

When increasing antimony content in the glass, more and more Sb_2Se_3 crystals are formed in the glass ceramic. It can be seen from Figure 2-30 (b) that the formed Sb_2Se_3 crystals show a rod-like clustered structure, whereas Cu_2GeSe_3 nanocrystals may grow on the Sb_2Se_3

crystals. This composite morphology is further proved by the HRTEM (high resolution transmission electron microscope) images of 40GeSe$_2$-40Sb$_2$Se$_3$-20CuI (as shown in Figure 2-31a). The obtained glass ceramic of 40GeSe$_2$-40Sb$_2$Se$_3$-20CuI contains micrometer-sized crystalline domains. Each domain is composed of rod-like Sb$_2$Se$_3$ crystals whose diameter is 10-30 nm, between them there may exist interconnected nanocrystals of Cu$_2$GeSe$_3$. This unique structure probably provides a conductive channel in the glass ceramic, and therefore leads to the obvious enhancement of conductivity. Moreover, the nano crystal grains of n-type Sb$_2$Se$_3$ and p-type Cu$_2$GeSe$_3$ are found to be contacted each other in the glass ceramic of 40GeSe$_2$-40Sb$_2$Se$_3$-20CuI (Figure 2-31(b)), thereby providing the possibility to form a p-n semiconductor nano-junction, which could greatly promote the separation of photo-generated charge carriers. Therefore, the potential nano-junction may be another reason explaining the strongest photocurrent obtained in glass ceramic of 40GeSe$_2$-40Sb$_2$Se$_3$-20CuI. Based on above analysis, the photocurrent is not only determined by the yield of photo-generated carriers, but also by the separation and transport of these carriers. These factors are determined by the material nature and morphology. The latter may play a decisive role in the generation of photocurrent in glass ceramic.

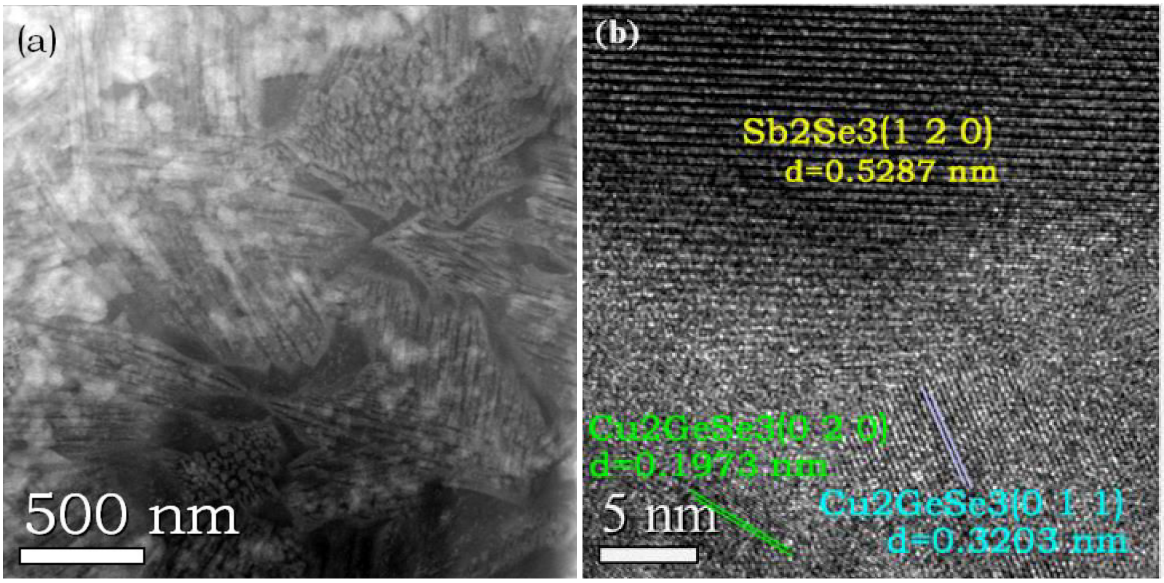

Figure 2-31 HRTEM images of as-prepared glass ceramic of 40GeSe$_2$-40Sb$_2$Se$_3$-20CuI

Furthermore, the addition of CuI also has important effects on the structure and properties of the glass ceramics. As shown in Figure 2-32, in cases of a fixed content of Sb$_2$Se$_3$ (around 40 mol%), the crystalline phases are greatly changed with the increase of CuI content and the decrease of GeSe$_2$. For the base glass of 60GeSe$_2$-40Sb$_2$Se$_3$, the main crystalline phase is Sb$_2$Se$_3$ if we exclude the diffraction peak around 21° as discussed earlier. Meanwhile, a minor shift is observed in the peak positions of Sb_2Se_3 (221), indicating a small change in the lattice parameters. The diffraction angle (2θ) increases slightly from 31.24° to 31.27° due to the increase of rhombohedral unit cell volume (as shown in Figure 2-32b), which is generated by the difference in ionic radius of Ge^{4+} and Sb^{3+} ions [37]. Introducing CuI into the base glass may promote the crystallization of Sb_2Se_3, leading to the increase in diffraction peek intensity of Sb_2Se_3. When further increasing CuI to 20 mol%, the glass system becomes unstable with the formation of Cu_2GeSe_3 crystals. Moreover, the I^{2-} is found to dope the Sb_2Se_3 plane, leading to an obvious shift of diffraction peak (about 0.13°) toward small angle, since the ionic radius of I^{2-} (2.2 Å) is larger than that of Se^{2-} (1.9 Å). However, the excessive CuI (usually up to 30 mol%) may induce the formation of SbSeI crystals. As the energy gap of SbSeI is about 1.7 eV [38], the absorption of sunlight is less efficient than Sb_2Se_3, probably resulting in the decrease of photocurrent. Furthermore, with the doping of I^{2-}, the Sb_2Se_3 is changed from p-type to n-type, so the n-type Sb_2Se_3 can combine with p-type Cu_2GeSe_3, leading to the formation of a p-n junction in the glass ceramic of $40GeSe_2$-$40Sb_2Se_3$-20CuI.

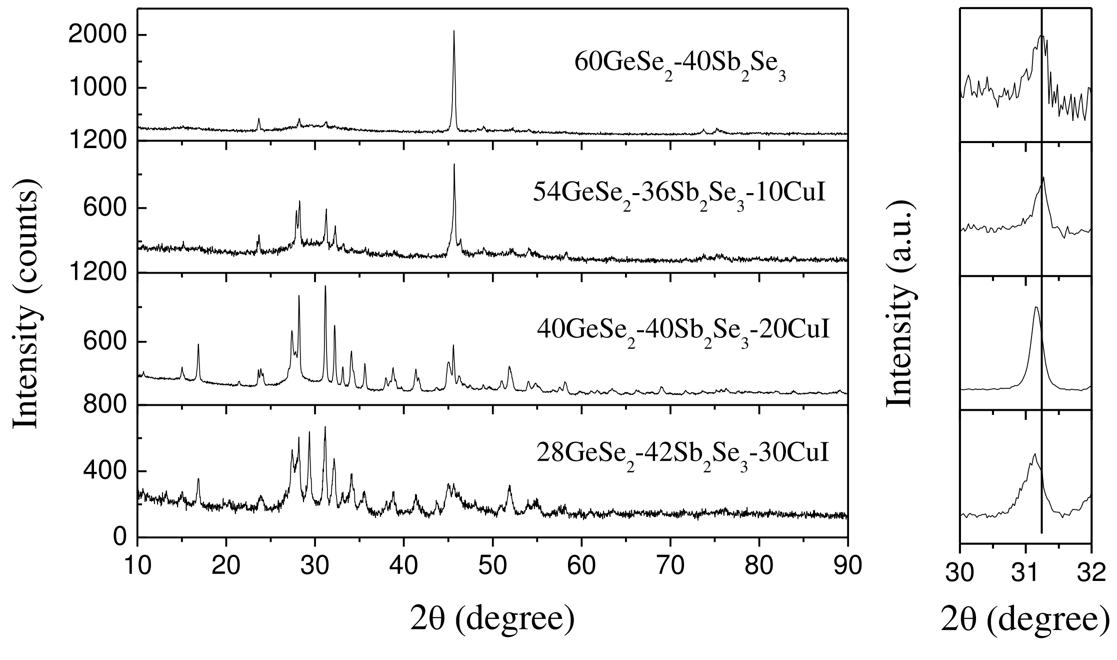

Figure 2-32 XRD patterns of different glass ceramics with various CuI content: (a) 2θ=10°~90°; (b) 2θ=30°~32°

As shown in Figure 2-33, the EDS elemental mapping of $40GeSe_2$-$40Sb_2Se_3$-20CuI glass ceramic reveals that there exist two interconnected regions, including iodine and antimony rich region, as well as germanium and copper rich region, whereas selenium element distributes throughout the sample. The overlap between iodine and antimony further confirms the doping of I^{2-} ions in the lattice of Sb_2Se_3.

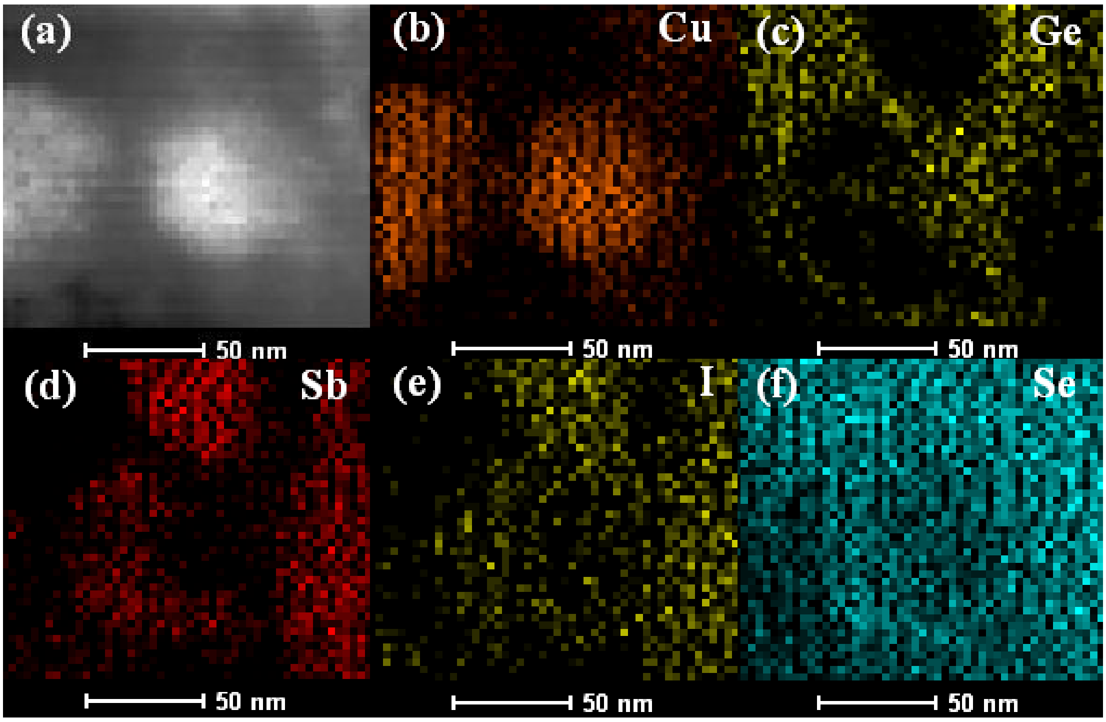

Figure 2-33 STEM images and EDS elemental maps of the glass ceramic

5 Conclusion

This chapter is devoted to a fast screening of glass ceramics in the $GeSe_2$-Sb_2Se_3-CuI system in relationship with the PEC properties. The glass ceramic with the highest photocurrent is obtained by controlling the crystallization of the 40$GeSe_2$-40Sb_2Se_3-20CuI glass. More detailed studies indicate that the photocurrent generated by the glass ceramics is not only determined by the composition, but also by the morphology of the glass ceramic. The obtained 40$GeSe_2$-40Sb_2Se_3-20CuI glass ceramic contains micrometer-sized crystalline domains. Each domain is composed of parallel Sb_2Se_3 rods with a typical diameter around 10-30 nm. On these nano-rods, there exist interconnected nanocrystals of Cu_2GeSe_3. This unique structure probably promotes carrier separation and provides a conductive channel, leading to a high photocurrent intensity in the glass ceramic. The detailed mechanism will be further studied later in this work.

Reference

[1] L. Calvez, P. Lucas, M. Rozé, H.L. Ma, J. Lucas, X.H. Zhang, Influence of gallium and alkali halide addition on the optical and thermo–mechanical properties of $GeSe_2$-Ga_2Se_3 glass, Appl. Phys. A, 89 (2007) 183-188.

[2] L. Calvez, H.L. Ma, J. Lucas, X.H. Zhang, Selenium-based glasses and glass ceramics transmitting light from the visible to the far-iR, Advanced Materials, 19 (2007) 129-132.

[3] L. Calvez, Nouveaux verres et vitrocéramiques transparents dans l'infrarouge pour l'imagerie thermique, PhD thesis, University of rennes 1, 2006.

[4] X. Zhang, M.A. Hongli, J. Lucas, A new class of infrared transmitting glass-ceramics based on controlled nucleation and growth of alkali halide in a sulphide based glass matrix, Journal of Non-Crystalline Solids, 337 (2004) 130-135.

[5] C.F. Bohren, D.R. Huffman, Absorption and scattering of light by small particles, Wiley, 1983.

[6] S. Zhu, H. Ma, L. Calvez, X. Zhang, J. Lucas, J.-L. Adam, H. Shang, T. Rouxel, Optical and mechanical properties of far infrared transmitting glass–ceramics, Journal of Non-Crystalline Solids, 353 (2007) 1298-1301.

[7] A. Chandola, R. Pino, P.S. Dutta, Below bandgap optical absorption in tellurium-doped GaSb, Semiconductor Science and Technology, 20 (2005) 886.

[8] F. Seitz, The modern theory of solids, McGraw-Hill Book Company, Incorporated, New York, 1940.

[9] X. Zhang, L. Calvez, H.L. MA, X. FAN, Y. Xu, A. Lafond, Chalcogenide glass-ceramics with photoelectric properties and method for the manufacture thereof, WO2013190235 A2, Patents, 2013.

[10] Z. Strnad, Glass-ceramic materials: Liquid phase separation, Nucleation and Crystallization in Glass, Glass Science and Technology, New York, 1986.

[11] R. Becker, Die Keimbildung bei der ausscheidung in metallischen mischkristallen, Annalen der Physik, 424 (1938) 128-140.

[12] G. Borelius, Kinetics of precipitation in supercooled solid solutions, Transactions of the American Institute of Mining and Metallurgical Engineers, 191 (1951) 477-484.

[13] R.F. Speyer, Y. Berta, K.-S. Hong, S.H. Risbud, The mechanism of nucleation and growth from $CdGeAs_2$ glass, Journal of Non-Crystalline Solids, 110 (1989) 235-248.

[14] M.M. Kržmanc, U. Došler, D. Suvorov, The nucleation and crystallization of $MgO–B_2O_3–SiO_2$ glass, Journal of the European Ceramic Society, 31 (2011) 2211-2219.

[15] M. Shapaan, E.R. Shaaban, Studying the crystallization behavior of the $Se_{85}S_{10}Sb_5$ chalcogenide semiconducting glass by DSC and X-ray diffraction, Journal of Physics and Chemistry of Solids, 71 (2010) 1301-1305.

[16] P. Dabas, K. Hariharan, Nucleation and crystallization kinetics of rapidly quenched lithium pyrophosphate glass, Solid State Ionics, 243 (2013) 42-49.

[17] A.-M. Hu, K.-M. Liang, M. Li, D.-L. Mao, Effect of nucleation temperatures and time on crystallization behavior and properties of $Li_2O–Al_2O_3–SiO_2$ glasses, Materials Chemistry and Physics, 98 (2006) 430-433.

[18] P. Wang, L. Yu, H. Xiao, Y. Cheng, S. Lian, Influence of nucleation agents on crystallization and machinability of mica glass–ceramics, Ceramics International, 35 (2009) 2633-2638.

[19] http://www.geology.um.maine.edu/geodynamics/microdynamics/ellemodules/nucleation/theory.html.

[20] Y. Ledemi, Verres et vitrocéramiques à base de chalco – halogénures dopés par des ions de terres rares pour la luminescence dans le visible, PhD thesis, University of Rennes 1, 2008, 66-70.

[21] D. Turnbull, J.C. Fisher, Rate of nucleation in condensed systems, The Journal of Chemical Physics, 17 (1949) 71-73.

[22] http://www.just.edu.jo/~aobeidat/PDF/research/Nucleation/Nucleation2.pdf.

[23] F.S. Ham, Diffusion-limited growth of precipitate particles, Journal of Applied Physics, 30 (1959) 1518-1525.

[24] B. Chavillon, Synthèse et caractérisation d'oxydes transparents conducteurs de type p pour application en cellules solaires à colorant, PhD thesis, Univesity of Nantes, 2011, 48-52.

[25] R. Krishnan, Fundamentals of semiconductor electrochemistry and photoelectrochemistry, Encyclopedia of Electrochemistry, Wiley-VCH Verlag GmbH & Co. KGaA, 2007.

[26] D. Wei, G. Amaratunga, Photoelectrochemical cell and its application in optoelectronics, International Journal of Electrochemical science, 2 (2007) 897-912.

[27] http://en.wikipedia.org/wiki/Quantum_efficiency.

[28] M.F. Kotkata, H.T. El-Shair, M.A. Afifi, M.M. Abdel-Aziz, Effect of thallium on the optical properties of amorphous $GeSe_2$ and $GeSe_4$ films, Journal of Physics D: Applied Physics, 27 (1994) 623.

[29] M. Olivier, J.C. Tchahame, P. Němec, M. Chauvet, V. Besse, C. Cassagne, G. Boudebs, G. Renversez, R. Boidin, E. Baudet, V. Nazabal, Structure, nonlinear properties, and photosensitivity of $(GeSe_2)_{100-x}(Sb_2Se_3)_x$ glasses, Optical Materials Express, 4 (2014) 525.

[30] M.A. Villarreal, B.J. Fernández, M. Pirela, A. Velásquez-Velásquez, Electrical properties of the ternary compound Cu_2GeSe_3, Revista Mexicana de Fisica, 53 (2007) 303-306.

[31] http://periodic.lanl.gov/34.shtml.

[32] N.B. Chaure, J. Young, A.P. Samantilleke, I.M. Dharmadasa, Electrodeposition of p–i–n type $CuInSe_2$ multilayers for photovoltaic applications, Solar Energy Materials and Solar Cells, 81 (2004) 125-133.

[33] Y. Zhou, M. Leng, Z. Xia, J. Zhong, H. Song, X. Liu, B. Yang, J. Zhang, J. Chen, K. Zhou, J. Han, Y. Cheng, J. Tang, Solution-processed antimony selenide heterojunction solar cells, Advanced Energy Materials, (2014).

[34] F. Dimroth, High-efficiency solar cells from III-V compound semiconductors, physica status solidi (c), 3 (2006) 373-379.

[35] C.J. Stolle, T.B. Harvey, B.A. Korgel, Nanocrystal photovoltaics: a review of recent progress, Current Opinion in Chemical Engineering, 2 (2013) 160-167.

[36] P.S.L. Narasimham, A. Giridhar, S. Mahadevan, Electrical conductivity studies on families of glasses of the Ge-Sb-Se system, Journal of Non-Crystalline Solids, 43 (1981) 365-378.

[37] S.A. Saleh, Preparation of degenerate n-type $Sb_{65}Ge_xSe_{35-x}$ alloys with a small grain size and their thermoelectric properties, Journal of physics, 2 (2013) 4-11.

[38] J.F. Alward, C.Y. Fong, M. El-Batanouny, F. Wooten, Electronic and optical properties of SbSBr, SbSI and SbSeI, Solid State Communications, 25 (1978) 307-310.

Chapter 3

Optimization of the crystallization process of the $40GeSe_2$-$40Sb_2Se_3$-20CuI glass ceramic

1 Introduction

The properties of glass ceramics are controlled by the composition and microstructure, whereas the microstructure is often responsible for the mechanical and especially many functional properties, such as optical transmission, photoelectricity, photocatalysis etc [1-3]. In the chapter 2, the optimum composition of glass ceramic has been determined after a systematic screening. The highest photocurrent has been obtained with the partially crystallized $40GeSe_2$-$40Sb_2Se_3$-20CuI glass. The main objective of this chapter is to optimize the crystallization process of this selected glass in relation particularly to the microstructure and the photoelectric properties of the obtained glass ceramics.

The crystallization process can determine the microstructure of a glass ceramic. There are two main approaches to get crystals in the base glass [4, 5]. The first one, commonly used for preparing glass ceramics, is to crystallize the base glass by a two-stage heat treatment**.** The first stage is a low-temperature heat treatment at the temperature with a high nucleation rate, leading to the formation of a high density of nuclei in the base glass [6]. A high density of nuclei is favorable for forming a microstructure consisting of a large number of small crystals. The second stage is a higher temperature heat treatment, resulting in the growth of nuclei at a reasonable rate. The second crystallization technique is a single-stage heat treatment. This method is based on the fact that there is generally temperature overlap of the nucleation and crystal growth processes. Heat treatment at one carefully selected temperature may allow the generation of nuclei and crystal growth occur simultaneously [7].

The nucleation and crystal growth phenomena are sensitive to the composition of base glass which can be thermal-dynamically more or less stable [8]. For the glass composition of $40GeSe_2$-$40Sb_2Se_3$-20CuI, it has found that the necessary overlap occurs between the nucleation and growth rate curves, as demonstrated in chapter 2. Therefore, the two types of crystallization process can be used to prepare glass ceramics from this base glass.

In this chapter, the influence of different crystallization processes on the microstructure and properties of as-prepared glass ceramics was investigated. A reproducible process will be proposed to regulate the structure of such glass ceramic material in order to obtain some specific properties.

2 Glass ceramics prepared by a single-stage heat treatment

2.1 Influence of annealing temperature on the microstructure and properties

Figure 3-1 shows the XRD patterns of the prepared glass ceramics of 40$GeSe_2$-40Sb_2Se_3-20CuI with different annealing temperatures. In order to promote the crystallization at lower temperature, the annealing time is extended from 1 h (annealing duration used in the systematic screening described in the previous chapter) to 5 h. It can be seen that no crystal is formed when annealing the sample at 230 °C. With the increase of the annealing temperature, the intensity of diffraction peaks gradually increases, indicating that high temperature favors the crystal growth. However, the annealing temperature has no effect on the crystallized phases and all the samples annealed above 230 °C contain the main crystalline phase of Sb_2Se_3 and a second phase of Cu_2GeSe_3.

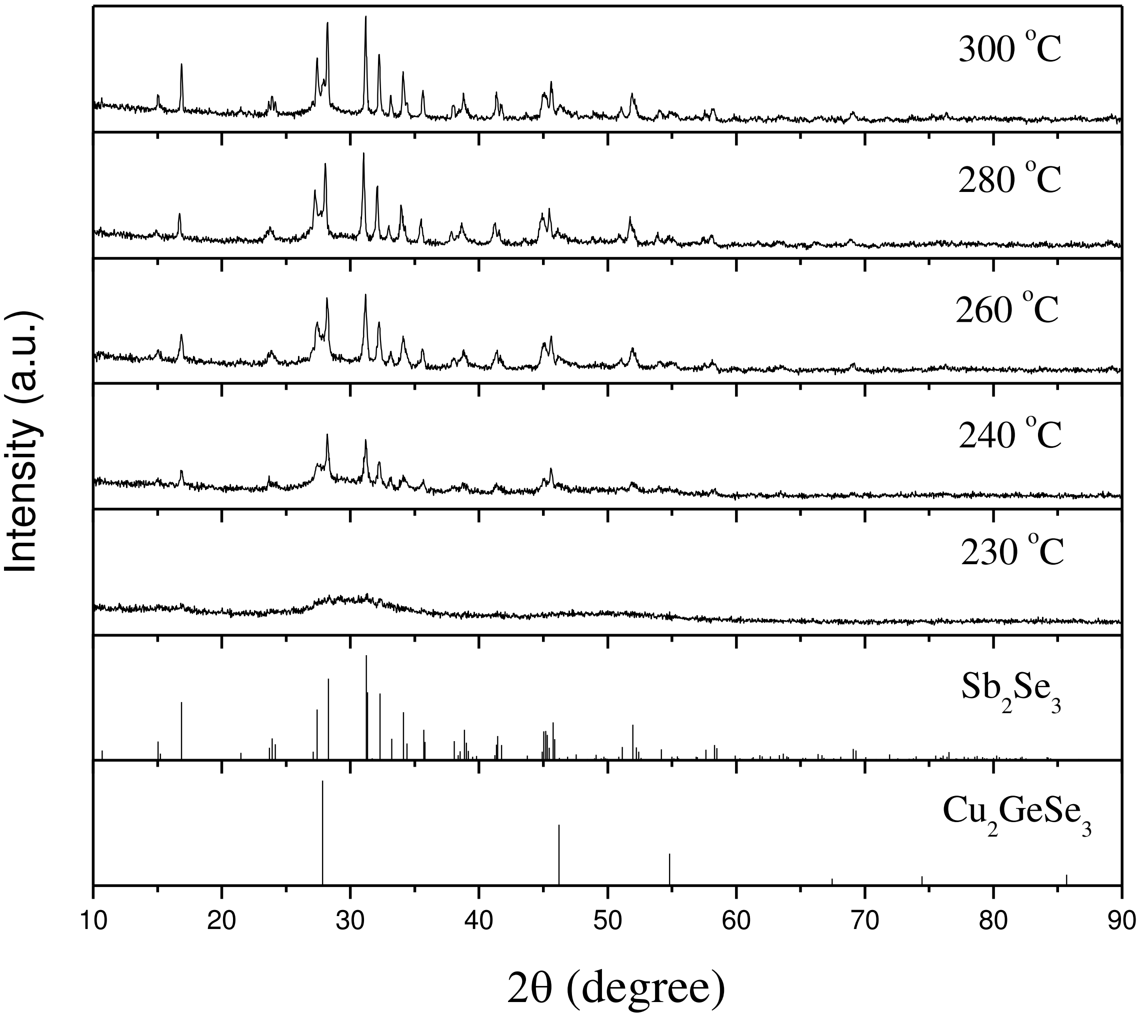

Figure 3-1 XRD patterns of the glass ceramics with different annealing temperature

Figure 3-2 shows SEM images of the glass ceramics prepared at different annealing temperatures. The SEM image of the sample prepared at 230 °C displays a typical morphology of glass, which is consistent with the XRD result. When annealing the base glass at 260 °C for 5h, a large amount of crystals are formed. The particles grow up when further increasing the annealing temperature to 300 °C, leading to bigger crystals. The conductivity of the glass ceramics are shown in Figure 3-3. With the increase of annealing temperature, the conductivity first increases and then decreases. It seems that an excessive annealing temperature is not favorable for the formation of the conductive channels mentioned in the chapter 2.

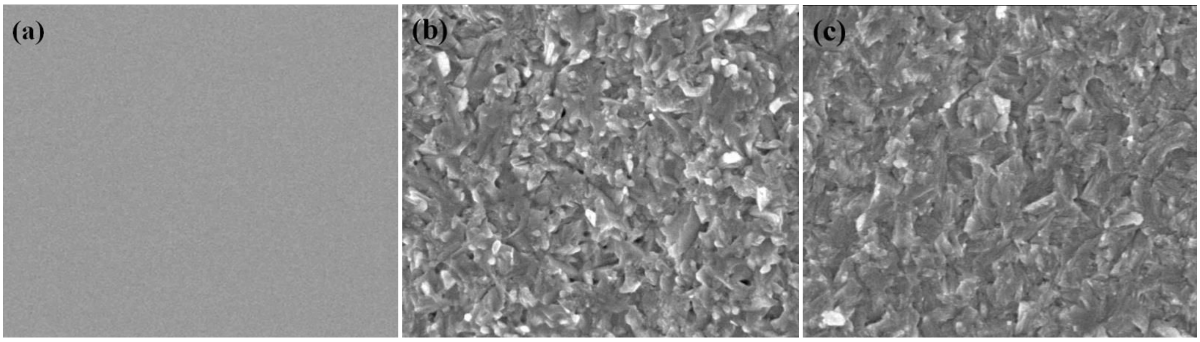

Figure 3-2 SEM images of the glass ceramics obtained with different annealing temperature: (a) 230 °C; (b) 260 °C;(c) 300 °C

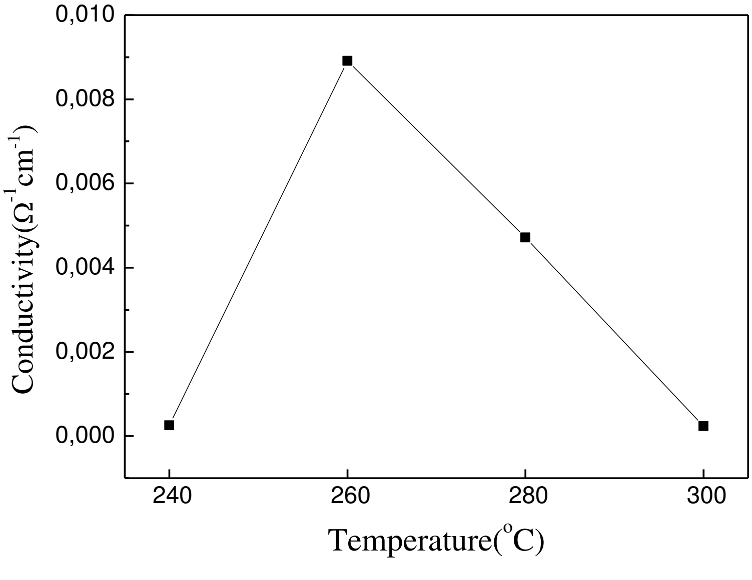

Figure 3-3 Conductivities of the glass ceramics with different annealing temperatures

Figure 3-4 shows the dark and light current-voltage characteristics of the glass ceramics obtained with different annealing temperatures. For the glass ceramic annealed at 240 °C, the photocurrent is very weak. This may be due to its relatively low crystallinity and poor conductivity (as shown in Figure 3-3). When the annealing temperature is increased to 260 °C, the photocurrent is enhanced obviously and reaches -21.27 μA at a bias voltage of -0.5 V. However, with further increasing annealing temperature from 260 °C to 300 °C, the photocurrent and the conductivity significantly decrease. As discussed in chapter 2, the properties of a glass ceramic are highly dependent on its microstructure. The fast growth of crystals at an excessively high temperature is obviously not favorable for building conductive channels inside the glass ceramic. The probable mechanism will be discussed later

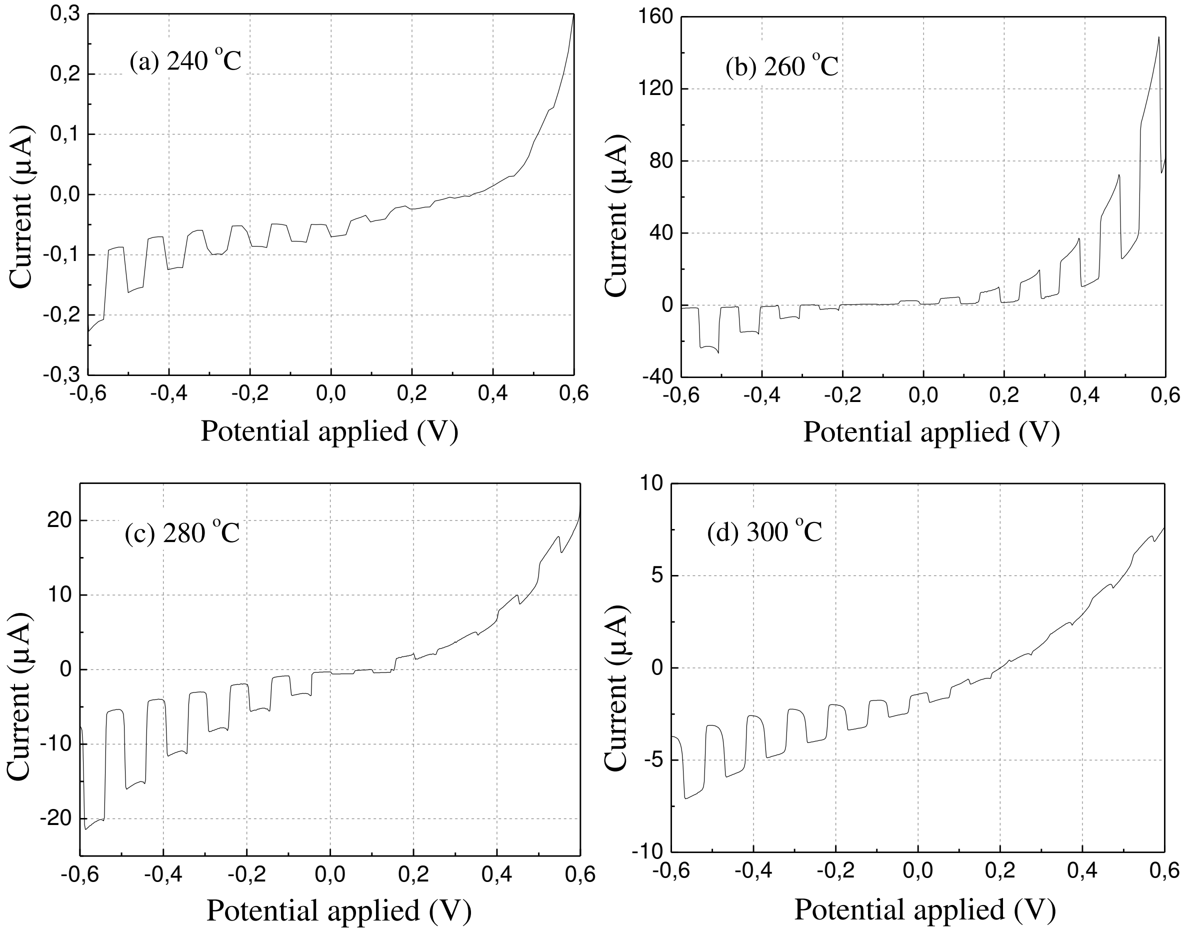

Figure 3-4 Current-voltage characteristics of the glass ceramics with different annealing temperatures under chopped visible light illumination

2.2 Influence of annealing time on the microstructure and properties

Figure 3-5 shows the XRD patterns of the glass ceramics of $40GeSe_2$-$40Sb_2Se_3$-20CuI prepared at 260 °C with different annealing times. The XRD patterns of the samples all display the crystalline diffraction peaks of Sb_2Se_3 and Cu_2GeSe_3 and their intensity increases with the extension of annealing time, indicating that the amount of crystals is increased in the glass ceramics. Moreover, the width of the diffraction peaks gradually decreases with increasing annealing time due to the growth of crystal grains [9].

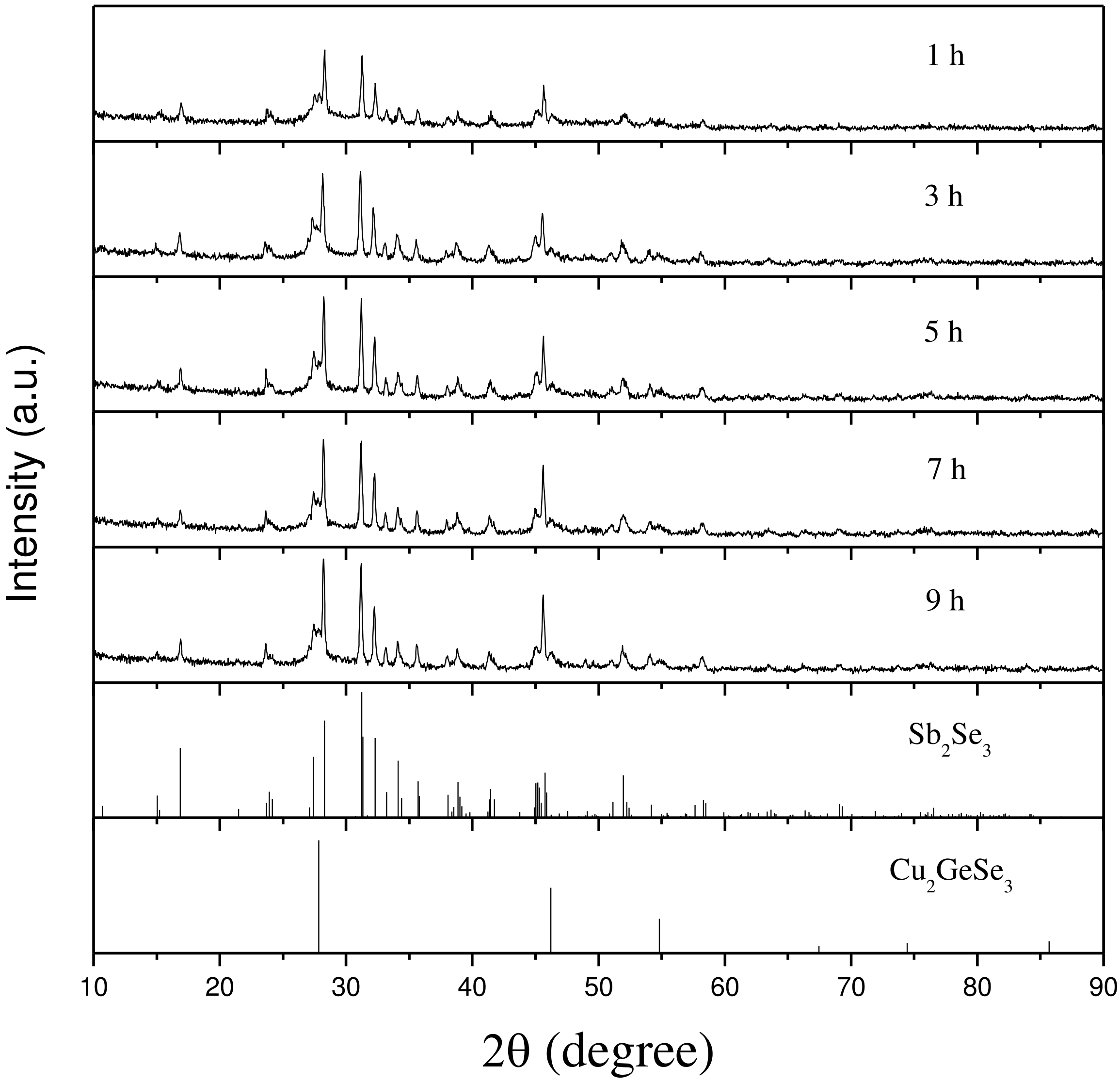

Figure 3-5 XRD patterns of the glass ceramics prepared at 260 °C for different annealing times (The diffraction intensities are normalized)

Figure 3-6 shows the typical SEM images of $40GeSe_2$-$40Sb_2Se_3$-20CuI with different annealing times. It can be seen from the Figure 3-6a that when the base glass is annealed for 1h, many clusters of Cu_2GeSe_3 and Sb_2Se_3 crystal grains are formed and are dispersed in the glass matrix. The conductive crystalline phase is separated by the nonconductive glass phase, leading to the poor conductivity of the glass ceramic. Consequently, the conductivity of this sample is only 3.23×10^{-8} $\Omega^{-1}\cdot cm^{-1}$ (as shown in Figure 3-7). However, when the annealing time is increased to 9h, the cluster of Cu_2GeSe_3 and Sb_2Se_3 crystals connects to each other.

Consequently, the different conductive regions can be interconnected, leading to the formation of the so-called ‘conductive channels’ in the glass ceramic. Actually, when the annealing time is increased to 3h and above, the glass ceramics show similar morphology and have conductivity with the same order of magnitude (10^{-2} $\Omega^{-1}\cdot cm^{-1}$, as shown in Figure 3-7). This morphology increases the conductivity of the glass ceramic, and the sample annealed for 9h obtains much higher conductivity of 2.44×10^{-2} $\Omega^{-1}\cdot cm^{-1}$.

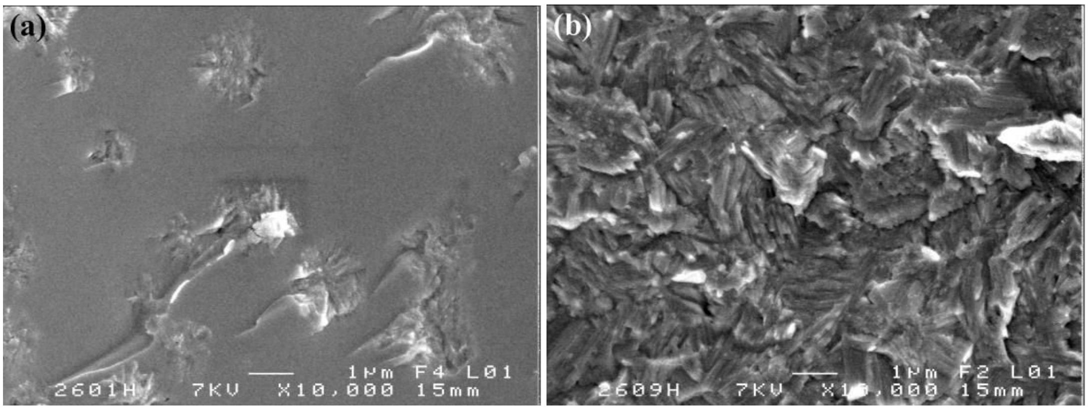

Figure 3-6 SEM images of the glass ceramics with different annealing times: (a) 1h; (b) 9h

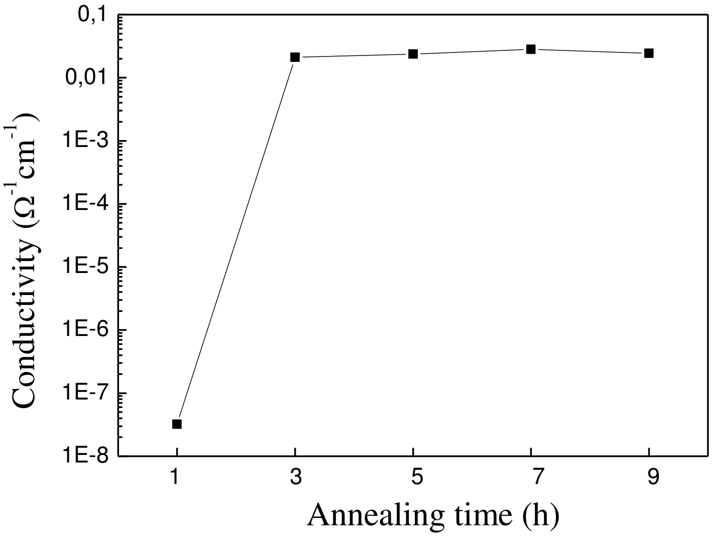

Figure 3-7 Conductivities of the glass ceramics with different annealing times

Figure 3-8 shows the dark and light current-voltage characteristics of the glass ceramics with different annealing times. Since the glass ceramic annealed at 260 °C for 1h shows poor conductivity of 3.23×10^{-8} $\Omega^{-1}\cdot cm^{-1}$, no measurable photocurrent is generated in this sample. When the annealing time is increased to 3h, the photocurrent generated from this sample is about -25.70 µA at a bias voltage of -0.5 V. The photocurrent is changed with further increase of annealing time, but on the whole the samples show good photocurrents from -18.23 µA to -27.65µA. The highest photocurrent is generated from the sample annealed for 9h.

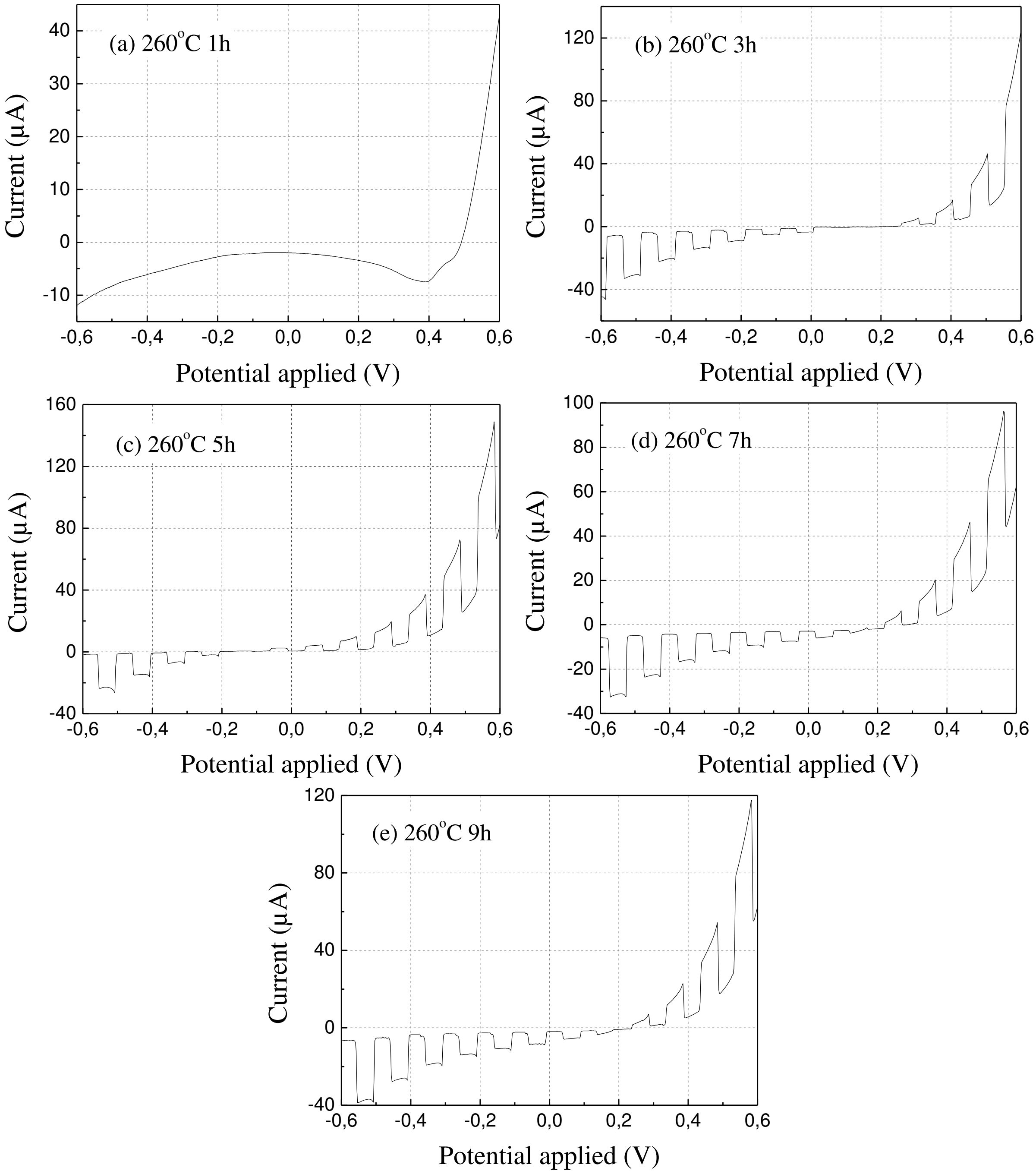

Figure 3-8 Current-voltage characteristics of the glass ceramics with different annealing times under chopped visible light illumination

3 Glass ceramics prepared by a two-step heat treatment

It has been seen that the crystallization process can have a decisive influence on the properties of the glass ceramics. Therefore, we have decided to perform a thermal-dynamic study of the base glass in order to determine the optimum thermal treatment for nucleation and for crystal growth.

3.1 Determination of the nucleation rate

The optimum nucleation temperature is determined for the base glass of $40GeSe_2$-$40Sb_2Se_3$-20CuI by using the following method. The base glass is firstly isothermally nucleated in the 200-250 ^{o}C range and then a normal DSC analysis is performed with the nucleated samples. The nucleation rate is considered as proportional to surface of the crystallization peak. Once the optimum temperature is fixed, the optimum nucleation time can be determined by using the same procedure. The base glass is nucleated at the optimum temperature for different times (10-240 min), followed by a standard DSC analysis.

Figure 3-9 gives the definitions of the parameters used for analyzing the DSC results, including DSC peak temperature (T_p), DSC peak height $(\delta T)_p$, and DSC peak area (integral area). In this study, $(\delta T)_p$ is considered as proportional to the nucleation rate, whereas the crystallization peak area proportional to the density of nuclei formed during the nucleation stage [10].

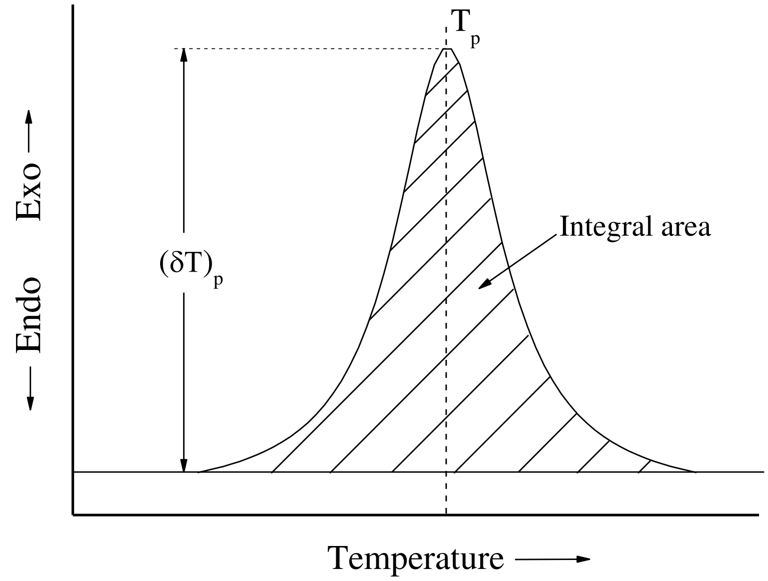

Figure 3-9 Different parameters used for analyzing the DSC measurement

Figure 3-10 shows the DSC curves for the $40GeSe_2$-$40Sb_2Se_3$-20CuI samples with different nucleation temperatures. The initial base glass shows an exothermic crystallization peak with T_p of 304 °C. When nucleating the base glass at 200 °C for 1h, the crystallization peak begins to shift to lower temperature. With further increasing the nucleation temperature to 220 °C, the T_p changes from 302 °C to 294 °C. The decrease in the peak temperature can be used to explain the decrease of glass stability due to the increase of nuclei with the nucleation temperature. At the same time, a small endothermic peak appears at relatively low temperature. When the nucleation temperature is continuously increased from 220 °C to 250 °C, there is no significant shift in the position of the large endothermic peak as the concentration of nuclei may reach saturation [10]. However, the small endothermic peak disappears, indicating that partial crystallization occurs during nucleation process [11]. Combining the results of XRD patterns, shown in Figure 3-11, it can be deduced that the small endothermic peak is associated to the crystallization of the Sb_2Se_3, whereas the large endothermic peak corresponds to Cu_2GeSe_3, another crystalline phase of $40GeSe_2$-$40Sb_2Se_3$-20CuI glass ceramic.

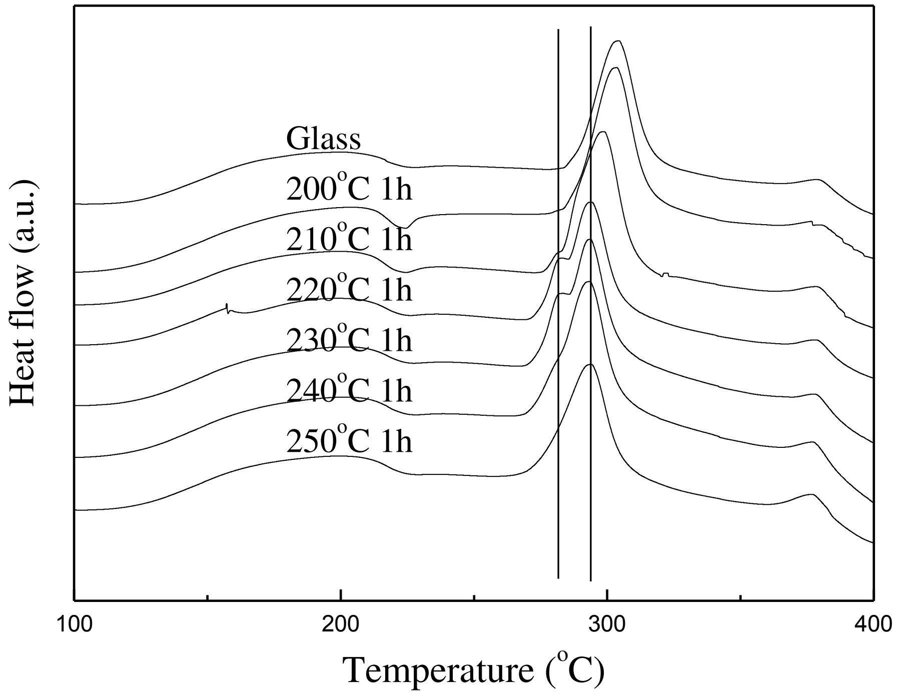

Figure 3-10 DSC curves for the $40GeSe_2$-$40Sb_2Se_3$-20CuI samples nucleated at different temperatures for 1h

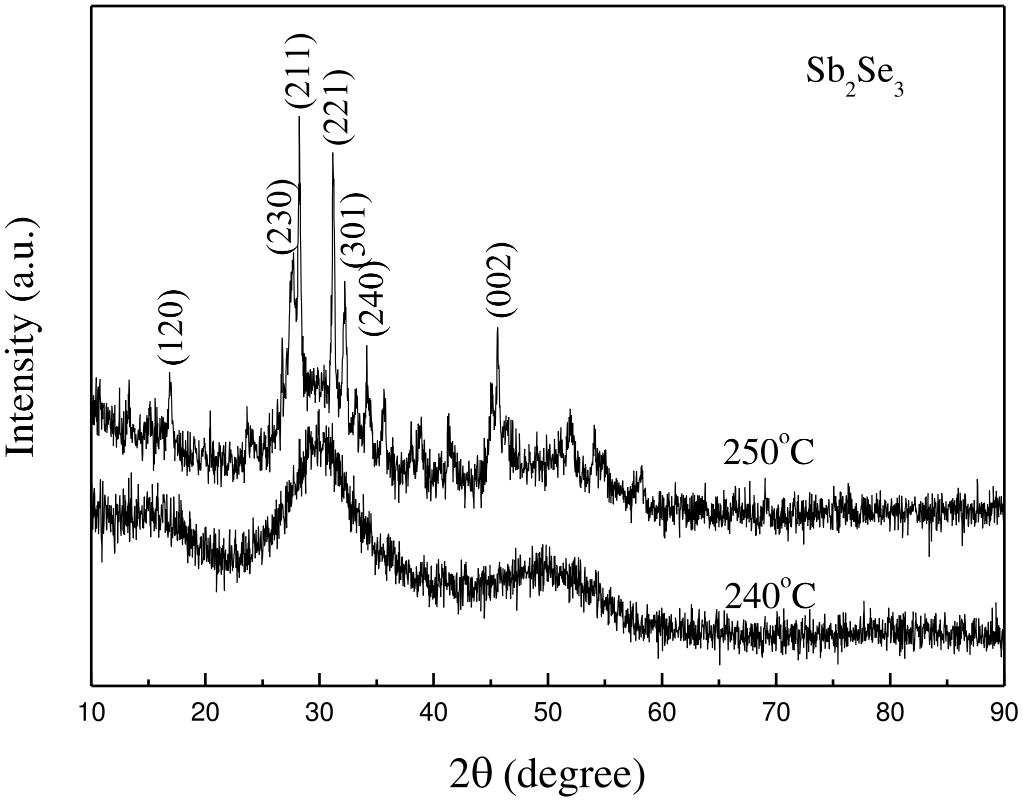

Figure 3-11 XRD patterns of the $40GeSe_2$-$40Sb_2Se_3$-20CuI samples nucleated at 240 °C and 250 °C for 1h

It is clear that the nucleation temperature is critical to the crystallization of Sb_2Se_3. Peak fitting is carried out in order to separate the two exothermic crystallization peaks in DSC curves, associated respectively to the crystallization of Sb_2Se_3 and Cu_2GeSe_3. All the corresponding parameters $(\delta T)_p$, integral area and T_p, are thus obtained. The plot of $(\delta T)_p$ versus the nucleation temperature is shown in Figure 3-12, which is considered important for describing the nucleation and crystallization behavior of a glass. For a given amount of glass nucleated at selected temperatures for a fixed time, the quasi nucleation rate versus temperature curve can be determined by plotting the $(\delta T)_p$ as a function of nucleation temperature [10]. The nucleation temperature of 224±5 °C with the highest nucleation rate can be obtained from the Figure 3-12. The plot of the integral area versus the nucleation temperature is given in Figure 3-13, which follows the same trends as in Figure 3-12. With the increase of nucleation temperature, the integral area first increases and then decreases. It is indicated that the amount of generated Sb_2Se_3 nuclei increases with the nucleation temperature, but decreases due to the crystallization of Sb_2Se_3 at the excessive high nucleation temperatures. Therefore, it is logic to conclude that the most efficient nucleation temperature range is around 225 °C.

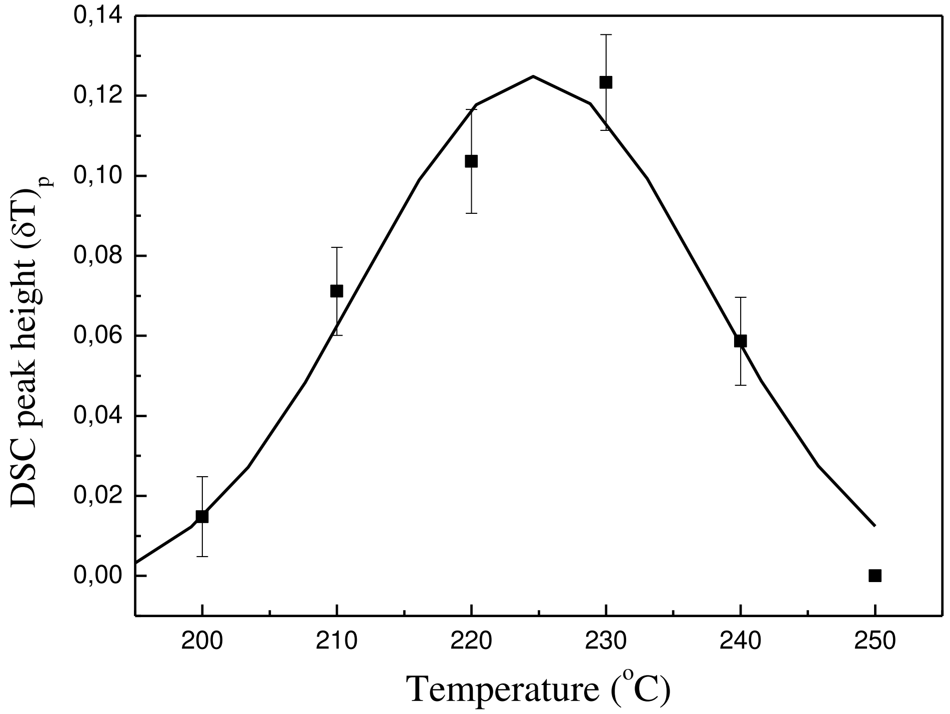

Figure 3-12 Plot of the $(\delta T)_p$ versus the nucleation temperature

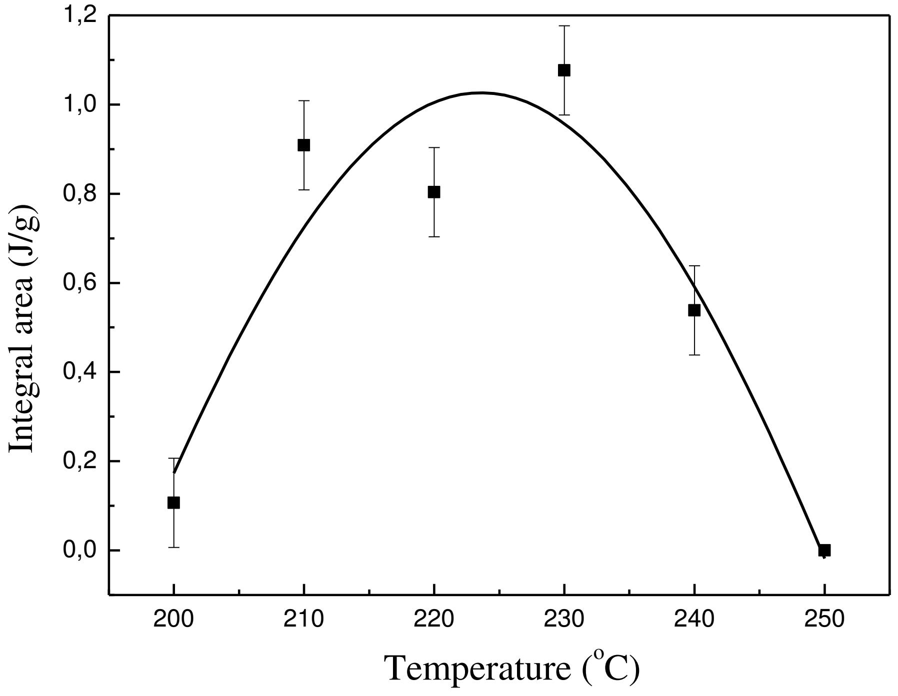

Figure 3-13 Plot of the integral area versus the nucleation temperature

Based on the above analysis, we chose the annealing temperature of 220 ^{o}C, slightly lower than the optimum nucleation temperature to carry out the investigation on the effect of nucleation time. We try to minimize crystallization during the nucleation process. Figure 3-14 shows the DSC curves for the 40$GeSe_2$-40Sb_2Se_3-20CuI samples with different nucleation times. With the increase of nucleation time, the exothermic crystallization peak of Sb_2Se_3 exhibits the similar variation as that shown in Figure 3-10.The crystallization peak position begins to shift to lower temperature after nucleation for 2 h. It was indicated earlier that the partial crystallization of Sb_2Se_3 occurs in the nucleation process at relative high nucleation temperature, leading to the change of crystallization behaviors of Sb_2Se_3 during the DSC measurements. The plot of the integral surface versus the nucleation time is shown in Figure 3-15. It can be seen that the optimum nucleation time is around 100 minutes for generating a high number of Sb_2Se_3 nuclei.

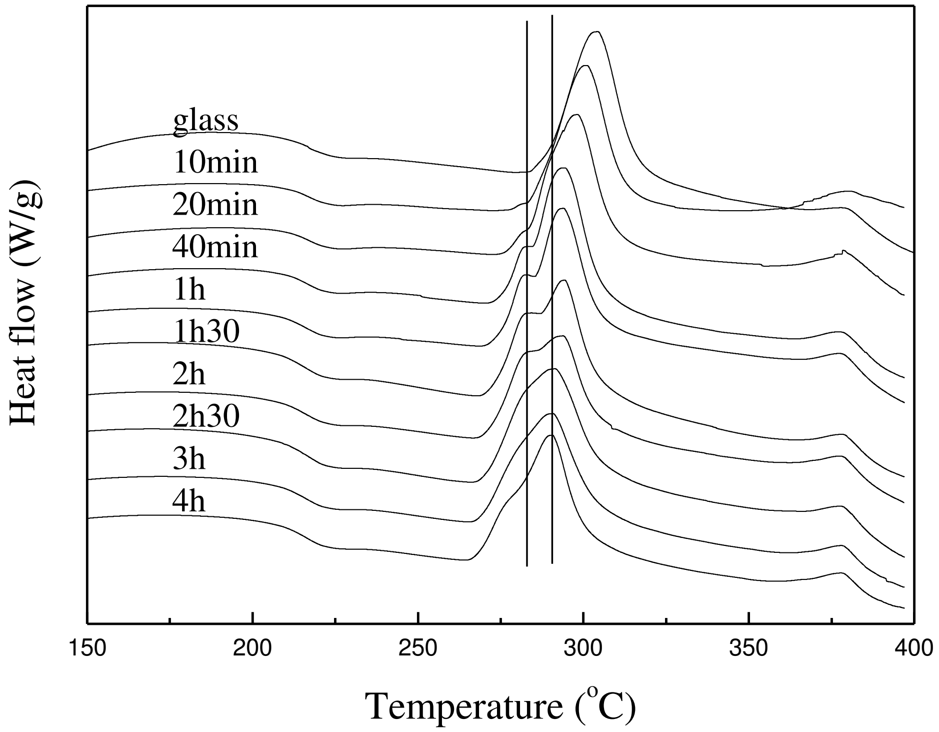

Figure 3-14 DSC curves for the 40$GeSe_2$-40Sb_2Se_3-20CuI samples nucleated at 220 °C for different times

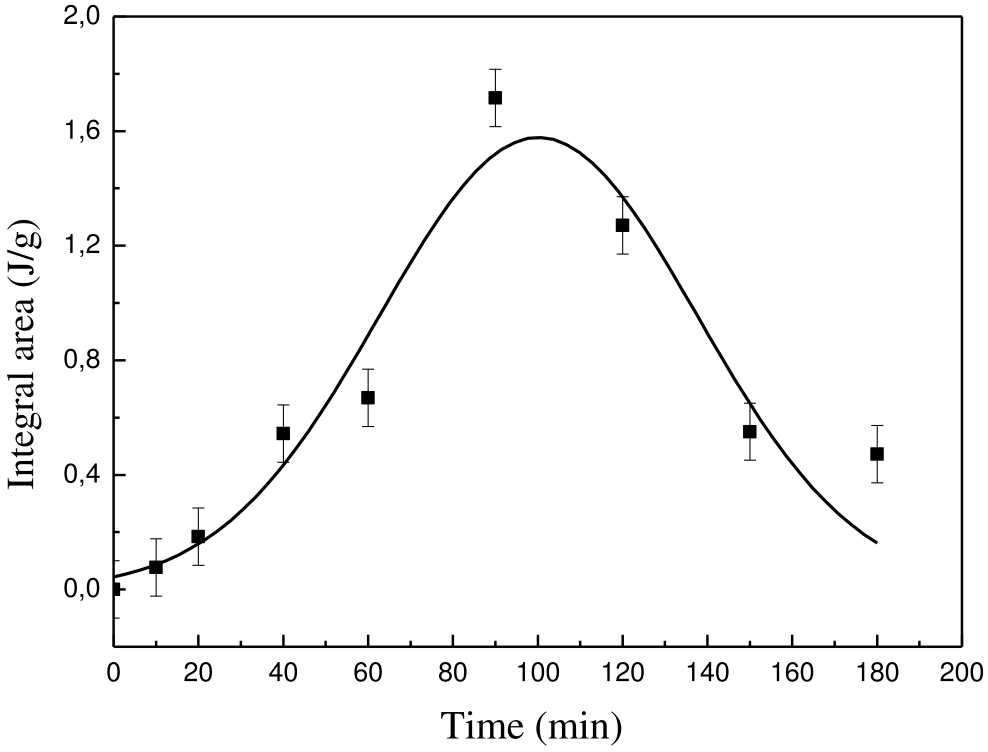

Figure 3-15 Plot of the integral area versus the nucleation time

3.2 Optimization of the crystallization process

3.2.1 Influence of crystallization temperature on the microstructure and properties

In order to determine the optimum crystallization conditions of the glass ceramics, the base glass nucleated under optimum conditions (nucleating at 220 °C for 90 min) is isothermally crystallized in the 270 - 320 °C range. Then, the photoelectric property and the electric conductivity of the as-prepared samples are measured to determine the best crystallization temperature. Subsequently, the pre-nucleated samples are crystallized at the optimum crystallization temperature for different times (0.5 - 4 h), and the optimum crystallization time can also be determined by the results of PEC and conductivity measurements.

Figure 3-16 shows the XRD patterns of different glass ceramics which were prepared at different temperatures. The X-ray diffraction peaks of the samples can be assigned to Sb_2Se_3 and Cu_2GeSe_3, and the intensity of peaks all increase with the crystallization temperature, indicating that the amount and size of crystals are increased in the glass ceramics. The Sb_2Se_3

crystal size is determined by using the Scherrer equation. The results show that the crystal size changes from 31 nm to 41 nm with the increase of crystallization temperature.

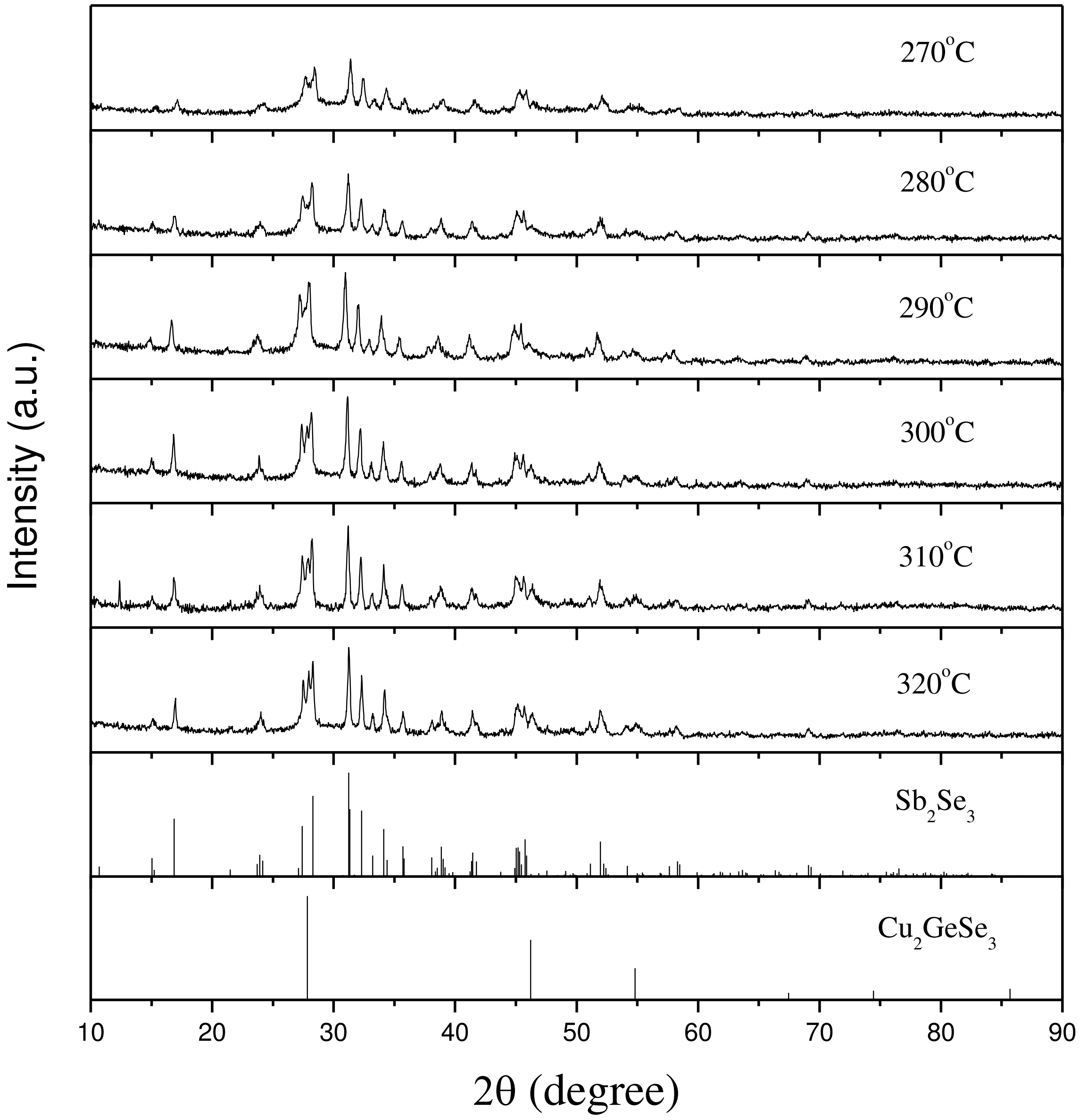

Figure 3-16 XRD patterns of the glass ceramics prepared by crystallizing the pre-nucleated glasses at different temperatures for 1 h

The morphology of different glass ceramics is shown in Figure 3-17. From the SEM images, some rod-like crystals can be found in the sample crystallized at 270 °C, but the contour of crystals is not clear due to the relatively low crystallinity. When increasing the crystallization temperature to 280 °C, the contour of crystal becomes clear and the characteristic clusters of crystals can be distinguished in the SEM image. With the further increase of crystallization temperature, the crystal size increases obviously. Especially for the samples crystallized above 300 °C, some micron-scale particles appear in the sample, corresponding to the large flat surface region in the SEM image. By examining the results of the DSC analysis shown in Figure 3-14, it can be seen that the crystallization temperatures used here are higher than the crystallization temperature determined by the DSC analysis, leading to the significant growth of Sb_2Se_3 and Cu_2GeSe_3.

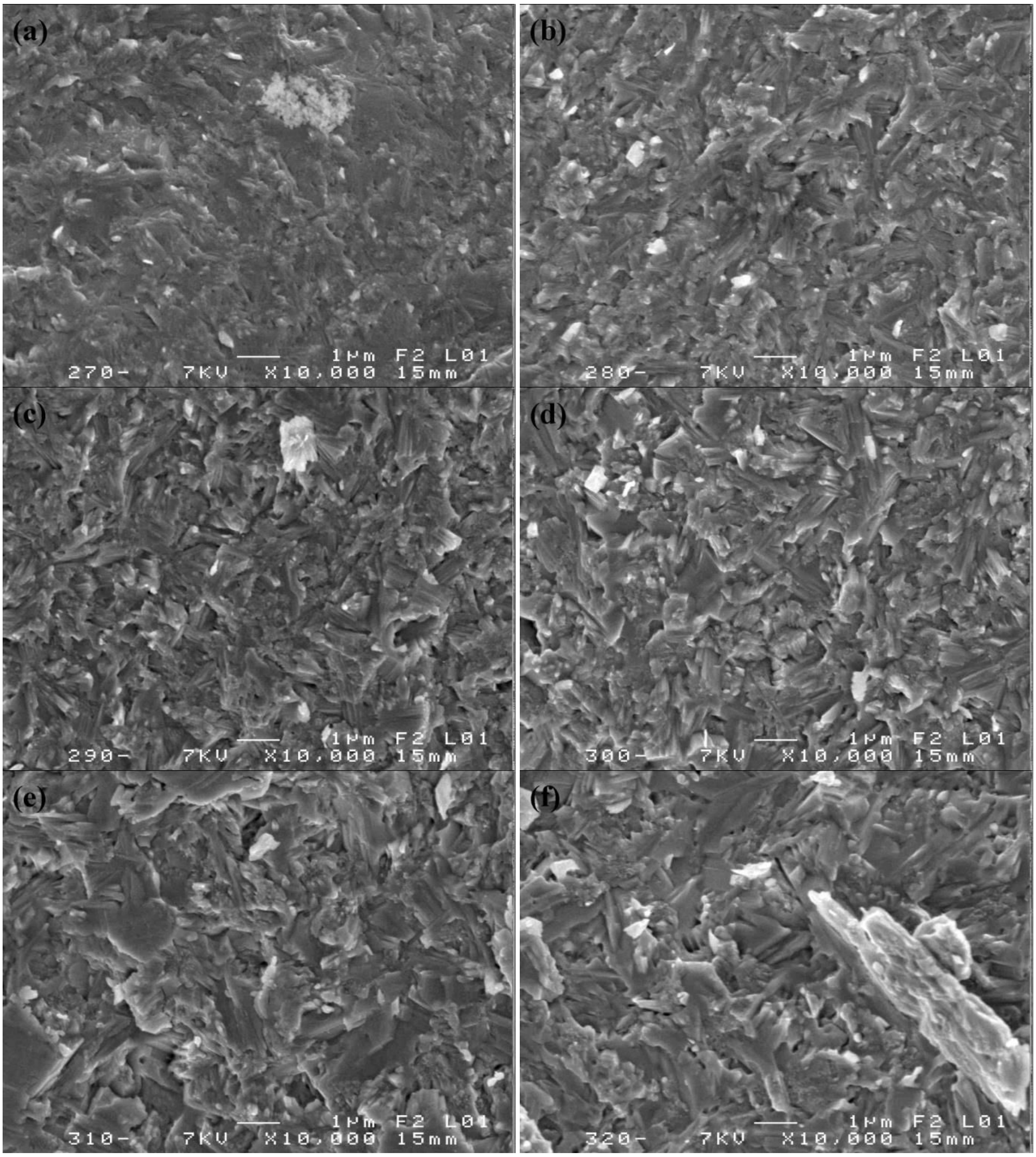

Figure 3-17 SEM images of the cross section of the glass ceramics prepared by crystallizing the pre-nucleated (220 °C for 90 min) glasses at different temperatures for 1 h: (a) 270 °C; (b) 280 °C; (c) 290 °C; (d) 300 °C; (e) 310 °C; (f) 320 °C

Figure 3-18 shows SEM images with higher magnification for two selected glass ceramics. It can be clearly seen that the rod-like clustered structure is formed in the glass ceramics crystallized at 280 ^{o}C, and some Cu_2GeSe_3 particles with size of about 100 nm are observed on the clustered structure. However, for the glass ceramics crystallized at 320 ^{o}C, the rod-like clustered structure disappears and is replaced by the large particles with smooth surface. This means that at this relatively high crystallization temperature, crystal growth of Sb_2Se_3 is promoted, leading to bigger but fewer crystals. At the same time, the crystal growth of Cu_2GeSe_3, with higher crystallization temperature, seems not affected significantly. These conductive crystals are located between the Sb_2Se_3 crystals and not on these crystals. This structure will have important consequence on the electric conductivity of the glass ceramic.

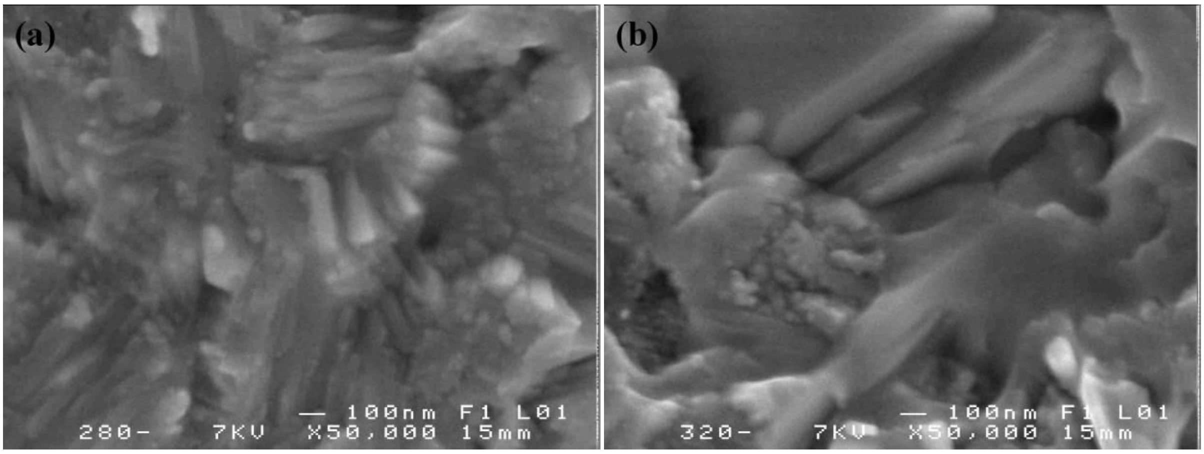

Figure 3-18 High multiple SEM images of the glass ceramics prepared by crystallizing the pre-nucleated glass at different temperature for 1 h: (a) 280 ^{o}C; (b) 320 ^{o}C

Figure 3-19 shows the electric conductivities of the glass ceramics with different crystallization temperatures. With the increase of crystallization temperature, the conductivity first increases and then decreases. Based on the analysis in the chapter 2, we have concluded that the conductivity of the glass ceramics is attributed to the formation of the conductive channels. These conductive channels are fabricated by the micron-scale crystalline domains, consisting of the parallel Sb_2Se_3 nano-rods and the interconnected nano-crystals of Cu_2GeSe_3 on the nano-rods. Therefore, when the crystalline domains tend to be increased with increase of crystallization temperature, the conductivity of the glass ceramics is increased, and the sample prepared at 280 ^{o}C has the highest conductivity of 2.1×10^{-2} $\Omega^{-1}\cdot cm^{-1}$. However, the excessive high crystallization temperature (300 ^{o}C and above) will particularly accelerate the growth of Sb_2Se_3 crystals, as discussed earlier. The Cu_2GeSe_3 crystals cannot follow the growth of Sb_2Se_3. Consequently, the conductive channel cannot be formed in this case, leading to the poor conductivity.

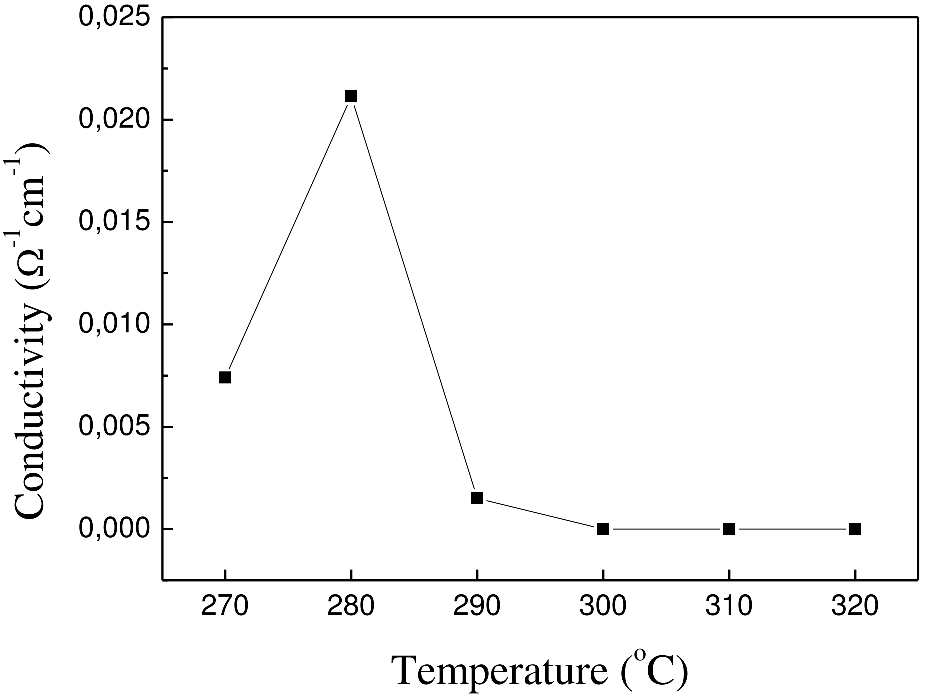

Figure 3-19 Conductivities of the glass ceramics prepared by crystallizing the pre-nucleated glass at different temperatures for 1 h

The photoelectric properties of the glass ceramics shows a similar variation with the conductivity as shown in Figure 3-20. The photocurrent is generated by the transfer of photo-generated carriers, which is determined by the conductivity of glass ceramic. Therefore, there is no photocurrent generation from the sample with poor conductivity. For the sample prepared at 280 °C, the highest photocurrent is achieved, so the optimum crystallization temperature can be determined as 280 °C. However, this photocurrent intensity is much lower than the highest photocurrent intensity of the sample prepared by a single-step heat treatment process discussed above. This is not surprising as we know now that the conductive channels are formed when the two crystals (Sb_2Se_3 and Cu_2GeSe_3) grow together with relatively low rate. This is the case with the one-step heat treatment at relatively low temperatures.

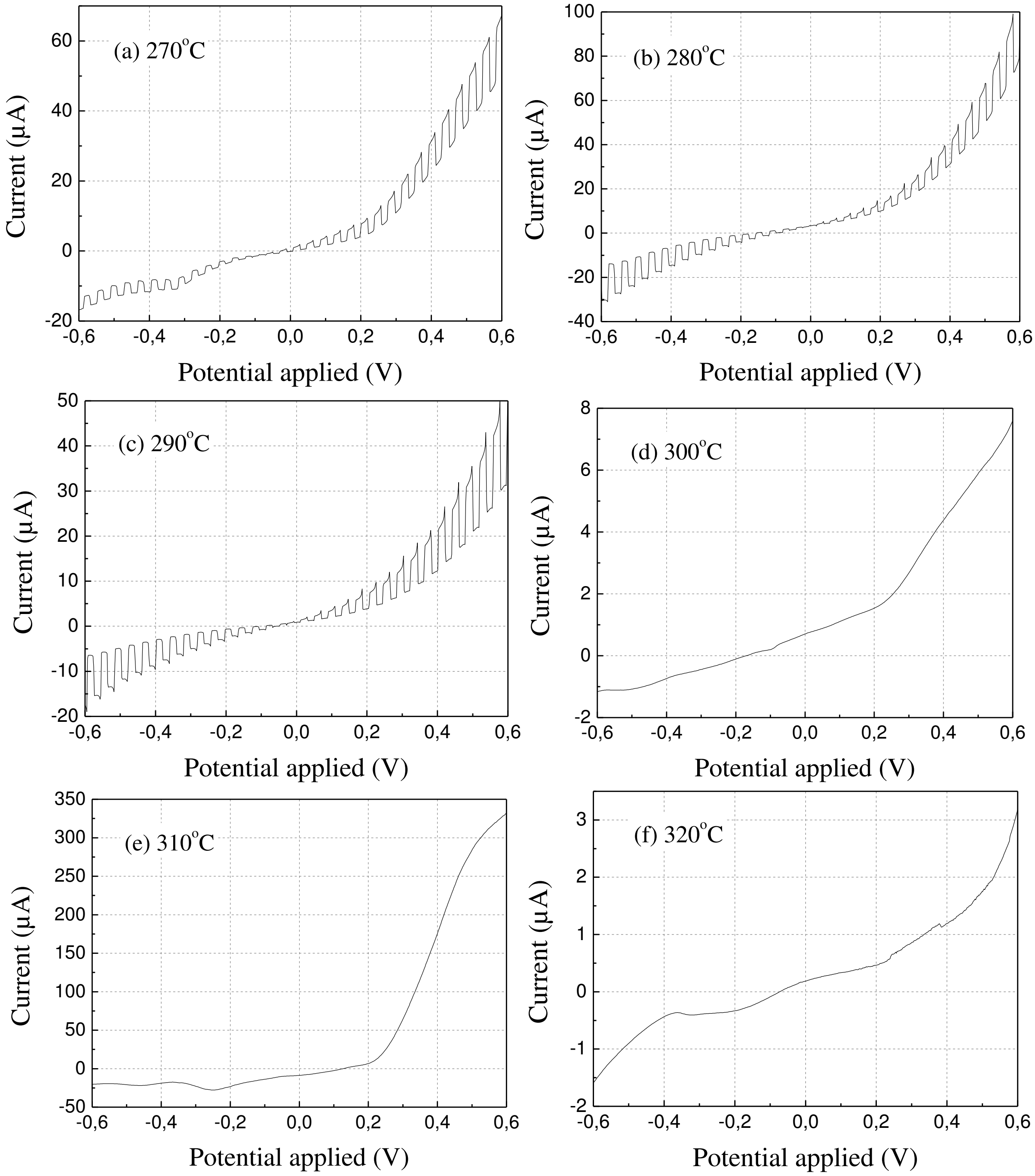

Figure 3-20 Current-voltage characteristics of the glass ceramics with different crystallization temperature under chopped visible light illumination

3.2.2 Influence of crystallization time on the microstructure and properties

Figure 3-21 shows the XRD patterns of the glass ceramics with different crystallization times. It can be seen that all the samples contain two crystallized phases of Cu_2GeSe_3 and Sb_2Se_3. With the increase of the crystallization time, the intensity of the diffraction peaks is enhanced due to the increase of crystal content and size. The Sb_2Se_3 crystal size is determined by using the Scherrer equation and changes from 31nm to 35 nm with the increase of crystallization time.

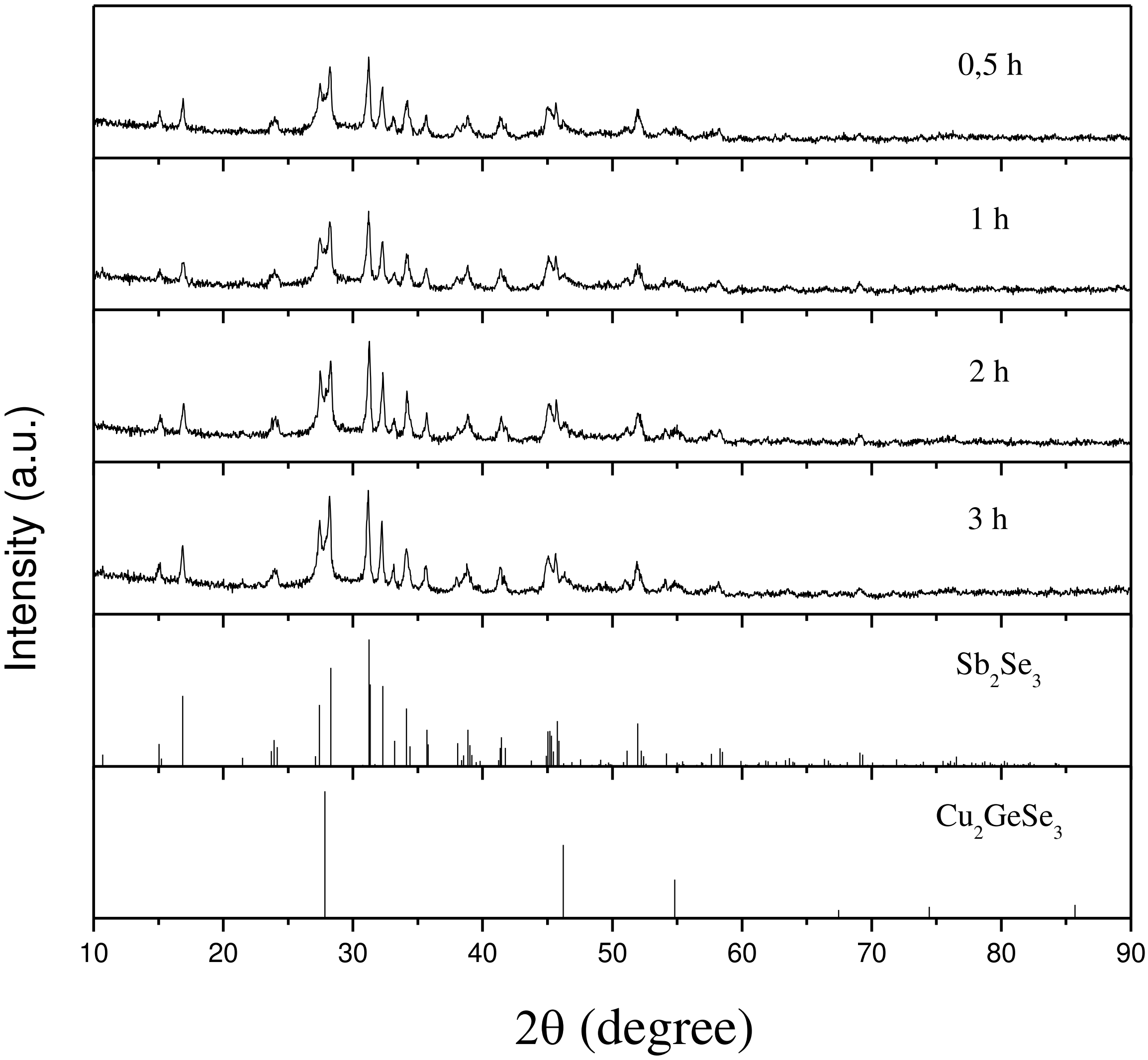

Figure 3-21 XRD patterns of the glass ceramics prepared by crystallizing the prenucleated glass at 280 °C for different time

Unlike the samples prepared at different crystallization temperatures, the samples crystallized at 280 °C for different times maintain the same conductivity of 10^{-2} $\Omega^{-1}\cdot cm^{-1}$. It can be seen from Figure 3-22 that, the photocurrent intensity is increased when increasing crystallization time from 0.5h to 1 h. However, with further extension of crystallization time, the photocurrent intensity is decreased although all the samples have the same conductivity. The difference of photocurrent intensity cannot be attributed here to the difference of conductivity. It is probably associated to the separation efficiency of photo-generated charge carriers due to the increase of particle size [12].

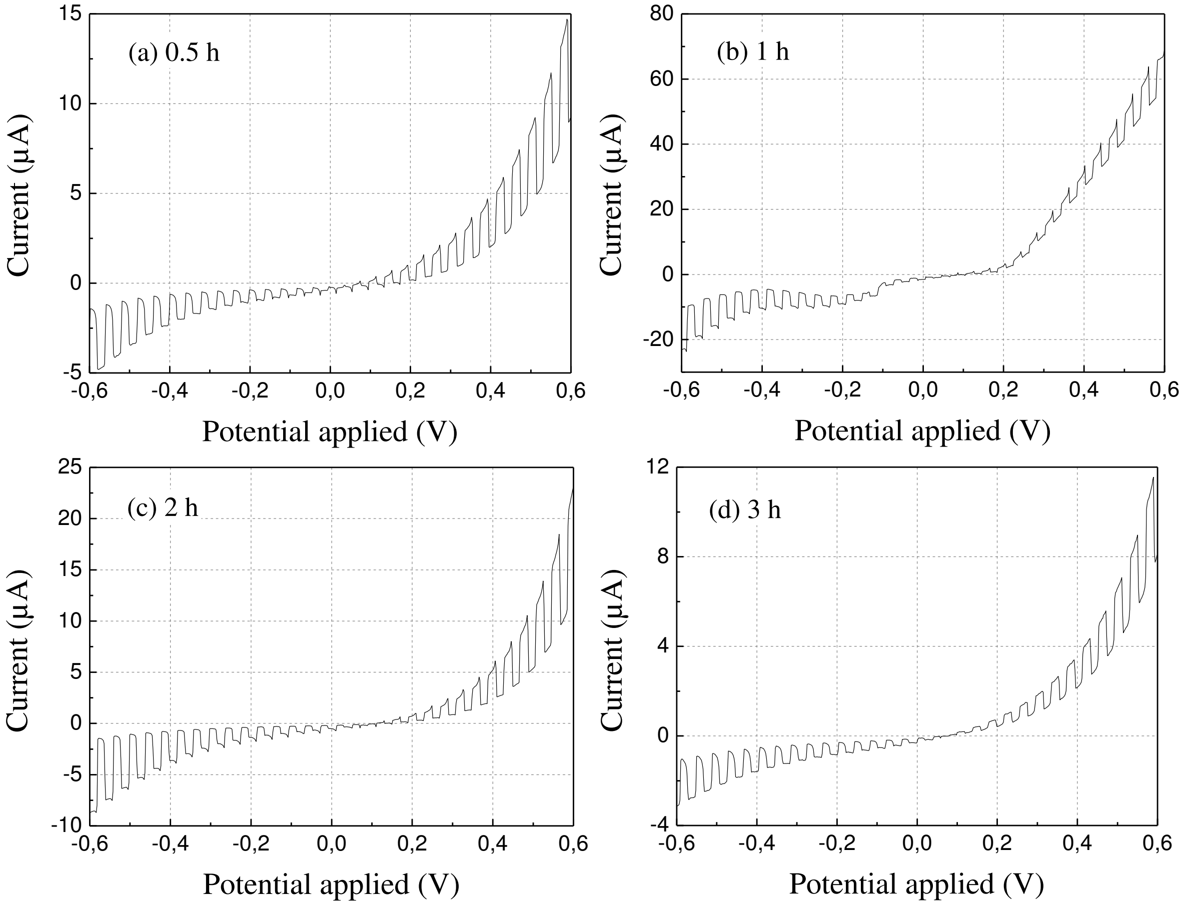

Figure 3-22 Current-voltage characteristics of the glass ceramics with different crystallization time under chopped visible light illumination

3.3 Discussion

Based on these results, it can be concluded that the single-stage heat treatment is more efficient than the two-stage heat treatment for the preparation of glass ceramics with enhanced photoelectric properties. For the base glass with the composition of 40GeSe$_2$-40Sb$_2$Se$_3$-20CuI, the crystallization temperature of Sb$_2$Se$_3$ is lower than that of Cu$_2$GeSe$_3$. According to the DSC analysis, overlap occurs between the crystallization of these two crystals. When the base glass is crystallized at relative low temperature (eg. 260 ^{o}C) by using the process of single-stage heat treatment, the Sb$_2$Se$_3$ will crystallize first, thereby providing the growth sites for Cu$_2$GeSe$_3$ crystals. More importantly, the crystallization temperature used for fabricating the glass ceramic is much lower than the crystallization peak temperature of Cu$_2$GeSe$_3$ on the

DSC curve, leading to low growth rate of Cu_2GeSe_3 crystals. In this case, small Cu_2GeSe_3 crystal grains will grow on the surface of Sb_2Se_3 crystals and connect to each other, resulting in the formation of the characteristic micron-scale crystalline domains with conductive channels. As shown in Figure 3-6, with the increase of crystallization time, these functional domains are interconnected in the whole glass ceramic. The conductivity and the photocurrent intensity are therefore increased.

On the contrary, when crystallizing the base glass through a two-stage heat treatment process, the nucleation stage will significantly decrease the crystallization temperature (as shown in Figure 3-10 and Figure 3-14). For obtaining a high conductivity, it is essential to use a relatively low crystallization temperature (eg. 280 °C) for having comparable crystal growth for Sb_2Se_3 and Cu_2GeSe_3. In this case, the Cu_2GeSe_3 can follow the growth of Sb_2Se_3 to form conductive channels.

It has also been observed that even with comparable electrical conductivity, the best glass ceramic obtained with one-step heat treatment shows much higher photocurrent compared to the best glass ceramic obtained with a two-step thermal treatment (nucleation followed by crystal growth). The possible reason can be the following: with the one-step crystallization process at low temperature (eg. 260 °C), the crystal growth rate is low for both Sb_2Se_3 and Cu_2GeSe_3. These two crystals grow together, forming conductive channels and heterojunctions. The presence of these junctions will be evidenced in the following chapter. These junctions will of course promote charge separation, leading to high photocurrent. With the glass ceramic obtained by using a two-step heat treatment, the pre-nucleation obviously promotes the crystal growth of Sb_2Se_3. Even with a crystal growth at relatively low temperature (eg. 280 °C), it is more difficult for Cu_2GeSe_3 to follow the growth rate of Sb_2Se_3 and to cover the Sb_2Se_3. Conductive channels can be formed with lower density and consequently less heterojunctions, explaining the lower photocurrent intensity.

4 Conclusion

In this chapter, the influence of different crystallization processes on the microstructure and photoelectrical properties of the glass ceramics is investigated. The results show that the crystallization process has a critical influence on the microstructure and the photoelectrical properties of the glass ceramics. The ideal crystallization scenario seems to the following: the

Sb_2Se_3 rods firstly grow in the matrix, followed by the in-situ growth of Cu_2GeSe_3 nanocrystals on the Sb_2Se_3. Compared with the two-step heat treatment process, the single-step process at a low temperature is a more efficient strategy to obtain the rod-like clustered composite structure. It is believed that with crystallization at low temperature, the crystal growth rate is low and comparable for both Sb_2Se_3 and Cu_2GeSe_3. This will facilitate the growth of the conductive and cubic Cu_2GeSe_3 on the needle-like Sb_2Se_3, leading to interconnected conductive channels and heterojunctions which are of course favorable for photo-generated carrier separation. This will be further discussed and evidenced in the following chapter.

Reference

[1] F. Meng, Z. Sun, Enhanced photocatalytic activity of silver nanoparticles modified TiO_2 thin films prepared by RF magnetron sputtering, Materials Chemistry and Physics, 118 (2009) 349-353.

[2] A.E. Shalan, M.M. Rashad, Y. Yu, M. Lira-Cantú, M.S.A. Abdel-Mottaleb, Controlling the microstructure and properties of titania nanopowders for high efficiency dye sensitized solar cells, Electrochimica Acta, 89 (2013) 469-478.

[3] B.C. Liu, C.H. Liu, L.J. Sun, B. Yi, Influence of ZnO microstructure variation on its photo electricity characteristics, Chinese Journal of Luminescence, 2 (2010) 013.

[4] Z. Strnad, Glass-ceramic materials: Liquid phase separation, Nucleation and crystallization in glass, Glass Science and Technology, New York, 1986.

[5] R.D. Rawlings, J.P. Wu, A.R. Boccaccini, Glass-ceramics: Their production from wastes—A review, Journal of Material Science, 41 (2006) 733-761.

[6] K.F. Kelton, Transient nucleation in glasses, Materials Science and Engineering: B, 32 (1995) 145-151.

[7] P. Gabbott, Principles and applications of thermal analysis, John Wiley & Sons, 2008.

[8] V.M. Fokin, O.V. Potapov, C.R. Chinaglia, E.D. Zanotto, The effect of pre-existing crystals on the crystallization kinetics of a soda–lime-silica glass. The courtyard phenomenon, Journal of Non-Crystalline Solids, 258 (1999) 180-186.

[9] G. Sanon, R. Rup, A. Mansingh, Growth and characterization of tin oxide films prepared by chemical vapour deposition, Thin Solid Films, 190 (1989) 287-301.

[10] C. Ray, D. Day, W. Huang, K. Lakshmi Narayan, T. Cull, K. Kelton, Non-isothermal calorimetric studies of the crystallization of lithium disilicate glass, Journal of non-crystalline solids, 204 (1996) 1-12.

[11] L. Calvez, Nouveaux verres et vitrocéramiques transparents dans l'infrarouge pour l'imagerie thermique, PhD thesis, University of Rennes 1, 2006.

[12] L.Q. Jing, X.J. Sun, J. Shang, W.M. Cai, Z.L. Xu, Y.G. Du, H.G. Fu, Review of surface photovoltage spectra of nano-sized semiconductor and its applications in heterogeneous photocatalysis, Solar Energy Materials and Solar Cells, 79 (2003) 133-151.

Chapter 4

Microstructure and semiconducting properties of the $40GeSe_2$-$40Sb_2Se_3$-$20CuI$ glass ceramic

1 Introduction

Charge photogeneration, dissociation and transport to external collectors are the key steps for efficient conversion of solar energy via photovoltaic effect or via photocatalytic production of chemical fuels. One single material cannot be optimum for all the three tasks. Organic solar cells have attracted much attention because of the low cost, flexibility and ease of processing. The introduction of internal donor-acceptor heterojunctions was a key breakthrough for improving the efficiency of polymer photovoltaic solar cells [1, 2]. The principle was to attribute one specific function (charge photogeneration or charge diffusion) to different molecules in order to overcome the mismatch between the exciton diffusion length (around 10 nm) and the optical absorption depth (more than 100 nm). In this way, each molecule can be optimized for a dedicated function [3, 4]. With the creation of an interpenetrating network, the carrier collection efficiency is improved by two orders of magnitude in comparison with bi-layer flat heterojunction devices [5-7]. Recently, semiconductor photocatalysts have attracted considerable attention for potential application in photocatalytic degradation of organic pollutents or water splitting [8]. Heterojunction structure has been extensively studied because of its efficiency for promoting separation of photogenerated charges [9-13].

Based on the studies described in previous chapters, we have tried to develop a new strategy for preparing an efficient interpenetrating inorganic heterojunction structure with two relatively narrow bandgap semiconductors, Sb_2Se_3 and Cu_2GeSe_3. These two crystals have complementary direct bandgap with, 1.0–1.2 eV for Sb_2Se_3 [9, 14] and 0.78 eV for Cu_2GeSe_3 [15], allowing efficient harvesting of solar energy from UV up to 1600 nm. Sb_2Se_3 has a high absorption coefficient of 10^5 cm^{-1} and is considered as a promising semiconductor for building heterojunctions to potentially achieve high energy conversion efficiency [16]. It has recently attracted more and more attention [17, 18], but its low conductivity of 10^{-6} $\Omega^{-1}\cdot cm^{-1}$ [19] is certainly a big issue for charge transport which can be ensured by the Cu_2GeSe_3 phase with a conductivity of 10^1 $\Omega^{-1}\cdot cm^{-1}$ [20]. The structure of Sb_2Se_3 is orthorhombic with cell parameters a=1.113 nm, b=1.142 nm and c=0.385 nm. It grows typically as rod-like crystals which can be easily interconnected [21]. This may be an important feature for building up an interconnected network. Whereas the structure of Cu_2GeSe_3 seems more diversified as cubic (a=0.555 nm), tetragonal (a=0.560 nm, b=0.548 nm) and orthorhombic (a=1.186 nm, b=0.396

nm and c=0.546 nm) phases are both reported [22, 23]. With our experimental conditions, only cubic phase was precipitated.

In this chapter, a detailed study on the microstructure and properties of the photoelectric glass ceramic will be carried out and the mechanism of charge photogeneration, separation and transport will also be discussed. All the studies will be performed on the $40GeSe_2$-$40Sb_2Se_3$-20CuI glass ceramic, obtained by annealing the precursor glass at 284 °C during 1 hour, except elsewhere specified.

2 Microstructure of the $40GeSe_2$-$40Sb_2Se_3$-20CuI glass ceramics

2.1 TEM and EDS analysis

Figure 4-1 shows the nanostructure and composition mapping of the glass ceramic. It can be seen from Figure 4-1(b) that the glass ceramic exhibits the characteristic rod-like clustered structure, which is in agreement with the SEM images discussed in the previous chapter. At the edge of the rod, nano p-n junctions between n-type Sb_2Se_3 and p-type Cu_2GeSe_3 crystals are formed [15, 24], as shown in Figure 4-1(a). Figure 4-1(c) shows the cross section of the rod-like clustered structure. It can be clearly seen from the EDS elemental mappings that antimony element is mainly enriched in the “light color” region, corresponding to Sb_2Se_3 phase, whereas copper and germanium elements mainly coexist in the “deep color” region, corresponding to Cu_2GeSe_3. The similar phenomenon is also observed in the EDS elemental maps of vertical section (as shown in Figure 4-1(d)). The results indicate that the Cu_2GeSe_3 nanocrystals grow on the surface of Sb_2Se_3 rods, and mainly connect to each other along the rod orientation, leading to the formation of such crystalline domains. Each domain is composed of the rod-like Sb_2Se_3 crystals and the interconnected Cu_2GeSe_3 nanocrystals exist between the rods (as shown in Figure 4-2). The oriented and relatively conductive Cu_2GeSe_3 aggregate provides a conductive microdomain for the glass ceramic.

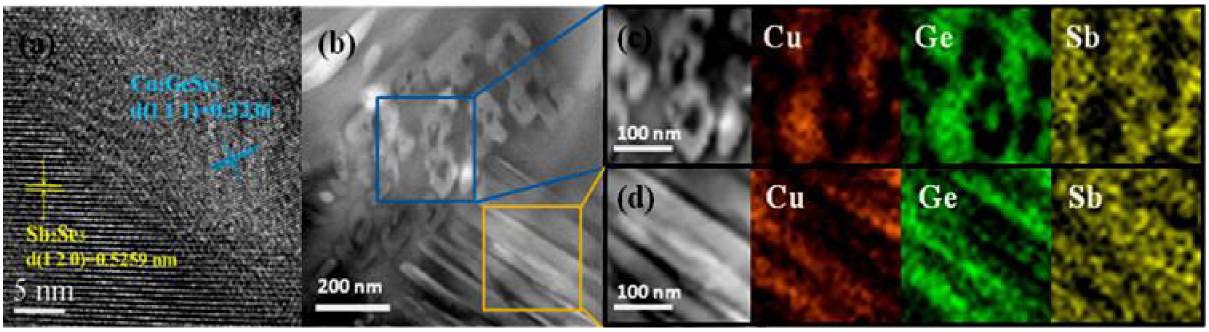

Figure 4-1 HRTEM and STEM images and EDS elemental maps of the glass ceramic

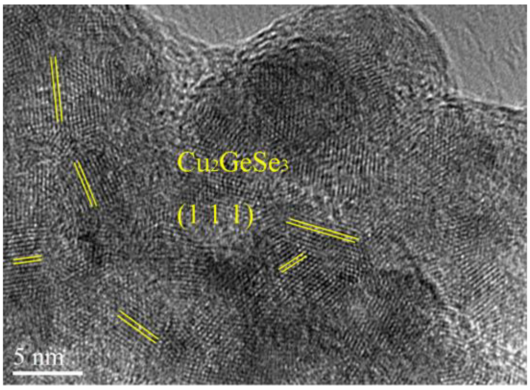

Figure 4-2 HRTEM image of Cu_2GeSe_3 nanocrystals in the glass ceramic

2.2 SEM analysis

However, the conductivity of the glass ceramics is determined not only by the formation of the conductive microdomain but also by the interconnection of these conductive microdomains at macroscopic scale. Actually, there exist three typical composite morphologies (as shown in Figure 4-3). In the first case (Figure 4-3(a)), the base glass is crystallized incompletely, and the conductive microdomain is therefore separated by the nonconductive glass phase, leading to the poor conductivity of the glass ceramic. In the second case (Figure 4-3(b)), the Sb_2Se_3 crystals grow up excessively and interconnect, resulting in the separation of the conductive microdomains as well as the corresponding poor conductivity. In the last case (Figure 4-3(c)), the conductive microdomains can interconnect well and form conductive region. It is easy to image that the conductive channels inside the glass ceramic are formed by a non (or poorly)-conductive Sb_2Se_3 network, covered by a conductive Cu_2GeSe_2 layer. Consequently, the glass ceramics with the third kind of morphology achieve relatively high conductivity.

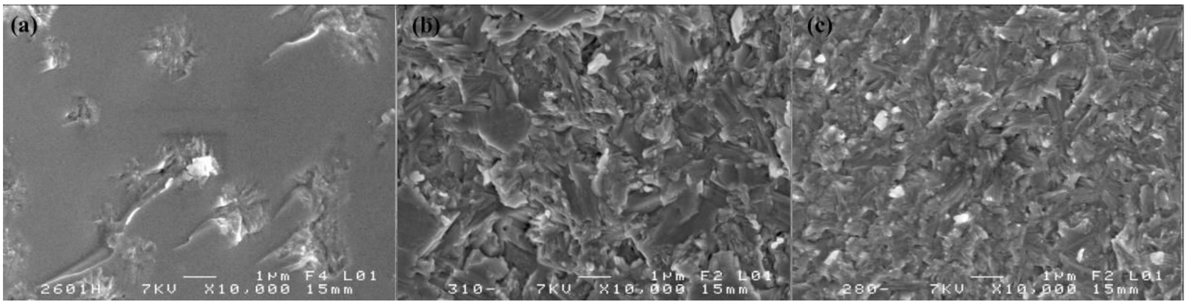

Figure 4-3 SEM images of typical morphology of the glass ceramics with different conductivities (a) 3.2×10^{-8} $\Omega^{-1}\cdot cm^{-1}$; (b) $<10^{-8}$ $\Omega^{-1}\cdot cm^{-1}$; (c) 2.1×10^{-2} $\Omega^{-1}\cdot cm^{-1}$

2.3 AFM analysis

The atomic force microscope (AFM) is one kind of scanning probe microscopes (SPM). Unlike traditional microscopes, the AFM does not rely on electromagnetic radiation, such as photon or electron beams, to create an image. An AFM is a mechanical imaging instrument that measures the three dimensional topography and physical properties of a surface [25].

2.3.1 Basic principles and presentation of the equipment

As shown in Figure 4-4, the AFM consists of a cantilever with a sharp probe at its end that is used to scan the specimen surface. When the tip of the probe is brought close to a sample surface, forces between the tip and the sample lead to a deflection of the cantilever, according to Hooke’s law [26]. Typically, the deflection is measured using a laser spot reflected from the top surface of the cantilever into an array of photodiodes. If the tip is scanned at a constant height, a risk would exist that the tip collides with the surface, causing damage. Hence, in most cases, a feedback mechanism is employed to adjust the tip-to-sample distance to maintain a constant force between the tip and sample.

The AFM can be operated in number of modes depending on the application. In our experiments, semi-contact mode (tapping mode) was chosen to scan the surface potential.

The surface potential mapping is carried out by scanning Kelvin probe microscope (SKM) which is integrated in an AFM system NTEGRA Prima (NT-MDT Company). Pt/Ir-coated silicon probes NSG01/Pt (NT-MDT Company) are used for these measurements.

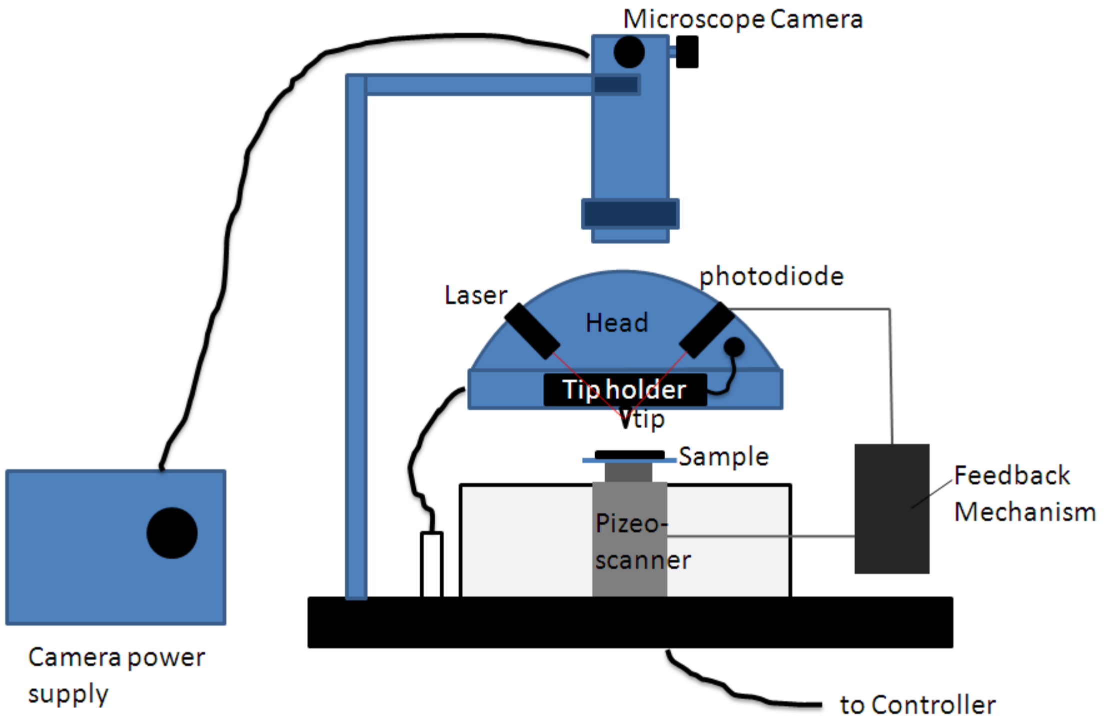

2 kind of camera: resolution 10 µm (standard), resolution 1 µm
2 kind of Head: AFM head, STM head
2 kind of tip holder: SKM (Scanning Kelvin-probe, bias voltage), SSRM (Scanning Spreading Resistance, ground)

Figure 4-4 Schematic presentation of atomic force microscope (AFM)

To obtain a surface potential image, the specimen is first scanned in tapping mode to determine the surface topography. During this scan, no external voltage is applied to the tip to make Van der Waal's force the most important factor. Using the built-in lift-mode feature of the AFM, potential scan line was retraced at a set lift height from the sample. It is important to choose a lift height where the cantilever can oscillate freely during the lifting cycle. Otherwise topography features will contribute to the surface potential image [27]. A 15 nm lift height was used in our experiment to prevent topographic cross talk. The scan frequency was 1 Hz, i.e. the acquisition time of a 256 x 256 pixel image was 8 min.

2.3.2 AFM surface potential

The influence of composite morphology on the conductivity of the glass ceramics can be further revealed by the AFM surface potential measurement. In our previous studies, we have found that the surface potential of the sample is decreased after crystallization, and the as-prepared glass ceramic achieves a relatively high conductivity at the same time (as shown in

Figure 4-5). Therefore, it can be deduced that the conductive region has lower surface potential than the non (or poorly)-conductive region in the same image for this system.

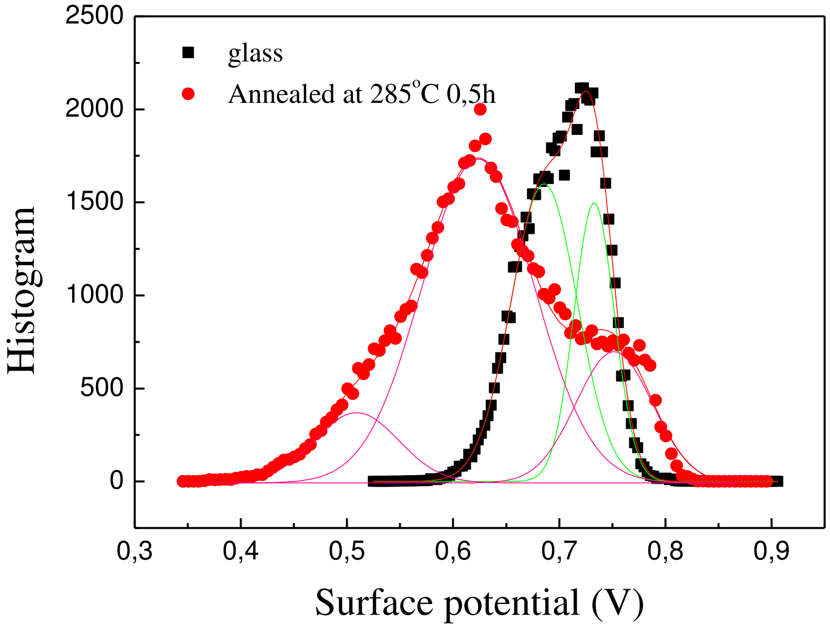

Figure 4-5 Histogram of AFM surface potential for the base glass before and after ceramisation

Figure 4-6 shows the typical AFM surface potential images of some representative glass ceramics. It can be seen from the Figure 4-6(a), for a non conductive glass ceramic, that the high surface potential regions interconnect and form a network, whereas the low surface potential regions separately exist in the network. Based on the previous results, it can be clearly seen that the conductive microdomains (low surface potential regions) are separated by the non-conductive phase (high surface potential regions), so the glass ceramic does not show any measurable conductivity. On the contrary, for the glass ceramic with high conductivity, the high surface potential regions and the low surface potential regions form an interpenetrating network. Consequently, although there still exist non-conductive phase (high surface potential regions) in the glass ceramic, the carriers can be transported through the interconnected conductive microdomains (low surface potential regions), leading to a relatively high conductivity.

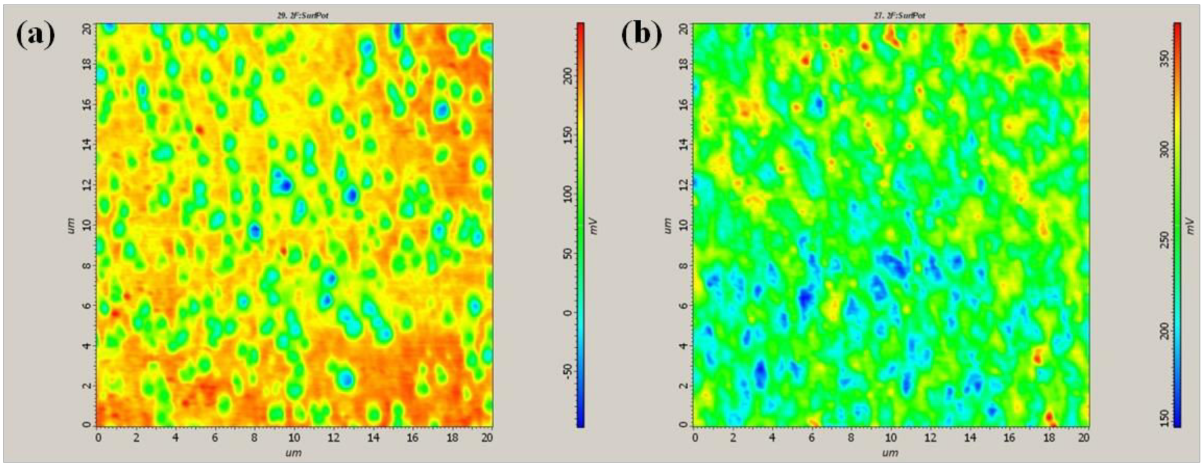

Figure 4-6 Typical AFM surface potential images of the glass ceramics with different conductivity: (a) $<10^{-8}$ $\Omega^{-1}\cdot cm^{-1}$; (b) 2.1×10^{-2} $\Omega^{-1}\cdot cm^{-1}$

3 Semiconductor properties of the $40GeSe_2$-$40Sb_2Se_3$-20CuI glass ceramics

For the fabrication of an efficient photoelectric material, there are three critical factors that need to be considered: (1) the material should efficiently respond to the whole solar spectrum as wide as possible; (2) the absorbed photons should be efficiently converted into the free charge carriers that can be efficiently separated; (3) the free charge carriers should be efficiently transported to the injecting contacts by the built-in electric field with high carrier mobility [28, 29]. Therefore, optical absorption property, photo-generated carrier lifetime, carrier mobility and conductivity are believed to be several main semiconductor properties, which determine whether such material can be a potential candidate for photoelectric applications [30].

3.1 Optical absorption

Figure 4-7 shows the absorption spectrum of the glass ceramic, obtained by measuring the diffuse reflectance. It can be seen that the glass ceramic exhibits a wide absorption from UV up to the infrared region (1800 nm). This absorption specturm is well matched with the solar spectrum. . Furthermore, the optical band gap widths is determined by plotting $(\alpha h\nu)^{1/2}$ versus photon-energy (as shown in Figure 4-8). The glass ceramic displays two obvious absorption edges, corresponding to the optical band gap widths of 1.0 eV and 0.24 eV respectively.

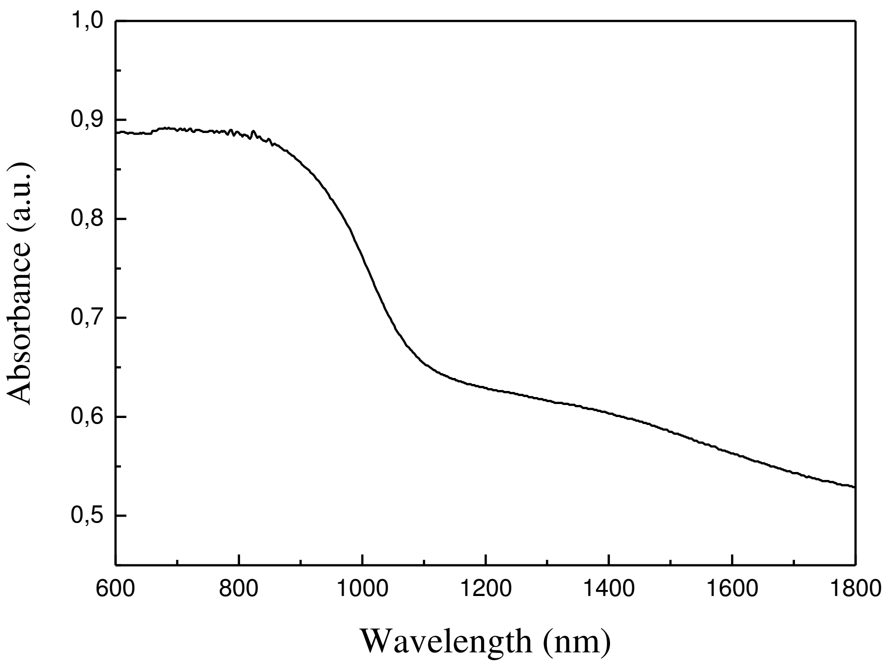

Figure 4-7 Absorption spectrum of the glass ceramic

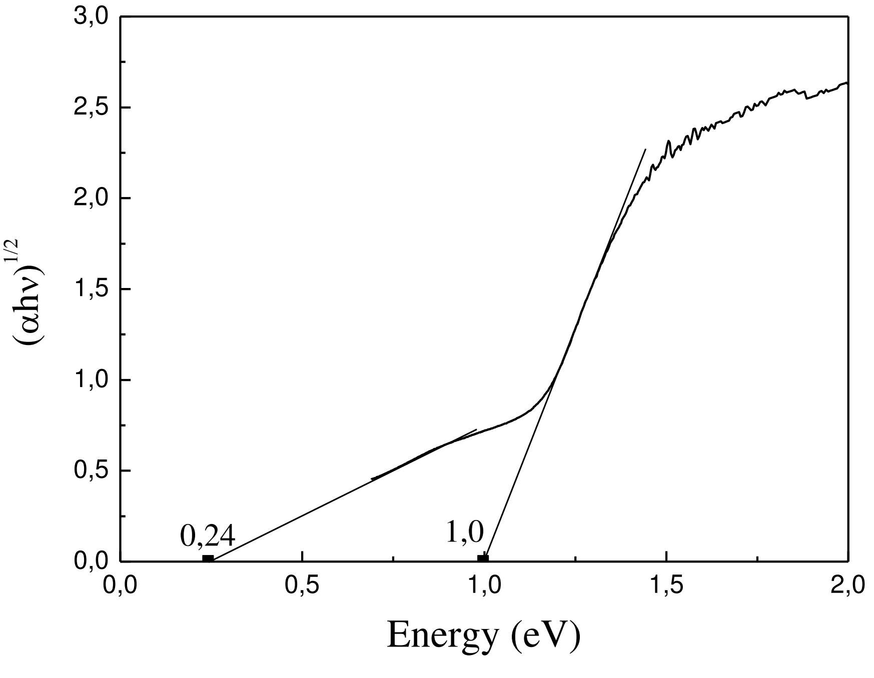

Figure 4-8 The dependence of $(\alpha h\nu)^{1/2}$ on photon-energy for the glass ceramic.

The optical absorption behavior of the glass ceramic is mainly determined by its composition and structure. There are mainly two crystalline phases, Sb_2Se_3 and Cu_2GeSe_3, in the glass ceramic. The Sb_2Se_3 has a direct band gap of 1.2 eV, corresponding absorption edge wavelength is 1033 nm [31]. Whereas the direct band gap of Cu_2GeSe_3 is about 0.78 eV, leading to the absorption of infrared light with wavelength up to 1590 nm [32, 33]. It has been confirmed that the doping of I^{2-} ions in the lattice of Sb_2Se_3 in the chapter 2. I-doping is expected to reduce the energy gap of Sb_2Se_3 due to the formation of impurity states in the band gap [34, 35]. Furthermore, the Cu_2GeSe_3 phase can also be non stoichiometric, leading to a decrease of the bandgap width. For example, copper vacancies, with Ge on Cu sites, and selenium interstitials are expected to be the dominant defect species, which will affect the band structure [15]. As an acceptor defect in Cu_2GeSe_3, copper vacancy may originate a shallow level in the band gap, leading to the acceptor level–to–valence band transition [15, 36]. Besides of impurity and defect levels, the possible band overlapping in Sb_2Se_3-Cu_2GeSe_3 composite system may also lead to the red shift of the optical absorption spectrum. The above factors together determine such wide absorption property of the glass ceramic.

3.2 Current-voltage characteristics

Current-voltage (I-V) measurements are important for examining the electrical properties of semiconducting materials. To measure these characteristics, two 1.8-mm metallic circle contacts were deposited onto the same face of each sample by electron beam evaporation. These contacts should have a separation of 2.5 mm. Silver contact was used for n-type samples while gold contact was used for p-type samples so that ohmic contacts could be obtained (as shown in Figure 4-9). Then 2-point method was then carried out in the dark to get the I-V characteristics.

Figure 4-9 Photograph of a sample with two contacts for I-V measurements

To be useful, the photo-generated carriers must be separated before their recombination. This separation can be greatly promoted by the built-in electric field thanks to the existence of heterojunctions evidenced earlier with the high-resolution transmission electron microscopy images showning clearly Sb_2Se_3-Cu_2GeSe_3 interface(as shown in Figure 2-32). In order to confirm the existence of internal heterojunction inside the glass ceramics, the I-V characteristics of different samples has been measured with two silver or gold contacts sputtered on the surface and the results are shown in Figure 4-10 (a). The ohmic character of the metallic contacts was preliminarily confirmed. The I-V curve clearly confirms the existence of heterojunctions which are randomly distributed inside the glass ceramic. These heterojunctions can be simplified as two opposite junctions connected in parallel (as shown in Figure 4-10(b)).

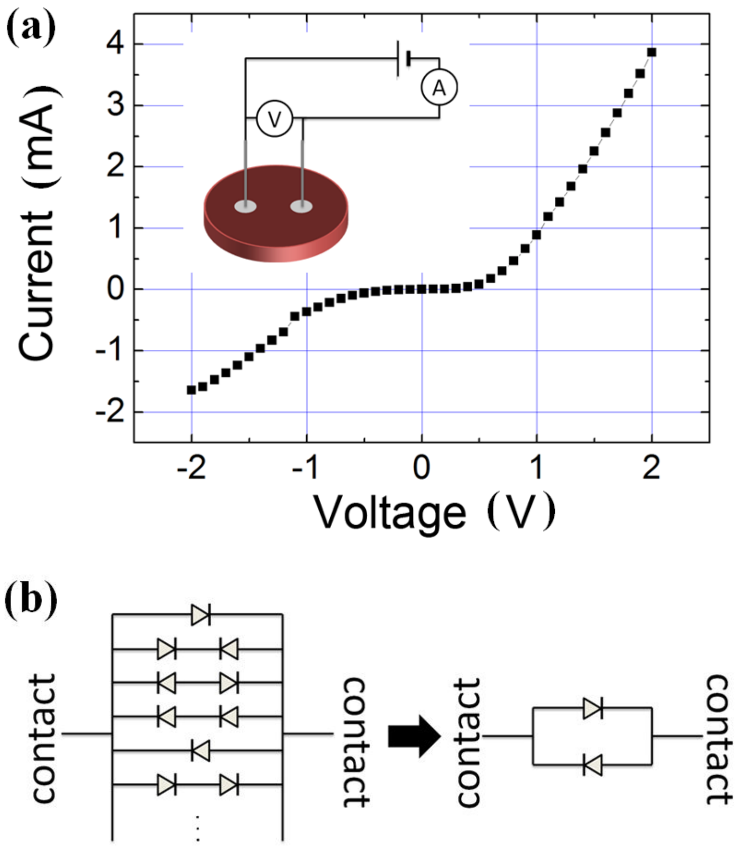

Figure 4-10 I-V curve of the glass ceramic

3.3 Charge carrier lifetime

In semiconductor physics, charge carrier’s lifetime is defined as the average time it takes to recombine with an opposite charge carrier. It is one of the most important parameters for the characterization of semiconductor used in the preparation of power electronic devices and photovoltaic solar cells [37].

3.3.1 Theoretic considerations

There are various recombination mechanisms even within a uniformly doped piece of semiconductor. The main types of recombination are intrinsic or radiative recombination, Shockley-Read-Hall (SRH) recombination and Auger recombination. SRH recombination is determined by the amount of impurities and defects in the semiconductor. For a semiconductor with indirect band-gap, SRH recombination is more important. Radiative (also known as band-to-band) recombination occurs when an electron falls from its state in the conduction band into the empty state in the valence band, by combining with the hole, resulting in light emission. Auger recombination is a process in which an electron and a hole recombine as a band-to-band transition, but the resulting energy is given off to another electron in the conduction band instead of just emitting a photon. The involvement of a third particle affects the recombination rate which makes it different from radiative recombination [34].

The lifetime of carriers in a bulk material τ_b is composed of a SRH lifetime τ_{SRH}, radiative lifetime τ_{rad} and Auger lifetime τ_A with the relation [38, 39]:

$$\frac{1}{\tau_b}=\frac{1}{\tau_{SRH}}+\frac{1}{\tau_{rad}}+\frac{1}{\tau_A} \tag{4.1}$$

Nowadays, various techniques have been proposed to measure minority carrier lifetime, such as PCD (photo conductivity decay), QSSPC (quasi-steady-state photoconductance) and SCCD/OCVD (short-circuit current/open-circuit voltage decay), etc [30]. In this work, the carrier lifetime is determined by the microwave photoconductivity decay (μ-PCD) method. In the μ-PCD method, the laser injection will produce electron-hole pairs, leading to the increase of conductivity. When the external laser injection is removed, the conductivity presents exponential decay over time, which indirectly reflects the extinction trend of minority carriers. The detection of μ-PCD method uses the principle that the variation of microwave is proportional to that of electrical conductivity. Compared with traditional PCD, microwave detection can not only guarantee the small deviation of minority lifetime, but also avoid the difficult preparation of ohmic electrodes [40].

3.3.2 Equipment

Lifetime measurements are carried out using a commercially available µ-PCD measurement system from Semilab (WT-2000) (as shown in Figure 4-11). The WT-2000 is a powerful tabletop measurement platform usable for different semiconductor materials. The system includes a XY measurement stage with the possibility of lifetime mapping over a surface.

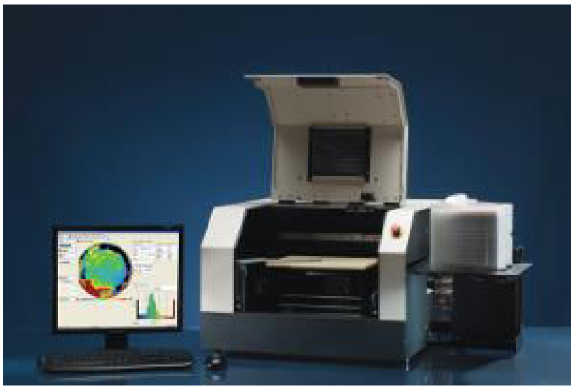

Figure 4-11 µ-PCD measurement system (WT-2000)

In this system, the excess charge carriers are generated by 200 ns light pulses from a 904 nm diode laser. The penetration depth of the laser depends on the absorption coefficient of the semiconductor and is about 30 µm for silicon. For the microwave detection, this system uses a frequency in the range of 10-11 GHz. The WT-2000 can be used to measure charge carrier lifetime distributions over a surface and a typical example is shown in Figure 4-12 for n-InP/n-InGaAs/n-InP [41].

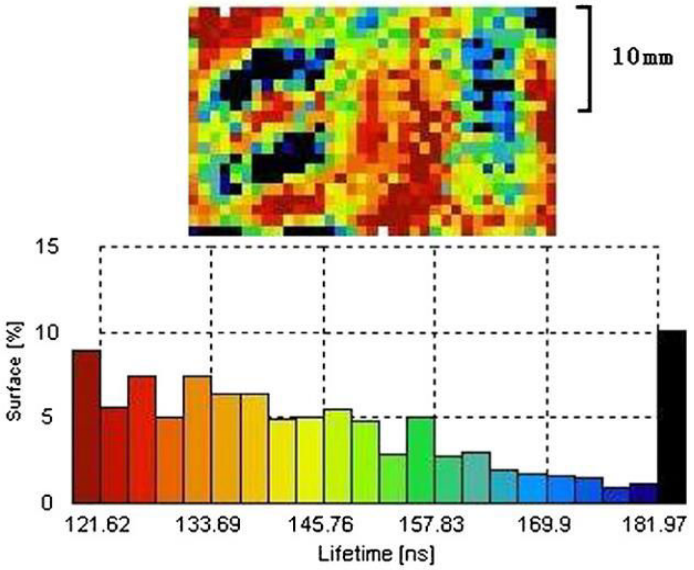

Figure 4-12 Lifetime map and distribution

3.3.3 Carrier lifetime of the 40GeSe$_2$-40Sb$_2$Se$_3$-20CuI glass ceramic

The existence of nano-junctions is of course extremely favorable for charge separation and this is probably one of the reasons why the composite materials show an extremely long lifetime of minority charge carriers of about 16 µs (as shown in Figure 4-13), compared for example to similar and well studied chalcopyrite CIGS with a lifetime typically shorter than 0.1 µs [42]. The inhomogeneity of lifetime is associated with the composite character of the material with randomly distributed conductive channels which will be illustrated below.

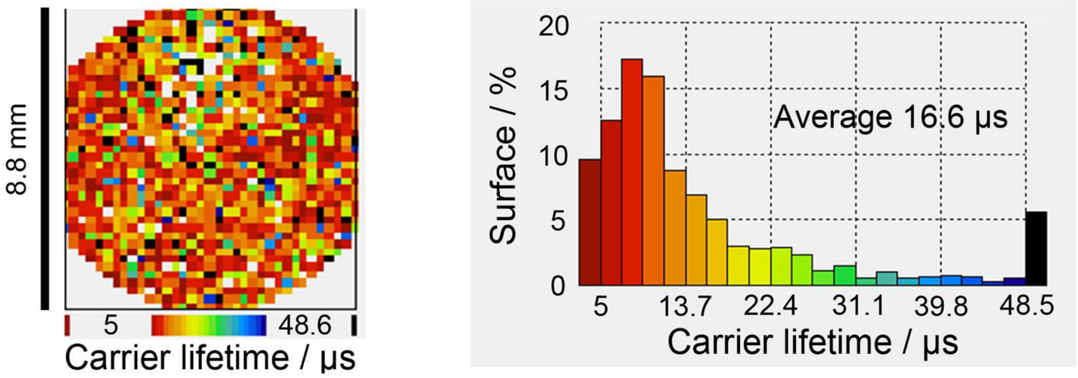

Figure 4-13 Spatial distribution of the minority charge carrier lifetime over the surface of the glass ceramic disk

3.4 Hall effect

When a current goes through a conductor subjected to a perpendicular external magnetic field, a voltage difference will appear, transverse to the electric current and to the magnetic field. This phenomenon is called Hall effect, which was discovered in 1879 by Edwin Herbert Hall while he was working on his doctoral degree at Johns Hopkins University in Baltimore, Maryland [43]. Hall effect can provide some essential parameters of a semiconductor such as conductivity type, carrier concentration, carrier mobility etc. It is now one of the most important methods for characterizing semiconductor materials.

3.4.1 Theoretical considerations

When a magnetic field is applied to a semiconductor with a direction which is not parallel to the moving direction of the charges, these charges will experience a force, called the Lorentz force. It will force the moving charge carriers deviate from its original straight path.

Consequently, positive and negative charges will be accumulated on both sides of the material. This leads to the creation of an electric perpendicular to the direction of the current. This electric field will eventually balance the Lorentz force to establish equilibrium. Therefore, a steady electrical potential difference, the Hall voltage, is created.

Since the glass ceramic disks are all circular, four symmetrical electrodes need to be uniformly deposited around the sample. The thickness of sample is about 1/3 of its diameter.

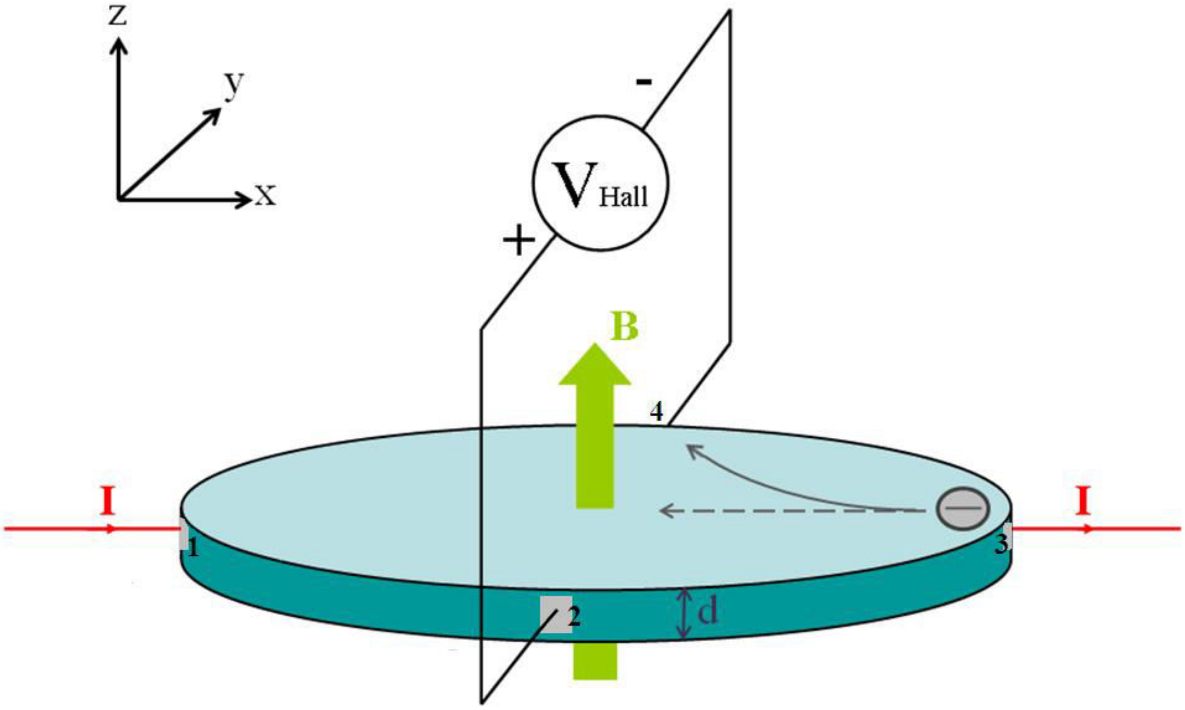

Figure 4-14 Schematic of a Hall effect measurement

For a simple conductor shown in Figure 4-14, the Hall voltage V_H is expressed by the equation

$$V_H = -\frac{IB}{nde} \tag{4.2}$$

where I is the current across the plate length, B is the magnetic field, d is the thickness of the disc, e is the elementary charge of electron and n is the charge carrier density. The Hall coefficient R_H is defined as the ratio of the induced electric field to the product of the current density and applied magnetic field:

$$R_H = \frac{E_y}{j_x B} = \frac{V_H d}{IB} = -\frac{1}{ne} \tag{4.3}$$

where j_x is the current density of the carrier electrons, and E_y is induced electric field.

3.4.2 Measurement

In our experiment, Accent HL5500PC Hall Effect measurement system as shown in Figure 4-15 is used to characterize our samples. The HL5500PC is a turn-key, high performance Hall System for the measurement of resistivity, carrier concentration and mobility in semiconductor.

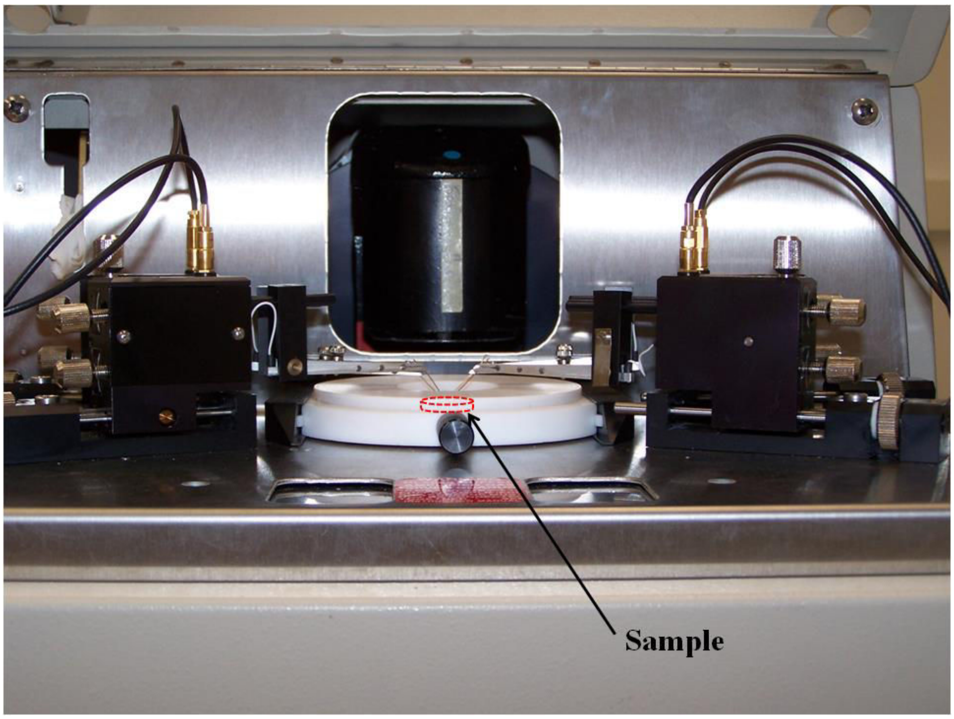

Figure 4-15 Hall effect measurement system (HL5500PC)

3.4.3 Charge carrier mobility and conductivity

Figure 4-16 shows Hall mobility of the glass ceramic versus magnetic flux density in different configurations (positive, negative and averaged). It can be seen that the glass ceramic exhibits relatively high Hall mobility in the range of 10^2 $cm^2 \cdot V^{-1} \cdot S^{-1}$, which is in the same order of magnitude with that of CIGS [44, 45]. High charge carrier mobility means a strong conductive ability. This is in agreement with the conductivity of about ~10^{-2} $\Omega^{-1} \cdot cm^{-1}$, measured with the four-point method, for this glass ceramic.

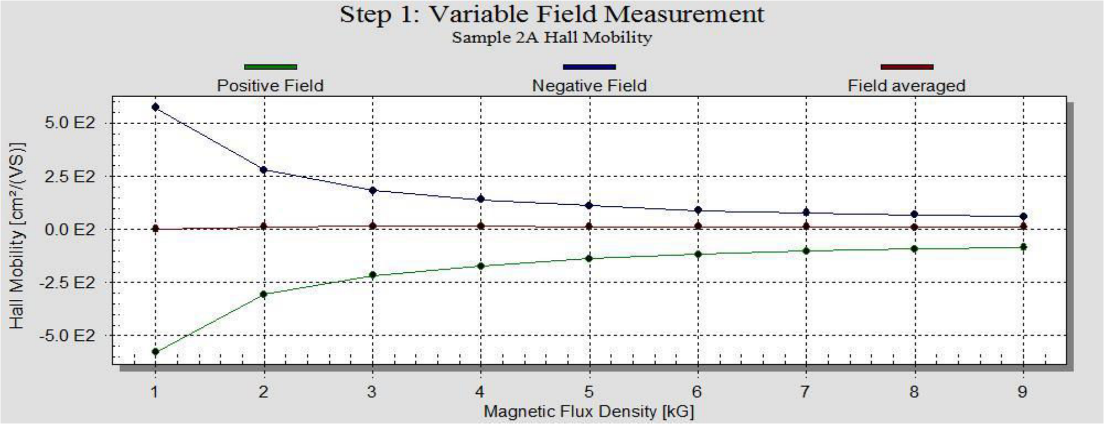

Figure 4-16 Hall mobility of the glass ceramic versus magnetic flux density

4 Photoelectric conduction mechanism of the glass ceramic

In order to better understand the photoconduction mechanism of this glass ceramics, a comparative study of PEC properties is carried out between Sb_2Se_3, Cu_2GeSe_3 and the glass ceramic. As shown in Figure 4-17, The PEC measurements, performed under an illumination of 100 w/m^2, give an intense photocurrent of 74 µA/cm^2 (at bias voltage of -0.6 V versus Ag/AgCl reference electrode) with the glass ceramic. With the same measurement conditions, the two crystallized phases individually give negligible photocurrent, less than 1 µA/cm^2. These results show the importance of coexistence of these two crystalline phases for generating strong photocurrent. It seems that the mesoscopic composite structure, rather than the material itself, is a decisive factor for achieving the high photoelectric property in the glass ceramic.

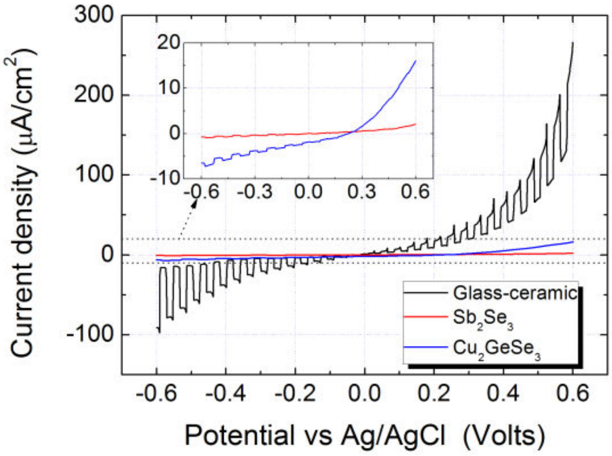

Figure 4-17 PEC measurement of Sb_2Se_3, Cu_2GeSe_3 and the glass ceramic under a chopped light source

Based on the analysis above, it can be found that there are two key factors affecting the photoelectric conduction of the glass ceramic, which finally determines the photoelectric property. One is the formation of a semiconductor heterojunction between Sb_2Se_3 and Cu_2GeSe_3, which can lead to a more efficient inter-particle carrier separation. Another one is the formation of a conductive channel in the glass ceramic, resulting in the obvious enhancement of conductivity, which can promote the mobility of photo-generated carriers. The possible mechanism of charge photogeneration, separation and transport can be proposed in Figure 4-18. Photons are efficiently and essentially absorbed by Sb_2Se_3 as well as by Cu_2GeSe_3, and then the heterojunction formed by n-type Sb_2Se_3 and p-type Cu_2GeSe_3 enhances the charge separation and the charge is efficiently collected by the network formed with interconnected rod-like Sb_2Se_3 crystals covered by conductive Cu_2GeSe_3. This network creates conductive channels, as evidenced by the AFM surface potential image showing more or less conductive channels (previous studies indicate that low surface potential means high conductivity in our case). Therefore, the photo-generated carriers can be transported though the conductive paths to the back contact, and the carrier collection efficiency is improved.

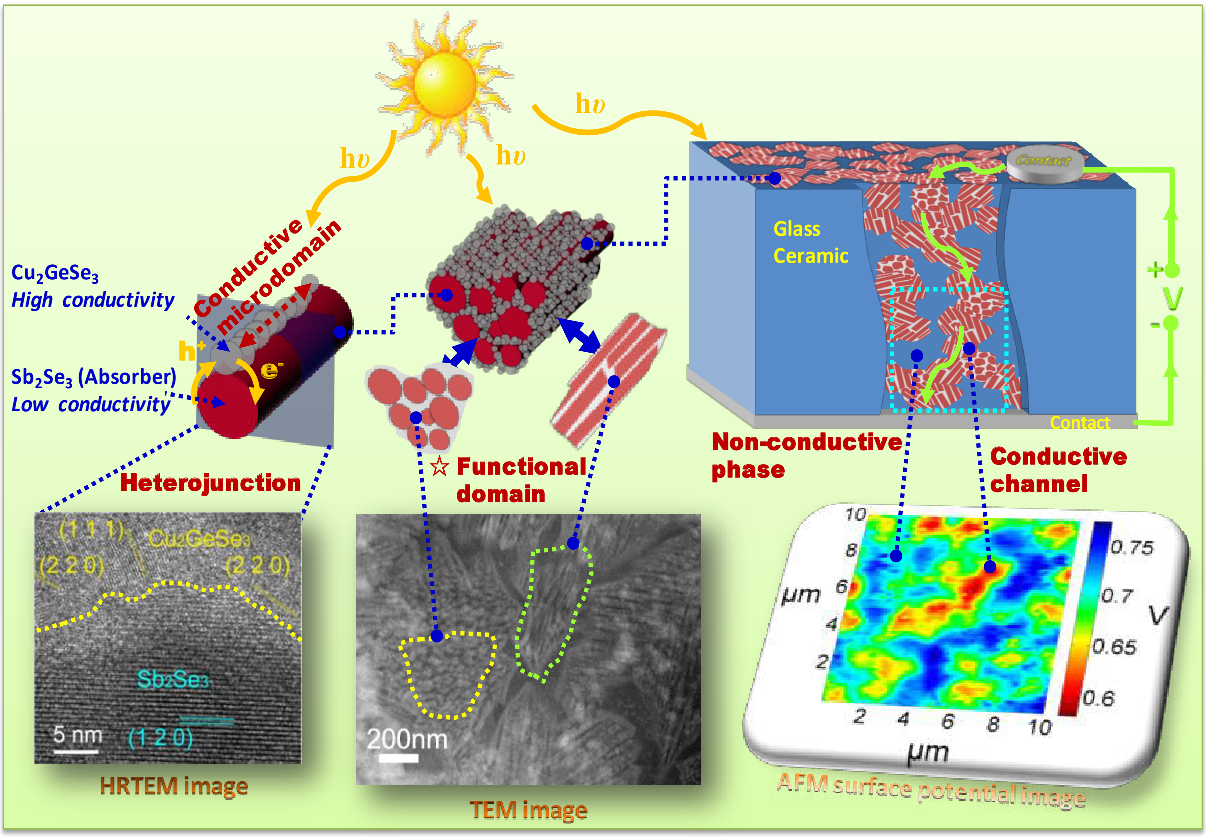

Figure 4-18 Mechanisms of charge photo-generation, dissociation and transport in the photoelectric glass ceramic

5 Conclusion

To summarize, we have demonstrated the feasibility of interpenetrating heterojunction network in a purely inorganic composite material, by controlling the crystallization of a $GeSe_2$-Ga_2Se_3-CuI glass. The network was formed by low conductive rod-like Sb_2Se_3 crystals, covered by highly conductive Cu_2GeSe_3 crystals. The Sb_2Se_3 and Cu_2GeSe_3 are efficient for charge photogeneration, the p-n junction formed by these two crystals greatly promotes the charge separation and the Cu_2GeSe_3 plays the role of efficient charge collector. This structure results in high photocurrent (at least 100 times higher than any of these two crystal individually) and exceptionally long lifetime of charge carriers (around 16 μs). In this way, much more materials, such as Sb_2Se_3 with many excellent features but low electrical conductivity can now be selected for photovoltaic application.

Reference

[1] G. Yu, J. Gao, J. Hummelen, F. Wudl, A. Heeger, Polymer photovoltaic cells: enhanced efficiencies via a network of internal donor-acceptor heterojunctions, Science-AAAS-Weekly Paper Edition, 270 (1995) 1789-1790.

[2] T.M. Clarke, J.R. Durrant, Charge photogeneration in organic solar cells, Chemical Reviews, 110 (2010) 6736-6767.

[3] F. Yang, M. Shtein, S.R. Forrest, Controlled growth of a molecular bulk heterojunction photovoltaic cell, Nature Materials, 4 (2005) 37-41.

[4] K. Vandewal, S. Albrecht, E.T. Hoke, K.R. Graham, J. Widmer, J.D. Douglas, M. Schubert, W.R. Mateker, J.T. Bloking, G.F. Burkhard, A. Sellinger, J.M.J. Fréchet, A. Amassian, M.K. Riede, M.D. McGehee, D. Neher, A. Salleo, Efficient charge generation by relaxed charge-transfer states at organic interfaces, Nat Mater, 13 (2014) 63-68.

[5] C. Chen, W. Ma, J. Zhao, Semiconductor-mediated photodegradation of pollutants under visible-light irradiation, Chemical Society Reviews, 39 (2010) 4206-4219.

[6] X. Chen, L. Liu, P.Y. Yu, S.S. Mao, Increasing solar absorption for photocatalysis with black hydrogenated titanium dioxide nanocrystals, Science, 331 (2011) 746-750.

[7] N.S. Sariciftci, D. Braun, C. Zhang, V.I. Srdanov, A.J. Heeger, G. Stucky, F. Wudl, Semiconducting polymer-buckminsterfullerene heterojunctions: Diodes, photodiodes, and photovoltaic cells, Applied Physics Letters, 62 (1993) 585-587.

[8] F. Lin, S.W. Boettcher, Adaptive semiconductor/electrocatalyst junctions in water-splitting photoanodes, Nat Mater, 13 (2014) 81-86.

[9] Y. Zhou, M. Leng, Z. Xia, J. Zhong, H. Song, X. Liu, B. Yang, J. Zhang, J. Chen, K. Zhou, J. Han, Y. Cheng, J. Tang, Solution-processed antimony selenide heterojunction solar cells, Advanced Energy Materials, (2014) .

[10] M.S. Gui, W.D. Zhang, Y.Q. Chang, Y.X. Yu, One-step hydrothermal preparation strategy for nanostructured WO_3/Bi_2WO_6 heterojunction with high visible light photocatalytic activity, Chemical engineering journal, 197 (2012) 283-288.

[11] J. Su, X.X. Zou, G.D. Li, X. Wei, C. Yan, Y.N. Wang, J. Zhao, L.J. Zhou, J.S. Chen, Macroporous V_2O_5–$BiVO_4$ composites: Effect of heterojunction on the behavior of photogenerated charges, The Journal of Physical Chemistry C, 115 (2011) 8064-8071.

[12] N. Wetchakun, S. Chaiwichain, B. Inceesungvorn, K. Pingmuang, S. Phanichphant, A.I. Minett, J. Chen, $BiVO_4/CeO_2$ Nanocomposites with high visible-light-induced photocatalytic activity, ACS Applied Materials & Interfaces, 4 (2012) 3718-3723.

[13] J.S. Jang, H.G. Kim, J.S. Lee, Heterojunction semiconductors: A strategy to develop efficient photocatalytic materials for visible light water splitting, Catalysis Today, 185 (2012) 270-277.

[14] E.A. El-Sayad, Compositional dependence of the optical properties of amorphous Sb_2Se_3–xS_x thin films, Journal of Non-Crystalline Solids, 354 (2008) 3806-3811.

[15] G. Marcano, D. Bracho, C. Rincón, G.S. Pérez, L. Nieves, On the temperature dependence of the electrical and optical properties of Cu_2GeSe_3, Journal of Applied Physics, 88 (2000) 822-828.

[16] C.E. Patrick, F. Giustino, Structural and electronic properties of semiconductor-sensitized solar-cell Interfaces, Advanced Functional Materials, 21 (2011) 4663-4667.

[17] N. Guijarro, T. Lutz, T. Lana-Villarreal, F. O'Mahony, R. Gómez, S.A. Haque, Toward antimony selenide sensitized solar cells: Efficient charge photogeneration at spiro-OMeTAD/Sb_2Se_3/metal oxide heterojunctions, The Journal of Physical Chemistry Letters, 3 (2012) 1351-1356.

[18] Y.C. Choi, T.N. Mandal, W.S. Yang, Y.H. Lee, S.H. Im, J.H. Noh, S.I. Seok, Sb_2Se_3-sensitized inorganic–organic heterojunction solar cells fabricated using a single-source precursor, Angewandte Chemie, 126 (2014) 1353-1357.

[19] M.R. Filip, C.E. Patrick, F. Giustino, GW quasiparticle band structures of stibnite, antimonselite, bismuthinite, and guanajuatite, Physical Review B, 87 (2013) 205125.

[20] M.A. Villarreal, B.J. Fernández, M. Pirela, A. Velásquez-Velásquez, Electrical properties of the ternary compound Cu_2GeSe_3, Revista Mexicana de Fisica, 53 (2007) 303-306.

[21] D. Wang, C. Song, X. Fu, X. Li, Growth of one-dimensional Sb_2S_3 and Sb_2Se_3 crystals with straw-tied-like architectures, Journal of Crystal Growth, 281 (2005) 611-615.

[22] G. Marcano, R. Márquez, Variable-range hopping conductivity and magnetoresistance in p-type Cu_2GeSe_3, Journal of Physics and Chemistry of Solids, 64 (2003) 1725-1727.

[23] B.K. Sarkar, A.S. Verma, P.S. Deviprasad, Temperature induced band gap shrinkage in Cu_2GeSe_3: Role of electron–phonon interaction, Physica B: Condensed Matter, 406 (2011) 2847-2850.

[24] C.B. Roy, D.K. Nandi, P.K. Mahapatra, Photoelectrochemical cells with n-type ZnSe and n-type Sb_2Se_3 thin film semiconductor electrodes, Electrochimica Acta, 31 (1986) 1227-1229.

[25] P.E. West, Introduction to atomic force microscopy: Theory, practice, applications, Pacific Nanotechnology, 2007.

[26] B. Cappella, G. Dietler, Force-distance curves by atomic force microscopy, Surface science reports, 34 (1999) 1-104.

[27] H.O. Jacobs, H.F. Knapp, S. Müller, A. Stemmer, Surface potential mapping: A qualitative material contrast in SPM, Ultramicroscopy, 69 (1997) 39-49.

[28] S.R. Forrest, The limits to organic photovoltaic cell efficiency, MRS bulletin, 30 (2005) 28-32.

[29] K. Cnops, B.P. Rand, D. Cheyns, B. Verreet, M.A. Empl, P. Heremans, 8.4% efficient fullerene-free organic solar cells exploiting long-range exciton energy transfer, Nat Commun, 5 (2014) 3406.

[30] D.K. Schroder, Semiconductor material and device characterization, John Wiley & Sons, 2006.

[31] K. Chandrasekharan, A. Kunjomana, Growth and microindentation analysis of pure and doped Sb_2Se_3 crystals, Turk J Phys, 33 (2009) 209-217.

[32] M. Morihama, T. Maeda, I. Yamauchi, T. Wada, Crystallographic and optical properties of narrow band gap Cu_2GeSe_3 and $Cu_2(Sn_{1-x}Ge_x)Se_3$ solid solution, Japanese Journal of Applied Physics, 53 (2014) 05FW06.

[33] M. Ibáñez, R. Zamani, W. Li, D. Cadavid, S. Gorsse, N.A. Katcho, A. Shavel, A.M. López, J.R. Morante, J. Arbiol, Crystallographic control at the nanoscale to enhance functionality: polytypic Cu_2GeSe_3 nanoparticles as thermoelectric materials, Chemistry of Materials, 24 (2012) 4615-4622.

[34] B. Van Zeghbroeck, Principles of semiconductor devices, Colorado University, (2004).

[35] S.K. Jain, P. Srivastava, Effect of nitrogen impurity on electronic properties of boron nanotubes, Advances in Condensed Matter Physics, 2014 (2014) 8.

[36] G. Marcano, C. Rincón, L.M. de Chalbaud, D.B. Bracho, G.S. Pérez, Crystal growth and structure, electrical, and optical characterization of the semiconductor Cu_2SnSe_3, Journal of Applied Physics, 90 (2001) 1847-1853.

[37] A. Cuevas, D. Macdonald, Measuring and interpreting the lifetime of silicon wafers, Solar Energy, 76 (2004) 255-262.

[38] V.C. Lopes, A.J. Syllaios, M.C. Chen, Minority carrier lifetime in mercury cadmium telluride, Semiconductor Science and Technology, 8 (1993) 824.

[39] http://pveducation.org/pvcdrom/characterisation/bulk-lifetime.

[40] A.P. Ramsa, H. Jacobs, F.A. Brand, Microwave techniques in measurement of lifetime in germanium, Journal of Applied Physics, 30 (1959) 1054-1060.

[41] Y. Lv, N. Wang, C. Zhuang, P. Li, B. Han, H. Gong, The uniformity of InGaAs in InP/InGaAs/InP by microwave photoconductivity decay (μ-PCD) carrier lifetime measurement, Semiconductor science and technology, 21 (2006) 771.

[42] W.K. Metzger, I.L. Repins, M.A. Contreras, Long lifetimes in high-efficiency Cu(In, Ga)Se_2 solar cells, Applied Physics Letters, 93 (2008) 022110-022113.

[43] E.H. Hall, On a New Action of the Magnet on Electric Currents, American Journal of Mathematics, 2 (1879) 287-292.

[44] M.G. Faraj, K. Ibrahim, A. Salhin, Effects of Ga concentration on structural and electrical properties of screen printed-CIGS absorber layers on polyethylene terephthalate, Materials Science in Semiconductor Processing, 15 (2012) 206-213.

[45] J. Lee, J.D. Cohen, W.N. Shafarman, The determination of carrier mobilities in CIGS photovoltaic devices using high-frequency admittance measurements, Thin Solid Films, 480–481 (2005) 336-340.

Chapter 5

Photocatalytic properties of the 40$GeSe_2$-40Sb_2Se_3-20CuI glass ceramic

1 Introduction

Semiconductor photocatalysis technology is a new type of green technologies for efficiently exploiting the solar energy with double environmental benefits: organic wastes can be transformed into useful energies (electricity or chemical fuels) [1-4]. Such technology is based on the use of the photo-generated charge carriers from semiconductors. The free photo-generated electrons or holes can respectively react with the adsorbed O_2 or H_2O on the semiconductor surface, leading to the formation of various active substances, such as $\cdot O_2^-$, $\cdot HO_2$, H_2O_2, $\cdot OH$ etc, which can decompose most organic pollutants [5, 6]. Therefore, efficient generation and separation of photo-generated carriers is the key for efficient semiconductor photocatalytic reaction [7-9].

In order to increase the amount of photo-generated charge carriers, the development of narrow band-gap semiconductors, for having a high absorption of photons in the visible region, has attracted much attention [10-12].New narrow band-gap semiconductors has been rapidly developed in recent years, including particularly sulfide semiconductors [13], multiple oxide semiconductors [14, 15] and nitride semiconductors [16]. However, with the decrease of band-gap width, the photo-generated electrons and holes recombine more easily. Since only the free photo-generated carriers can further react and form active radicals, leading to the decomposition of organic pollutants, the more easily-occurred recombination in some narrow band-gap semiconductors will decrease their photocatalytic activity although they can absorb more photons. Therefore, a number of methods have been developed to inhibit the recombination of photo-generated electron-hole pairs, such as doping [17, 18] and coupled semiconductor [19]. Recently, fabricating nano-heterojunction through in-situ growth route has become a rising method to develop highly efficient semiconductor composite. The nano-heterojunction can have more efficient interparticle electron transfer between the two components due to the size effect of particles and the intimate contact between heterophase nanoparticles [19, 20]. Consequently, nano-scale semiconductor heterojunction with narrow band gap can not only extend the absorption wavelength range to visible region, but also inhibit the recombination of photo-generated electron-hole pairs. This kind of junctions has become a promising strategy for improving the visible-light photocatalytic activity.

In the previous chapters, we have presented a novel glass ceramic with interesting photoelectric activity. This glass ceramic exhibits a relative intense absorption from UV up to the infrared region (240-2000 nm). More importantly, there forms nano-heterojunctions between Sb_2Se_3 and Cu_2GeSe_3 crystals, leading to an efficient separation of photo-generated electrons and holes. Such unique features make it interesting as a photocatalyst. Therefore, in this chapter, the $40GeSe_2$-$40Sb_2Se_3$-20CuI glass ceramic is used as a photocatalyst for decomposing organic pollutants.

2 Evaluation method of photocatalytic activity

The photocatalytic activity of the selected glass ceramics is evaluated by decomposing methyl orange (MO), taken as an example, in aqueous solution under visible light illumination. Figure 5-1 shows the molecular structure of MO, the UV-vis absorption spectrum and the color of MO aqueous solution., It can be seen that the MO aqueous solution has a characteristic large absorption peaked at 464 nm, attributed to the -N=N- chromophore [21]. This chromophore can be oxidized during photocatalytic reaction, leading to the discoloration of the solution. Therefore, the absorbance of the solution can be used to monitor the photocatalytic activity and a low residual absorbance indicates of course a high reaction activity of the photocatalyst [22, 23].

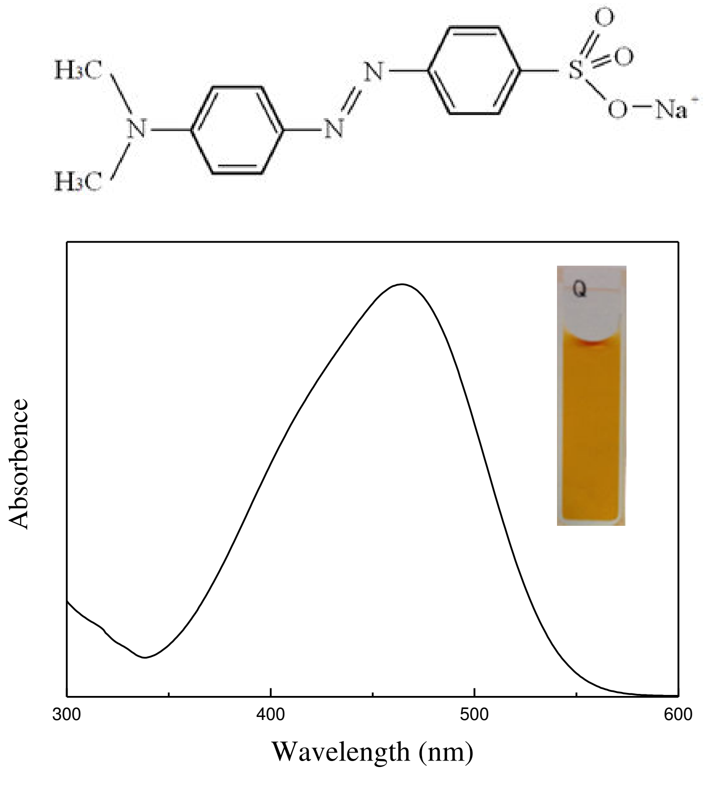

Figure 5-1 Molecular structure of MO and a typical UV-vis absorption spectrum and color of MO aqueous solution

The schematic presentation of the photocatalytic reactor is shown in Figure 5-2. A 35 W CDM-T Philips metal halide lamp with a 420 nm UV-cutoff filter is used as the visible light source. Prior to the test, a precise amount of glass ceramic powders are dispersed into 10 mL MO solution by ultrasonic dispersion for 5 min. The suspension is magnetically stirred throughout the process of photocatalytic reaction. When the reaction time is reached, the suspension is centrifuged (4000 rpm, 5 min) to remove the glass ceramic particles from the solution.

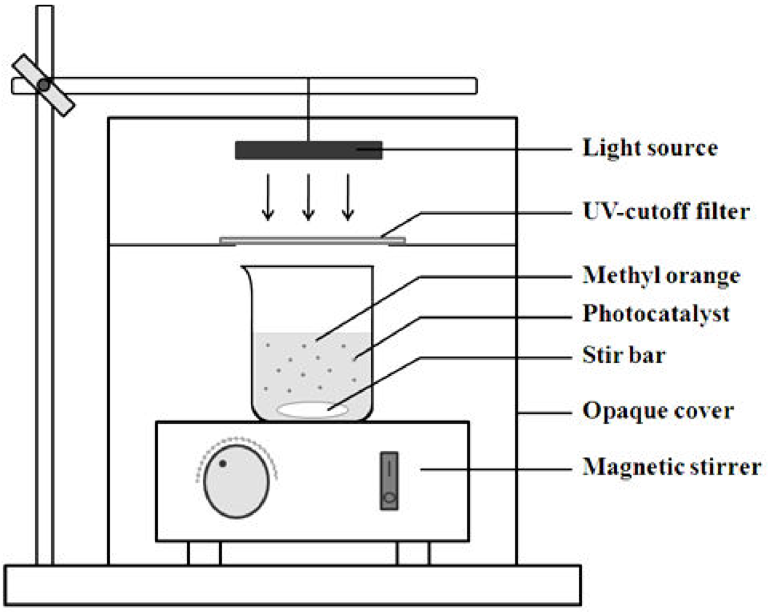

Figure 5-2 Schematic presentation of the photocatalytic reactor

The absorbance of the solution before and after the photocatalystic reaction, always without the photocatalyst, is measured by using a UV-vis spectrophotometer. The characteristic absorption peak of MO aqueous solution at 464 nm is used to calculate the decomposition ratio P, according to the following equation:

$$P = \frac{A_0 - A_t}{A_0} \times 100\% \tag{5.1}$$

where A_0 and A_t are absorbance at the maximum absorption wavelength of the solution, respectively at time 0 and time t.

The photocatalytic activity can also be monitored by a normalized concentration of MO. According to the Lambert-Beer law [24], the normalized concentration of the solution equals to the normalized maximum absorbance, i.e., $C_t/C_0 = A_t/A_0$. Here C_t and C_0 are the concentration of the solutions respectively at time t and time 0. Therefore, the normalized concentration can be directly determined by using a UV-vis spectrophotometer.

3 Photocatalytic activities of different glass ceramics

A simple method for comparing samples with different photocatalytic activities is to evaluate the ptotocatalytic decomposition ratio of a selected pollutant as function of time. Since the difference of photocatalytic activities between various photocatalysts is not always obvious or tends to be particularly small at the initial or final stage of the photocatalytic reaction, it is better to choose a detection time in the middle stage of the photocatalytic reaction. The choice of an optimum detection time is mainly dependent on the particle size of the photocatalyst (for powder photocatalyst), photocatalyst concentration, pollutant concentration and other ptotocatalytic reaction conditions, such as the wavelength and the illumination intensity of light source, and the uniformity of the suspension, etc [25-27].

Particle size is an important parameter influencing strongly the photocatalytic activity of powder photocatalyst. Smaller particle size will induce higher photocatalytic activity due to its higher specific surface [28]. In all our experiments, the glass ceramic is manually grinded into powders and then the powders are successively sieved through 30 μm and 20 μm sieves to obtain powders with two different size characteristic, <20 μm or between 20 μm ~30 μm. Whereas the powder with particle size >30 μm will be further grinded. The photocatalytic activities of these two powders are evaluated by decomposing MO. However, for the glass ceramic powders with smaller particle size (<20 μm), a part of the powders greatly smaller than 20 μm, remains floating on the surface of the MO solution even after ultrasonic dispersion for 10 min. The other part of the powders is in suspension in the MO solution. This phenomenon is mainly due to the hydrophobic feature of the powders and the small particle size. The floating powders will decrease the light absorption of the glass ceramic powders in the solution, leading to lower photocatalytic activity (as shown in Figure 5-3). Therefore, we choose the glass ceramic powders with particle size between 20 μm and 30 μm for the photocatalytic reaction.

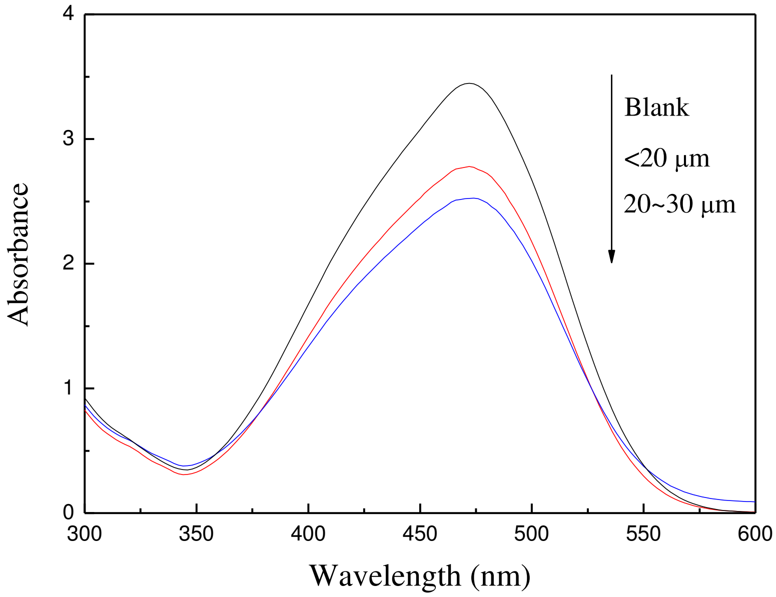

Figure 5-3 UV-vis absorption spectra of MO solutions before and after photocatalytic reaction with different particle sizes of glass ceramic powders for the same duration

In order to determine the suitable photocatalytic reaction conditions, photocatalyst dosage, MO concentration and illumination time are investigated by a orthogonal experiment of three factors and three levels (as shown in Table 5-1), whereas the other experiment parameters such as the wavelength of and the illumination intensity of the light source, and the stirring rate of the suspension are fixed.

Table 5-1 Different parameters used for the photocatalytic decomposition of Methyl orange

Reaction systems	Photocatalyst dosage (mg)	MO concentration (mg/L)	Illumination time (h)
a	10	20	0.5
b	10	40	1
c	10	50	1.5
d	20	20	1
e	20	40	1.5
f	20	50	0.5
g	40	20	1.5
h	40	40	0.5
i	40	50	1

Figure 5-4 shows the UV-vis absorption spectra of the MO solutions before and after photocatalytic reaction under different conditions and the corresponding decomposition ratio (defined by equation 5.1) per hour, which can be more or less considered as a decomposition rate. There is no doubt that the photocatalytic reaction is accelerated by increasing photocatalyst dosage at the same MO concentration. When fixing the dosage of photocatalyst (such as 10 mg or 20 mg), a lower MO concentration has a higher decomposition rate. However, for the high photocatalyst dosage of 40 mg, although the decomposition ratio at low MO concentration (reaction system g) achieves a high P value of 90.8%, this rate is lower than that at high MO concentration (reaction system h). The likely reason is that the decomposition of MO in the reaction system g achieves high level before the detection time of 1.5 h. Moreover, it also can be seen that excessively high initial concentration of MO leads to the formation of sawtooth profiles on the absorption curve (as shown in Figure 5-4(c)). In this case, a large amount of MO dye and intermediates will absorb the light, so the light intensity on the photocatalyst is weakened, leading to the decrease of photocatalytic reaction rate [29, 30]. Consequently, a suitable photocatalytic reaction conditions can be determined as a reaction system with a photocatalyst dosage of 40 mg and a MO concentration of 40 mg/L.

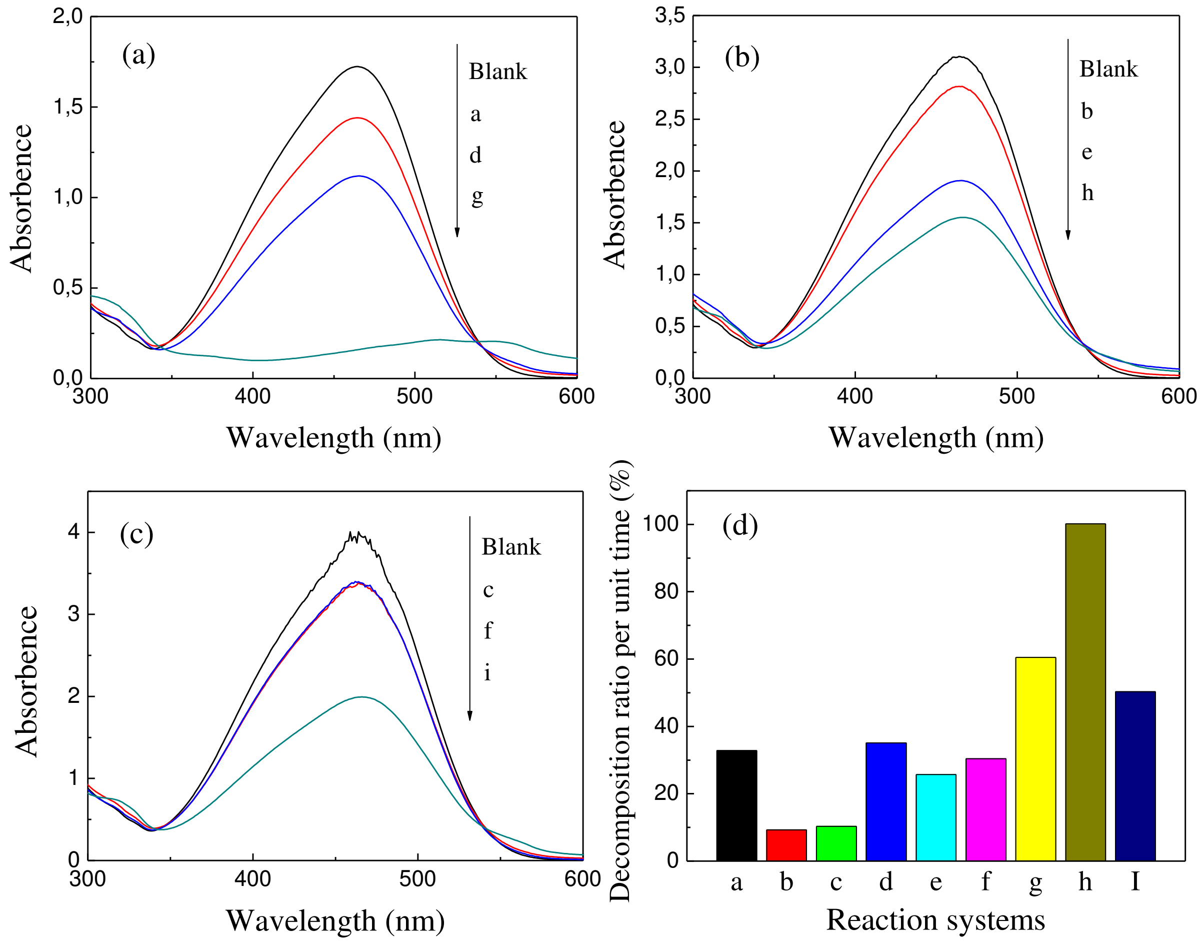

Figure 5-4 UV-vis absorption spectra of MO solutions before and after photocatalytic reaction under different conditions detailed in table 5-1

Here, the photocatalytic activity of two series glass ceramics is evaluated. Figure 5-5(a) shows the UV-vis absorption spectra of MO solutions before and after photocatalytic reaction with different $40GeSe_2$-$40Sb_2Se_3$-$20CuI$ glass ceramics, prepared by a single-stage thermal annealing at 260 °C for different times. The photocatalytic activity of the glass ceramic is enhanced with an increase of annealing time from 1 h to 3 h. However, when further extending the annealing time above 7 h, the photocatalytic activity of glass ceramic is gradually decreased. Figure 5-5(b) displays the corresponding color change of MO solutions. Whereas for another series of glass ceramics, prepared by a two-stage heat treatment with different temperatures, the glass ceramic prepared at 270 °C exhibits the highest photocatalytic activity, leading to the most obvious color-fading of the MO solution. With an increase of the annealing temperature, the photocatalytic activity of the glass ceramics first decreases and then increases (as shown in Figure 5-6).

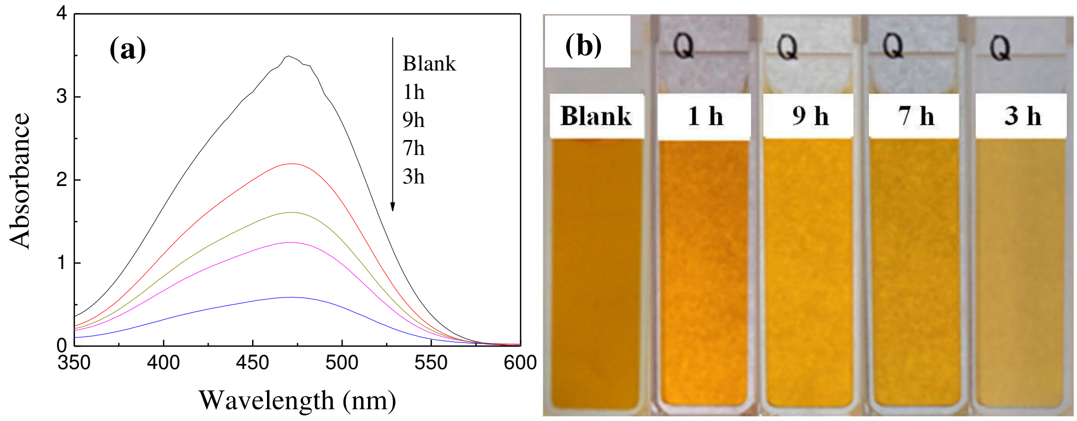

Figure 5-5 (a) UV-vis absorption spectra and (b) corresponding color of MO solutions before and after photocatalytic reaction over different $40GeSe_2$-$40Sb_2Se_3$-$20CuI$ glass ceramics prepared by a single-stage heat treatment at 260 °C for different times

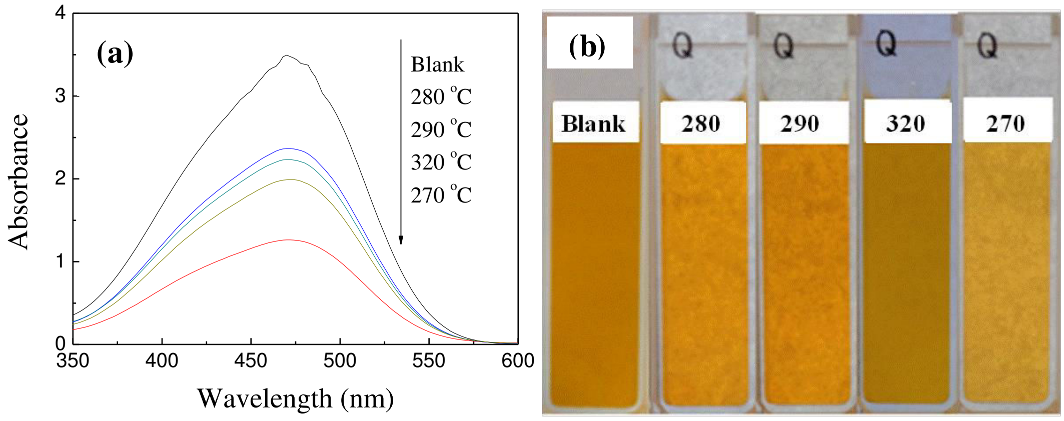

Figure 5-6 (a) UV-vis absorption spectra and (b) corresponding color of MO solutions before and after photocatalytic reaction over different $40GeSe_2$-$40Sb_2Se_3$-$20CuI$ glass ceramics prepared by a two-stage heat treatment with different temperatures

The photocatalytic activity of a material is known to be dependent on the photo-generation and separation of charge carriers [7]. The comparison of structure, conductivity and photocatalytic decomposition rate of MO between different glass ceramics is shown in Figure 5-7. The analysis of these data leads to the following remarks:

(1) The formation of nano-scale heterojunctions and conductive microdomains leads to high photocatalytic activity. It is well known that some materials with high conductivity and carrier mobility such as a graphene can efficiently promote the separation of photo-generated electron-hole pairs when coupled with semiconductors [31]. The above results indicated that highly conductive Cu_2GeSe_3 nanocrystals grow on the surface of Sb_2Se_3 rods, forming nano-scale heterojunctions and conductive microdomains in the glass ceramic. This structure can lead to a more efficient inter-particle carrier separation, thereby increasing the photocatalytic activity of these glass ceramics. Therefore, for the glass ceramic prepared at 260 ^{o}C for 1h (as shown in Figure 5-7), there is too much amorphous phase in the glass ceramic, considerably slowing down the transport of photo-generated charge carriers. The photocatalytic activity is enhanced when the base glass is annealed for 3 h leading to a more complete crystallization.

(2) Higher conductivity of glass ceramic does not lead necessarily to higher photocatalytic activity. The conductivity of a glass ceramic depends on the interconnection of the conductive microdomains at macroscopic scale in the glass ceramic. In order to fabricate this structure, it is necessary to extend annealing time or appropriately increase crystallization temperature (as shown in Figure 5-7). However, the increase of annealing time or crystallization temperature will increase the size of crystal grains. In general, a larger crystal grain may increase the migration distance of charge carriers, the electrons and holes photo-generated in the grain will take a longer time to reach the surface, leading to a higher recombination probability. Therefore, it can be seen form Figure 5-7 that the photocatalytic activity of glass ceramic is decreased with the increase of annealing time. Moreover, the photocatalytic activities of the glass ceramics prepared by the single-stage heat treatment are overall superior to that of the glass ceramics prepared by the two-stage heat treatment. Especially for the glass ceramic prepared at 260 ^{o}C for 1h, although it still contains a certain amount of glass phase, its photocatalytic activity (with decomposition rate of 37.2%) is comparable to that of the fully-crystallized glass ceramic (with decomposition rate of 36.0%), prepared at 290 ^{o}C with the two-stage heat treatment. This result further confirms that an excessively large size of crystal grains will lead to poor photocatalytic activity probably due to a higher recombination probability of photo-generated carriers.

(3) Crystal defect is another factor which can influence the photocatalytic activity of glass ceramic. It can be observed that the photocatalytic activity is slowly increased when changing crystallization temperature from 280 °C to 320 °C for the glass ceramics prepared by the two-stage heat treatment. The most likely reason is that the rod-like Sb_2Se_3 grow up more smoothly with less defects at the relatively high temperature, thanks to the higher mobility of the atoms leading to less stress in the crystals. Since crystal defects may become a recombination center of photo-generated electron-hole pairs [32], a high degree of crystallinity can increase photocatalytic activity due to lower defect level in the crystals.

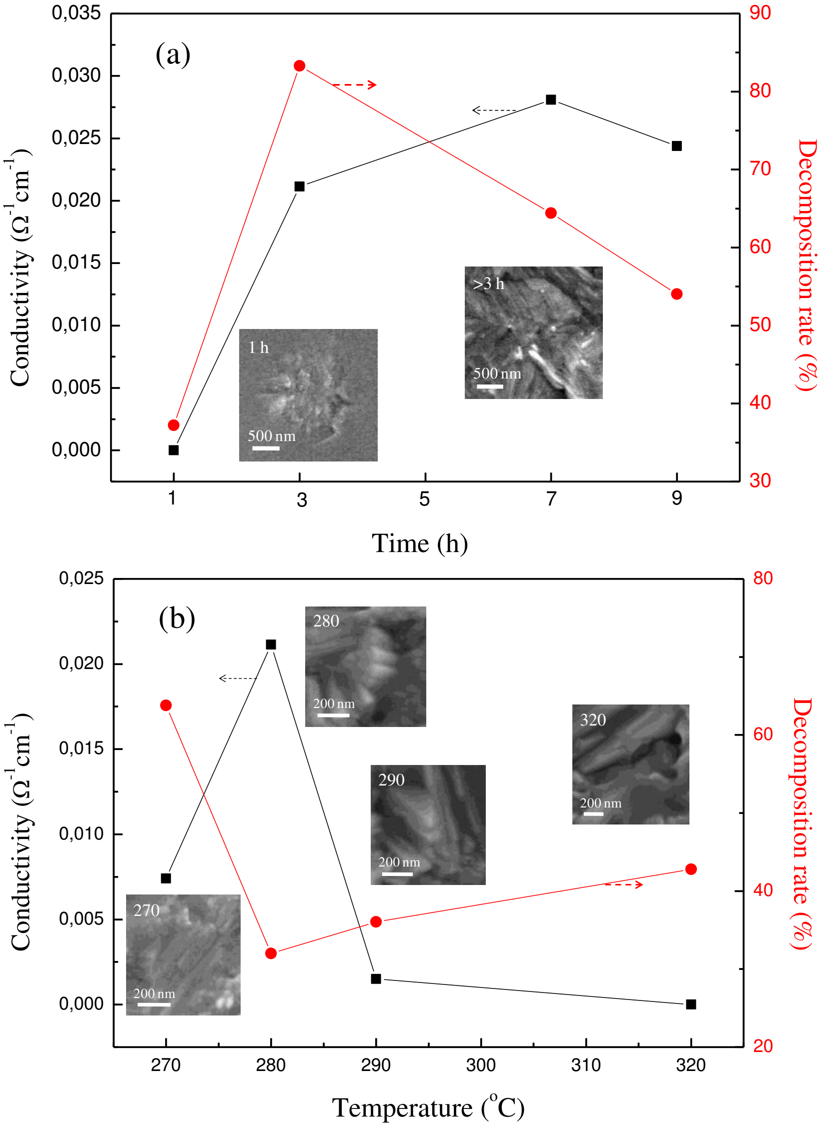

Figure 5-7 SEM images, conductivities and photocatalytic decomposition rates of MO for different glass ceramics prepared (a) by a single-stage heat treatment at 260 °C for different times; (b) by a two-stage heat treatment with different temperatures.

4 Photocatalytic reaction process of MO over the glass ceramic

Figure 5-8 illustrates the UV-vis absorption spectra of MO solutions photocatalytic degraded by the glass ceramic for different times. It can be seen that the absorption peak of the initial MO solution shifts from its characteristic value of 464 nm to 470 nm, which may be due to a detection error generated by the relatively high concentration of MO solution, leading to a very high absorption and a very low signal level. The absorption peek of MO solution at 464 nm is associated with the azo bond (–N=N–) [21] and is asymmetric. The broad absorption peak can be deconvoluted into two peaks centred at 464nm and 443 nm (as shown in Figure 5-9). This peak centred at 443 nm is attributed to a reverse photo-isomerization of the azobenzene compound, namely, an azobenzene molecule will change from thermodynamically stable trans structure (E-type) to cis structure (Z-type) under excitation of visible light (as shown in Figure 5-10) [33, 34]. The absorption peak centred at 276 nm is due to benzene charge-transfer absorption [35].

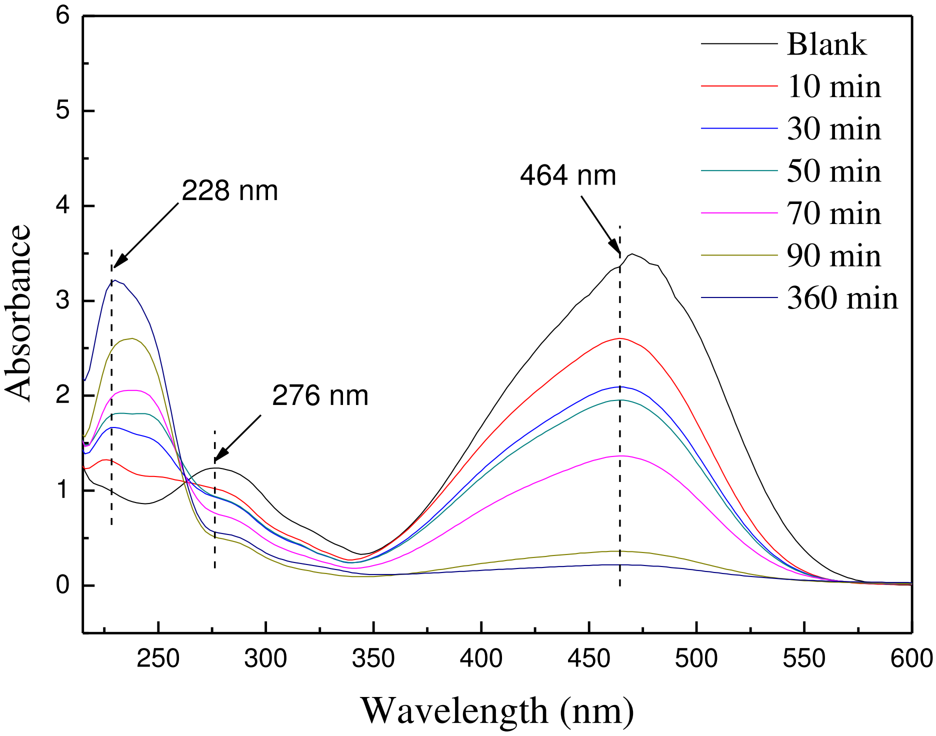

Figure 5-8 UV-vis absorption spectra of MO solutions before and after photocatalytic reaction for different times

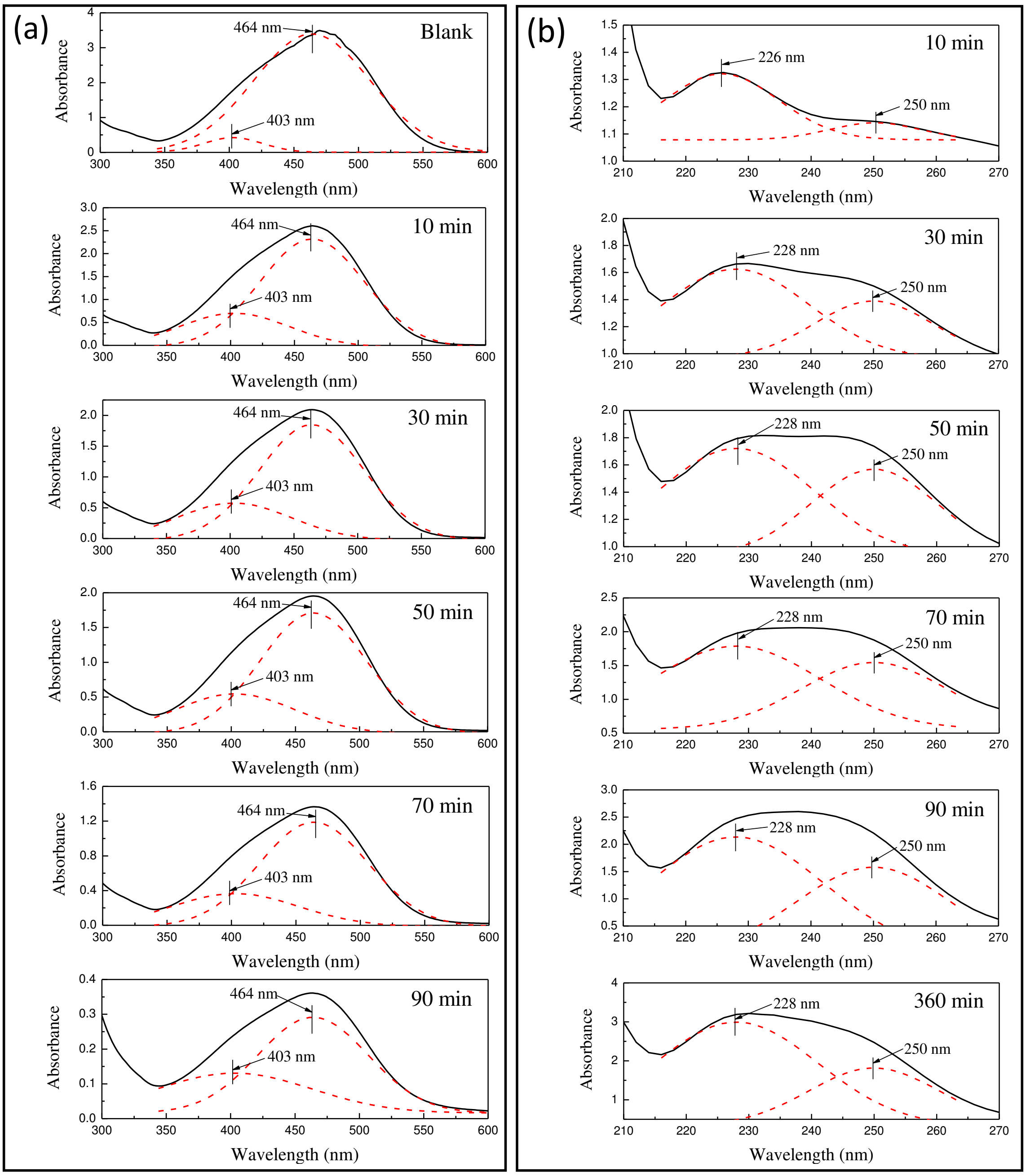

Figure 5-9 Peak fitting of UV-vis absorption spectra of MO solutions before and after photocatalytic reaction for different times

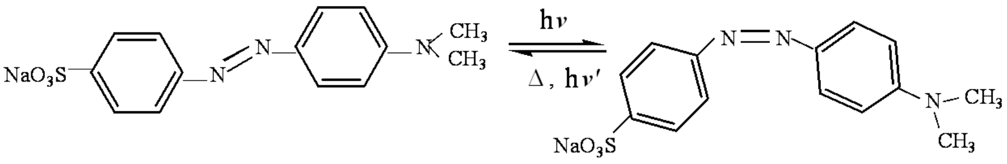

(E-type) (Z-type)

Figure 5-10 Photo–isomerization of MO molecular under light irradiation

With the progress of the photocatalytic reaction, the absorption peaks centred at 464 nm, 443 nm and 276 nm decrease gradually, and a new absorption peak ranged from 228 nm to 250 nm appears simultaneously, indicating that some intermediates may be generated. This new absorption peak can be deconvoluted into two peaks located at 228 nm (226 nm) and 250 nm, which probably correspond to 4-hydroxybenzenesulfonic acid sodium and 4-dimethylaminophenol respectively according to the Table 5-2.

Table 5-2 Single-ring aromatic intermediates of photodegraded MO azo [36-40]

Molecular formula	Maximum absorption wavelength (nm)	Molecular formula	Maximum absorption wavelength (nm)
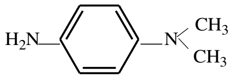	200	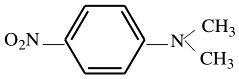	387
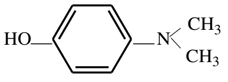	251	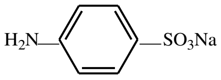	<200
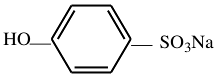	228	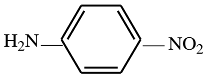	381
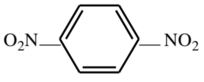	255	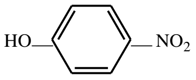	318
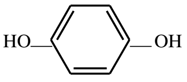	223	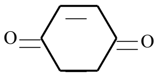	243
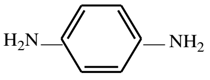	243	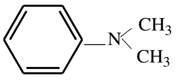	200
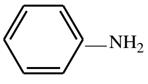	235	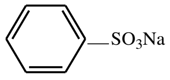	264
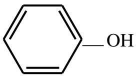	211	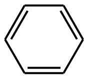	201

The N-demethylation of MO will occur due to the attack of hydroxyl radicals on the N,N-dimethyl groups, generating sulfanilic sodium and N,N-dimethylamino aniline, leading to the consequent decolorization [40, 41]. However, these products cannot be detected in the UV-vis absorption spectra ranged from 210 nm - 600 nm as its maximum absorption wavelength is shorter than 200 nm [41, 42]. With the N-demethylation of MO, the hydroxylation with deamination of the former two products occurs simultaneously, leading to the formation of 4-

hydroxybenzenesulfonic acid sodium and 4-dimethylaminophenol [41], which have characteristic UV-vis absorption peaks at 228 nm and 251 nm respectively according to Table 5-2. These results are in good agreement with the deconvolution of the absorption peak. Therefore, the amount of these two intermediates increases with the photocatalytic reaction time, which is illustrated by the increase of the corresponding absorption peaks (as shown in Figure 5-9). After 6 hours of photocatalytic reaction, the absorption intensity at 228 nm increases more obviously. This is likely because a hydroquinone (the most hydroxylated direct product) is produced from the degradation of 4-hydroxybenzenesulfonic acid sodium and 4-dimethylaminophenol. Hydroquinone has a maximum absorption peak of 223 nm [43], leading to the shift of the total absorption peak to shorter wavelength region. Therefore, the likely photocatalytic degradation pathway for MO in this reaction system can be proposed as shown in Figure 5-11. The glass ceramic photocatalyst exhibits a good oxidative deamination ability and its photocatalytic reaction process is different from that of most other photocatalysts reported before [36, 44]. Actually, this process is similar to the electrochemical oxidation process [41].

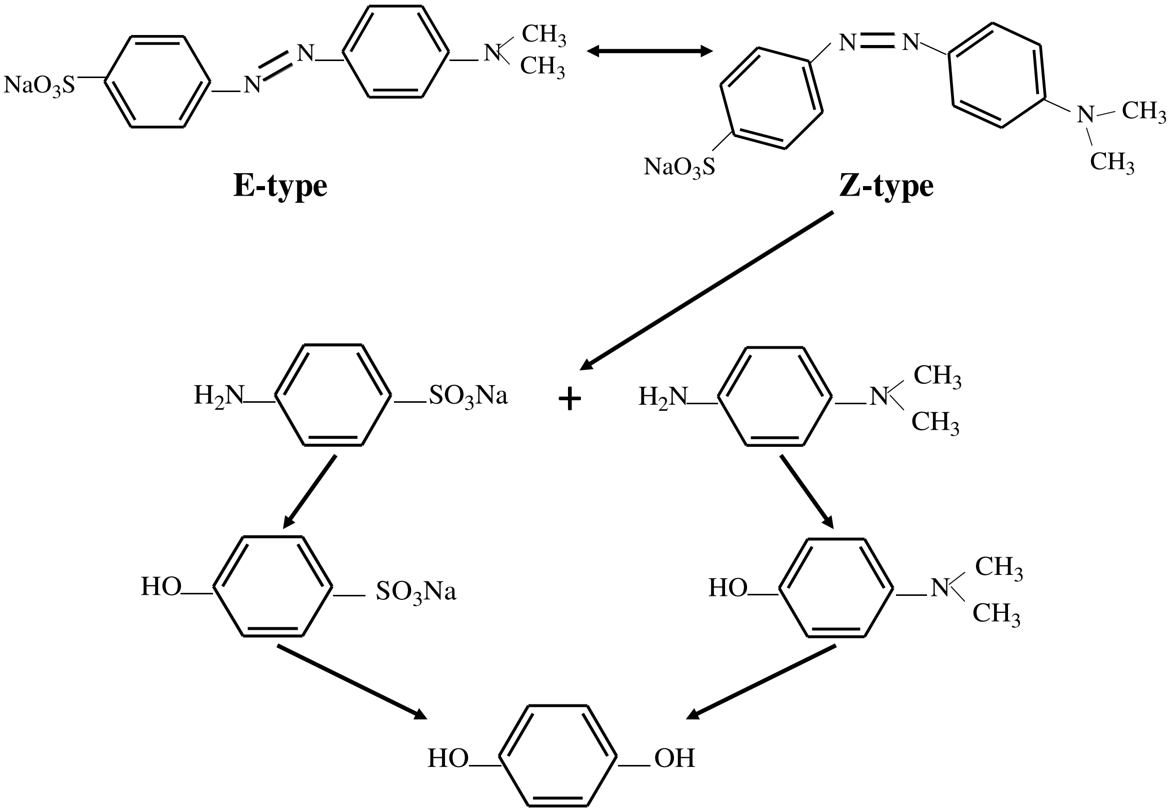

Figure 5-11 Main pathways proposed for MO photodegraded by the glass ceramic under visible light.

Figure 5-12 shows the plots of $\ln(C_0/C_t)$ versus photocatalytic reaction time for the glass ceramic photocatalyst and the commercially available P25 TiO_2 nano powders. We take the pseudo-first-order model, expressed by the equation of $\ln(C_0/C_t) = kt$, where k is the apparent first-order rate constant, to describe these two reactions for comparison. It is clear that the glass ceramic show a more complex photocatalytic mechanism, as described above.

It can be seen from Figure 5-12(a) and (b) that the glass ceramic exhibits an excellent photocatalytic degradation rate of 0.02108 h^{-1}, which is about 3.5 times higher than that of P25 TiO_2 nano powders (as shown in equation 5.2 and 5.3). It is interesting to note that a different photocatalytic reaction system with a photocatalyst dosage of 100mg and a MO concentration of 10 mg/L is adopted for the P25 TiO_2 nano powders due to its low visible photocatalytic activity. Therefore, under the same photocatalytic reaction conditions, the glass ceramic achieves a higher photocatalytic degradation rate of 0.03135 h^{-1} (as shown in Figure 5-12c and equation 5.4), which is about 5.3 times higher than that of P25 TiO_2 nano powders. Moreover, considering that the particle size of the glass ceramic powders between 20 μm- 30 μm is much larger than P25 TiO_2 nano powders (about 30 nm), the photocatalytic activity of the glass ceramic might be greatly improved just by decreasing the particle size. The fitting degree for the glass ceramic is quite low (R=0.87175 and 0.91559 respectively), indicating that the photocatalytic reaction over the glass ceramic is more complicated than P25 TiO_2 nano powders and there may exist some unknown time-dependent factors affecting the photocatalytic reaction.

$$\ln(C_0 / C_t) = 0.02108t \tag{5.2}$$

$$\ln(C_0 / C_t) = 0.00596t \tag{5.3}$$

$$\ln(C_0 / C_t) = 0.03135t \tag{5.4}$$

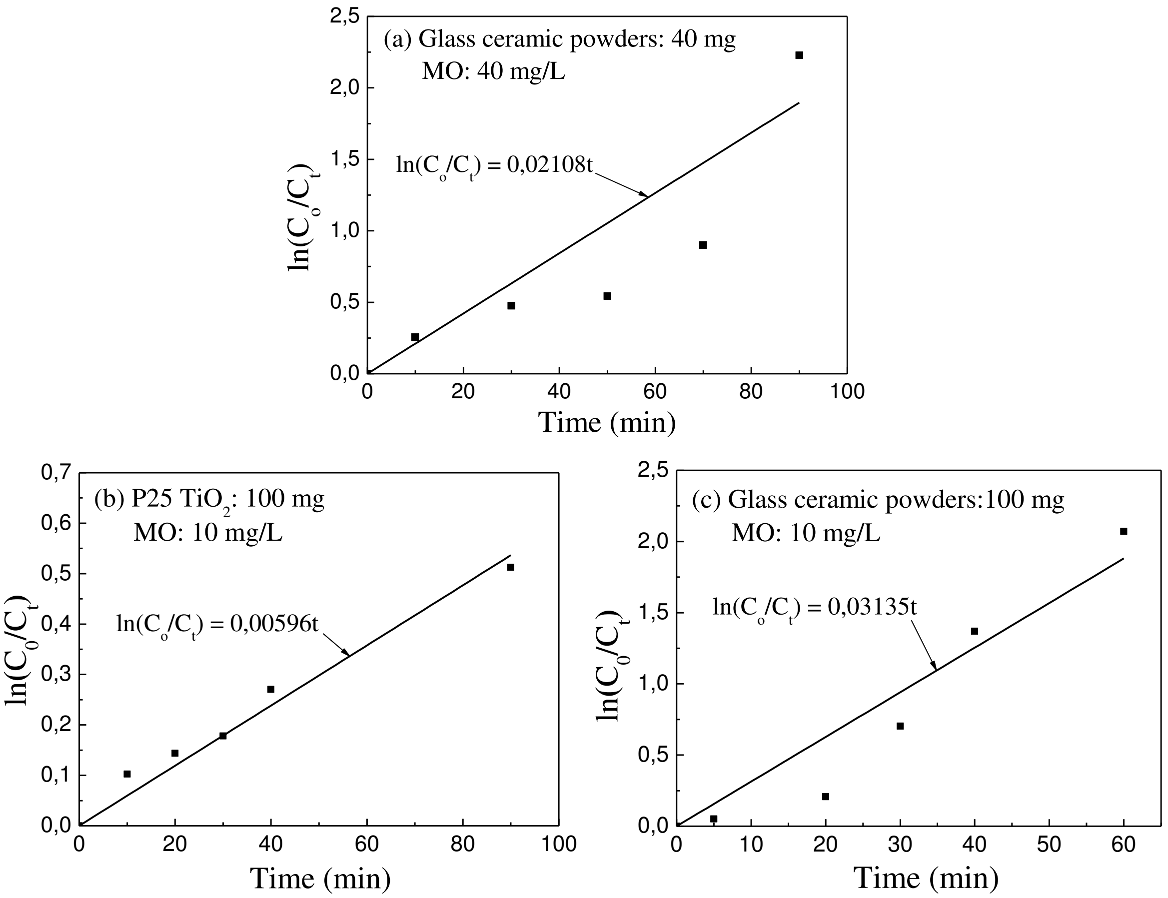

Figure 5-12 Plots of ln(C_0/C_t) versus photocatalytic reaction time for different photocatalytic reaction systems

5 Conclusion

The formation of nano-scale heterojunctions and conductive microdomains can induce an efficient separation of photo-generated carriers, leading to a high photocatalytic activity. Therefore, it is unnecessary to form conductive channels in the whole glass ceramic for the photocatalytic application. Moreover, in order to form conductive channels, the necessary increase of annealing time or/and temperature may decrease the photocatalytic activity due to its relatively large crystal grain size. This photocatalyst has a good oxidative deamination ability and high photocatalytic activity, demonstrating its potential as an efficient photocatalyst.

Reference

[1] M.R. Hoffmann, S.T. Martin, W. Choi, D.W. Bahnemann, Environmental applications of semiconductor photocatalysis, Chemical Reviews, 95 (1995) 69-96.

[2] A. Mills, S. Le Hunte, An overview of semiconductor photocatalysis, Journal of photochemistry and photobiology A: Chemistry, 108 (1997) 1-35.

[3] A. Fujishima, T.N. Rao, D.A. Tryk, Titanium dioxide photocatalysis, Journal of Photochemistry and Photobiology C: Photochemistry Reviews, 1 (2000) 1-21.

[4] P.K. Robertson, Semiconductor photocatalysis: an environmentally acceptable alternative production technique and effluent treatment process, Journal of cleaner production, 4 (1996) 203-212.

[5] D. Chen, M. Sivakumar, A.K. Ray, Heterogeneous photocatalysis in environmental remediation, Developments in Chemical Engineering and Mineral Processing, 8 (2000) 505-550.

[6] C. McCullagh, N. Skillen, M. Adams, P.K. Robertson, Photocatalytic reactors for environmental remediation: a review, Journal of Chemical Technology and Biotechnology, 86 (2011) 1002-1017.

[7] W. Li, C. Liu, Y. Zhou, Y. Bai, X. Feng, Z. Yang, L. Lu, X. Lu, K.Y. Chan, Enhanced photocatalytic activity in anatase/TiO_2(B) core−shell nanofiber, The Journal of Physical Chemistry C, 112 (2008) 20539-20545.

[8] M. Liu, D. Jing, Z. Zhou, L. Guo, Twin-induced one-dimensional homojunctions yield high quantum efficiency for solar hydrogen generation, Nature communications, 4 (2013) 2278.

[9] F.E. Osterloh, B.A. Parkinson, Recent developments in solar water-splitting photocatalysis, MRS bulletin, 36 (2011) 17-22.

[10] J. Tang, J. Ye, Photocatalytic and photophysical properties of visible-light-driven photocatalyst $ZnBi_{12}O_{20}$, Chemical physics letters, 410 (2005) 104-107.

[11] P. Wang, B. Huang, X. Zhang, X. Qin, H. Jin, Y. Dai, Z. Wang, J. Wei, J. Zhan, S. Wang, J. Wang, M.H. Whangbo, Highly efficient visible-light plasmonic photocatalyst Ag@AgBr, Chemistry – A European Journal, 15 (2009) 1821-1824.

[12] B.B. Kale, J.O. Baeg, S.M. Lee, H. Chang, S.J. Moon, C.W. Lee, $CdIn_2S_4$ nanotubes and “marigold” nanostructures: A visible-light photocatalyst, Advanced Functional Materials, 16 (2006) 1349-1354.

[13] I. Tsuji, H. Kato, H. Kobayashi, A. Kudo, Photocatalytic H_2 evolution reaction from aqueous solutions over band structure-controlled $(AgIn)_xZn_{2(1-x)}S_2$ solid solution photocatalysts with visible-light response and their surface nanostructures, Journal of the American Chemical Society, 126 (2004) 13406-13413.

[14] A. Kudo, K. Omori, H. Kato, A novel aqueous process for preparation of crystal form-controlled and highly crystalline $BiVO_4$ powder from layered vanadates at room temperature and its photocatalytic and photophysical properties, Journal of the American Chemical Society, 121 (1999) 11459-11467.

[15] Y. Huo, Y. Jin, Y. Zhang, Citric acid assisted solvothermal synthesis of $BiFeO_3$ microspheres with high visible-light photocatalytic activity, Journal of Molecular Catalysis A: Chemical, 331 (2010) 15-20.

[16] J. Wu, W. Walukiewicz, W. Shan, K.M. Yu, J.W. Ager, E.E. Haller, H. Lu, W.J. Schaff, Effects of the narrow band gap on the properties of InN, Physical Review B, 66 (2002) 201403.

[17] S.D. Sharma, D. Singh, K. Saini, C. Kant, V. Sharma, S. Jain, C. Sharma, Sol–gel-derived super-hydrophilic nickel doped TiO_2 film as active photo-catalyst, Applied Catalysis A: General, 314 (2006) 40-46.

[18] W. Zhang, Y. Li, S. Zhu, F. Wang, Surface modification of TiO_2 film by iron doping using reactive magnetron sputtering, Chemical physics letters, 373 (2003) 333-337.

[19] L. Ge, C. Han, J. Liu, Novel visible light-induced gC_3N_4/Bi_2WO_6 composite photocatalysts for efficient degradation of methyl orange, Applied Catalysis B: Environmental, 108 (2011) 100-107.

[20] H. Yan, H. Yang, TiO_2–gC_3N_4 composite materials for photocatalytic H_2 evolution under visible light irradiation, Journal of alloys and compounds, 509 (2011) L26-L29.

[21] M.I. Litter, R.J. Candal, J.M. Meichtry, Advanced oxidation technologies: Sustainable solutions for environmental treatments, Taylor & Francis, 2014.

[22] J.-C. Xu, M. Lu, X.Y. Guo, H.L. Li, Zinc ions surface-doped titanium dioxide nanotubes and its photocatalysis activity for degradation of methyl orange in water, Journal of Molecular Catalysis A: Chemical, 226 (2005) 123-127.

[23] W.F. Yao, H. Wang, X.H. Xu, S.X. Shang, Y. Hou, Y. Zhang, M. Wang, Synthesis and photocatalytic property of bismuth titanate $Bi_4Ti_3O_{12}$, Materials Letters, 57 (2003) 1899-1902.

[24] K. Danzer, Analytical chemistry: theoretical and metrological fundamentals, Springer, 2007.

[25] S. Kansal, M. Singh, D. Sud, Studies on photodegradation of two commercial dyes in aqueous phase using different photocatalysts, Journal of hazardous materials, 141 (2007) 581-590.

[26] J. Feng, X. Hu, P.L. Yue, Novel bentonite clay-based Fe-nanocomposite as a heterogeneous catalyst for photo-Fenton discoloration and mineralization of Orange II, Environmental science & technology, 38 (2004) 269-275.

[27] Y. Ohko, K. Hashimoto, A. Fujishima, Kinetics of photocatalytic reactions under extremely low-intensity UV illumination on titanium dioxide thin films, The Journal of Physical Chemistry A, 101 (1997) 8057-8062.

[28] Z. Zhang, C.-C. Wang, R. Zakaria, J.Y. Ying, Role of particle size in nanocrystalline TiO_2-based photocatalysts, The Journal of Physical Chemistry B, 102 (1998) 10871-10878.

[29] B. Neppolian, H. Choi, S. Sakthivel, B. Arabindoo, V. Murugesan, Solar light induced and TiO_2 assisted degradation of textile dye reactive blue 4, Chemosphere, 46 (2002) 1173-1181.

[30] S. Sakthivel, B. Neppolian, M. Shankar, B. Arabindoo, M. Palanichamy, V. Murugesan, Solar photocatalytic degradation of azo dye: comparison of photocatalytic efficiency of ZnO and TiO_2, Solar Energy Materials and Solar Cells, 77 (2003) 65-82.

[31] G. Chen, M. Sun, Q. Wei, Y. Zhang, B. Zhu, B. Du, Ag_3PO_4/graphene-oxide composite with remarkably enhanced visible-light-driven photocatalytic activity toward dyes in water, Journal of hazardous materials, 244 (2013) 86-93.

[32] X.H. Wu, C.R. Elsass, A. Abare, M. Mack, S. Keller, P.M. Petroff, S.P. DenBaars, J.S. Speck, S.J. Rosner, Structural origin of V-defects and correlation with localized excitonic centers in InGaN/GaN multiple quantum wells, Applied Physics Letters, 72 (1998) 692-694.

[33] H. Dürr, H. Bouas-Laurent, Photochromism: Molecules and systems, Elsevier Science, 2003.

[34] A. Dirksen, E. Zuidema, R. Williams, L. De Cola, C. Kauffmann, F. Vögtle, A. Roque, F. Pina, Photoactivity and pH sensitivity of methyl orange functionalized poly (propyleneamine) dendrimers, Macromolecules, 35 (2002) 2743-2747.

[35] G.D. Costanzo, S. Goyanes, S. Ledesma, Using photosensitive dye to improve multi walled carbon nanotubes dispersion, Journal of Physics: Conference Series, 274 (2011) 012117.

[36] I.K. Konstantinou, T.A. Albanis, TiO_2-assisted photocatalytic degradation of azo dyes in aqueous solution: kinetic and mechanistic investigations: A review, Applied Catalysis B: Environmental, 49 (2004) 1-14.

[37] S.R. Laboratories, Sadtler standard spectra: Ultraviolet spectra, Sadtler, 1996.

[38] C. Galindo, P. Jacques, A. Kalt, Photochemical and photocatalytic degradation of an indigoid dye: a case study of acid blue 74 (AB74), Journal of Photochemistry and Photobiology A: Chemistry, 141 (2001) 47-56.

[39] J.M. Joseph, H. Destaillats, H.-M. Hung, M.R. Hoffmann, The sonochemical degradation of azobenzene and related azo dyes: rate enhancements via Fenton's reactions, The Journal of Physical Chemistry A, 104 (2000) 301-307.

[40] C. Galindo, P. Jacques, A. Kalt, Photodegradation of the aminoazobenzene acid orange 52 by three advanced oxidation processes: UV/H_2O_2, UV/TiO_2 and VIS/TiO_2: Comparative mechanistic and kinetic investigations, Journal of Photochemistry and Photobiology A: Chemistry, 130 (2000) 35-47.

[41] C. Ramírez, A. Saldaña, B. Hernández, R. Acero, R. Guerra, S. Garcia-Segura, E. Brillas, J.M. Peralta-Hernández, Electrochemical oxidation of methyl orange azo dye at pilot flow plant using BDD technology, Journal of Industrial and Engineering Chemistry, 19 (2013) 571-579.

[42] J. Fan, Y. Guo, J. Wang, M. Fan, Rapid decolorization of azo dye methyl orange in aqueous solution by nanoscale zerovalent iron particles, Journal of Hazardous Materials, 166 (2009) 904-910.

[43] J. Zhang, A. Zhou, Q. Xie, W. Wei, A long path length spectroelectrochemical behavior analysis of the coabsorption system, Talanta, 52 (2000) 903-908.

[44] T. Tong, J. Zhang, B. Tian, F. Chen, D. He, Preparation of Fe^{3+}-doped TiO_2 catalysts by controlled hydrolysis of titanium alkoxide and study on their photocatalytic activity for methyl orange degradation, Journal of Hazardous Materials, 155 (2008) 572-579.

General conclusions and perspectives

The photoelectrical properties of the 40$GeSe_2$-40Sb_2Se_3-20CuI glass ceramics were found by chance when we studied the $GeSe_2$-Sb_2Se_3 based glass ceramics for infrared transmission. During the past ten years, in order to obtain glasses with controllable crystal growth, some new compositions have been studied by introducing halides such as CsCl, CsBr, CsI, RbI, PbI_2, ZnI_2, CuI into this system. Previous works indicated that CuI can be introduced into these glasses in large quantity, leading to controllable crystallization. However, glass ceramics from the $GeSe_2$-Sb_2Se_3-CuI system demonstrated unusual optical absorption in the mid infrared region (2-10 μm). Indeed, the absorption increases with increasing wavelength, indicating the existence of free charge carriers. Consequently, a more detailed study was then performed.

At the beginning, a fast screening of glass ceramics in the $GeSe_2$-Sb_2Se_3-CuI system in relationship with the photo-electro-chemical properties was carried out. Surprisingly, the highest photocurrent was still only achieved in the glass ceramic with the 1st selected composition of 40$GeSe_2$-40Sb_2Se_3-20CuI. Further studies indicated that the 40$GeSe_2$-40Sb_2Se_3-20CuI glass ceramic has a unique microstructure, consisting of interconnected micrometer-size crystalline domains. Each domain was composed of parallel Sb_2Se_3 rods, between which Cu_2GeSe_3 nanocrystals are concentrated. This structure was believed to play an important role in the generation of photocurrent in glass ceramic. Consequently, it is necessary to study the crystallization mechanism in order to optimize the microstructure of the 40$GeSe_2$-40Sb_2Se_3-20CuI glass ceramic. Two kinds of crystallization method, i.e. single-stage and two-stage thermal treatment processes, were investigated by following the structure-property relationship of the obtained glass ceramics. The single-stage heat treatment process was found to be a more efficient strategy to obtain such rod-like clustered domain, especially by crystallizing the base glass at relatively low temperature for long time. This thermal treatment is so far the best way to prepare glass ceramics with the highest photocurrent intensity.

Further studies of the microstructure and other properties of the 40$GeSe_2$-40Sb_2Se_3-20CuI glass ceramic revealed its detailed structure information as well as the mechanism of charge photogeneration, separation and transport. The Cu_2GeSe_3 nanocrystals grew on the surface of iodine-doped Sb_2Se_3 rods, leading to the formation of p-n junctions. At the same time, the relatively conductive Cu_2GeSe_3 nanocrystals connected to each other along the doped Sb_2Se_3 rod orientation, thereby forming a conductive microdomain. The interconnected conductive microdomains eventually provided macroscopic conductive channels for the glass ceramic. Consequently, the photo-generated charge carriers firstly can be efficiently separated by the p-n junctions, and then transported though the conductive channels in the glass ceramic, leading to exceptionally long lifetime of charge carriers (around 16 μs) and high photocurrent (at least 100 times higher than any of Sb_2Se_3 and Cu_2GeSe_3 individually). Moreover, this glass ceramic also exhibited a high photocatalytic activity and the demonstration was made through the photocatalytic decomposition of methyl orange selected as an example. Therefore, this glass ceramic can be considered as an efficient photocatalyst, even still much more work need to be done.

To the best of our knowledge, this is the first report on interpenetrating heterojunctions in glass ceramic systems or even in inorganic materials. Similar microstructures are even relatively new for organic materials and have received much attention. This kind of bulk heterojunctions has led to a key breakthrough for improving the efficiency of polymer photovoltaic solar cells.

This pioneer work could be interesting for developing a totally new family of glass ceramic with highly efficient photoelectrical and photocatalytic activities. The final objective is of course to contribute to the design of totally new materials for converting efficiently the solar energy into electrical or chemical energy. Of course, up to now, the exact structure-property relationship, the charge photo-generation mechanism as well as certain properties are still to be understood. We believe that this work is only the beginning of an important research topic. Future studies could be carried out in the directions:

(1) Developing new material systems with still more efficient semiconducting phases. The two innovative features provided by this unique structure are conductive channels and randomly distributed nano p-n junctions along the conductive channels. The fabrication of conductive channels opens the possibility of using materials with low electrical conductivity but excellent properties (high absorption, efficient charge photogeneration…) for photovoltaic application. Moreover, a multiple-heterojunction system, which may contain several semiconductors having complementary bandgap for better covering the entire solar spectrum, could also be fabricated along a conductive channel to increase the conversion efficiency of the whole solar spectrum.

(2) Developing new material systems to achieve low cost. The glass ceramic is prepared by crystallizing the base glass with the composition of $40GeSe_2$-$40Sb_2Se_3$-$20CuI$. Therefore, even if copper is totally with germanium to form Cu_2GeSe_3, 75% of germanium stays in the glass matrix. Based on our current understanding, the residual glassy phase does not play an important role for obtaining the interesting photoelectric properties of the glass ceramic. Consequently, the content of germanium could probably be decreased to achieve low cost.

Moreover, looking for new low-cost and highly conductive alternative materials to fabricate a conductive channel may be another potential research direction of the glass ceramic.

(3) Optimizing the glass ceramic for photovoltaic application. In this thesis, we just presented a new glass ceramic with unique microstrcture as well as corresponding basic photoelectric properties. But how to use it for photovoltaic application is unclear, and other properties of this glass ceramic also need to be further investigated from the viewpoint of photovoltaic application. Moreover, the preparation of a glass-ceramic film for a potential application in photoelectric film devices is also a promising work, which is ongoing in our laboratory.

(4) Optimizing the glass ceramic for photocatalytic application. The glass ceramic can be used as a new photocatalyst due to its high photocatalytic activity illustrated by the good oxidative deamination ability. However, for its application, there is still many works to do. Firstly, as a highly efficient photocatalyst, the particle size of the glass ceramic powders need to be further decreased to achieve high specific surface area. Secondly, considering the recovery of photocatalyst, loading technology of the glass ceramic powders, for example by preparing glass-ceramic coating, is certainly to be developed. Finally, the design of photocatalytic reactor based on the glass-ceramic photocatalyst is also an important work, especially for the design of gas-phase photocatalytic reactor considering the hydrophobic feature of the glass ceramic. Surface modification of the glass ceramic may be also necessary.

VU :	VU :
Le Directeur de Thèse (Nom et Prénom)	**Le Responsable de l'École Doctorale**

VU pour autorisation de soutenance

Rennes, le

Le Président de l'Université de Rennes 1

Guy CATHELINEAU

VU après soutenance pour autorisation de publication :

Le Président de Jury,
(Nom et Prénom)

Abstract

A totally new family of glass ceramics with a unique microstructure was fabricated by controlling the crystallization of the $GeSe_2$-Sb_2Se_3-CuI glass system. The influences of the material composition and the crystallizing process of the precursor glasses on the microstructure and photocurrent of the prepared glass ceramics were investigated. An optimized composition, $40GeSe_2$-$40Sb_2Se_3$-20CuI, was particularly studied with the following significant results:

(1) After a systematic study, it was found that this particular composition shows the highest photocurrent density among all studied glasses in the pseudo-ternary $GeSe_2$-Sb_2Se_3-CuI system. It is also demonstrated that the photocurrent generated by different glass ceramics is not only determined by the composition, but also by the composite microstructure of the glass ceramic, which is determined by the ceramisation process. This process was then carefully studied. Compared with the two-step heat treatment process, the single-step process at a low temperature is a more efficient strategy to build up an efficient composite microstructure, which promotes charge carrier separation and provides a conductive channel, leading to a high photocurrent intensity in the glass ceramic.

(2) The above-mentioned unique composite microstructure is composed of interconnected conductive microdomains, formed by low conductive rod-like Sb_2Se_3 crystals, covered by relatively high conductive Cu_2GeSe_3 nanocrystals. The most likely process for efficient photogeneration of charges is proposed as follows: photons are efficiently and essentially absorbed by Sb_2Se_3 as well as by Cu_2GeSe_3, and then the heterojunction formed by n-type Sb_2Se_3 and p-type Cu_2GeSe_3 promotes the charge separation, whereas the oriented and relatively conductive Cu_2GeSe_3 aggregate provides a conductive channel and plays the role of efficient charge collector. This structure results in exceptionally long lifetime of charge carriers (around 16 μs) and high photocurrent (at least 100 times higher than any of Sb_2Se_3 and Cu_2GeSe_3 individually).

(3) The formation of nano-heterojunctions between Sb_2Se_3 and Cu_2GeSe_3 crystals within a single conductive microdomain can fully lead to an efficient separation of photo-generated electrons and holes. Therefore, for the photocatalytic application, it is unnecessary to form conductive channels (interconnected conductive microdomains) in the whole glass ceramic. Moreover, in order to form conductive channels, the necessary increase of annealing time or/and temperature may decrease the photocatalytic activity due to its relatively large crystal grain size. The optimized glass ceramic exhibits a good oxidative deamination ability and high photocatalytic activity, demonstrating its potential as an efficient photocatalyst.

Keywords: chalcogenide glasses; glass ceramic; heterojunction; photovoltaic effect; photocatalysis

RESUME

Une nouvelle famille de vitrocéramiques, avec une microstructure inédite, a été fabriquée par une cristallisation contrôlée des verres dans le système $GeSe_2$-Sb_2Se_3-CuI. L'influence de la composition et du processus de cristallisation des verres de base, sur la microstructure et sur l'intensité du photo-courant des vitrocéramiques a été étudiée. Une composition optimisée, le $40GeSe_2$-$40Sb_2Se_3$-20CuI, a été particulièrement étudiée avec des résultats suivants :

(1) Après une étude systématique , il a été constaté que cette composition donne la plus forte intensité de photo-courant parmi tous les verres étudiés dans ce système pseudo-ternaire $GeSe_2$-Sb_2Se_3-CuI. Il a été également démontré que le photo-courant généré par différentes vitrocéramiques est non seulement déterminé par la composition, mais aussi par la microstructure composite de la vitrocéramique, qui est déterminée par le processus de céramisation. Ce processus de céramisation a ensuite été optimisé. Par rapport au procédé de traitement thermique en deux étapes, le procédé en une seule étape à basse température est une stratégie plus appropriée pour obtenir une microstructure efficace, favorisant la séparation des charges, construisant des canaux conducteurs et donnant une intensité de photo-courant élevée dans la vitrocéramique.

(2) La microstructure composite inédite, discutée ci-dessus est composée de micro-domaines conducteurs interconnectés, formées par des cristaux Sb_2Se_3 faiblement conducteur en forme de tiges, couverts par des nano-cristaux de Cu_2GeSe_3 beaucoup plus conducteurs. Le procédé le plus probable de la photo-génération efficace des charges est le suivant: les photons sont efficacement et essentiellement absorbés par Sb_2Se_3 ainsi que par Cu_2GeSe_3. Les hétérojonctions formées par les Sb_2Se_3 du type n et les Cu_2GeSe_3 du type p, favorisent la séparation de charges, tandis que les Cu_2GeSe_3 interconnectées et conductrices fournissent des canaux conducteurs et jouent ainsi le rôle de collecteur efficace de charges. Il en résulte ainsi une très longue durée de vie des porteurs de charge (environ 16 µs) et un fort photo-courant (au moins 100 fois plus élevé que Sb_2Se_3 ou Cu_2GeSe_3 séparément).

(3) La formation de nano-hétérojonctions entre les cristaux Sb_2Se_3 et Cu_2GeSe_3 dans un seul micro-domaine peut conduire à une séparation efficace des électrons et des trous photo-générés. Par conséquent, pour application photo-catalytique, il n'est pas nécessaire de former des canaux conducteurs (conducteurs interconnectés des micro-domaines) dans l'ensemble de la vitrocéramique. De plus, la formation de ces canaux conducteurs, nécessiterait une augmentation de la durée ou/et la température de recuit, pouvant conduire à une diminution de l'activité photo-catalytique à cause de la taille relativement grande des grains cristallins. Les vitrocéramiques optimisées montrent une bonne capacité de désamination oxydative et une forte activité photo-catalytique en général, démontrant ainsi son potentiel en tant que photo-catalyseur efficace.

Mots-clés: verres de chalcogénures ; vitrocéramiques; hétérojonction; effet photovoltaïque; photo-catalyse